Positron Production in Multiphoton Light-by-Light Scattering

Thomas Koffas

Stanford Linear Accelerator Center
Stanford University
Stanford, CA 94309

---

*Ph.D. thesis, University of Rochester

Positron Production in

Multiphoton Light-by-Light Scattering

by

Thomas Koffas

Submitted in Partial Fulfillment

of the

.Requirements for the Degree

Doctor of Philosophy

Supervised by

Professor A. C. Melissinos

Department of Physics and Astronomy

The College

Arts and Sciences

University of Rochester

Rochester, New York

1998

Curriculum Vitae

Thomas Koffas ███████████████████████ He received his bachelor's degree in Physics from the University of Athens in 1993. As an undergraduate he worked at the Delphi experiment at CERN during the summer of 1991 and then in the NESTOR experiment under Professor L. K. Resvanis. In the summer of 1993 he started graduate studies towards his Ph.D. degree in the Physics Department of the University of Rochester, where he joined the E-144 collaboration under Professor A. C. Melissinos. The present thesis contains the results of the work done within that collaboration.

Acknowledgments

It is hard to express my thanks and gratitude to all the people that helped and worked with me during my graduate student career. First I would like to thank the people at the University of Rochester, who advised me during my first steps of graduate work, Pat Borelli, Tom Haelen, Larry Kuntz and Alan Fry. David Reis shared with me innumerable hours of studying for classes and working in the lab at SLAC and in addition his friendship as a side benefit.

At SLAC a number of people in the E-144 collaboration were instrumental for the success of the experiment and the completion of this thesis. Much of my initial work involved working with the University of Rochester people based at SLAC, among which Theofilos Kotseroglou, Steve Boege and Charlie Bamber were the more prominent. Professor David Meyerhofer, the driving force behind the laser, shared with me at least a small fraction of his vast knowledge about lasers. Long discussions with Glenn Horton-Smith, Kostya Shmakov, Clive Field and Kirk McDonald were a constant source of inspiration and their ideas and observations are reflected in this thesis. But most of all I would like to thank Christian Bula my main advisor especially during the most recent years at SLAC. Most of the data analysis presented in this thesis is laid on the foundations that he first built.

I would also like to thank the people in the broader E-144/FFTB family at SLAC, who helped me during my accelerator work. Jim Spencer was the first to introduce me in the field of beam optics. Peter Tenenbaum taught me a lot about final focusing configurations and also shared with me his excitement for real time accelerator operations. I am most thankful to David Burke for his constant support and trusting in my capabilities and for helping me to take advantage of as much as possible of the numerous opportunities for learning about accelerator physics offered at SLAC.

My highest acknowledgment is due to my advisor and mentor during my graduate student career, Adrian Melissinos. He is an excellent teacher and advisor. His unique physical insight is of the kind that makes a physicist great. His continuous encouragement for hard work was essential for completing this thesis.

Last but not least I would like to thank my parents Georgios and Amalia for their love and constant support, my brother Mattheos for, among other things, sharing with me the good and bad moments of a graduate student's life and my Greek friend of old P. Kousoulis for being a friend even from 10,000 miles away.

Abstract

We present the results of an experimental study on e^+e^- pair production during the collision of a low emittance 46.6 GeV electron beam with terawatt laser pulses from a Nd:glass laser at 527 nm wavelength and with linear polarization. The experiment was conducted at the Final Focus Test Beam facility in the Stanford Linear Accelerator Center. Results with a 49.1 GeV electron beam are also included. A signal of 106 ± 14 positrons for the 46.6 GeV electron beam case and of 22 ± 10 positrons for the 49.1 GeV case above background, has been detected. We interpret the positrons as the products of a two-step process during which laser photons are backscattered to high energy gamma photons that absorb in their turn several laser photons in order to produce a e^+e^- pair. The data compare well with the existing theoretical models. This is the first observation in the laboratory of inelastic light-by-light scattering with only real photons. Alternatively, the data are interpreted as a manifestation of the spontaneous breakdown of the vacuum under the influence of an intense external alternating electric field.

Contents

List of Tables

List of Figures

Chapter 1

Introduction

1.1 Physical Motivation

Quantum electrodynamics (QED) has been tested extensively in the weak field regime, where the theoretical perturbative methods lead to results that agree to a fantastic accuracy with the measured data. In the case of strong fields the application of perturbative techniques is of limited applicability and the different processes can be treated only within a semi-classical theoretical frame. This strong field region has traditionally been defined as the one for which external electrostatic fields approach or exceed the QED critical field strength

$$\mathcal{E}_{crit} = m^2/e = 1.32 \times 10^{16} \text{ V/cm} \quad (\hbar = c = 1) \tag{1.1}$$

which is defined as the field for which the energy gain of an electron, when accelerated along a distance equal to its Compton wavelength, is equal to its rest mass. Developments in intense "table-top" laser technology, allow short light pulses to achieve field strengths of the order of $\sim 10^{11}$ V/cm over a small focal spot area. Such a laser, employed in an experiment at the Stanford Linear Accelerator Center (SLAC), achieved a peak field strength of 3×10^{10} V/cm. In the rest frame of a 46.6 GeV electron, as provided by the two-mile long linac at SLAC, and for head-on collisions,

this is equivalent to 5.6×10^{15} V/cm and very close to the critical QED field strength. In fields of this strength various nonlinear effects become dominant.

The production of e^+e^- pairs during the scattering was of two real photons was first considered by Breit and Wheeler:

$$\omega_1 + \omega_2 \longrightarrow e^+e^- \qquad (1.2)$$

The cross section for this process was calculated to be of the order of πr_0^2, where r_0 the classical electron radius [1]. Notice that this interaction differs from the Bethe-Heitler process which involves one real and one virtual photon from the field of the nucleus [2]. Interaction 1.2 has never been observed in the laboratory, although it is believed to occur in astrophysical processes [3]. Already in their paper Breit and Wheeler commented on the hopelessness of observing such a process in the laboratory, due to insufficient photon densities available experimentally and the smallness of the cross-section.

The availability of strong external fields provided by intense lasers, led to a reconsideration of the Breit-Wheeler process by Reiss [4] and others [5], [6]. It is clear that energy conservation dictates that the minimum center-of-mass (CM) energy of the interacting photons for the production of one pair, must be at least $2m \approx 1$ MeV. This obviously precludes the production of a pair by two colliding laser beams. Nevertheless sufficient CM energy can be achieved if the laser beam interacts with a very energetic photon beam, like the one produced by the backscattering of the laser beam off a high energy electron beam. For a green laser with wavelength $\lambda = 527$ nm (2.35 eV), a minimum gamma energy of 111 GeV is necessary. Even at SLAC with a 46.6 GeV electron beam, the maximum energy of the backscattered gamma from a 527-nm laser is only 29.2 GeV. But in strong electromagnetic fields, as the one that the laser mentioned above can deliver, the initial states for the production of a pair, can involve more than one laser photon [4] and in fact the number of the interacting

photons becomes very large as the dimensionless invariant parameter η defined as,

$$\eta = \frac{e\sqrt{-\langle A_\mu A^\mu \rangle}}{m} = \frac{e\mathcal{E}_{rms}}{m\omega_0} \quad (\hbar = c = 1) \qquad (1.\text{:})$$

approaches or exceeds unity. In Eq. 1.3 ω_0 is the laser laboratory energy, $\mathcal{E}_{rms}$ the root-mean-square of the electric field of the laser, A^μ is the 4-vector potenti and m, e are the mass and charge of the electron. For the peak electric field 3×10^{10} V/cm $\Rightarrow \mathcal{E}_{rms} = 2.2 \times 10^{10}$ V/cm, for a 527-nm laser, $\eta \simeq 0.36$.

Therefore the pair production can be viewed as the result of a two-step proces first the interaction

$$e^- + n\omega_0 \longrightarrow e'^- + \omega_\gamma \qquad (1.\text{·})$$

necessary to produce the high energy backscattered gamma ω_γ takes place and it followed by

$$\omega_\gamma + n\omega_0 \longrightarrow e^+e^- \qquad (1.\text{:})$$

which can be considered as the generalization of the single photon Breit-Wheel process. For a 29 GeV gamma and a 527-nm laser, this last interaction becom accessible for $n \geq 4$ photons. The two processes can take place at two differe interaction regions; in the first region the high energy gammas are produced a are then transported to the second region where the pairs are produced. They c also happen within the focal region of a single laser, where the energetic gamm produced by the first interaction (by multiphoton Compton scattering) can intera with n laser photons, while still inside the laser focus, and produce pairs. In fact, t latter configuration is the one used to interpret the observed positron data report in this thesis. A possible background source in this case is the process

$$e + n\omega_0 \longrightarrow e'e^+e^- \qquad (1.\text{·})$$

to which we refer as the trident process. For a 527-nm laser the trident proce requires $n \geq 5$ laser photons colliding with a 46.6 GeV electron beam.

E144 Detectors and Diagnostics
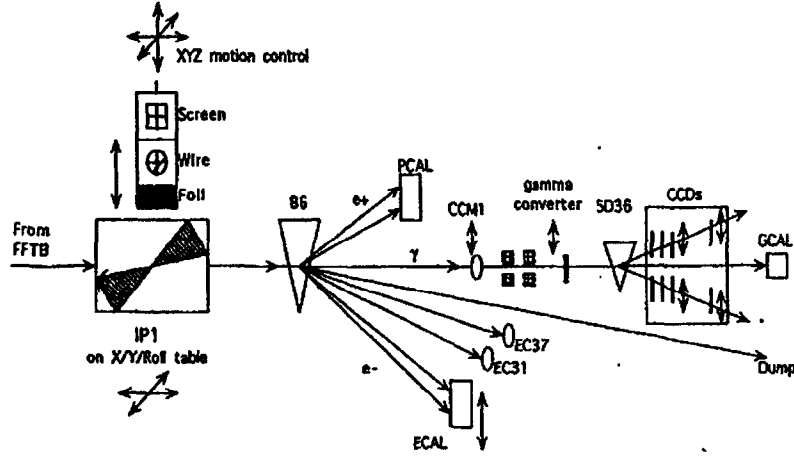
Figure 1.1: Schematic of the experimental setup.

In the case where the process of Eq. 1.5 involves many laser photons simultaneously, we can consider it as an interaction with the field as a whole and not with individual quanta. Then we can interpret it as a barrier penetration process, where virtual e^+e^- pairs become real when they are spatially separated by the external field with the expenditure of energy. The potential energy necessary for this is $e\mathcal{E}\Delta l \geq 2m$ and for Δl of the order of a Compton wavelength, it leads to the value of the critical QED field strength. The probability for penetrating a barrier with "thickness" Δl is given by

$$P \sim \exp\left(-\frac{\pi m^2}{e\mathcal{E}}\right) = \exp\left(-\frac{\pi}{\Upsilon}\right) \quad (\hbar = c = 1) \tag{1.7}$$

where

$$\Upsilon = \mathcal{E}^*/\mathcal{E}_{crit} \tag{1.8}$$

an invariant and dimensionless quantity; $\mathcal{E}^*$ is the field as seen in the pair rest frame. These reactions will be discussed extensively in the following chapter, while the final comparison with the measured data is given in the last chapter of this thesis.

1.2   Experimental Overview
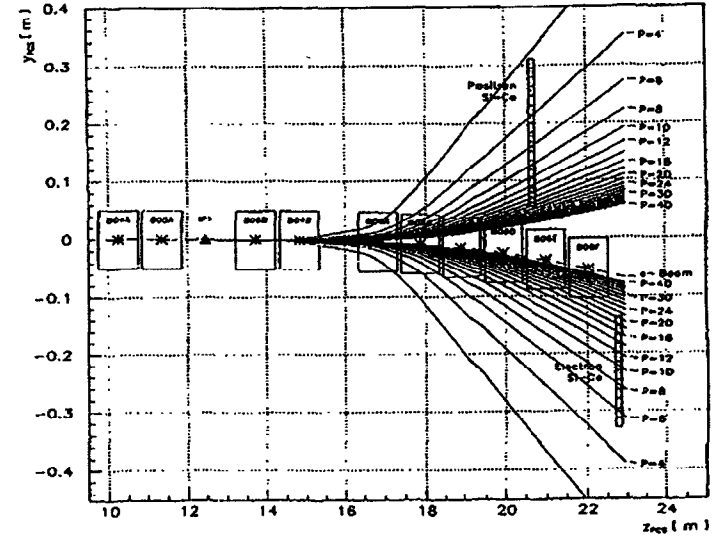
Figure 1.2: Schematic of the FFTB dumpline, where the E-144 experiment is located.

The experiment (SLAC,E-144), was carried out in the Final Focus Test Beam (FFTB) line at the Stanford Linear Accelerator Center (SLAC). FFTB is a prototype beam line designed to study the focusing of high energy electron beams down to 50 nanometer spot sizes, which is one of the major challenges that need be addressed in the Next Linear Collider (NLC) design [7]. The exact location of the E-144 experimental setup is the FFTB dump or extraction line. A schematic of the magnets in that line is shown in Fig. 1.2. Fig. 1.1 shows the layout of the detectors and diagnostics used during the data collection. The electron beam is brought down to the interaction region (IP), which is located 12 m downstream of the FFTB Final Focus (FF), and is focused to a roughly 25 μm $\times$ 35 μm spot size. A set of 20 μm thick Al wires are used to measure the electron beam spot sizes at the IP. Electrons of energy 46.6 GeV or 49.1 GeV in 7 ps FWHM bunches containing 5-7 $\times 10^9$ electrons, were delivered

to the IP. The tuning of the electron beam and measurement of the beam size are described in more detail in chapter 3.
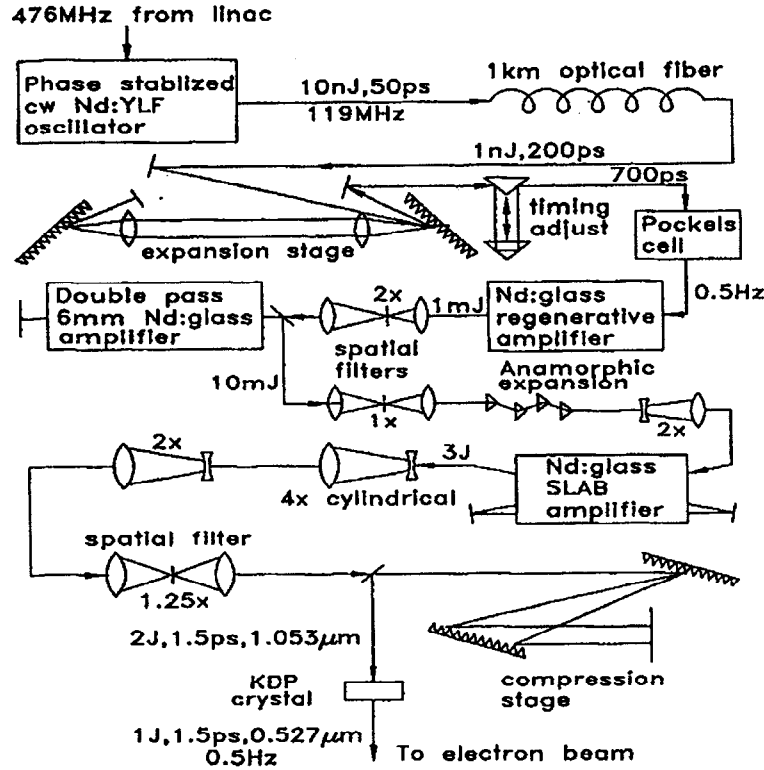
Figure 1.3: Overview of the laser system.

The laser is a Table Top Terrawatt (T^3) laser, that operates at a 0.5 Hz repetition rate. A schematic of the laser is shown in Fig. 1.3. It can deliver pulses at wavelength $\lambda = 1054$ nm, or after frequency doubling at $\lambda = 527$ nm (green) [8]. The polarization of the laser beam can be chosen to be either linear or circular, using a liquid crystal polarizer. Both IR and green laser pulses have been delivered at the interaction point, with maximum energies of 2 J and 1 J respectively. The laser pulse is focused down

to 2 times its diffraction limited area for the IR case, and 4.7 times for the green case, while the pulse lengths achieved are 1.5 ps for both wavelengths. Intensities above 10^{18} W/cm^2 at the laser focus have been achieved. The laser is based on the Chirped Pulse Amplification (CPA) technique and consists of a modelocked Nd:YLF oscillator, a Nd:glass regenerative amplifier, a two pass Nd:glass rod amplifier and finally a flashlamp-pumped Nd:glass slab amplifier. Synchronizing picosecond long electron and laser pulses is challenging and is achieved by full utilization of the accelerator's rf structure. The laser system, along with the timing of the two beams and their spatial alignment, is described in detail in chapter 4.

After passing through the interaction point, the electrons continue downstream through the FFTB/E-144 spectrometer, which consists of 6 permanent bend magnets (dipoles), with a mean field of 0.5 T. Four much weaker dipoles, are positioned around the IP, in order to reduce synchrotron radiation backgrounds in the forward direction. The arrangement of all the dipoles is shown in Fig. 1.2. Electrons and positrons exit the spectrometer and are detected by two silicon calorimeters positioned as shown in the figure. The tracks followed by charged particles, produced at the interaction point are also shown. The two calorimeters, referred to as ECAL and PCAL, are of similar construction [9]. They consist of alternating layers of silicon and tungsten. Each layer in ECAL is divided into 12 rows and 4 columns, resulting in 1.6 × 1.6 cm^2 active area pads. The longitudinal layers are grouped in 4 segments. In the case of PCAL, only 8 rows are used. In addition to the two calorimeters, an array of monitors and counters is also installed. The complete layout is shown in Fig. 1.1. Two monitors detecting electrons from nonlinear Compton scattering are located in front of ECAL; they intercept second- and third-order Compton scattered electrons, and are referred to as the N2 and N3 monitors. The monitor signals are used for the reconstruction of the laser intensity parameter η, as described in chapter 6. Both monitors are gas-Čerenkov detectors, due to the fact that this type of detectors is less sensitive to background radiation. Of similar design are the so called linear monitors [10]. There
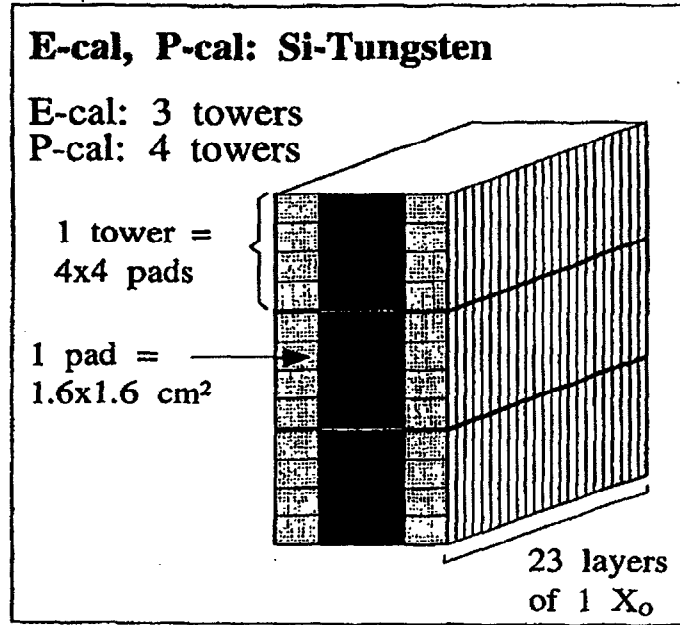
Figure 1.4: Schematic of a typical E-144 calorimeter.

are two types of linear counters, the ones that look at forward propagating Compton produced γ rays (CCM1), and the ones that look at Compton scattered electrons with two distinct energies 31 GeV (EC31) and 37 GeV (EC37). The linear counters are important during the first stages of the experiment, where laser-electron collisions are established. The electron linear counters, are also used in the estimates of η. All the detectors mentioned above, are described in chapter 5, both in terms of their technical design and also in terms of their calibration and signal reconstruction.

A pair spectrometer based on a dipole magnet with maximum transverse kick of $P_\perp = 250$ GeV, is located ~ 46 m downstream of the IP in the forward γ line, and is used to detect e^+e^- pairs from converted Compton γ's. The dispersion is in the horizontal plane and the particles are detected by using silicon CCD detectors. A
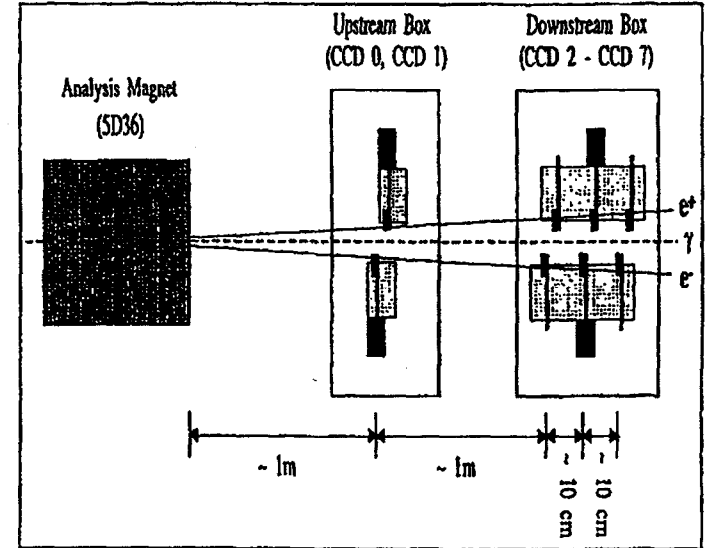
Figure 1.5: Schematic of the CCD γ detector.

schematic of the CCD detectors is shown in Fig. 1.5. There is a total of 8 CCD detectors arranged in 4 pairs. The first is about 7 mm away from the photon beam, while the other three are 13 mm away. Each CCD consists of 770 × 1150 pixels, and since the active area per CCD is 17 mm × 26 mm, we get a pixel size of ~ 20 μm, with a resolution $\sigma < 10$ μm. More details about the data collected with the CCD's are given in Appendix 3. A silicon calorimeter at the end of the gamma line is used as a redundant photon monitor.

The triggers for the experiment are provided by a single PDU which is tunable both in time delay and in repetition rate, and is synchronized with the fiducial of the accelerator rf. The primary trigger is 10 Hz, which is subsequently subdivided to 0.5 Hz to provide the laser trigger, and to a "3 Hz" trigger that fires every 200 ms, 400 ms and 2000 ms. The events collected are classified as data events (laser ON), when both the laser and electron beams are present, background events when only the electron
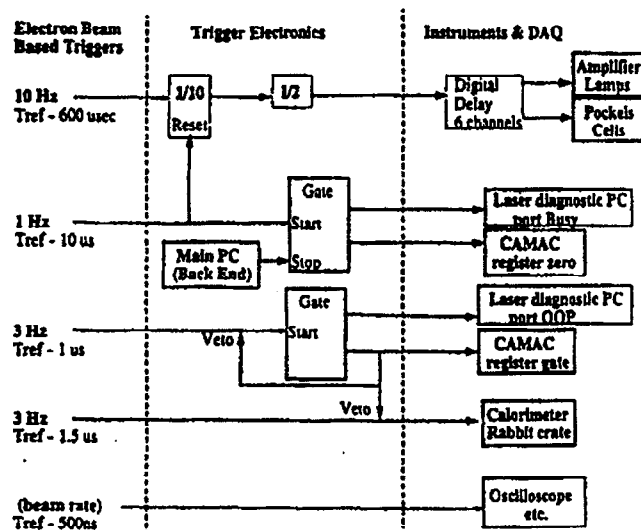
Figure 1.6: E-144 Trigger Logic.

Figure 1.7: Schematic of the E-144 data acquisition system.

beam is present, and pedestal events, useful for the measurement of electronic noise in the detector signals, when no beams are present at all. We collect twice as many background events as data events. A schematic of the trigger electronics is shown in Fig. 1.6. The moderate event rate and data volume, allow for an inexpensive data acquisition (DAQ) solution, based on IBM compatible PC's connected by a local ethernet using the standard TCP/IP protocols. The main part of the DAQ system consists of a back-end (BE) computer and several front-end computers (FE). The back-end controls and synchronizes the DAQ and provides the interface to the user, while the front-end computers collect the data and respond to command messages sent by the back-end. A third computer type are the display computers that provide for on-line monitoring of the acquired data. A schematic of the data acquisition system is shown in Fig. 1.7. Once a trigger signal passes through the logic, further triggers are blocked, until the logic is reset by a ready signal from the back-end computer. Upon

receiving a trigger signal, each front-end computer collects its assigned set of data and transmits them over the ethernet to the back-end, where the data are assembled and stored to disk. Disks of 2 GByte capacity can be used for data storage, allowing for more than 10 days of non-stop running. The back-end broadcasts the collected data to the display computers, as soon as it finishes processing the event. One display computer is normally installed in the accelerator's control room for use during the beam tuning.

Chapter 2

Theory

In this section the theoretical aspects of concern in this thesis are discussed. Where useful some quantitative examples of important parameters, based on the experimental conditions, are given. In the first section the description of an electron inside an external field is given and the parameter η first presented in the previous chapter, is formally introduced. Following that an extensive discussion of the multiphoton or nonlinear Compton scattering is done, where the cross sections and the event rates are explicitly derived. This is due to the fact that the subsequently discussed multiphoton Breit-Wheeler pair production is related to the nonlinear Compton scattering by crossing symmetry. In the last section of this chapter, the alternative barrier penetration picture of the pair production, which we also tend to call spontaneous vacuum breakdown, is finally discussed. An understanding of both the photon and the vacuum breakdown pictures is important, since the measured data are compared to the predictions of both.

2.1 Notation and Units

In the calculations presented in this chapter we use the natural system of units for which $\hbar = c = 1$. In order to go back to the CGS system of units recall that

$$\hbar c = 197.3 \text{ MeV} \cdot \text{fm} , \quad 1 \text{ fm } = 10^{-13} \text{ cm} \tag{2.1}$$

The classical electron radius, which we will very often meet in the subsequent formulae, is

$$r_0 = \frac{e^2}{4\pi m} = \frac{\alpha}{m} = \frac{1}{137} \frac{197.3 \text{ MeV} \cdot \text{fm}}{0.511 \text{ MeV}} = 2.82 \times 10^{-13} \text{ cm} \tag{2.2}$$

Similarly the Compton wavelength of an electron is

$$\lambda_e = \frac{1}{m_e} = \frac{197.3 \text{ MeV} \cdot \text{fm}}{m_e c^2} = 3.86 \times 10^{-11} \text{ cm} \tag{2.3}$$

To derive cross sections in the normal units of area, we note that

$$1(\text{ GeV })^{-2} \equiv \frac{(\hbar c)^2}{(1 \text{ GeV })^2} = 0.39 \text{ mb} , \quad 1 \text{ mb } = 10^{-27} \text{ cm}^2 \tag{2.4}$$

For 4-vector products we use the metric $g_{\mu\mu} = (1, -1, -1, -1)$. Then the dot product of two 4-vectors a and b is defined as:

$$(ab) = a_\mu b^\mu = a_0 b_0 - \vec{a}\vec{b} = a_0 b_0 - a_1 b_1 - a_2 b_2 - a_3 b_3$$
$$= a_0 b_0 - a_x b_x - a_y b_y - a_z b_z \tag{2.5}$$

where we denote regular 3-vectors as $\vec{a}$ and $\vec{b}$. The notation (ab) is used throughout this chapter for 4-vector dot products. For a particle with 4-vector momentum $p_\mu = (E, \vec{p}) = (E, p_1, p_2, p_3)$, we have

$$p^2 = E^2 - (\vec{p})^2 = m^2 \tag{2.6}$$

where m is the rest frame mass of the particle.

2.2 Free Electron in an Intense Laser Field

2.2.1 Classical Analysis

The motion of a free electron in a plane electromagnetic wave is a well known problem in classical physics. The so called steady-state motion of the electron in the field of such a wave, can be easily calculated in the frame where the electron is on average at rest [12]. The calculation is further simplified if we consider a circularly polarized plane electromagnetic wave [11]. For such a wave the electric and magnetic field vectors $\vec{\mathcal{E}}$ and $\vec{\mathcal{B}}$, have a constant amplitude and rotate at the angular frequency ω of the wave, on a plane perpendicular to the direction of the wave propagation. In such a wave the electron motion is circular with angular velocity ω, and with the electron velocity $\vec{v}$ parallel to the magnetic field vector $\vec{\mathcal{B}}$. We can then write,

$$p_\perp \omega = e\mathcal{E} \tag{2.7}$$

where $p_\perp$ the transverse component of the electron momentum, inside the field of the wave. Allowing for the possibility of relativistic velocities, $p_\perp$ can be written as

$$p_\perp = \gamma m \beta_\perp, \quad \beta_\perp = v_\perp = \omega r \tag{2.8}$$

with r the radius of the circular electron trajectory. We can now define the quantity η as:

$$\eta \equiv \gamma \beta_\perp = \frac{e\mathcal{E}}{m\omega} = \frac{p_\perp}{m} \tag{2.9}$$

Using Eq. 2.9, we can rewrite the relativistic quantities γ and $\beta_\perp$ as:

$$\gamma = \sqrt{1+\eta^2} \quad \text{and} \quad \beta_\perp = \eta/\sqrt{1+\eta^2} \tag{2.10}$$

The radius of the electron's circular trajectory can be easily derived from Eq. 2.7 and Eq. 2.8 and is:

$$r = \frac{e\mathcal{E}}{\gamma m\omega^2} \tag{2.11}$$

or since $\omega = 2\pi/\lambda$,

$$r = \frac{\eta}{\sqrt{1+\eta^2}}\frac{\lambda}{2\pi} \le \frac{\lambda}{2\pi} \tag{2.12}$$

Here λ is the wavelength of the electromagnetic wave. It is convenient to redefine the parameter η as

$$\eta^2 = \frac{e^2\langle \mathcal{E}^2 \rangle}{m^2\omega^2} \tag{2.13}$$

where the average is taken with respect to time. Clearly η is a dimensionless parameter.

The quantity η can be directly related to the laser intensity I. The intensity of a traveling electromagnetic wave is

$$I = uc \tag{2.14}$$

where u the energy density of the electromagnetic field. It can be written as

$$u = \frac{1}{2}\varepsilon_0 \mathcal{E}^2 + \frac{1}{2\mu_0}\mathcal{B}^2 \tag{2.15}$$

with ε_0 and μ_0 the permitivity and permeability of the free space respectively. Using the definition of the speed of light

$$c = \frac{1}{\sqrt{\varepsilon_0 \mu_0}} \tag{2.16}$$

and the fact that for an electromagnetic wave $\mathcal{E} = \mathcal{B}/c$, we can finally rewrite the laser intensity as:

$$I = \varepsilon_0 \mathcal{E}^2 c = \sqrt{\frac{\varepsilon_0}{\mu_0}}\mathcal{E}^2 = \frac{1}{Z_0}\mathcal{E}^2 \tag{2.17}$$

The quantity Z_0 is called the vacuum impedance and has the value $Z_0 = 377\ \Omega$. Since $\mathcal{E}$ is the instantaneous electric field, it will be more useful if we average Eq. 2.17 over time. Then we find

$$\langle I \rangle = \frac{1}{Z_0}\langle \mathcal{E}^2 \rangle = \frac{1}{Z_0}\mathcal{E}_{rms}^2 \tag{2.18}$$

and substituting in Eq. 2.13, we get finally:

$$\eta^2 = 3.65 \times 10^{-19} I\lambda^2 \quad \text{for } I \text{ in W/cm}^2 \text{ and } \lambda \text{ in } \mu\text{m} \tag{2.19}$$

As an example for peak laser intensities at the focus of $\sim 1.3 \times 10^{18}$ W/cm^2, which have been reached during the E-144 data runs using a green laser pulse with wavelength $\lambda = 527$ nm, we can find from Eq. 2.19 that $\eta \simeq 0.36$.

One important consequence of the above analysis, is that a free electron executing a relativistic motion inside the electromagnetic field of a plane wave, appears to have an "increased" mass. This can be easily seen. The total energy and the rest mass of an electron, are related to its momentum through the expression

$$m^2 = E^2 - p^2 \qquad (2.20)$$

In general $p^2 = p_\perp^2 + p_\parallel^2$ and so this last expression becomes:

$$m^2 = E^2 - p_\parallel^2 - p_\perp^2 \qquad (2.21)$$

Using Eq. 2.9, we get:

$$m^2 = E^2 - p_\parallel^2 - \eta^2 m^2 \implies E^2 - p_\parallel^2 = m^2(1 + \eta^2) \qquad (2.22)$$

What this last relation implies, is that the electron does not appear to execute any transverse motion with frequency ω, but instead it behaves as having an effective mass

$$\bar{m} = m\sqrt{1 + \eta^2} \qquad (2.23)$$

We will refer to this mass "increase" as the mass shift. Although the mass shift has been derived here classically, it has first been noted in the solutions of the Dirac equations for free electrons in a plane electromagnetic wave. We will examine this last statement in more detail in the next section.

Up to this point we have treated the electron motion assuming the electron initially at rest. This is not a realistic assumption, since an electron at rest will be expelled from the strong field region of the laser focus by the ponderomotive force [13]. There is a very strong analogy to the reflection of low frequency light off an electron plasma. From the dispersion relation for light in a plasma we have

$$\omega^2 = k^2 + \omega_p^2 \qquad (2.24)$$

where ω_p the plasma frequency. The photon inside the plasma has an effective mass

$$m_{eff}^2 = (\hbar\omega_p)^2 \qquad (2.25)$$

Photons with frequencies $\omega < \omega_p$ will not penetrate into the plasma. In the case of an electron in an intense photon field, we have seen that its mass increases by $\Delta m^2 = \eta^2 m^2$. If we consider the photon field as some kind of a photon plasma, then the quantity $\eta m/\hbar$ plays the role of the plasma frequency. In this case electrons with initial momenta less than ηm, or equivalently, initial velocities such that $\gamma\beta < \eta$, will be expelled from the photon field. Therefore we need relativistic electrons in order to probe intense photon beams.

2.2.2 Quantum Mechanical Analysis

Dirac's equation for an electron moving in a plane electromagnetic field can be solved exactly [14]. For our presentation here we follow [15]. We start from Dirac's equation for a plane electromagnetic field with a 4-vector k^μ ($k^2 = 0$):

$$[\gamma(p - eA) - m]\psi = 0 \qquad (2.26)$$

Here A^μ is the 4-vector potential which depends on the 4-vector coordinates only through the combination

$$\phi = (kx) \qquad (2.27)$$

so that we can write:

$$A^\mu = A^\mu(\phi) \qquad (2.28)$$

Throughout this section we assume that the 4-vector potential satisfies the Lorentz gauge condition,

$$\partial_\mu A^\mu = k_\mu A^{\mu'} = 0 \qquad (2.29)$$

the prime denoting differentiation with respect to ϕ. Since differentiation of A with respect to ϕ, returns A multiplied by some constant in front, we can omit the constant

and rewrite the Eq. 2.29 as

$$kA = 0 \qquad (2.30)$$

Eq. 2.26 can be brought to the more useful form

$$[(p - eA)^2 - m^2 - \frac{1}{2}ieF_{\mu\nu}\sigma^{\mu\nu}]\psi = 0 \qquad (2.31)$$

where $F_{\mu\nu}$ the field tensor,

$$F_{\mu\nu} = k_\mu A_\nu' - k_\nu A_\mu' \qquad (2.32)$$

and $\sigma_{\mu\nu}$ the antisymmetric matrix 4-tensor

$$\sigma_{\mu\nu} = \frac{1}{2}(\gamma^\mu\gamma^\nu - \gamma^\nu\gamma^\mu) \qquad (2.33)$$

We assume solutions of Eq. 2.31 of the form,

$$\psi = e^{-ipx}F(\phi) \qquad (2.34)$$

p being a constant 4-vector. Without any loss of generality we can impose on p the condition

$$p^2 = m^2 \qquad (2.35)$$

In other words p is the electron 4-momentum vector, when the field is removed. Substituting ψ in Eq. 2.31, with the expression in Eq. 2.34, we can solve for $F(\phi)$,

$$F = exp\left\{-i\int_0^{kx}\left[\frac{e}{(kp)}(pA) - \frac{e^2}{2(kp)}A^2\right]d\phi + \frac{e(\gamma k)(\gamma A)}{2(kp)}\right\}\frac{u}{\sqrt{(2p_0)}} \qquad (2.36)$$

where $u/\sqrt{(2p_0)}$ is an arbitrary constant Dirac spinor. Taking into account the fact that all the higher than the first powers of $(\gamma k)(\gamma A)$, are zero we can expand the second term of the exponential and find,

$$exp\left(\frac{e(\gamma k)(\gamma A)}{2(kp)}\right) = 1 + \frac{e}{2(kp)}(\gamma k)(\gamma A) \qquad (2.37)$$

Using this in the expression for $F(\phi)$, we can write the solution ψ as:

$$\psi = \left[1 + \frac{e}{2(kp)}(\gamma k)(\gamma A)\right]\frac{u}{\sqrt{(2p_0)}} e^{iS} \qquad (2.38)$$

with

$$S = -px - \int_0^{kx}\left[\frac{e}{(kp)}(pA) - \frac{e^2}{2(kp)}A^2\right]d\phi \qquad (2.39)$$

The solution must satisfy the free Dirac equation at time $t = -\infty$, when the wave is switched on and since $A \to 0$ when $kx \to -\infty$. That means that u must satisfy

$$(\gamma p - m)u = 0 \qquad (2.40)$$

Thus $u = u(p)$ is the same as the bispinor amplitude of a free electron.

If we define the kinetic momentum operator as $p - eA = i\partial - eA$, then its expectation value is:

$$\psi^*(p^\mu - eA^\mu)\psi = \bar{\psi}\gamma^0(p_\mu - eA^\mu)\psi \qquad (2.41)$$

A direct computation of this last expression gives us:

$$p^\mu - eA^\mu + k^\mu\left(\frac{e(pA)}{(kp)} - \frac{e^2A^2}{2(kp)}\right) + \text{terms with odd powers of } A^\mu \qquad (2.42)$$

The time average of the 4-vector, denoted by q^μ, in Eq. 2.42 is

$$q^\mu = p^\mu - \frac{e^2\langle A^2\rangle}{2(kp)}k^\mu \qquad (2.43)$$

We will call the 4-vector q^μ the quasi-momentum 4-vector. Defining the "effective mass" m_* of the electron in the field as $q^2 = m_*^2$, we find that

$$\bar{m} = m\sqrt{1 - \frac{e^2\langle A^2\rangle}{m^2}} \qquad (2.44)$$

Introducing the parameter $\eta^2 = -e^2\langle A^2\rangle/m^2$, we can rewrite Eq. 2.43 and Eq. 2.44 as:

$$q^\mu = p^\mu + \frac{\eta^2 m^2}{2(kp)}k^\mu \qquad (2.45)$$

$$\bar{m} = m\sqrt{1 + \eta^2} \qquad (2.46)$$

It is clear from the last expression that the dimensionless parameter η is a dimensionless Lorentz invariant. In fact the expression for the electron mass inside the field,

linearly polarized plane wave (laser). For a circularly polarized wave we write:

$$A = a_1 \cos\phi + a_2 \sin\phi \tag{2.49}$$

$$a_1 = (0, a, 0, 0) \tag{2.50}$$

$$a_2 = (0, 0, a, 0) \tag{2.51}$$

$$\text{with } \phi = (kx) \tag{2.52}$$

As before $k^\mu = (\omega, \vec{k})$ is the wave 4-vector and we assume that the Lorentz gauge is valid, *i.e.* $a_1 k = a_2 k = 0$. Obviously,

$$a_1^2 = a_2^2 = -a^2, \quad (a_1 a_2) = 0 \tag{2.53}$$

Similarly for a linearly polarized wave we have:

$$A = a_1 \cos\phi \tag{2.54}$$

$$a_1 = (0, a, 0, 0) \tag{2.55}$$

The wave function of an electron inside the field of a plane electromagnetic wave, is given by Eq. 2.38 and Eq. 2.39. It is convenient to change the normalization so that $\psi(p)$ corresponds to unit average number density of particles, in the same way that the wave functions for free particles are normalized to one particle per unit volume. Then the normalization expression in Eq. 2.47 implies that the electron wave function needs to be multiplied by the factor $\sqrt{\frac{p_0}{q_0}}$, and so it becomes:

$$\psi(p) = \left[1 + \frac{e}{2(kp)}(\gamma k)(\gamma A)\right] \frac{u}{\sqrt{(2q_0)}} e^{iS(p)} \tag{2.56}$$

where, as before,

$$S(p) = -px - \int_0^{kx} \left[\frac{e}{(kp)}(pA) - \frac{e^2}{2(kp)}A^2\right] d\phi \tag{2.57}$$

In the case of a circular wave, substituting in Eq. 2.57, the expression for A, and after performing the integration we find:

$$S(p) = -(qx) - \frac{e}{(kp)}(pa_1) \sin\phi + \frac{e}{(kp)}(pa_2) \cos\phi \tag{2.58}$$

Again q^μ is the quasi-momentum as defined in Eq. 2.43 and which now becomes:

$$q^\mu = p^\mu + e^2 \frac{a^2}{2(kp)} k^\mu \tag{2.59}$$

We can therefore write the electron wave function as

$$\psi(p) = \left[1 + e\frac{(\gamma k)(\gamma a_1)}{2(kp)}\cos\phi + e\frac{(\gamma k)(\gamma a_2)}{2(kp)}\sin\phi\right] e^{-i(qx) - i\tilde{a}_1 \sin\phi + i\tilde{a}_2 \cos\phi} \times \frac{u(p)}{\sqrt{2q_0}} \tag{2.60}$$

where

$$\tilde{a}_1 = e\frac{(pa_1)}{(kp)}, \ \tilde{a}_2 = e\frac{(pa_2)}{(kp)} \tag{2.61}$$

Similarly for the linearly polarized wave we find

$$\psi(p) = \left[1 + e\frac{(\gamma k)(\gamma a_1)}{2(kp)}\cos\phi\right] e^{-i(qx) - i\tilde{a}\sin\phi + i\tilde{b}\sin 2\phi} \times \frac{u(p)}{\sqrt{2q_0}} \tag{2.62}$$

with

$$\tilde{a} = e\frac{(pa_1)}{(kp)}, \ \tilde{b} = -\frac{\eta^2 m^2}{4(kp)} \tag{2.63}$$

The S-matrix for the transition of an electron from the state $\psi(p)$ to the state $\psi(p')$, with the emission of a photon that has a 4-vector $k^{\mu'} = (\omega, \vec{k}')$, and polarization 4-vector ϵ' is

$$S_{fi} = -ie \int \bar{\psi}(p')(\gamma \epsilon'^*)\psi(p)\frac{e^{ik'x}}{\sqrt{2\omega'}}d^4x \tag{2.64}$$

This S-matrix describes the scattering of an electron in a field and not the scattering of an electron off a photon. The electromagnetic field is treated semi-classically, using its 4-vector potential A^μ, while the electron wave functions are modified accordingly in order to account for the presence of the electromagnetic field. Substituting in Eq. 2.64 the electron wave function for a circularly polarized wave from Eq. 2.60 and after some algebra, we find that the S-matrix becomes

$$S_{fi} = -\frac{ie}{\sqrt{2q_0 2q_0' 2\omega'}} \int e^{i[(q'x) - (qx) + (k'x)]} e^{-ic_1 \sin\phi + ic_2 \cos\phi} \bar{u}(p)$$
$$\left[(\gamma\epsilon'^*) + \frac{e}{2}\left(\frac{(\gamma a_1)(\gamma k)(\gamma\epsilon'^*)}{(kp')} + \frac{(\gamma\epsilon'^*)(\gamma k)(\gamma a_2)}{(kp)}\right)\cos\phi\right.$$

$$\left.+\frac{e}{2}\left(\frac{(\gamma a_2)(\gamma k)(\gamma\epsilon'^*)}{(kp')} + \frac{(\gamma\epsilon'^*)(\gamma k)(\gamma a_2)}{(kp)}\right)\sin\phi\right.$$
$$\left.+\frac{e^2 a^2 (\epsilon'^* k)(\gamma a_1)}{2(kp)(kp')}\right] u(p) \, d^4x \tag{2.65}$$

where

$$c_1 = e\left(\frac{(pa_1)}{(kp)} - \frac{(p'a_1)}{(kp')}\right), \ c_2 = e\left(\frac{(pa_2)}{(kp)} - \frac{(p'a_2)}{(kp')}\right) \tag{2.66}$$

For a linearly polarized wave the corresponding S-matrix becomes

$$S_{fi} = -\frac{ie}{\sqrt{2q_0 2q_0' 2\omega'}} \int e^{i[(q'x) - (qx) + (k'x)]} e^{-i\alpha\sin\phi + i\beta\sin 2\phi} \bar{u}(p)$$
$$\left[(\gamma\epsilon'^*) + \frac{e}{2}\left(\frac{(\gamma a_1)(\gamma k)(\gamma\epsilon'^*)}{(kp')} + \frac{(\gamma\epsilon'^*)(\gamma a_1)(\gamma k)}{(kp)}\right)\cos\phi\right.$$
$$\left.+\frac{e^2 a^2 (\epsilon'^* k)(\gamma k)}{2(kp)(kp')}\cos^2\phi\right] u(p) \, d^4x \tag{2.67}$$

with

$$\alpha = e\left(\frac{(pa_1)}{(kp)} - \frac{(p'a_1)}{(kp')}\right), \ \beta = -\frac{\eta^2 m^2}{4}\left(\frac{1}{(kp)} - \frac{1}{(kp')}\right) \tag{2.68}$$

It is convenient for the rest of the calculations to rewrite the S-matrix elements for a circularly polarized wave as follows:

$$S_{fi} = -\frac{ie}{\sqrt{2q_0 2q_0' 2\omega'}} \int e^{i[(q'x) - (qx) + (k'x)]} e^{-ic\sin(\phi - \phi_0)} \bar{u}(p)$$
$$\left[(\gamma\epsilon'^*) + \frac{e}{2}\left(\frac{(\gamma a_1)(\gamma k)(\gamma\epsilon'^*)}{(kp')} + \frac{(\gamma\epsilon'^*)(\gamma k)(\gamma a_2)}{(kp)}\right)\cos\phi\right.$$
$$\left.+\frac{e}{2}\left(\frac{(\gamma a_2)(\gamma k)(\gamma\epsilon'^*)}{(kp')} + \frac{(\gamma\epsilon'^*)(\gamma k)(\gamma a_2)}{(kp)}\right)\sin\phi\right.$$
$$\left.+\frac{e^2 a^2 (\epsilon'^* k)(\gamma a_1)}{2(kp)(kp')}\right] u(p) \, d^4x \tag{2.69}$$

where

$$c = \sqrt{c_1^2 + c_2^2}, \ \cos\phi_0 = \frac{c_1}{c}, \ \sin\phi_0 = \frac{c_2}{c} \tag{2.70}$$

As we can see from the last expression for the S-matrix elements for a circularly polarized wave, it contains three terms proportional to:

$$e^{-ic\sin(\phi - \phi_0)},$$

$$\cos\phi \quad e^{-ic\sin(\phi-\phi_0)},$$

$$\sin\phi \quad e^{-ic\sin(\phi-\phi_0)}$$

We can expand these terms in Fourier series and write,

$$e^{-ic\sin(\phi-\phi_0)} = \sum_{n=-\infty}^{+\infty} B_0(c,n)e^{-in\phi}$$

$$\cos\phi\, e^{-ic\sin(\phi-\phi_0)} = \sum_{n=-\infty}^{+\infty} B_1(c,n)e^{-in\phi} \tag{2.71}$$

$$\sin\phi\, e^{-ic\sin(\phi-\phi_0)} = \sum_{n=-\infty}^{+\infty} B_2(c,n)e^{-in\phi}$$

The coefficients in the Fourier series expansion are:

$$B_0(c,n) = \frac{1}{2\pi}\int_{-\pi}^{+\pi} e^{-ic\sin(\phi-\phi_0)+in\phi}d\phi$$

$$B_1(c,n) = \frac{1}{2\pi}\int_{-\pi}^{+\pi} \cos\phi e^{-ic\sin(\phi-\phi_0)+in\phi}d\phi \tag{2.72}$$

$$B_2(c,n) = \frac{1}{2\pi}\int_{-\pi}^{+\pi} \sin\phi e^{-ic\sin(\phi-\phi_0)+in\phi}d\phi$$

The functions inside the integrals of the last expressions, are periodic functions with a period of 2π and so we can write,

$$\int_{-\pi}^{+\pi} d\left(e^{-ic\sin(\phi-\phi_0)+in\phi}\right)d\phi = e^{in\phi_0}\int_{-\pi-\phi_0}^{\pi-\phi_0} d\left(e^{-ic\sin\phi'+in\phi'}\right) = 0, \quad \phi' = \phi - \phi_0$$

and therefore,

$$0 = \int_{-\pi}^{+\pi} d\left(e^{-ic_1\sin\phi+ic_2\cos\phi+in\phi}\right) = -ic_1 2\pi B_1 - ic_2 2\pi B_2 + in2\pi B_0$$

or,

$$c_1 B_1 + c_2 B_2 = n B_0 \tag{2.73}$$

The coefficients B_0, B_1 and B_2 in the Fourier series, can be expressed in terms of the Bessel functions of the first kind,

$$B_0(c,n) = J_n(z)e^{in\phi_0},$$

$$B_1(c,n) = \frac{1}{2}\left[J_{n+1}(z)e^{i(n+1)\phi_0} + J_{n-1}(z)e^{i(n-1)\phi_0}\right], \tag{2.74}$$

$$B_2(c,n) = \frac{1}{2i}\left[J_{n+1}(z)e^{i(n+1)\phi_0} - J_{n-1}(z)e^{i(n-1)\phi_0}\right]$$

where $z = c$, with c as defined in Eq. 2.70. For circular polarization the cross section possesses cylindrical symmetry and it is therefore independent of the orientation of the coordinate system with respect to the electron scattering plane. We can therefore choose the $\hat{x}$-axis to be on the electron scattering plane, where $\phi_0 = 0$, as defined in Eq. 2.70. Then the Fourier expansion coefficients $B_l, l = 0, 1, 2$, can be rewritten as:

$$B_0(c,n) = J_n(z),$$

$$B_1(c,n) = \frac{1}{2}\left[J_{n+1}(z) + J_{n-1}(z)\right], \tag{2.75}$$

$$B_2(c,n) = \frac{1}{2i}\left[J_{n+1}(z) - J_{n-1}(z)\right]$$

Clearly B_0 and B_1 are real functions, while B_2 is imaginary.

From the expression for the S-matrix elements in the case of linear polarization, we can see that it contains three terms proportional to:

$$e^{-i\alpha\sin\phi+i\beta\sin 2\phi},$$

$$\cos\phi \quad e^{-i\alpha\sin\phi+i\beta\sin 2\phi},$$

$$\cos^2\phi \quad e^{-i\alpha\sin\phi+i\beta\sin 2\phi}$$

Expanding again each one of the terms in Fourier series, we can write:

$$e^{-i\alpha\sin\phi+i\beta\sin 2\phi} = \sum_{n=-\infty}^{+\infty} A_1(\alpha,\beta,n)e^{-in\phi},$$

$$\cos\phi\, e^{-i\alpha\sin\phi+i\beta\sin 2\phi} = \sum_{n=-\infty}^{+\infty} A_1(\alpha,\beta,n)e^{-in\phi}, \tag{2.76}$$

$$\cos^2\phi\, e^{-i\alpha\sin\phi+i\beta\sin 2\phi} = \sum_{n=-\infty}^{+\infty} A_2(\alpha,\beta,n)e^{-in\phi}$$

$$\tag{2.77}$$

where the Fourier coefficients are as before,

$$A_0(\alpha,\beta,n) = \frac{1}{2\pi}\int_{-\pi}^{+\pi} e^{-i\alpha\sin\phi+i\beta\sin 2\phi+in\phi}d\phi,$$

$$A_1(\alpha,\beta,n) = \frac{1}{2\pi}\int_{-\pi}^{+\pi} \cos\phi e^{-i\alpha\sin\phi+i\beta\sin 2\phi+in\phi}d\phi, \tag{2.78}$$

$$A_2(\alpha,\beta,n) = \frac{1}{2\pi}\int_{-\pi}^{+\pi} \cos^2\phi e^{-i\alpha\sin\phi+i\beta\sin 2\phi+in\phi}d\phi$$

From these last expressions, it is clear that the coefficients A_l, $l = 0, 1, 2$ are real functions, since the integrands in the above expressions are odd functions of ϕ. Therefore we can rewrite them in the equivalent form

$$A_0(\alpha, \beta, n) = \frac{1}{2\pi} \int_{-\pi}^{+\pi} \cos[(\alpha - 2\beta \cos \phi) \sin \phi - n\phi]$$

$$A_1(\alpha, \beta, n) = \frac{1}{2\pi} \int_{-\pi}^{+\pi} \cos \phi \, \cos[(\alpha - 2\beta \cos \phi) \sin \phi - n\phi]$$

$$A_2(\alpha, \beta, n) = \frac{1}{2\pi} \int_{-\pi}^{+\pi} \cos^2 \phi \, \cos[(\alpha - 2\beta \cos \phi) \sin \phi - n\phi]$$

As in the circular polarization case, we can show that they satisfy the equation:

$$(n - 2\beta)A_0 - \alpha A_1 + 4\beta A_2 = 0 \tag{2.79}$$

In the case of circular polarization, substituting the Fourier expansions into the expression for the S-matrix elements, we find,

$$S_{fi} = \frac{1}{\sqrt{2q_0 2q_0' 2\omega'}} \int \sum_{n=-\infty}^{+\infty} e^{i(q'+k'-q-nk)x} M_{fi}^{(n)} d^4x \tag{2.80}$$

where

$$M_{fi}^{(n)} = -ie\bar{u}(p') \times \left\{ J_n \left[(\gamma \epsilon'^*) + \frac{e^2 a^2 (\epsilon'^* k)(\gamma a_1)}{2(kp)(kp')} \right] + \right.$$

$$\frac{e}{4} \left[\frac{[(\gamma a_1) - i(\gamma a_2)](\gamma k)(\gamma \epsilon'^*)}{(kp')} + \frac{(\gamma \epsilon'^*)(\gamma k)[(\gamma a_1) - i(\gamma a_2)]}{(kp)} \right] J_{n+1} + \tag{2.81}$$

$$\left. \frac{e}{4} \left[\frac{[(\gamma a_1) + i(\gamma a_2)](\gamma k)(\gamma \epsilon'^*)}{(kp')} + \frac{(\gamma \epsilon'^*)(\gamma k)[(\gamma a_1) + i(\gamma a_2)]}{(kp)} \right] J_{n-1} \right\} \times u(p)$$

But,

$$\int e^{i(q'+k'-q-nk)x} d^4x = (2\pi)^4 \delta^{(4)}(q' + k' - q - nk) \tag{2.82}$$

and so finally we can write the S-matrix as:

$$S_{fi} = \frac{1}{\sqrt{2q_0 2q_0' 2\omega'}} \sum_{n=-\infty}^{+\infty} M_{fi}^{(n)} (2\pi)^4 \delta^{(4)}(q' + k' - q - nk) \tag{2.83}$$

Similarly for the case of linear polarization we find:

$$S_{fi} = \frac{1}{\sqrt{2q_0 2q_0' 2\omega'}} \sum_{n=-\infty}^{+\infty} M_{fi}^{(n)} (2\pi)^4 \delta^{(4)}(q' + k' - q - nk) \tag{2.84}$$

where

$$M_{fi}^{(n)} = \bar{u}(p') \times \left[(\gamma \epsilon'^*) A_0 \right.$$

$$+ \frac{e}{2} \left(\frac{(\gamma a_1)(\gamma k)(\gamma \epsilon'^*)}{(kp')} + \frac{(\gamma \epsilon'^*)(\gamma a_1)(\gamma k)}{(kp)} \right) A_1 \tag{2.85}$$

$$\left. + \frac{e^2 a^2 (\epsilon'^* k)(\gamma k)}{2(kp')(kp)} A_2 \right] \times u(p)$$

The matrices $M_{fi}^{(n)}$, for each of the two cases of circular and linear polarization as defined in Eq. 2.81 and Eq. 2.85, are the amplitudes for the emission of a photon k' after the absorption from the wave of n photons with 4-vector momenta k. The differential probability per unit volume and time is then defined as:

$$dW_n = \mid M_{fi}^{(n)} \mid^2 \frac{d^3\vec{k}' d^3\vec{q}'}{(2\pi)^6 \cdot 2\omega' \cdot 2q_0 \cdot 2q_0'} (2\pi)^4 \delta^{(4)}(q' + k' - nk - q) \tag{2.86}$$

It can be shown [15] that we can replace

$$\delta^{(4)}(q' + k' - nk - q) \frac{d^3\vec{q}' d^3\vec{k}'}{q_0' \omega'} \to \frac{d\phi du}{(1+u)^2}, \quad u = \frac{(kk')}{(kp')} \tag{2.87}$$

and so Eq. 2.86 becomes

$$dW_n = \frac{\mid M_{fi}^{(n)} \mid^2}{32\pi^2 q_0} \frac{d\phi du}{(1+u)^2} \tag{2.88}$$

In order to calculate the differential cross section we need to divide the differential probability by the photon flux, i.e.

$$d\sigma_n = \frac{dW_n}{j}, \quad j = cN_\gamma \equiv N_\gamma \tag{2.89}$$

where j is the photon flux density and N_γ the photon density (1/cm^3) in the electron rest frame. The photon flux is defined as

$$j = \frac{\mid \langle \vec{P} \rangle \mid}{\omega} = -\langle A^2 \rangle \omega = \frac{\eta^2 m^2}{e^2} \omega \tag{2.90}$$

and for the last step we used the definition of η from Eq. 2.48. Substituting in Eq. 2.89, we find

$$d\sigma_n = \frac{e^2 \mid M_{fi}^{(n)} \mid^2}{32\pi^2 \eta^2 m^2 (kp)} \frac{d\phi du}{(1+u)^2} = \frac{r_0^2 m^2}{2(kp)} \frac{1}{\eta^2} \frac{\mid M_{fi}^{(n)} \mid^2}{e^2 m^2} \frac{d\phi du}{(1+u)^2} \tag{2.91}$$

where for the last step we have used $r_0 = e^2/(4\pi m) = 2.82 \times 10^{-13}$ cm the classical electron radius and that

$$q_0\omega = (kp) \tag{2.92}$$

which is true in the rest frame of the electron. The computation of the amplitude $|M_{fi}^{(n)}|^2$ involves averaging over the polarizations of the initial electrons and summation over the polarizations of all the final particles. We can therefore write

$$|M_{fi}^{(n)}|^2 = \frac{e^2}{2} \, \mathrm{Tr}\left[\bar{\mathcal{M}}(\gamma q' + m)\mathcal{M}(\gamma q + m)\right] \tag{2.93}$$

Here $\mathcal{M}$, are the matrices in Eq. 2.81 and Eq. 2.85 and the factor of 1/2 comes from averaging over the spins of the initial electrons. Substituting in the expression for the differential cross section, we find finally

$$\frac{d\sigma_n}{d\phi du} = 2r_0^2 \frac{m^2}{(s - m^2)} \frac{1}{\eta^2} \frac{1}{(1 + u)^2} \frac{\mathrm{Tr}\left[\bar{\mathcal{M}}(\gamma q' + m)\mathcal{M}(\gamma q + m)\right]}{4m^2} \tag{2.94}$$

In this last expression we have also used

$$s = (k + p)^2 = 2(kp) + m^2 \tag{2.95}$$

In the case of circularly polarized light, after computing the trace from Eq. 2.93, the differential cross section becomes

$$\frac{d\sigma_n}{du} = 2\pi r_0^2 \frac{m^2}{(s - m^2)} \frac{1}{\eta^2} \frac{1}{(1 + u)^2} \left[-4J_n^2(z) + \eta^2\left(2 + \frac{u^2}{(u+1)}\right)\left(J_{n+1}^2(z) + J_{n-1}^2(z) - 2J_n^2(z)\right)\right] \tag{2.96}$$

where

$$z = 2n\frac{\eta}{\sqrt{1 + \eta^2}}\sqrt{\frac{u}{u_n}\left(1 - \frac{u}{u_n}\right)}, \quad u_n = \frac{2n(kp)}{m^2}, \quad u = \frac{(kk')}{(kp')} \tag{2.97}$$

Since the case of circular polarization is characterized by azimuthal symmetry, we can immediately integrate over $d\phi$. This is already done in Eq. 2.96. Similarly for the case of the linear polarization, the differential cross section can be written as

$$\frac{d\sigma_n}{du} = 2r_0^2 \frac{m^2}{(s - m^2)} \frac{1}{\eta^2} \int_0^{2\pi} \frac{d\phi}{(1 + u)^2}\left[-2A_0^2 + 2\eta^2\left(2 + \frac{u^2}{(1 + u)}\right)(A_1^2 - A_0A_2)\right] \tag{2.98}$$

In order to get the total cross section in both laser polarization cases, we have to sum over all the possible numbers n of initial field photons k that are absorbed before the emission of a photon k' and also integrate over du, i.e.

$$\sigma = \sum_{n=1}^{+\infty} \int_0^{u_n} \frac{d\sigma_n}{du} \, du \tag{2.99}$$

When $\eta \ll 1$ we can expand the differential cross section 2.96 in powers of η. For any number n of participating laser photons this leads to the expression:

$$\frac{d\sigma_n}{du} = 2\pi r_0^2 \frac{m^2}{(s - m^2)} \frac{1}{(1 + u)^2}\left(\frac{1}{(n-1)!}\right)^2\left(n\sqrt{\frac{u}{u_n}\left(1 - \frac{u}{u_n}\right)}\right)^{2n-2}\eta^{2n-2} \times$$
$$\left[-4\frac{u}{u_n}\left(1 - \frac{u}{u_n}\right) + 2 + \frac{u^2}{u+1}\right] \tag{2.100}$$

For the special case where $n = 1$, we find that the above expression becomes

$$\frac{d\sigma_1}{du} = 2\pi r_0^2 \frac{m^2}{(s - m^2)} \frac{1}{(1 + u)^2}\left[2 + \frac{u^2}{1 + u} - 4\frac{u}{u_1}\left(1 - \frac{u}{u_1}\right)\right] \tag{2.101}$$

with $u_1 \approx 2(kp)/m^2 = (s - m^2)/m^2$. Integrating now over du from $0 \to u_1$, as suggested by Eq. 2.99, we find

$$\sigma_1 = 2\pi r_0^2 \frac{1}{u_1}\left[\left(1 - \frac{4}{u_1} - \frac{8}{u_1^2}\right)\log(1 + u_1) + \frac{1}{2} + \frac{8}{u_1} - \frac{1}{2(1 + u_1)^2}\right] \tag{2.102}$$

This result agrees, as it should be, with the Klein-Nishina formula for the scattering of a photon by an electron. We can similarly expand the differential cross section in Eq. 2.98 for linearly polarized laser light, in powers of η when $\eta \ll 1$. The expressions are rather complicated and we do not reproduce them here. In the special case again of $n = 1$, the expression for linearly polarized laser light turns out to be identical to the one shown in Eq. 2.101 for circular polarization. This is expected since the Klein-Nishina cross section is independent of the laser polarization, and therefore our series expansions in powers of η, should always reproduce the Klein-Nishina result, regardless of the initial state of the laser polarization.

2.3.2 Kinematics and Rates of Nonlinear Compton Scattering

In the previous section we derived the nonlinear Compton scattering cross sections for both circular and linear polarizations of the initial photons. In order to perform the computations there, we interpreted such a process as the emission of a photon through the scattering of an electron off an electromagnetic field. Such an interpretation allowed for the computation of the S-matrix elements, by applying the Born approximation. The electron wave functions were modified in order to account for the presence of the electromagnetic field, while the field itself was treated semi-classically by using its 4-vector potential A^μ. In this section we are interested in the kinematics of this process, in particular in the lab frame energies of the outgoing photons. For this reason we can describe the nonlinear Compton scattering, as the scattering of an electron off n laser photons, where n can have any integer value of 1 and higher. In other words we describe the process

$$n\omega + e^- \longrightarrow \gamma + e^-$$

Here γ is the produced high energy photon. We denote the initial and final photon 4-vectors as nk^μ and k'^μ respectively. For the electron momenta we have to use their corresponding quasi-momenta q^μ and q'^μ, as they are defined in Eq. 2.45. Fig. 2.1 shows a diagram of such a process.

Energy and momentum conservation laws for the above process give us:

$$nk^\mu + q^\mu = k'^\mu + q'^\mu \tag{2.103}$$

Multiplying Eq. 2.103 with k'_μ on both sides, and using the fact that $k'_\mu q'^\mu = nk_\mu q''$, we find:

$$nk'_\mu k^\mu + k'_\mu q^\mu = nk_\mu q'' \tag{2.104}$$

This last expression can be used to calculate the energy of the scattered photon in
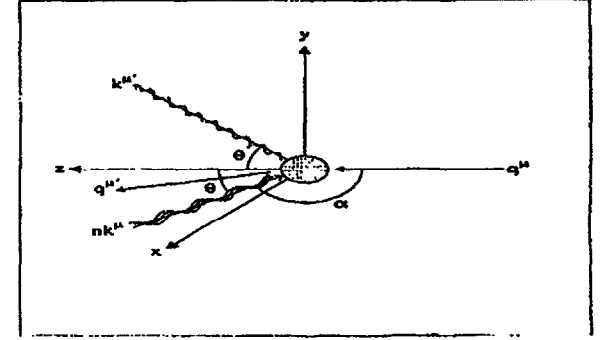
Figure 2.1: Schematic of the nonlinear Compton scattering process. In the diagram shown q^μ and q'^μ are the 4-vector momenta of the initial and final electron, nk^μ a k'^μ that of the initial n laser photons and the final gamma respectively. The an $\theta = \pi - \alpha$ is the angle between the initial electron and laser beams.

the laboratory frame. We find after some algebra:

$$\omega' = \frac{2n\gamma^2\omega(1 + \beta\cos\theta)}{2\gamma^2(1 - \beta\cos\theta') + \left(\frac{2n\gamma\omega}{m} + \frac{n^2}{1+\beta\cos\theta}\right)(1 - \sin\theta\sin\theta' + \cos\theta\cos\theta')} \tag{2.10}$$

In the last expression $\theta = 17° = \pi - \alpha$, where α is the direction of the laser propagati with respect to the electron beam in the laboratory frame; θ' is the angle of t scattered gamma again with respect to the direction of the incoming electron bea finally $\beta = v$, where v is the initial electron velocity and $\gamma = E/m$, E and m bei the energy and mass of the initial high energy electron. The angle θ' is very small a of the order of $1/\gamma \sim 10^{-5}$ radians. For an electron beam with 46.6 GeV, as it is t case at the Stanford Linear Accelerator (SLAC), $\beta \simeq 1$, and so Eq. 2.105 becomes

$$\omega' = \frac{2n\gamma^2\omega(1 + \cos\theta)}{\cos\theta' + \left(\frac{2n\gamma\omega}{m} + \frac{n^2}{1+\cos\theta}\right)(1 - \sin\theta\sin\theta' + \cos\theta\cos\theta')} \tag{2.10}$$

It is clear that the maximum scattered photon energy occurs for $\theta' = 0°$ (whi corresponds to 180° backscattering from the point of view of the incoming electr
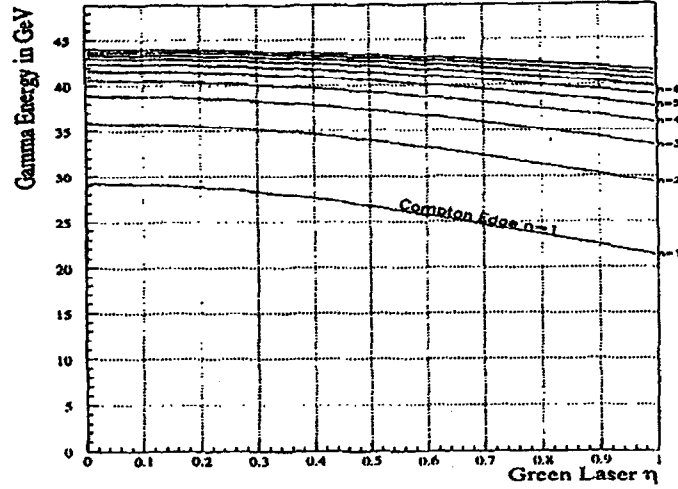
Figure 2.2: Kinematic edges for backscattered gammas for $0 \leq \eta \leq 1$ and for different number of participating laser photons n.

beam), and is:

$$\omega'_{max} = \frac{2n\gamma^2\omega(1 + \cos\theta)}{1 + \frac{2n\gamma\omega}{m}(1 + \cos\theta) + \eta^2} \qquad (2.107)$$

Equivalently the minimum energy of the recoil electron will be $E_{min} = E_0 - \omega'_{max}$. For an incident electron beam of 46.6 GeV, the maximum gamma energies, for $0 \leq \eta \leq 1$ and for number of laser photons $n = 1, \ldots 10$, are shown in Fig. 2.2.

We would like to calculate the differential event rates per recoil electron energy (dN/dE) for the nonlinear Compton scattering where a different number of initial laser photons n is involved each time. We will call each of these processes individually as an n-th order Compton scattering process, the nonlinear cases corresponding to $n > 1$. In order to find the rates, we need to know the densities of the initial electron and photon (laser) beams. For both densities we assume 3-dimensional Gaussian distributions, cylindrical for the electron beam and focused for the laser pulse. As it

is shown in Fig. 2.1, the interacting laser and electron beams have an angle $\alpha = 163°$. In order to describe the electron and photon densities, we define two coordinate systems, the Laser Coordinate System (LCS) (x', y', z') and the Electron Coordinate System (ECS) (x, y, z). The relations between the coordinates of the two systems are:

$$x' = -z\sin\alpha + x\cos\alpha \qquad (2.108)$$

$$y' = y \qquad (2.109)$$

$$z' = z\cos\alpha + x\sin\alpha \qquad (2.110)$$

The waist of a diffraction limited focused Gaussian laser beam propagating along z' with a focal point at $z' = 0$ is given by [16]

$$r(z') = r_0\sqrt{1 + (\frac{z'}{z_R})^2} \qquad (2.111)$$

where

$$r_0 = (\frac{\sqrt{2}}{\pi})f_\# \lambda \qquad (2.112)$$

$$z_R = (\frac{4}{\pi})f_\#^2 \lambda \qquad (2.113)$$

and $f_\# = f/D$ is the f-number of the focusing optic (f the focal length and D the diameter of the laser beam) and λ the laser wavelength. As a result the diffraction limited spot size is:

$$A_0 = \pi r_0^2 = (\frac{2}{\pi})(f_\# \lambda)^2 \qquad (2.114)$$

To accomodate for the case that the focused spot area A is not the diffraction limited, i.e. the minimum spot size achievable with the optics used, the factor a is introduced defined as $a = A/A_0$, and in this case Eq. 2.111 becomes:

$$r(z') = r_0\sqrt{a + (\frac{z'}{z_R})^2} \qquad (2.115)$$

Then the photon density can be defined as:

$$\rho_\omega(x', y', z', t) = \frac{N_\omega}{(2\pi)^{3/2}\sigma_{x'}(z')\sigma_{y'}(z')\sigma_{z'}} \exp\left[-\frac{x'^2}{2\sigma_{x'}^2(z')} - \frac{y'^2}{2\sigma_{y'}^2(z')} - \frac{(z' - \mu_{x'}(t))^2}{2\sigma_{x'}^2}\right] \qquad (2.116)$$

Here N_ω is the total number of photons in the laser pulse and $\mu_{z'}(t) = c \cdot t$ is the center of the laser pulse at time t. The widths of the Gaussian distributions are given by

$$\sigma_{x'}(z') = \sigma_{y'}(z') \approx \frac{r(z')}{\sqrt{2}} = \frac{f_\# \lambda}{\pi}\sqrt{a + (\frac{z'}{z_r})^2} \qquad (2.117)$$

$$\sigma_{z'} = \frac{c \cdot \tau_{laser}}{2.355} \qquad (2.118)$$

where τ_{laser} is the FWHM of the laser pulse.

In the case of the electron density, we can write similarly

$$\rho_e(x,y,z,t) = \frac{N_e}{(2\pi)^{3/2}\sigma_x\sigma_y\sigma_z}\exp\left[-\frac{x^2}{2\sigma_x^2} - \frac{y^2}{2\sigma_y^2} - \frac{(z - \mu_z(t))^2}{2\sigma_z^2}\right] \qquad (2.119)$$

where again N_e is the number of electrons in each beam bunch and $\mu_z(t) = c \cdot t$ the center of the electron bunch at time t. The width σ_z is given by

$$\sigma_z = \frac{c \cdot \tau_{beam}}{2.355} \qquad (2.120)$$

with τ_{beam} the FWHM of the beam bunch.

Once we have computed the electron and photon densities, we can find the differential rate for different orders of nonlinear Compton scattering by applying the formula

$$\frac{dN_n}{dE} = \frac{d\sigma_n}{dE}v_{rel}\int_{-\infty}^{+\infty} d\vec{x} \cdot dt \cdot \rho_e \cdot \rho_\omega \qquad (2.121)$$

where v_{rel} is the relative velocity of the laser and electron beams and $d\sigma_n/dE$ denotes the differential cross section for either circular or linear polarization, as shown in Eq. 2.96 and Eq. 2.98 modified for the above as:

$$\frac{d\sigma_n}{dE} = 2\pi r_0^2 \frac{m^2}{(s - m^2)}\frac{1}{\eta^2}\frac{1}{\gamma m}\left[-4J_n^2(z) + \eta^2\left(2 + \frac{u^2}{(u+1)}\right)(J_{n+1}^2(z) + J_{n-1}^2(z) - 2J_n^2(z))\right]$$

$$\frac{d\sigma_n}{dE} = 2r_0^2 \frac{m^2}{(s - m^2)}\frac{1}{\eta^2}\int_0^{2\pi}\frac{d\phi}{\gamma m}\left[-2A_0^2 + 2\eta^2\left(2 + \frac{u^2}{(1+u)}\right)(A_1^2 - A_0 A_2)\right] \qquad (2.122)$$

In order to find these last expressions we make use of

$$\frac{du}{(1 + u)^2} \sim \frac{dE}{\gamma m} \quad \text{if } \gamma \gg \eta \qquad (2.123)$$
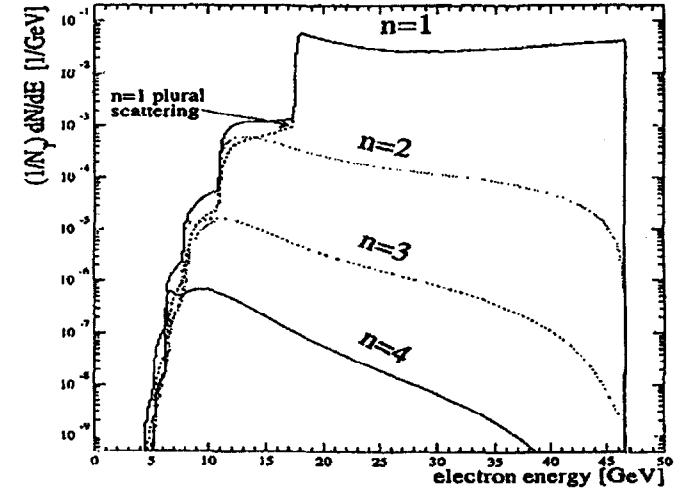
Figure 2.3: Energy spectra of the scattered electrons for Compton scattering process involving 1, 2, 3, 4 laser photons. The vertical axis shows the electron rates per (GeV energy bins, normalized to the total number of the produced $n = 1$ (linea Compton γ's. The horizontal axis is the scattered electron energy in GeV, found subtracting from the 46.6 GeV incident electron beam energy the produced γ ener as it is given by Eq. 2.105. The plural scattering line accounts for multiple line Compton scatterings. For this plot $\eta = 0.25$ and $\lambda = 527$ nm. The laser beam linearly polarized.

which in our case is always true. In order to get the correct units, Eq. 2.121 needs be multiplied by the factor $c/\hbar c$. Since, as already mentioned in the previous sectic the differential cross section when $\eta \ll 1$ is proportional to η^{2n-2}, the correspondi differential rate is expected to be proportional to η^{2n}. This is because the phot density term ρ_ω in Eq. 2.121 can be rewritten as

$$\rho_\omega = \frac{m^2\omega\eta^2}{8\pi e^2} \qquad (2.12$$

introducing one additional η^2 term in the expression for the differential rate. Fig. 2 shows the scattered electron rates normalized to the produced $n = 1$ gammas, as

function of the scattered electron energy $E = E_0 - \omega'$, with $E_0 = 46.6$ GeV and ω' given by Eq. 2.105. A linearly polarized green ($\lambda = 527$ nm) laser pulse with a laser field intensity parameter $\eta = 0.25$ is used. The rates of the first four orders of Compton scattering are clearly visible. The spectrum of the plural Compton scattering is also shown. With plural scattering we mean two consequtive linear Compton scatterings performed by the same electron while still inside the laser focus, or three such linear Compton scatterings, or a combination of a linear Compton scattering and a second-order nonlinear Compton scattering etc.. For example, the differential rate for two consequtive linear Compton scatterings can be estimated from the expression

$$\frac{dN_d}{dE} = (\frac{d\sigma_1}{dE})^2 v_{rel}^2 \int_{-\infty}^{+\infty} d\vec{x} \cdot dt \cdot \rho_\omega \cdot \int_{-\infty}^{t} dt' \cdot \rho_e \cdot \rho_\omega \tag{2.125}$$

The plural scattering rate is of the same order with the second-order Compton scattering rate and has the same kinematics. Clearly their rates increase with the time that the electrons spend inside the laser focus, or equivalently with the size of the laser focus.

2.4 Pair Production in Light-by-Light Scattering

2.4.1 Kinematics for Pair Production Process

In this section we will consider the process

$$n\omega + \gamma \longrightarrow e^+ + e^-$$

which we call the multiphoton Breit-Wheeler process (MPBW), since it can be thought as a generalization of the usual Breit-Wheeler process where more than one photon interact simultaneously with a single high energy photon designated here by gamma. For the calculations in this section we will denote the n-photon 4-vector as nk^μ, the gamma 4-vector as k_γ^μ and the e^+ and e^- 4-vector momenta as q_+^μ and q_-^μ, where the reasons for using the quasi-momenta expressions as defined in Eq. 2.45, are evident.

The high energy photon is produced during the multiphoton Compton scattering process

$$n\omega + e^- \longrightarrow \gamma + e^-$$

For our study we would like to consider the case of the maximum energy gamma (backscattered gamma) produced in such a process as given by Eq. 2.107. A schematic
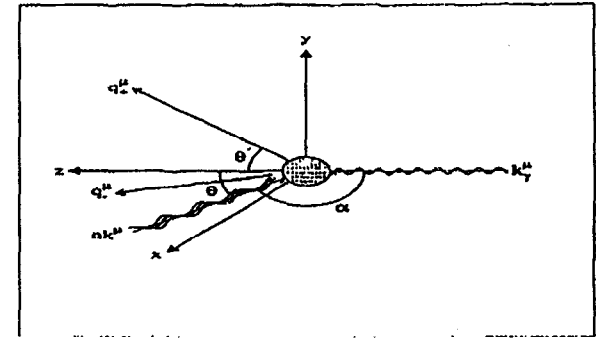
Figure 2.4: Schematic of the multiphoton Breit-Wheeler process. In the diagram shown nk^μ and k_γ^μ are the 4-vectors of the initial n laser photons and the initial gamma respectively, while q_+^μ and q_-^μ the 4-vector momenta of the final e^+e^- pair. The angle $\theta = \pi - \alpha$ is considered to be 17° for the calculations in this section.

of the multiphoton Breit-Wheeler process is shown in Fig. 2.4. We assume that the high energy gamma beam crosses the laser beam at an angle $\alpha = \pi - \theta = 163°$, where the angles α and θ are shown in Fig. 2.4.

From momentum and energy conservation we have:

$$nk^\mu + k_\gamma^\mu = q_+^\mu + q_-^\mu \tag{2.126}$$

The above expression can be brought to the equivalent form:

$$nk_\mu k_\gamma^\mu = k_{\gamma\mu} q^\mu + nk_\mu q_-^\mu \tag{2.127}$$

From this last equation, after some algebra, we can find that the energy spectrum of the produced electrons and positrons is bounded by the two roots of

$$E_e = \frac{\omega_\gamma}{2} \pm \frac{\omega_\gamma}{2}\sqrt{1 - \frac{2m^2(1+\eta^2)}{n\omega\omega_\gamma(1-\cos\alpha)}} \qquad (2.128)$$

where ω_γ is the energy of the incident gamma and ω is the energy of each of the participating n laser photons. Obviously in Eq. 2.128 the square root argument needs to be positive and this requirement gives the expression for the energy threshold for pair production via n laser photons

$$\omega_\gamma^{min} = \frac{2m^2(1+\eta^2)}{n\omega(1-\cos\alpha)} \qquad (2.129)$$

The minimum gamma energy for pair production depends not only on the number of participating laser photons, but also on the laser intensity parameter η, because of the mass shift effect, discussed earlier. Fig. 2.5, shows the required minimum gamma energy for pair production for different numbers of participating laser photons and for different values of the laser intensity parameter η, in the case of a green laser ($\lambda = 527$ nm, $\omega = 2.35$ eV). For example in the case of the backscattered $n = 1$ gamma, $\omega_\gamma = 29.2$ GeV and with $\eta = 0.2$, for the laser parameters used in section 2.2.1, we find that the minimum number of laser photons is 4. For higher η values, as can be seen from Fig. 2.5, the minimum number of photons is 5 or higher. Fig. 2.6, shows the most probable distribution of the number of laser photons contributing to pair production through the multiphoton Breit-Wheeler process. The laser parameter η used in the simulation is $\eta = 0.36$. As Fig. 2.6 shows, the highest pair production rates are achieved by absorbing 5 photons, out of which 4 are low energy laser photons, while the fifth one is the energetic backscattered gamma produced earlier through the nonlinear Compton scattering.
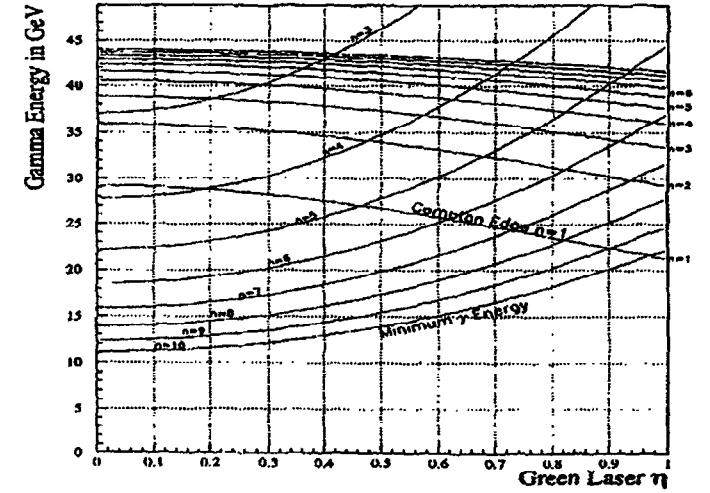
Figure 2.5: Minimum gamma energy required for pair production for different numbers of participating laser photons and for different values of the laser intensity parameter η. The maximum energy backscattered gammas are also shown for comparison.

2.4.2 Cross Section Calculations

In section 2.3 we considered the process

$$n\omega + e^- \longrightarrow \gamma + e^-$$

which we defined as the nonlinear Compton scattering, based on the fact that more than one photon, provided by an intense laser beam, is simultaneously participating in scattering off a single high energy electron. Here we denote as nk^μ the initial n-photon 4-vector, q^μ the initial electron 4-vector momentum and as k'^μ the final high energy photon 4-vector and q'^μ the final electron 4-vector momentum. For such a process the differential cross sections were derived for both linearly and circularly polarized laser photons, by applying the Born approximation in the calculation of the scattering matrix and using the electron wavefunction in the presence of an electromagnetic
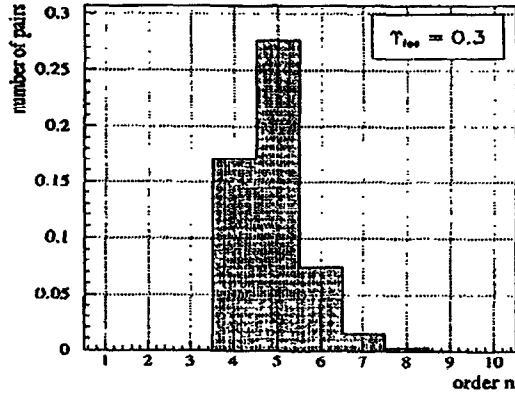
Figure 2.6: Distribution of the number n of photons participating in pair production through the multiphoton Breit-Wheeler process. It is obvious that the highest rates are achieved by the absorption of 5 photons that include 4 low energy laser photons plus the energetic backscattered gamma produced during the earlier step of the nonlinear Compton scattering process. The parameter Υ need not to worry us for the moment, since we will discuss it in more detail in section 2.5. Suffice to say here that for the plot shown the laser intensity parameter $\eta = 0.36$.

field—the so caled Volkov solution of the Dirac equation—, while the field itself was treated classically by using its 4-vector potential A^μ. In this section we would like to calculate the cross section for the process

$$n\omega + \gamma \longrightarrow e^+ + e^-$$

which we defined as the multiphoton Breit-Wheeler process. For the calculations in this section we will denote the n-photon 4-vector as nk^μ, the gamma 4-vector as k^μ_γ and the e^+ and e^- 4-vector momenta as q^μ_+ and q^μ_- respectively. Under this representation, the differential cross sections can be immediately derived from the

ones for nonlinear Compton scattering in Eq. 2.96 and in Eq. 2.98 by substituting $k'^\mu \to -k^\mu_\gamma$ and $p^\mu \to -p^\mu_+$.

In addition to the above substitution, implied by the fact that the two processes are related by crossing symmetry, we need to take into account the difference in the definition of u (for the multiphoton Compton scattering u is defined as in Eq. 2.97), and also the different final phase space states, spin statistics and normalization of the initial wavefunctions. In summary the necessary changes are:

$$\frac{u^2}{(u+1)} \to -4u$$

$$\frac{m^2}{(s-m^2)} \to \frac{m^2}{s} \quad \text{(massless initial particles)}$$

$$\frac{du}{(u+1)^2} \to -\frac{du}{4u\sqrt{u(u-1)}} \quad \text{(final state phase space)}$$

$$1 \to 1 \quad \text{(the same spin statistics factor for unpolarized photons)}$$

$$1 \to 2 \quad \text{(factor of 2 more due to the normalization of the initial states)}$$

Under these changes the differential cross section for the multiphoton Breit-Wheeler pair production using n circularly polarized laser photons becomes

$$\frac{d\sigma_n}{du} = 4\pi r_0^2 \frac{m^2}{s} \frac{1}{\eta^2} \frac{1}{u\sqrt{u(u-1)}} \left[J_n^2(z) + \frac{\eta^2}{2}(2u-1)(J_{n+1}^2(z) + J_{n-1}^2(z) - 2J_n^2(z)) \right]$$

(2.130)

where

$$z = \frac{2\eta}{u_1\sqrt{1+\eta^2}}\sqrt{u(u_n-u)}, \quad u_1 = \frac{(kk_\gamma)}{2\bar{m}^2}, \quad u_n = nu_1, \quad u = \frac{(kk_\gamma)^2}{4(kq_-)(kq_+)} \quad (2.131)$$

and for linear polarization

$$\frac{d\sigma_n}{du} = 2r_0^2 \frac{m^2}{s} \frac{1}{\eta^2} \int_0^{2\pi} \frac{d\phi}{u\sqrt{u(u-1)}} \left[A_0^2 + 2\eta^2(2u-1)(A_1^2 - A_0 A_2) \right] \quad (2.132)$$

The total cross section for multiphoton Breit-Wheeler pair production for both polarization cases is found by summing up the differential cross sections in Eq. 2.130 and in Eq. 2.132 over all the possible numbers n of participating photons, and integrating

over du, i.e.

$$\sigma = \sum_{n=n_0}^{+\infty} \int_1^{u_n} \frac{d\sigma_n}{du} \, du \qquad (2.133)$$

where of course the summation starts from the minimum number of laser photons n_0 that are needed to create an e^+e^- pair (see previous section). More conveniently we
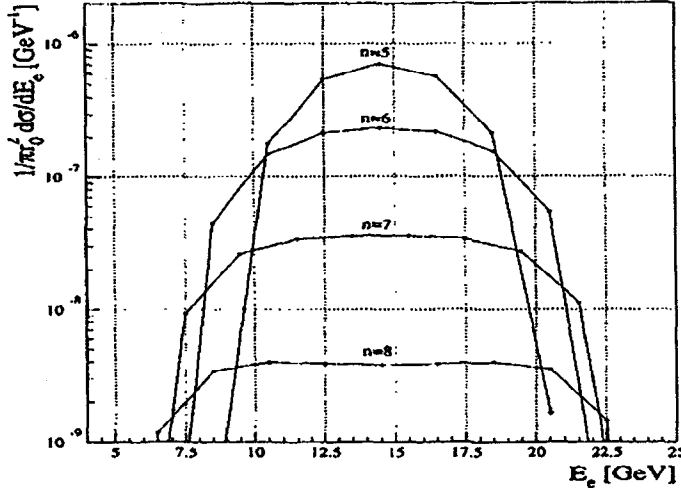
Figure 2.7: Multiphoton Breit-Wheeler differential cross sections $d\sigma/dE_e$ per produced electron energy, in units of [GeV^{-1}], as a function of the energy of the pair electron. The laser photons are circularly polarized and their wavelength is $\lambda = 527$ nm (green laser). The differential cross section is divided by πr_0^2, where r_0 the classical electron radius as defined in section 2.1. The contributions to the total cross section of the processes that involve $n = 5, 6, 7, 8$ laser photons are shown. The laser intensity parameter η is kept fixed at 0.25, while the backscattered gamma energy is 29.2 GeV. Under these conditions we need at least 5 laser photons in order to produce an e^+e^- pair.

can rewrite the differential cross sections for circular and linear polarizations in the form

$$\frac{d\sigma_n}{dE_e} = 4\pi r_0^2 \frac{m^2}{s} \frac{1}{\eta^2} \frac{2}{\omega_\gamma} \left[J_n^2(z) + \frac{\eta^2}{2}(2u - 1)(J_{n+1}^2(z) + J_{n-1}^2(z) - 2J_n^2(z)) \right]$$

$$\frac{d\sigma_n}{dE_e} = 4r_0^2 \frac{m^2}{s} \frac{1}{\eta^2} \int_0^{2\pi} \frac{d\phi}{\omega_\gamma} \left[A_0^2 + 2\eta^2(2u - 1)(A_1^2 - A_0 A_2) \right] \qquad (2.134)$$

where E_e and ω_γ the energies of the produced pair electron and of the initial high energy photon respectively. In order to bring the differential cross-sections in this last form we made use of the approximation

$$\frac{du}{u\sqrt{u(u - 1)}} \sim \frac{2dE_e}{\omega_\gamma}, \quad \text{when } \omega_\gamma \gg n\omega \qquad (2.135)$$

which under our experimental conditions is always true. Fig. 2.7 shows the differential Breit-Wheeler cross section as a function of the energy of the produced pair electron. A green ($\lambda = 527$ nm) circularly polarized laser is assumed and the laser intensity parameter $\eta = 0.25$. The backscattered initial gamma has an energy of 29.2 GeV. Under these conditions we need at least 5 laser photons in order to produce a e^+e^- pair. The contributions to the total differential cross section of the processes that involve $n = 5, 6, 7, 8$ photons are shown. The differential cross section is normalized to πr_0^2, where r_0 the classical electron radius, as defined in section 2.1.

Up to this point we have assumed that the high energy photon that participates in the pair creation process is unpolarized. This is not a realistic assumption since the gamma is produced through the nonlinear Compton scattering, in which case it acquires the polarization of the initial laser photons [17]. This needs to be taken into account for a computation of the multiphoton Breit-Wheeler cross section [50]. Let us consider the case of linearly polarized laser photons. We start by defining the polarization of the backscattered gamma beam as:

$$P(u) = \frac{\sum_n (d\sigma_{n\parallel}/du) - \sum_n (d\sigma_{n\perp}/du)}{\sum_n (d\sigma_{n\parallel}/du) + \sum_n (d\sigma_{n\perp}/du)} \qquad (2.136)$$

Here $d\sigma_{n\parallel}/du$ is the differential cross section for a gamma produced through the nonlinear Compton scattering with polarization parallel to the polarization of the laser photons, and $d\sigma_{n\perp}/du$ is the differential cross section for a gamma produced with polarization perpendicular to the polarization of the laser photons. It can be

shown [50] that those two differential cross sections have the expressions

$$\frac{d\sigma_{n\parallel}}{du} = 2r_0^2 \frac{m^2}{(s-m^2)} \frac{1}{\eta^2} \int_0^{2\pi} \frac{d\phi}{(1+u)^2} \left[-2A_0^2 \sigma' + 4\eta^2 \left(1 + \frac{u^2}{4(u+1)}\right)(A_1^2 - A_0 A_2) \right]$$

$$\frac{d\sigma_{n\perp}}{du} = 2r_0^2 \frac{m^2}{(s-m^2)} \frac{1}{\eta^2} \int_0^{2\pi} \frac{d\phi}{(1+u)^2} \left[-2A_0^2(1-\sigma') + \eta^2 \frac{u^2}{1+u}(A_1^2 - A_0 A_2) \right] \tag{2.137}$$

where the parameter σ' is defined as

$$\sigma' = 2\eta^2 \left[\frac{n}{4\beta} - \frac{1}{2} - (\frac{\alpha}{8\beta})^2 \right] \tag{2.138}$$

while the rest of the parameters follow the definitions presented in section 2.3.1. It is clear from the last expressions that

$$\frac{d\sigma_{n\parallel}}{du} + \frac{d\sigma_{n\perp}}{du} = \frac{d\sigma_n}{du} \tag{2.139}$$

the last differential cross section being the one derived for unpolarized gammas, as it is shown in Eq. 2.98 of section 2.3.1. The fraction of gammas with polarization parallel to the polarization of the initial laser photons, will be:

$$P_\parallel(u) = \frac{\sum_n (d\sigma_{n\parallel}/du)}{\sum_n (d\sigma_{n\parallel}/du) + \sum_n (d\sigma_{n\perp}/du)} = \frac{1 + P(u)}{2} \tag{2.140}$$

A generalization of the unpolarized differential Breit-Wheeler cross section in Eq. 2.132 for the case of polarized gamma beam with polarization $P(u)$ as defined in Eq. 2.136, is

$$\frac{d\sigma_{nP}}{du} = 2r_0^2 \frac{m^2}{s} \frac{1}{\eta^2} \int_0^{2\pi} \frac{d\phi}{u\sqrt{u(u-1)}} \left\{ 2(1-P)A_0^2 + 2(2P-1)\sigma'A_0^2 + 4\eta^2(u-P)(A_1^2 - A_0 A_2) \right\} \tag{2.141}$$

where σ' is defined again by the expression in Eq. 2.138. For the special cases of gammas with polarization parallel (P=1) or perpendicular (P=0) to the polarization of the laser photons, it can be written as:

$$\frac{d\sigma_{n\parallel}}{du} = 2r_0^2 \frac{m^2}{s} \frac{1}{\eta^2} \int_0^{2\pi} \frac{d\phi}{u\sqrt{u(u-1)}} \left[2A_0^2 \sigma' + 4\eta^2(u-1)(A_1^2 - A_0 A_2) \right]$$

$$\frac{d\sigma_{n\perp}}{du} = 2r_0^2 \frac{m^2}{s} \frac{1}{\eta^2} \int_0^{2\pi} \frac{d\phi}{u\sqrt{u(u-1)}} \left[2A_0^2(1-\sigma') + 4\eta^2 u(A_1^2 - A_0 A_2) \right] \tag{2.142}$$

It follows from the last two expressions that

$$\frac{(d\sigma_{n\parallel}/du) + (d\sigma_{n\perp}/du)}{2} = \frac{d\sigma_n}{du} \tag{2.143}$$

where the last differential cross section is the unpolarized cross section shown in Eq. 2.132. Although we have discussed the polarization effects on the multiphoton pair production assuming linearly polarized laser photons, this effect is also important in the case where the laser photons are characterized by circular polarization. In such a case we cannot of course define the polarization of the produced backscattered gammas as being parallel or perpendicular to the laser polarization, but we can alternatively introduce the concept of the produced gammas conserving or not conserving the helicity of the initial circularly polarized laser photons. The helicity of a photon is defined as the projection of its spin to the direction of the photon momentum $\vec{k}$. Since photons are massless particles they are characterized by only two helicity states +1 (positive) and -1 (negative). In this case the polarization of the backscattered gamma beam can be defined in analogy with Eq. 2.136 as:

$$P(u) = \frac{\sum_n (d\sigma_n^p/du) - \sum_n (d\sigma_n^n/du)}{\sum_n (d\sigma_n^p/du) + \sum_n (d\sigma_n^n/du)} \tag{2.144}$$

Since the data presented in this document are taken by using linearly polarized laser photons, we will refrain from discussing the circular polarization effects on the pair production cross sections. The interested reader can refer to [18], [50].

As a final remark we would like to mention, that the differential cross sections for Breit-Wheeler pair production, can be shown to vary as η^{2n-2} when $\eta \ll 1$, for both linear and circular laser polarizations. As a consequence the corresponding differential rates will vary as η^{2n}.

2.5 Spontaneous Vacuum Breakdown

In Eq. 2.131, we have defined the invariant u_1 as

$$u_1 = \frac{(kk_\gamma)}{2\bar{m}^2} \tag{2.145}$$

with k_γ^μ the 4-vector of the high energy gamma and k^μ the 4-vector of each of the participating laser photons. We can now introduce the invariant κ

$$\kappa = \frac{(kk_\gamma)}{m^2}\eta = e\sqrt{\langle (F_{\mu\nu}k_\gamma^\nu)^2\rangle}/m^3 \qquad (2.146)$$

where $F_{\mu\nu}$ the electromagnetic field 4-tensor and the average is again taken with respect to time. Substituting Eq. 2.146 into Eq. 2.145 we find:

$$u_1 = \frac{\kappa}{2\eta\sqrt{1+\eta^2}} \qquad (2.147)$$

Also the quantity z, from Eq. 2.131, can be rewritten as:

$$z = \frac{4\eta^2\sqrt{1+\eta^2}}{\kappa}\sqrt{u(u_n - u)}, \quad u = \frac{(kk_\gamma)^2}{4(kq_-)(kq_+)}, \quad u_n = nu_1 \qquad (2.148)$$

For the case of the nonlinear Compton scattering we can introduce in analogy to κ the invariant Υ, which we can define as

$$\Upsilon = \frac{(kp)}{m^2}\eta = e\sqrt{\langle (F_{\mu\nu}p^\nu)^2\rangle}/m^3 \qquad (2.149)$$

where k^μ the 4-vector for each of the participating laser photons, p^μ the 4-vector momentum of the probing electron. The average is taken again with respect to time. Substituting this last expression in the quantity z from Eq. 2.97 we find

$$z = \frac{\eta^2\sqrt{1+\eta^2}}{\Upsilon}\sqrt{u(u_n - u)}, \quad u_n = \frac{2n(kp)}{\tilde{m}^2}, \quad u = \frac{(kk')}{(kp')} \qquad (2.150)$$

It is clear that the two expressions for the quantities z for both the nonlinear Compton scattering and the multiphoton pair production have similar forms, which outlines once more the fact that the two processes are related by crossing symmetry. More important is the similarity in the definitions of the two invariants κ and Υ, that have exactly the same form with the only exception of the different 4-vector momentum used for the probing particle (electron for nonlinear Compton scattering, high energy gamma for multiphoton pair creation). We can move one more step ahead in the definitions of κ and Υ and perform the 4-vector products for each one of them. Making use of the definition of the laser intensity parameter η

$$\eta = \frac{e\mathcal{E}_{rms}}{m\omega} \qquad (2.151)$$

and taking also into account the geometry of the two processes as shown in Fig. 2 and Fig. 2.1, we obtain:

$$\kappa = \frac{(1-\cos\alpha)\omega\omega_\gamma}{m^2}\eta \approx \frac{(1-\cos\alpha)\omega_\gamma}{m}\frac{\mathcal{E}_{rms}}{\mathcal{E}_{crit}} \qquad (2.15)$$

$$\Upsilon = \frac{(1-\cos\alpha)\omega\gamma}{m}\eta \approx \frac{(1-\cos\alpha)\gamma\mathcal{E}_{rms}}{\mathcal{E}_{crit}} = \frac{\mathcal{E}^*}{\mathcal{E}_{crit}} = \frac{e\mathcal{E}^*}{m^2} \qquad (2.15)$$

Here α is the angle between the directions of the initial particles, ω the energy each of the participating laser photons, ω_γ the energy of the high energy gamma, the energy of the probing electron, $\mathcal{E}_{rms}$ the rms electric field strength at the las focus, $\gamma = E/m$ the Lorentz factor, $\mathcal{E}^*$ the electric field at the laser focus as viewe at the electron rest frame and finally $\mathcal{E}_{crit} = m^2/e$ the quantum electrodynami (QED) critical field strength. Physically $\mathcal{E}_{crit}$ can be interpreted as the field strengt for which the energy gain of an electron accelerated over a Compton wavelength defined in Eq. 2.3, equals the electron rest energy. For example using $\alpha = 163°$ find that for a 46.6 GeV electron $\Upsilon = 0.82\eta$ and that for a 29.2 GeV backscatter gamma $\kappa = 0.51\eta$.

The importance of introducing the QED critical field $\mathcal{E}_{crit}$ will be revealed imm diately. The quantum field theory ground state ("vacuum") is characterized by qua tum fluctuations during which short lived "virtual" e^+e^- pairs are created and th anihilated again. In the presence of a strong external field, the vacuum can becon unstable and the short lived pairs can be separated spatially and become real partic in exchange to some energy expenditure provided by the external field. In this ca the work of such a field in a distance of one Compton wavelength of the electro should provide the energy of $2m$; hence $e\mathcal{E}/m \sim m$ and therefore $\mathcal{E} \sim m^2/e = \mathcal{E}_{crit}$ t QED critical field introduced earlier. This phenomenon has been calculated by Schwinger [19] for the case of an intense static electric effect (an effective Lagrangi for such a process was first proposed by W. Heisenberg and H. Euler [20]). The ca of a purely static electric field can be described in terms of a quantum-mechanic tunneling of a positron from the Dirac sea through the classically forbidden zone

width $2m$ under the influence of an external potential energy $V(x) = e\mathcal{E}x$ [21]. The probability of such a process is

$$P \sim \exp\left(-2 \int_{x_-}^{x_+} \sqrt{m^2 - (e\mathcal{E}x)^2} dx\right) = \exp\left(-2 \int_{x_-}^{x_+} q(x) dx\right) \qquad (2.154)$$

with $x_\pm$ the points where $q(x_\pm) = 0$. Then we can rewrite the last expression as

$$P \sim \exp\left(-\frac{2m^2}{e\mathcal{E}} \int_{-1}^{+1} \sqrt{1 - y^2} dy\right) = \exp\left(-\frac{\pi m^2}{e\mathcal{E}}\right) = \exp\left(-\frac{\pi}{\Upsilon}\right) \qquad (2.155)$$

where in the last step we have used the definition of Υ provided earlier, but substituting the peak to the RMS value of the electric field. The expression in Eq. 2.155, is essentially the probability for producing one pair. A careful calculation (as in [19]) yields

$$P = \frac{\alpha\mathcal{E}^2}{\pi^2} \sum_{n=1}^{+\infty} \frac{1}{n^2} \exp\left(-\frac{n\pi}{\Upsilon}\right) \qquad (2.156)$$

where the successive terms in the summation can be interpreted as the individual probabilities for producing $1, 2, \ldots, n$ pairs.

In our experimental conditions where the e^+e^- pair is produced via an intense external laser field, the assumption of a purely static electric field is not valid. In addition the peak electric field in the laboratory frame is only $\mathcal{E} \sim 3 \times 10^{10}$ V/cm and approaches the critical value only in the rest frame of the 46.6 GeV incident electrons ($\mathcal{E}^* \simeq 2\gamma\mathcal{E} \simeq 1.8 \times 10^5 \mathcal{E}$). Nevertheless Brezin and Itzykson [22] have shown that pair production can also occur in vacuum under the influence of an alternating field. Some simplifying assumptions are made, namely that the individual laser photon energy ω is much smaller than the rest mass of the electron ($\omega \ll m$) and also that Υ is sufficiently smaller than 1. The first assumpttion is readily fulfilled in the case of a green laser where $\omega = 2.35$ eV, while the second is approximately satisfied in our experimental setup, where Υ reaches a maximum value of 0.3 when defined in the rest frame of the incident electron. Under these assumptions only the probability for the production of one pair is significant. It is important to stress the fact that no assumptions for the laser intensity parameter η are made, although the oscillating
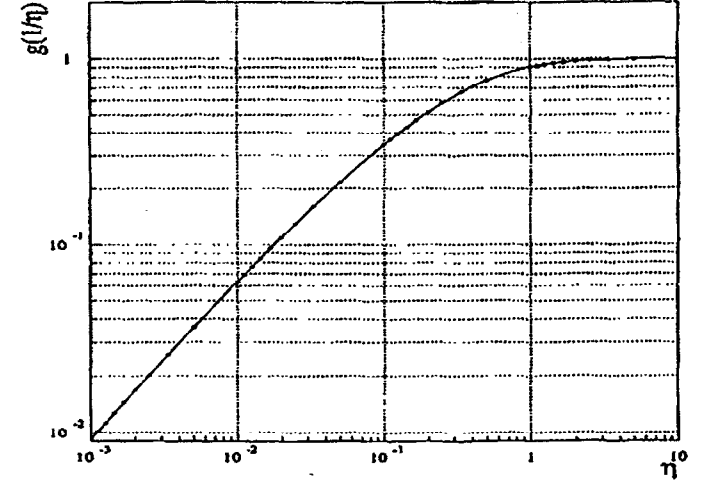
Figure 2.8: Plot of the function $g(\eta)$ as defined in Eq. 2.158.

field is assumed to be constant in space. The final expression for the probability of a single pair production is then found to be

$$P = \frac{\alpha\mathcal{E}^2}{\pi} \frac{1}{g(z) + \frac{1}{2}zg'(z)} \exp\left(-\frac{\pi}{\Upsilon}g(z)\right) \qquad (2.157)$$

where $g(z)$ is a smooth and monotonically increasing function defined as

$$g(z) = \frac{4}{\pi} \int_0^1 dx \left(\frac{1 - x^2}{1 + x^2 z^2}\right)^{1/2}, \quad z = 1/\eta \qquad (2.158)$$

and is plotted in Fig. 2.8. The normalization of $g(z)$ is chosen so that $g(0) = 1$. Notice here that Υ is defined in the rest frame of the produced e^+e^- pair and the peak value of the external electric field is used.

It is interesting to check the low frequency limit ($z \ll 1 \Rightarrow \eta \gg 1$) of Eq. 2.157. Then

$$g(z) = 1 - \frac{1}{8}z^2 + O(z^4), \quad z \ll 1 \qquad (2.159)$$

and keeping only the first term Eq. 2.157 becomes

$$P \simeq \frac{\alpha \mathcal{E}^2}{\pi} \exp\left(-\frac{\pi}{\Upsilon}\right), \quad \eta \gg 1 \qquad (2.160)$$

which agrees with the static field result of Eq. 2.156, when only the first term in the summation is kept, except of a factor of $1/\pi$. We also check the low field limit $(z \gg 1 \Rightarrow \eta \ll 1)$. In this case the field induces only a weak perturbation on the vacuum state and we expect that the response will be expanded in powers of the perturbation. Then

$$g(z) = (4/\pi z)\ln(2z) + O(1/z), \quad z \gg 1 \qquad (2.161)$$

and keeping again only the first term, we can rewrite Eq. 2.157 as:

$$P \simeq \frac{\alpha \mathcal{E}^2}{8}\left(\frac{e\mathcal{E}}{2m\omega}\right)^{4m/\omega}, \quad \eta \ll 1 \qquad (2.162)$$

The exponent $2m/\omega$ can be interpreted as the minimum number of laser photons required to produce the pair. The general formula in Eq. 2.157 interpolates between the two limits.

Chapter 3

The Electron Beam

This chapter examines the electron beam aspect of the experiment. As it has been already mentioned in the previous chapter, the experiment was carried out at the Stanford Linear Accelerator Center (SLAC), and in particular in the FFTB line Fig. 3.1 shows a schematic of the linear accelerator at SLAC, while Fig. 3.2 shows the location of the FFTB line with respect to the other existing lines at SLAC. FFTB is at the end of the 2-mile long linac, right after the area that the e^- and e^+ beams are directed to the arcs that carry them to the SLC collider hall (the BSY line). FFTB does not introduce any further acceleration of the electrons entering from the linac but it is a purely beam optics line, designed for the focusing of electron beams down to submicron level spot sizes. Such a tight focusing of a charged particle beam, is one of the main characteristics of the design for the Next Linear Collider (NLC). It is the existence of such a capability in the FFTB line, that makes it the ideal location of an experiment that studies the pair production from true light-by-light scattering, such as the E-144 experiment. Small focal spot sizes for an electron beam increase the number of electrons that traverse the focal region of an equally tightly focused laser beam, and therefore the corresponding event rate. In this chapter some important characteristics of the electron beam in a linear accelerator are discussed, and the concept of the beam emittance is introduced. Then a brief description of
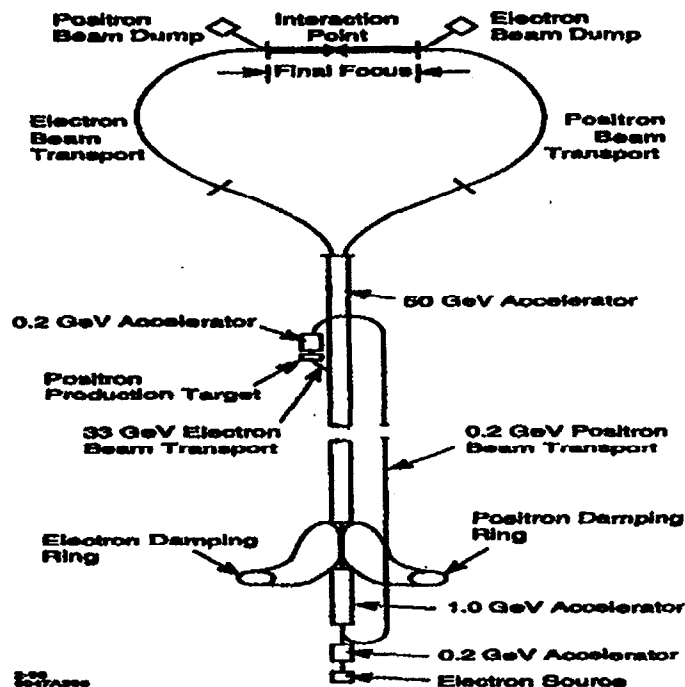
Figure 3.1: The Stanford Linear Collider (SLC).

the FFTB line is given, followed by the beam tuning needed for the pair production experiments.

3.1 General Characteristics of the e^- Beam

3.1.1 Beam Charge and Bunch Length

In a linear collider, like the SLAC accelerator, the beam of the accelerated charged particles, in our case electrons and positrons, consists of bunches of particles, that traverse the linac and then are delivered down to the experimental area. The number
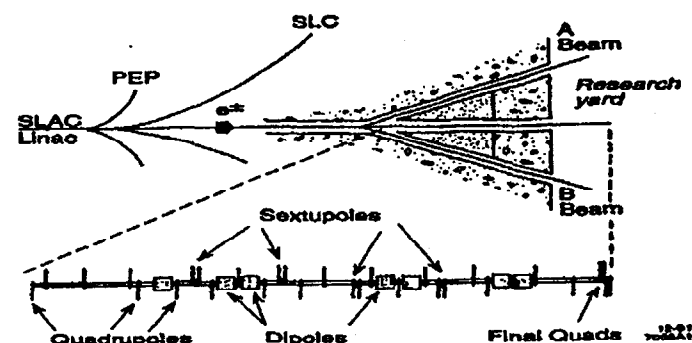
Figure 3.2: Location of the FFTB line with respect to other existing accelerator line: at SLAC. The straight line right before the big "triangle", denotes the SLAC linac The lines marked as SLC are the two arcs that send the e^- and e^+ beams to the collider hall, as it is shown in Fig. 3.1. FFTB is at the end of the 2-mile long linac.

of bunches that are accelerated by the linac in every second, define the operating frequency of the accelerator. In the case of the FFTB, this operating frequency i: 30 Hz, while for the pair production studies in true light-by-light scattering (E-14 experiment), the operating frequency drops down to 10 Hz. The laser fires at a rat of 0.5 Hz, or once every two seconds, and therefore only one every 20 electron bunche interact with the laser beam. In addition two more electron bunches, from the sam 2-second period for which no laser pulse is present, are used for background estimate: Bunching of an electron beam is necessary for the efficient acceleration of the electron in an RF accelerator, like the SLAC linac. Due to the oscillating nature of the RI field, not all the particles of a constant (cw) beam would have been accelerated. A SLAC the initial bunching of the electron beam is done right after the electron sourc using prebunchers, that establish bunches with a FW of 18 ps. This bunching need to be re-established after the electrons exit the damping ring (we will discuss th purpose for using damping rings later in this section), since the bunch length tend to increase with the time that the electrons are stored inside the damping ring. Thi is achieved by using the so called North Ring to Linac (NRTL) compressor, locate

right after the damping ring in the line that transports the electron beam from the damping ring to the main linac for further acceleration. Fig. 3.3 shows the north
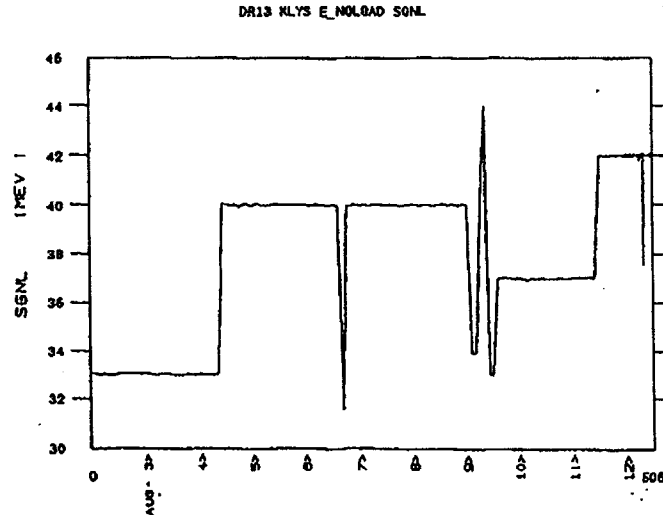
Figure 3.3: The north RTL compressor voltage settings during the August 1996 data run. The horizontal axis is time in days and the vertical axis the compressor voltage in MVolts.

dumping ring compressor voltage during the period of the E-144 data run. There is a direct correlation between the high voltage applied to the compressor and the resulting beam bunch length. The calibration of the North RTL compressor at SLAC, where the RMS value of the bunch length is correlated to different applied high voltages, is shown in Fig. 3.4 [23], while Fig. 3.3, shows the compressor high voltage settings, during the positron data taking period. Using the calibration and the compressor voltage setting history plot, we can derive the RMS value of the bunch length of the electron beam used, during the data taking period. This is summarized in table 3.1.

The number of particles in a single bunch define the beam charge and can be measured by using toroids. These are consisted of a magnetic ring of known magnetic
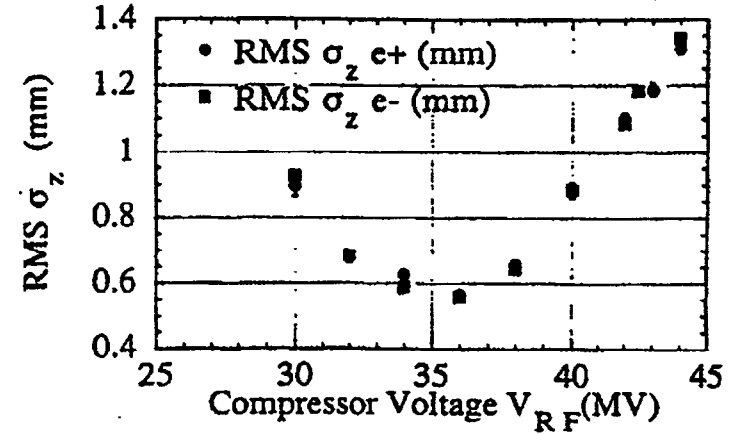
Figure 3.4: The north RTL compressor calibration curve. The RMS bunch length of an e^- or a e^+ beam down the linac in units of mm is shown.

Run Number	Compressor Voltage [MV]	RMS Bunch Length [mm]
15100–15199	33.0	0.64
15200–15385	40.0	0.90
15386–15392	31.6	0.68
15393–15537	40.0	0.90
15538–15626	37.0	0.60
15627–15670	42.0	1.10

Table 3.1: List of the North RTL compressor voltages and the corresponding electron beam bunch lengths using the calibration shown in Fig. 3.4. We need to scale the above numbers by 2.355 in order to translate them in FWHM.

permeability μ, around of which an N-turn coil is wound. When the electron beam passes through the ring an emf voltage is induced which acts to oppose the magnetic

field of the beam. The combination of the magnetic core, the coil and the electrical resistance R of the coil, combine to produce a current transformer. The current I_c measured on the coil, is directly related to the beam current I_b by:

$$I_c = \frac{I_b}{N} \tag{3.1}$$

The sensitivity of such a device is,

$$S = \frac{R}{\sqrt{1 + (\frac{\omega_l}{\omega})^2}} \tag{3.2}$$

where $\omega_l = \frac{R}{L}$ and L the coil inductance, defined as,

$$L = \frac{N^2 \mu A}{l} \tag{3.3}$$

Here A is the cross sectional area and l the circumference of the magnetic core. The voltage across the coil is

$$V(t) = \frac{I_b R}{N} e^{-(\frac{R}{L})t} \tag{3.4}$$

It is clear from Eq. 3.2, that in order to reduce the low bandwidth cutoff, we need to reduce ω_l. On the other hand this reduces the signal amplitude, as it is evident from Eq. 3.4. A balance between those two requirements needs to be established.

Although there are many toroids in the linac and in the FFTB line, only two of them are directly integrated to the data acquisition system, and read out on a pulse-to-pulse basis. Those are toroids I6 in the FFTB entrance and toroid I7 in the FFTB dump line. The second toroid is calibrated by injecting a 60 ns pulse of various amplitudes and reading the output number of ADC counts. The resulting calibration in units of 10^{10} e$^-$ per pulse is:

$$Ne^- = 3.250 \times 10^{-3} (ADC - 85.01)^{0.8939} \tag{3.5}$$

The average pedestal in this calibration is 86.29 with a readout-to-readout RMS of 7 ADC counts. Toroid I6 has not been directly calibrated, but it can always be cross-calibrated using toroid I7. The result of such a cross-calibration is shown in Eq. 3.6

again in units of 10^{10} e$^-$ per pulse.

$$Ne^- = -0.9419 \times 10^{-2} + 0.6288 \times 10^{-3} \, I6 \tag{3.6}$$

Here I6 is the number of ADC counts from toroid I6. The pedestal is 151.4 counts with a readout-to-readout RMS of 11 counts. In general during the 46.6 GeV runs the average beam charge was found to be $\sim 7 \times 10^9$ e$^-$, while during the 49.1 GeV the beam charge was a little smaller at $\sim 5 \times 10^9$ e$^-$ per bunch.

3.1.2   Beam Emittance

Each particle in an electron beam, or for that reason in any other charged particle beam, can be represented by a point in the six-dimensional phase space with coordinates $(x, p_x, y, p_y, \sigma_z, E_0)$, where p_x and p_y are the transverse momenta (the electron beam propagates along the $\hat{z}$-axis), σ_z is the RMS bunch length, and E_0 is the electron beam energy. Very often instead of the beam energy the relative energy spread $\Delta E/E_0$ is used. In the same way the slopes of the particle trajectories x' and y', which are proportional to the transverse momenta, are also used instead. For the purposes of this section we will concentrate on the transverse motion of the particles in an electron beam, defining a four-dimensional phase space with coordinates (x, x', y, y'). The region occupied by the beam electrons in this phase space is called the beam emittance and it is generally denoted with ϵ. It is obvious that we can define two emittances ϵ_x and ϵ_y, each corresponding to one of the two transverse directions x and y. The concept of the beam emittance provides us with a practically useful tool in describing an electron beam in a transport line consisting of drift spaces, dipoles and quadrupoles, since knowledge of the area occupied by the particles of an electron beam at the beginning of the line, enables us to determine the location and distribution of the electron beam at any other location of the same transport line, without having to calculate the trajectory of each individual particle separately. Furthermore, for beam transport lines, where the Lorentz force is the only acting macroscopic force,

Liouville's theorem can be proved to be true. This theorem states that particles that are within a closed boundary in phase space at one point of the beam transport line, will remain within that closed boundary at any other point of the same beam line.

The area occupied by the particles of the beam in phase space is an ellipse described by the equation:

$$\gamma x^2 + 2\alpha x x' + \beta x'^2 = \epsilon \tag{3.7}$$

Here α, β, γ and ϵ are ellipse parameters. The area enclosed by that ellipse is of course $\pi\epsilon$. Eq. 3.7 is exactly the definition of the beam emittance. Although it is written for the x, x' plane, a similar relation holds also for the y, y' plane, allowing us to introduce two beam emittances, one for each transverse plane as already mentioned earlier. Fig. 3.5 shows the beam ellipse in the (y, y') plane, and gives a geometric interpretation of the parameters α, β and γ. It is obvious from that picture that $\sqrt{\beta\epsilon}$ represents the beam extent in the $x(y)$ direction and therefore is a measure of the beam size, while $\sqrt{\gamma\epsilon}$ is the beam divergence. The coupling parameter α becomes zero at a beam waist. All three ellipse parameters α, β, γ are functions of the distance s that the beam travels along the beam transport line, and in this respect they are often called the betatron functions, since they were first introduced to describe the oscillatory motion of charged particles in betatrons [24]. Restricting ourselves for simplicity in the (x, x') plane, we can write the expression that gives the transformation of the particle trajectory from an initial point $s = 0$ at the beginning of the beam line to a point $s \neq 0$ further downstream as:

$$\begin{pmatrix} x \\ x' \end{pmatrix} = \begin{pmatrix} C(s) & S(s) \\ C'(s) & S'(s) \end{pmatrix} \begin{pmatrix} x_0 \\ x_0' \end{pmatrix} \tag{3.8}$$

The 2×2 matrix shown in Eq. 3.8, is the matrix product of the 2×2 matrices characterizing each of the elements—drift spaces, dipoles, quadrupoles etc.— that make up the beam transport line. Using Eq. 3.8 and the fact that the area of the phase space ellipse is invariant, we find that the transformation between the ellipse
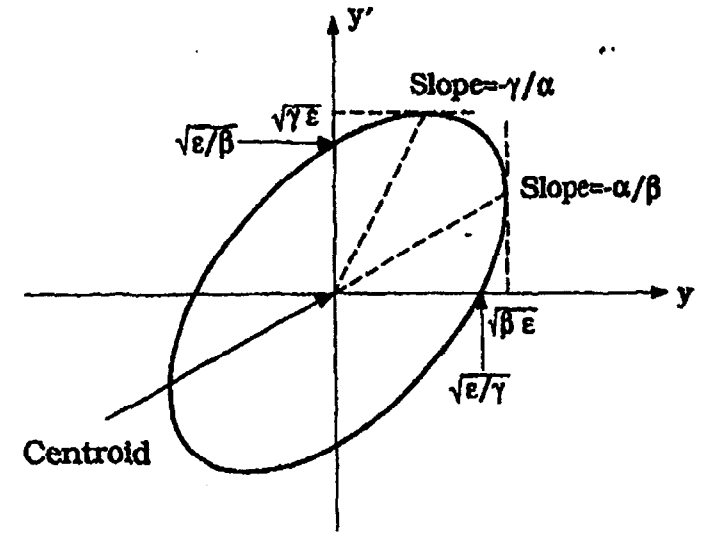
Figure 3.5: A drawing of the beam ellipse, here in the (y, y') plane. The area enclosed by the ellipse is equal to $\pi\epsilon$. Clearly $\sqrt{\beta\epsilon}$ is the extent of the beam in the y direction and therefore gives us the beam size, and $\sqrt{\gamma\epsilon}$ is the beam divergence. The coupling parameter α is 0 when the beam is at a waist position in the transport line. All three parameters α, β and γ are functions of the distance s along the beam line, and in this respect they are called the betatron functions.

parameters α_0, β_0 and γ_0 at the initial point $s = 0$ and the parameters α, β and γ at the final point s is given by:

$$\begin{pmatrix} \beta \\ \alpha \\ \gamma \end{pmatrix} = \begin{pmatrix} C^2 & -2SC & S^2 \\ -CC' & (S'C + SC') & -SS' \\ C'^2 & -2S'C' & S'^2 \end{pmatrix} \begin{pmatrix} \beta_0 \\ \alpha_0 \\ \gamma_0 \end{pmatrix} \tag{3.9}$$

The parameters α, β and γ are better known as the Twiss parameters, and satisfy the very important identity:

$$\beta\gamma - \alpha^2 = 1 \tag{3.10}$$

Although the area of the beam ellipse remains the same as the beam travels through
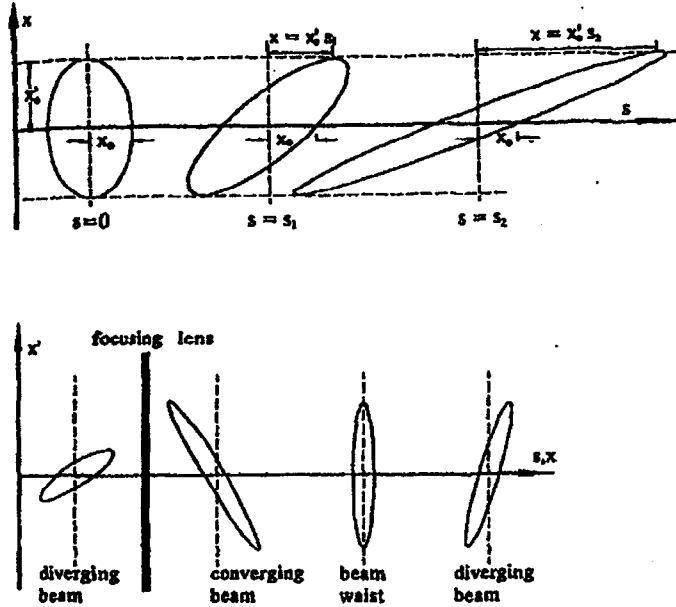
Figure 3.6: A drawing that shows how the the beam ellipse transforms through a transport line. The top plots show that in the case of a drift space. The beam starts with a waist at point $s = 0$ and then it gradually diverges as it travels along the drift distance. The ellipticity and the orientation of the ellipse change continuously and the ellipse rotates clockwise. The second plot shows how the beam ellipse varies when the beam passes through a focusing quadrupole magnet. The initially diverging beam becomes now converging (notice the change in the ellipse orientation) and it eventually reaches a waist. Then it starts to diverge again until another focusing quadrupole is met (from Particle Accelerator Physics by H.Wiedemann).

the transport line, the ellipticity and orientation on the other hand, continuously change. This is shown very clearly in Fig. 3.6. A vertical ellipse indicates a beam waist. An ellipse rotated counter-clockwise indicates a converging beam, while an ellipse rotated clockwise indicates a diverging beam.

The equation for an n-dimensional ellipse can be written in the form:

$$u^T \sigma^{-1} u = 1 \qquad (3.11)$$

where the symmetric matrix σ needs to be determined and u is the coordinate vector defined by

$$u = \begin{pmatrix} x \\ x' \\ y \\ y' \\ \vdots \end{pmatrix} \qquad (3.12)$$

u^T being the transpose of u. Applying Eq. 3.11 to the two-dimensional phase space we get for the ellipse equation:

$$\sigma_{11}x^2 + 2\sigma_{12}xx' + \sigma_{22}x'^2 = 1 \qquad (3.13)$$

Comparison with Eq. 3.7 defines the 2×2 matrix σ as:

$$\sigma = \begin{pmatrix} \sigma_{11} & \sigma_{12} \\ \sigma_{12} & \sigma_{22} \end{pmatrix} = \epsilon \begin{pmatrix} \beta & -\alpha \\ \alpha & \gamma \end{pmatrix} \qquad (3.14)$$

The matrix σ is called the beam matrix. The volume of the two-dimensional phase space area is:

$$V_2 = \pi\sqrt{\det \sigma} = \pi\sqrt{\sigma_{11}\sigma_{22} - \sigma_{12}^2} = \pi\epsilon \qquad (3.15)$$

This is consistent with our earlier definition of the beam emittance.

3.1.3 Measurement of the Beam Emittance

As it is clear from the previous section, the beam emittance is a measure of both the size and the divergence of the particle beam, and therefore we cannot measure it directly. If however we measure the beam size at different locations of the beam line, so that different elements of the beam matrix are probed, the beam emittance can be

determined. We follow the procedure described in [25]. Using the definition of the beam matrix from Eq. 3.15, we have:

$$\sigma_{11}\sigma_{22} - \sigma_{12}^2 = \epsilon^2 \tag{3.16}$$

and we can therefore measure the beam emittance if we find a way to determine the beam matrix σ. In order to determine the beam matrix at the point P_0 of the beam transport line, we need to have at least three beam size monitors, like wires, downstream of that point at locations P_1, P_2 and P_3. A typical wire scanner used in the SLAC linac, is shown in Fig. 3.8. A horizontal, a vertical and a skew wire are mounted on the same yoke. The wire is moved by a stepper motor through the electron beam, the horizontal wire if we are trying to measure the vertical beam width, the vertical wire otherwise, and bremsstrahlung γ's are produced. A downstream detector measures this signal as a function of the wire position. The signal should have a Gaussian shape, and its RMS value gives us the beam size, after quadratic subtraction of the wire size itself. From Eq. 3.9 and 3.14 we can write for the beam sizes found at the locations P_i, three equations of the form:

$$\sigma_{i,11} = C_i^2\sigma_{11} + 2S_iC_i\sigma_{12} + S_i^2\sigma_{22} \tag{3.17}$$

or in matrix form,

$$\begin{pmatrix} \sigma_{1,11} \\ \sigma_{2,11} \\ \sigma_{3,11} \end{pmatrix} = \begin{pmatrix} C_1^2 & 2C_1S_1 & S_1^2 \\ C_2^2 & 2C_2S_2 & S_2^2 \\ C_3^2 & 2C_3S_3 & S_3^2 \end{pmatrix} \begin{pmatrix} \sigma_{11} \\ \sigma_{12} \\ \sigma_{22} \end{pmatrix} = M_\sigma \begin{pmatrix} \sigma_{11} \\ \sigma_{12} \\ \sigma_{22} \end{pmatrix} \tag{3.18}$$

Here C_i and S_i are the elements of the transformation matrix from P_0 to P_i and $\sigma_{i,jk}$ are the elements of the beam matrix at P_i. Eq. 3.18 can be solved for the beam matrix elements σ_{ij} at the point P_0

$$\begin{pmatrix} \sigma_{11} \\ \sigma_{12} \\ \sigma_{22} \end{pmatrix} = (M_\sigma^T M_\sigma)^{-1} M_\sigma^T \begin{pmatrix} \sigma_{1,11} \\ \sigma_{2,11} \\ \sigma_{3,11} \end{pmatrix} \tag{3.19}$$
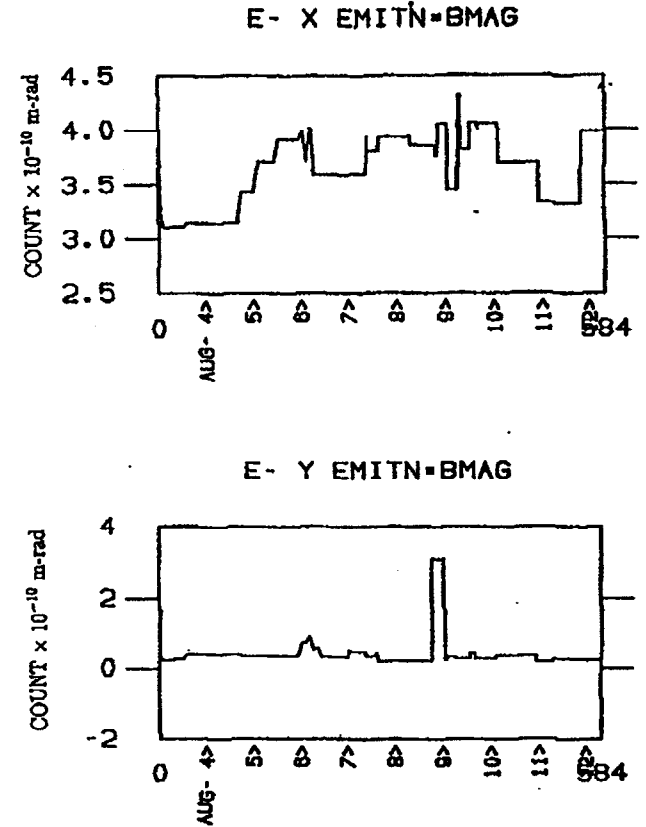
Figure 3.7: History curve of the emittance measurements in sector 28 of linac during the data run. The vertical curve shows the emittance in units of 10^{-10} m-rad, while the horizontal axis is time in days.

The matrix M_σ is known from the elements of the beam transport line between the points P_0 and P_i. The solution vector can be used in Eq. 3.16 to calculate finally the beam emittance.

The above method is utilized in the emittance measurements performed in the linac. There are three locations that this is done: the first is right after the extraction
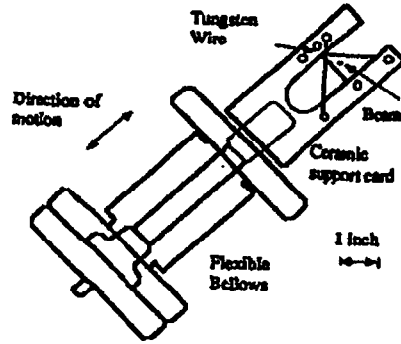
Figure 3.8: Schematic of a typical SLC type wire, where a horizontal, a vertical and a skew wire are mounted on the same yoke.

from the damping ring in sector 2; the second near the center of the linac in sector 11; and the third near the end of the linac in sector 28. The first measurement is important, since it checks the operational efficiency of the damping rings. The main purpose of a damping ring is to reduce (damp) the emittances of the incoming electron beams in all planes. Due to the emission of synchrotron radiation, the emittance of the electron beam is reduced in circular accelerators according to

$$\sigma_j^2(t) \; = \; \sigma_{i,j}^2 e^{-\left(\frac{2t}{\tau_j}\right)} + \sigma_{e,j}^2 \left[1 - e^{-\left(\frac{2t}{\tau_j}\right)}\right], \quad \text{with } j = x, y \qquad (3.20)$$

where $\sigma_{i,j}$ the injected into the damping ring beam size, $\sigma_{e,j}$ the equilibrium beam size, and τ_j the damping time. It is clear that the longer an electron beam is stored in a damping ring, the smaller the emittances will be. The measurement in sector 28 is the most important measurement in terms of the FFTB line setup, since it is the one made closest to the FFTB line itself. Fig. 3.7 shows the variation of the emittances measured in sector 28 of the linac with time during the E-144 data collection run [26]. In both cases normalized emittances ($\gamma\epsilon$) are shown, in units of 10^{-5} m·rad, since those remain invariant under acceleration. To translate into the laboratory frame we have to divide the normalized emittances by a factor of 9×10^4, and therefore we use units of 10^{-10} m·rad. The FFTB design emittances are $\gamma\epsilon_x = 3 \times 10^{-5}$ m·rad and

$\gamma\epsilon_y = 3 \times 10^{-6}$ m·rad. As is shown in Fig. 3.7 during the E-144 run the horizontal emittance tends almost always to be higher than the design for the FFTB, while the vertical emittance for most of the time is close or even below the design value.

3.2 FFTB Line Setup

In principle FFTB can be divided in six distinct regions, each one of them serving a specific purpose, as it will become apparent as we go on describing them [28].
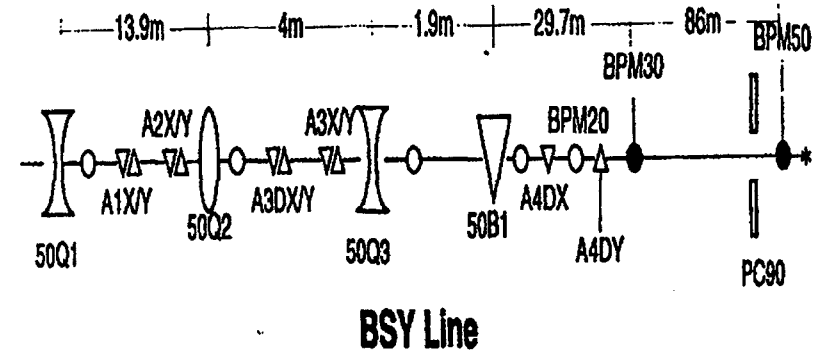
Figure 3.9: Schematic of the Beam Switch Yard (BSY) line right before the FFTB. The dark BPMs are used by the FFTB Launch Feedback described in the text.

Right in front of the FFTB line, is the Beam Switch Yard (BSY) line. Although not part of the FFTB proper, it contains modules important for the FFTB operations. A schematic of the BSY line is shown in Fig. 3.9. The important elements from the FFTB point of view are the Beam Position Monitors (BPM) 30 and 50 that measure the position and angle of the incoming electron beam, and the corrector pairs A3DX/Y and A4DX/Y that are used by the launch feedback described later, to correct the orbit measured by those two BPMs. The bending magnet 50B1 needs to be off (degaussed) during the FFTB operations. The main FFTB line follows right after and it is shown in Fig. 3.10. The Beta Match Line is the first optical module
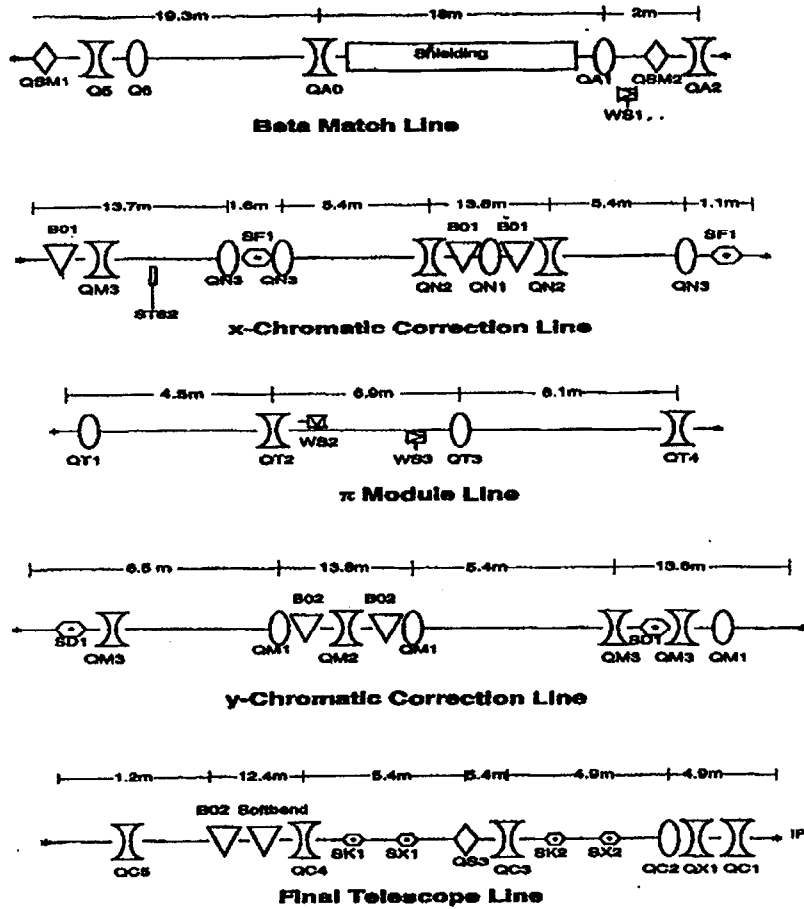
Figure 3.10: Schematic of the five main optical modules of the FFTB line described in the text.

in the FFTB line. The five quadrupole magnets in this region are used to match the parameters of the incoming beam to those desired at the Focal Point (FP). The exact procedure for doing this will be described in the next section. The wire shown in the line is used to measure the incoming beam parameters, which we need to know
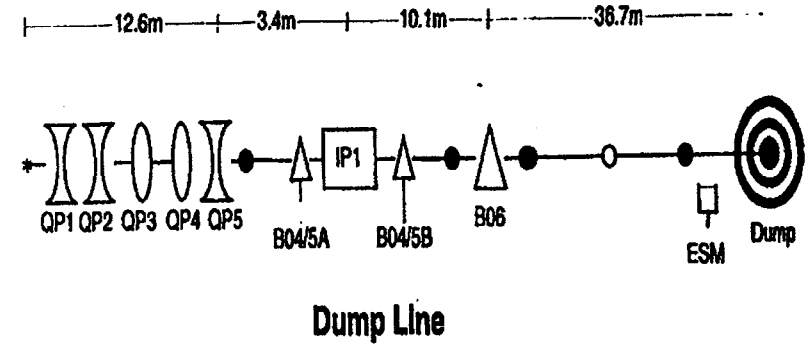
Dump Line

Figure 3.11: Schematic of the FFTB Dump line. Its purpose is to guide the electron beam to the dump. The electron laser interaction point is shown with the name IP1. The bending magnets around it, actually depict pairs of soft bending magnets, while B06 stands for a series of 6 permanent bending magnets.

in order to properly perform the beta match. The next three lines are used for the chromatic corrections needed on the incoming beam. If we define the chromaticity of a beam as the measure of the change in focusing power with the energy spread of the focused electrons, then it can be shown that the focused size of an electron beam with a finite energy spread is:

$$\sigma^*_{x,y} = \sigma^*_0 \left[1 + \xi^2 (\frac{\sigma_R}{E})^2 \right] \qquad (3.21)$$

Here ξ is the chromaticity, $\sigma^*_0 = \epsilon_{x,y}\beta^*_{x,y}$ the focal beam size of a zero chromaticity beam, and $\frac{\sigma_R}{E}$ the beam energy spread. We can see that the existence of chromaticity enlarges the focal beam size and we need therefore to eliminate or at least minimize it [28]. This is what the chromatic correction lines do. The sextupoles shown are the ones primarily used for that purpose. In order to correct mainly the horizontal chromaticity in the CCSX line, the optics are adjusted so that $\beta_x \gg \beta_y$ at the SF sextupole locations. Exactly the opposite condition needs to be established at the SD sextupoles in the CCSY line, in order to correct the vertical chromaticity. This "exchange" of beta functions is done in the middle line called the Beta Exchanger.

During this the beam reaches a horizontal and a vertical waist at the locations of the two wires WS2 and WS3 respectively, that are shown in the line. The measurements of the two wires are useful for checking the validity of the established beta match. We come therefore down to the Final Telescope line which, as its name implies, is the main focusing element in the FFTB line. The most important magnets here are the three final quads which perform the main focusing. The sextupoles and the skew quad shown, can be used to correct residual sextupole abberations and coupling due to rolled quadrupoles before the focal point. The dump line is the final region in the FFTB and is used to guide the electron beam to the dump. The electron-laser interaction point is located here as Fig. 3.11 shows. The BPMs shown are used for beam energy measurements and energy feedbacks as it is explained later in this section.

Prior to tuning the electron beam to the configuration required for E-144, the beam needs to be brought to the FFTB line and then steered down to the interaction area. Several parameters of the incoming beam, such as its position and angle, and also its energy need to be measured, adjusted and maintained in such a way so that the beam quality at the interaction region is optimal. In addition, the beam backgrounds need to be adequately reduced, before any further beam tuning is carried out. After an extensive period of FFTB running a specific procedure has been introduced, which is generally known as the beam to dump procedure [27]. Also before any FFTB/E-144 run the FFTB line is surveyed using mechanical techniques and the magnets are placed with an expected accuracy of 100 μm in the horizontal plane and 50 μm in the vertical plane.

Incoming position and angle jitter to the FFTB line are translated through the FFTB optics to focal point jitter, whether that focal point is the FFTB final focus or the focal point further downstream at the E-144 interaction area. For E-144 this jitter affects the spatial overlap between the electron and laser beams, resulting in large variations of the nonlinear Compton scattering and positron production rates. To

alleviate this problem the FFTB launch feedback is introduced [28]. This system uses BPMs 30 and 50 in the BSY line separated by 86 meters to reconstruct the position and angle of the incoming beam, and a pair of correctors (A3DX/Y, A4DX/Y) in each plane, located in the same line, to hold the BPM readings to some reference values (see Fig. 3.9). The incoming electron beam is steered through the BSY line so that all the obstacles are avoided and collimator PC90 is adequately cleared, based on the evidence of the loss monitors in the area. The readings of the two BPMs 30 and 50 for which the beam skirted all the obstacles, are the reference values used in the launch feedback and are known as the FFTB launch Criterion. Assuming that the BPM errors are uncorrelated and that the BPM resolution is 1 μm, the expected resolution of the position and angle at the first BPM is 1 μm and 0.016 μrad. The primary function of the launch feedback is to correct slow drifts and to decouple the FFTB steering from slow and/or DC effects upstream (such as quad strength changes, etc..).

Because of the arrangement of the FFTB line, the energy related properties of the electron beam can be measured more easily at the FFTB's extraction line [28]. A wire scanner (ESM) and a cluster of BPMs can be used to provide information on the pulse-to-pulse energy jitter and on the energy spectrum. The BPMs are separated by drift spaces and/or bend magnets (see Fig. 3.11), resulting in the simplest possible system that can be used to reconstruct the beam energy. The last BPM of such a system will have the highest resolution of both the incoming vertical angle and the energy, and the energy measurement will be correlated to the vertical angle. An energy feedback can then be introduced which uses the readings of those BPMs and klystrons at the end of the linac. Beam steering confuses the energy feedback, and therefore it is disabled during such an operation. The energy jitter measured at the extraction line is of the order of $\delta E/E = 10^{-4}$ or 7 MeV. Since the linac contains 240 klystrons, even a single klystron failure (cycling) can result in energy excursions of 35 times the RMS value quoted earlier. Under such conditions the last BPM fails completely and the energy feedback fails to restore the nominal energy. To prevent

this, a low resolution BPM has been installed between the bend magnets and the last BPM. Its measurement is weighed slightly during the energy fit and it becomes important only when the last BPM fails. Its role is to rescue the energy feedback and make it restore a nominal energy value that will enable the last BPM to read properly.

In linear accelerators the constant production and extraction of particle bunches, requires a vigorous beam collimation system in order to eliminate particles at large excursions from the average position, angle, or energy. FFTB's primary set of collimators consists of the linac collimators located at the last 300 m of the accelerator. The first set (sectors 28-29) perform the primary collimation, while the second set (sectors 29-30) removes the particles that have scattered off the first set of collimators. The linac collimators do not remove large energy oscillations and they are inadequate for areas characterized by very large betatron functions like the FFTB [28]. FFTB itself has two sets of collimators. The first consists of a pair of horizontal momentum jaws. Particles for which the added geometric and dispersive offsets are large enough so that they hit the jaws, are removed. Still this system is not adequate for the case of particles for which their geometric and dispersive offsets, though large enough, are of opposite sign. Therefore a second set of movable jaws, one horizontal and one vertical pair, are placed further downstream at a point where the dispersion is equal to the one at the location of the first set, but which are separated by optics that have the effect of inverting the sign of the geometric offset. Particles whose geometric and dispersive offsets are canceled out at the position of the first set will be eliminated here. In general setting up the FFTB collimation is a long procedure that requires considerable amount of trial and error. The two silicon calorimeters that look at the electron and positron signal provide the best background monitors during this procedure.

3.3 Beta Match

3.3.1 Reconstruction of the Incoming Beam
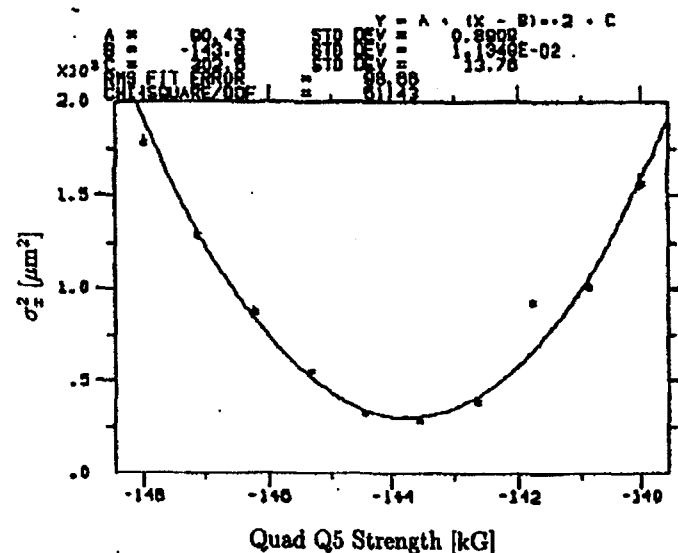
Figure 3.12: Measurement of the σ_x of the electron beam when the strength of quad Q5 is being varied. The vertical axis shows the horizontal spot size measured by a vertical wire downstream of the scanned quad in μm. The horizontal axis shows the quad strength in kGauss, defined as the integral of the field gradient over the whole magnet length.

The FFTB does not exercise full control over the 3 km linac and the BSY line. That means that the incoming beam parameters (β, α) will not necessarily be equal to the FFTB's design values. In addition no reliable coupling measurement can be made by using the sector 28 wire scanners. Therefore the FFTB uses its own set of wires for reconstructing the incoming beam's phase space. These are the x, y and v yokes of the WS1, near the end of the first section of FFTB, the Beta Match line (see Fig. 3.10). The method used in this case differs from the one described in section 3.1.3 and
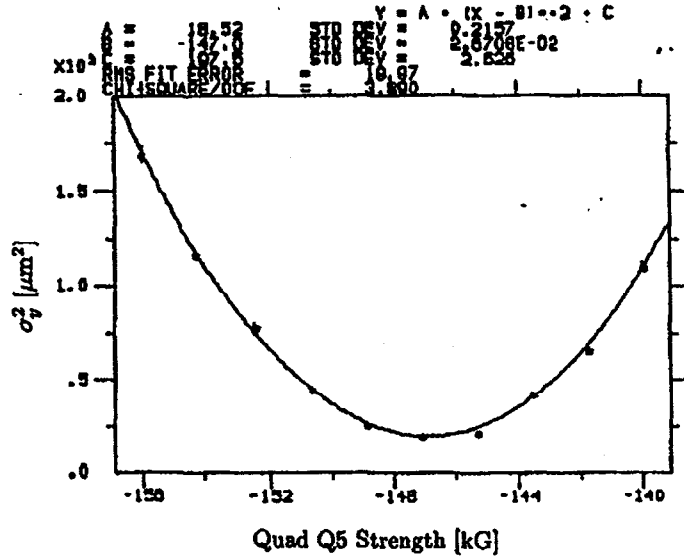
Quad Q5 Strength [kG]

Figure 3.13: Measurement of the σ_y of the electron beam when the strength of quad Q5 is being varied. The vertical axis shows the vertical spot size measured by a horizontal wire downstream of the scanned quad in μm. The horizontal axis shows the quad strength in kGauss, defined as the integral of the field gradient over the whole magnet length.

requires the focusing of the electron beam to a waist on the wire scanner, and then measuring the beam size as a function of the strength of an upstream quadrupole. In the case of no coupling between the x and y planes the situation is very simple. Suppose we want to measure the emittance and the Twiss parameters (β, α) at some point P_0, with our beam size monitor placed at the point P_1; a quadrupole of variable strength k is located between P_0 and P_1. In this section and for the rest of the chapter, we define the quadrupole strength as the integrated field gradient over the whole length of the magnet, assuming a constant pole tip field. This is true when the magnet length is much larger than its aperture as it is the case for FFTB. Then we

can write for the quadrupole strength

$$k = \frac{B_0\, l}{a} \tag{3.22}$$

where B_0 is the pole tip field at the center of the quad, and l, a are the length and the aperture radius of the quad. The units of a quadrupole magnet strength, as it is defined in Eq. 3.22 are therefore kG. By varying the quad strengths we measure the beam size $\sigma_{1,11}$ at P_1 as a function of the quad strength and compare it with the theoretical expectation:

$$\sigma_{1,11}(k) = C^2(k)\sigma_{11} + 2C(k)S(k)\sigma_{12} + S^2(k)\sigma_{22} \tag{3.23}$$

By fitting the parameters σ_{11}, σ_{12} and σ_{22} to match the measured curve, one can determine the beam emittance (see Eq. 3.16). This procedure does not automatically guarantee the measurement of the emittance with adequate precision. For the fit to be accurate, we need to vary the beam size at the wire scanner significantly, so that the nonlinear dependence on the quadrupole strength becomes apparent. Experience shows that the beam size at the point P_0 should be large and preferably divergent. In this case the variation of the quadrupole strength will drastically change the beam size at P_1, from a large value when the quad is underfocusing, to a small focal spot size when it is on tune, and back to a large value when it is overfocusing [25]. In the case of the FFTB, the incoming beam is focused on the wire scanner WS1 with five quadrupole magnets on the wire scanner WS1. Then the strength of the first of these quads (Q5) is varied while a beam size measurement is performed at each different magnet strength (see Fig. 3.10 for the arrangement of the quads and the wire scanner in the Beta Match line).

However, the x and y planes of the incoming beam are not uncoupled. This has been observed repeatedly during earlier FFTB runs. For example the normalized vertical emittance measured in sector 28, tends to be at least a factor of 2 smaller than the same quantity measured at the entrance of the FFTB. As already mentioned, the wire system in sector 28 cannot resolve xy coupling in phase space, and therefore the
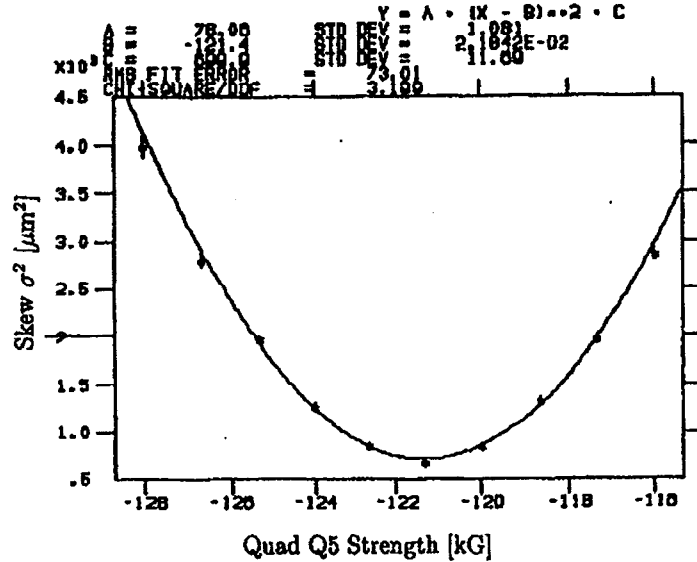
Figure 3.14: Variation of the spot size of the electron beam when the strength of quad Q5 is being scanned. The vertical axis shows the spot size measured by a 45° skew wire downstream of the scanned quad in μm. The horizontal axis shows the quad strength in kGauss, defined as the integral of the field gradient over the whole magnet length.

measured emittances are certainly underestimated. The first quad in the FFTB line is a weak skew quadrupole (QSM1), which when turned on changes the correlation between y and y'; it changes the y' values, which are proportional to x. By scanning the strength of this quad and measuring the y size of the beam at WS1, (and then the emittance as described earlier), we find that for QSM1 strengths of around 1 kG the measured emittances at WS1 become very close to the ones measured by the wire system in sector 28 of the linac.

Even when most of the xy coupling has been reduced by the use of the skew quad QSM1, it is still desirable to reconstruct the whole 4×4 beam matrix in (x, x', y, y'). Since this matrix is symmetric there are only 10 independent parameters that are

needed to be calculated. The in-plane elements (σ_{11}, σ_{12}, σ_{22}, for the x, x' plane and σ_{33}, σ_{34}, σ_{44} for the y, y' plane), can always be calculated using the method described earlier by just measuring the horizontal and vertical beam sizes at WS1 using a vertical and horizontal wire respectively. Two such scans are shown in Fig. 3.12 and Fig. 3.13. In order to find the coupling terms σ_{13}, σ_{14}, σ_{23} and σ_{24}, we need to use a 45° skew wire, usually denoted as the v wire, and mounted on the same wire scanner WS1, as Fig. 3.8 shows. We perform two different wire scans, either by varying the strengths of two upstream quadrupoles, or by varying the same quadrupole in each case, but using different magnet configurations. Such a scan is shown in Fig. 3.14. The method employed in this case is called the 4-D Quad Emit procedure and it has been developed by W.L.Spence [28], [29]. The algorithm uses the thick lens approximation to describe the beam line, and returns the beam matrix, the normal-mode and projected emittances, the Twiss parameters and the coupling parameters. Therefore the 4-D Quad Emit can be used to measure the residual coupling after the skew quadrupole QSM1 has been set to minimize the projected emittance. The incoming projected emittances thus measured are $\epsilon_x = 3.43 \times 10^{-10}$ m·rad and $\epsilon_y = 0.21 \times 10^{-10}$ m·rad.

3.3.2 Implementation and Verification

Once the incoming beam has been reconstructed, it is rather straightforward to compute the quadrupole strengths needed to produce the correct beam parameters at the FFTB's focal point. A host of different beam-optics programs (SAD, COMFORT, DIMAD, TRANSPORT) have been used successfully to that end. For the needs of the positron run, the desired $\beta^*_{x,y}$ at the FFTB focal point are 30 mm × 10 mm. This is a slightly divergent beam and it is used in order to ensure low background levels. Table 3.2 shows the strengths of the FFTB β-Match region quadrupoles necessary to achieve the $\beta^*_{x,y}$ mentioned above.

Once the β-Match has been implemented, it needs to be verified. The wire scanner

Quad Number	Quad Strength [kG]
QSM1	0.64
Q5	-153.20
Q6	157.70
QA0	-2.23
QA1	181.37
QA2	-317.72

Table 3.2: List of the quadrupole strengths in the FFTB β-Match line. Those are computed with the requirement that the $\beta^*_{x,y}$ at the FFTB focal point should be 30 mm × 10 mm. The quadrupole strength is the integrated field gradient, as it is defined in the text.

WS1 cannot be used any more in this case, since the dual image of the focal point on it disappears. Further downstream images can be provided for verification purposes, at the wire scanners WS2 (horizontal waist) and WS3 (vertical waist). The ultimate verification of course will be the spot size measurement at the FFTB focal point itself (wire WS6A). A much bigger image of the focal point further downstream can also be checked using wire WS6B. Table 3.3 shows the beam spot sizes predicted at those four locations. WS2 measures a $\sigma_x = 12.81$ μm, while WS3 measures $\sigma_y = 7.36$ μm, not too far off from the predicted values, although y does seem to be somewhat mismatched. The vertical spot size measurement at WS6A is very much off being at 2.2 μm. Several things can be done to improve that. First we can turn the two sets of sextupoles on in the FFTB line, which will help to remove any second order abberations (chromaticity). Second we can try to remove any residual coupling in the electron beam caused for example by rolled quads upstream from the focal point. This is achieved using one more skew quadrupole (QS3) located a few meters upstream of the final focus (see Fig. 3.10 for the arrangement of the magnets in the FFTB final telescope). We can again scan the strength of that quadrupole and measure the spot

Wire Number	σ_x [μm]	σ_y [μm]
WS2	10.32(12.81)	18.43
WS3	105.27	11.09(7.36)
WS6A	3.65(4.8)	0.70(1.6)
WS6B	56.87(64.9)	26.02(35.6)

Table 3.3: List of the electron beam spot sizes at different image locations in the FFTB line. The actually measured values are shown in brackets.
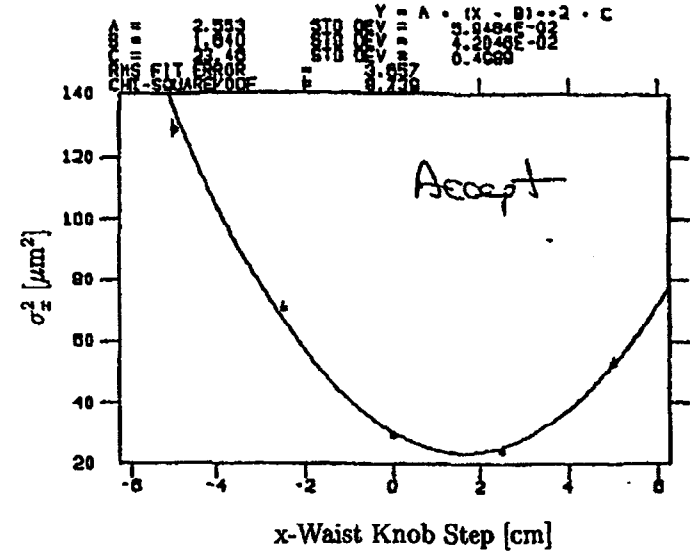
Figure 3.15: Scan of the position of the x-waist at the FFTB focal point using a waist knob that affects only σ_x.

sizes at the wire scanner WS6A. Third and last we can use the waist knobs which control the three last quads in front of the focal point to move the x or the y waist independently, by specific distances upstream or downstream. Such waist scans in
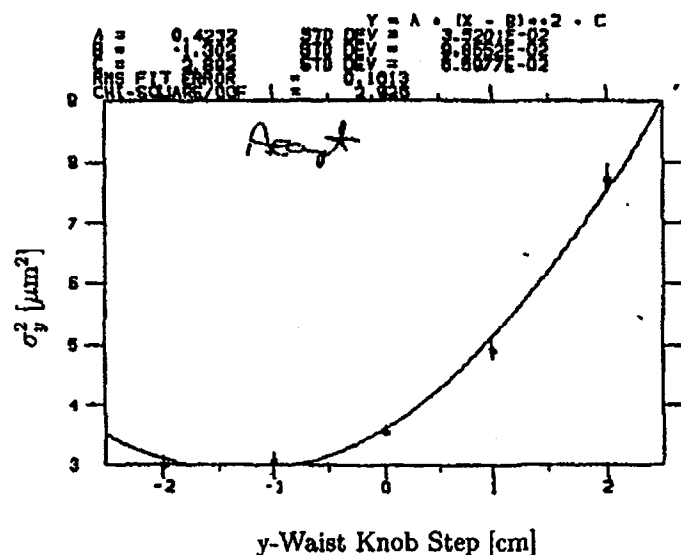
Figure 3.16: Scan of the position of the y-waist at the FFTB focal point using a waist knob that affects only σ_y.

both the x and y direction are shown in Fig. 3.15 and Fig. 3.16 respectively. After this tuning procedure is completed, the y spot size at the focal point is measured to be $\sim 1.6\ \mu$m, as it is shown in Fig. 3.17; the x spot size is measured to be $\sim 4.8\ \mu$m, and the beam size at the WS6B wire 64.9 μm $\times$ 35.6 μm. Although things have been improved there is still a serious discrepancy in both dimensions and especially in y. At this point an emittance measurement in sector 28 has to be made. Surprisingly the measurement returns projected emittances of $\epsilon_x = 4.3 \times 10^{-10}$ m·rad and $\epsilon_y = 0.4 \times 10^{-10}$ m·rad. Both are much bigger than the ones measured during the β-Match procedure and are compatible with the corresponding focal spot size measurements at WS6A. [1] Once the β-Match has been implemented and verified,

---

[1]Tuning of the linac emittances towards lower values can be a time consuming process and the emittances remained that high for several days during the positron run. When they were finally brought down to values close to the ones measured during the β-Match the spot size at the final
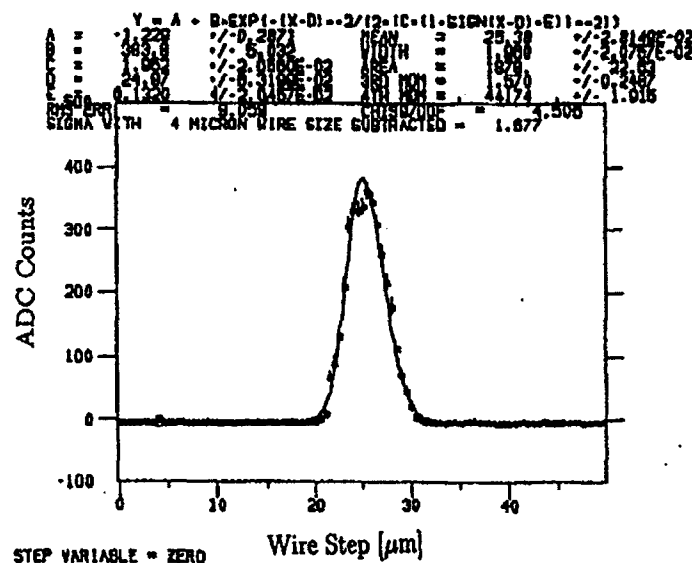
Figure 3.17: Measurement of σ_y in μm at the FFTB focal point. The size of the wire has already been subtracted.

we can go ahead and start the procedure for establishing a small spot size at the electron-laser interaction area (IP1), located ~ 12.5 m downstream of the FFTB final focus.

3.4 IP1 Spot Tuning

3.4.1 Tuning Procedure

The tuning for a small spot size at the laser-electron interaction point (IP1), is a procedure for transferring the waist already achieved at the FFTB final focus 12.5 m downstream. The procedure is not as simple as it may sound. For one, there are very few quads between the two locations, and the so called dump line quadrupoles, operate

---

focus was measured to be $\sim 0.8\ \mu$m.

at or almost at their maximum strength. This means that we have to use further upstream quads and therefore the waist at the final focus disappears. Furthermore the apertures of the dump line quads are very tight making it impossible to use any high divergence optics, since it would produce intolerable levels of background at the primary positron detector (PCAL). Clearly the beam spot size at IP1 can not remain as small as it is at the final focus. We do not want to touch any of the β-Match quads, no matter how significant their effect might be, because this will result to a complete mismatch of the incoming electron beam to the FFTB lattice. Furthermore the FFTB line should not be altered too much, since traditionally a positron run precedes or follows an FFTB run. We are left therefore with very few degrees of freedom that we can use.

The computation of the quadrupole strengths needed to focus the electron beam at IP1 is done by using TRANSPORT and the results have been cross-checked with the SLC online version of COMFORT and with DIMAD. Table 3.4 shows the required magnet strengths. Fig. 3.18 shows the spot sizes at different points in the last two sections of the FFTB line, that surround IP1. Although the β-Match used in the plot is different than the 30 mm $\times$ 10 mm that it is finally used, it still displays the main characteristics of the small IP1 spot tuning, since it utilizes the same magnets as shown in table 3.4. The predicted spot size at IP1 is 20 μm $\times$ 25 μm, in x and y respectively. Waist knobs that utilize the last quad doublet in front of IP1 (one vertically and one horizontally focusing quad), can also be used to move the x or the y waist around IP1. The knob settings are found by performing waist scans as discussed in section 3.3.2.

3.4.2 Measurement of the IP1 Spot Size

IP1 contains a system of x, y and v Al wires 20 μm thick, that can be remotely inserted in the beam path, using stepper motors with μm accuracy. A very accurate way of calibrating the x, y and z positions of the wires is necessary, since it is expected

Quad Number	Quad Strength [kG]
SF1A SF1B	35292.09
SD1A SD1B	17930.95
QC4	-106.45
QC3	-150.58
QC2	729.95
QP4	110.91

Table 3.4: List of the quadrupole strengths needed to give a waist at the IP1. Again integrated quad strengths are used following the definition given in table 3.2. The first two pairs are sextupole doublets that have the same strength. The last magnet is a quadrupole located in the FFTB extraction line.

to measure fairly small beam spot sizes. Although the self calibration of the x and z motors is accurate enough, this is not the case with the y motor which seems to move much faster downwards under the influence of the weight of the flag (for a schematic of the IP1 flag see section 4.4 of the next chapter) on which the wires are attached. For this reason the vertical position of the IP1 wires is measured using a Linear Voltage Distance Transducer (LVDT). LVDTs can be easily calibrated in the lab, with submicron accuracy. The calibration line which is fit with a low order polynomial, relates the voltage that the LVDT outputs to the actual position. Fig. 3.19 shows the calibration of the LVDT used in IP1 for the vertical wire position.

Two different methods to measure the IP1 spot size can be used. Both give compatible results. The first method scans the electron beam across the vertical or the horizontal IP1 wire, using the dither correctors closest to IP1. This method is easy to integrate with the rest of the SLC (SLAC Linear Collider) control program (SCP)

FFTB95 Small Spot Config-->Small IP1 Spot 18Aug95
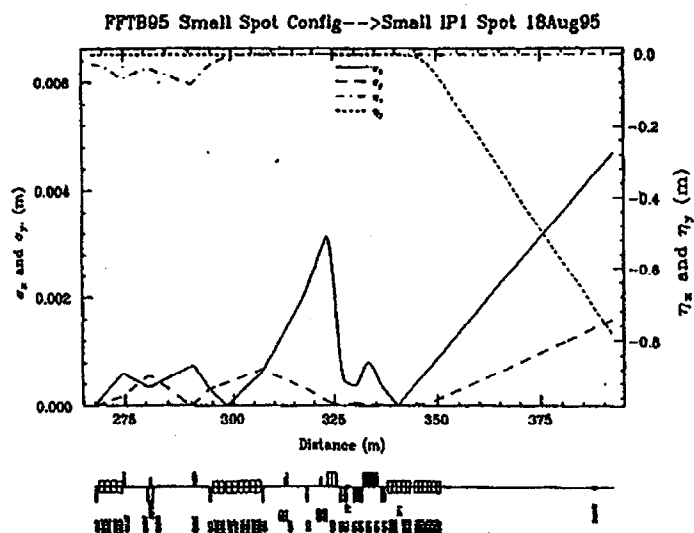
Figure 3.18: Simulation of the IP1 electron beam spot's σ_x and σ_y using TRANS-PORT. Although it is based on a different β-match than the one finally used, it nevertheless displays all the characteristics of a small IP1 spot tuning since it utilizes the same magnet configuration that has eventually been used.

and it is repeatedly used during the small-beam tuning procedure. In the second method the vertical or the horizontal IP1 wires are stepped through the electron beam. The second method is part of the main data acquisition system for E-144, but it is not part of the SLC control program. Fig. 3.20 and Fig. 3.21, show the IP1 beam sizes at the end of the beam tuning. There is a discrepancy between the predicted and the actually measured values especially in the y direction, and the projected emittances during this measurement have turned out to be bigger than expected. Table 3.5 shows the measured spot sizes using any of the two methods mentioned above, during the 46.6 GeV run period. As the table shows frequent tuning of the FFTB line and/or the linac itself is necessary in order to sustain reasonably small beam sizes. The continuous disagreement between the predicted and measured y beam
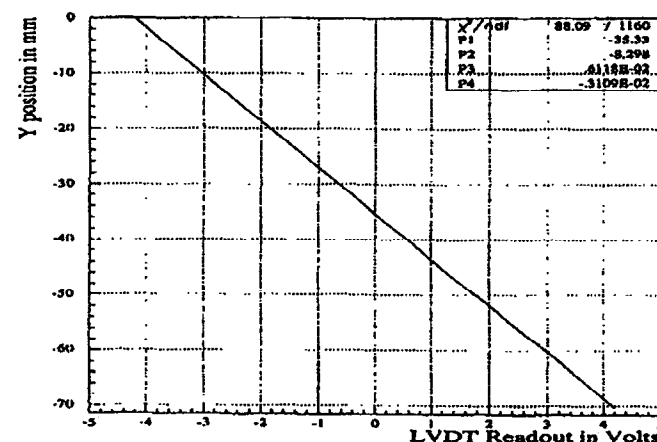
Figure 3.19: Calibration of the IP1 wire vertical mover. The position indicator is an LVDT that follows the functional expression shown and which is used in the wire scan algorithm.

Run Number	σ_x [μm]	σ_y [μm]
15100–15322	23.97	36.31
15323–15371	24.80	47.85
15372–15398	21.46	37.49
15401–15463	21.46	37.29
15470–15515	25.67	33.55

Table 3.5: List of the measured electron beam spot sizes during the 46.6 GeV data runs.

sizes during the whole period of the 46.6 GeV data run, indicates some considerable β mismatching.

Once the beam tuning and steering is done, we need to maintain the position,
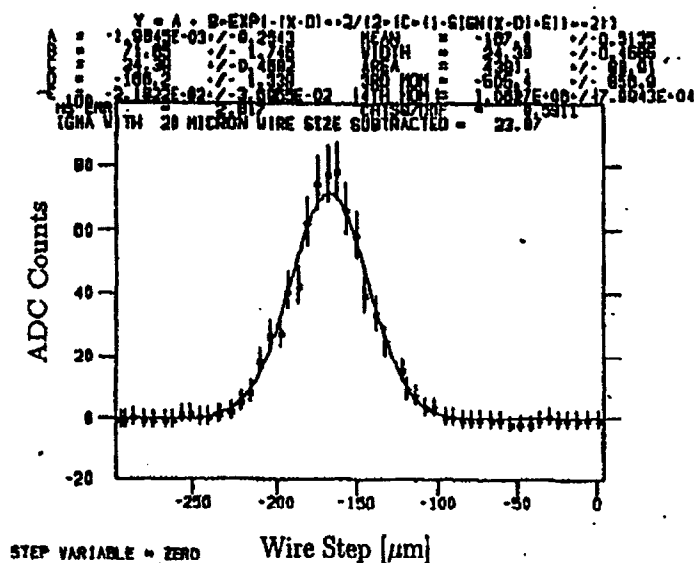
Figure 3.20: Measurement of σ_x of the spot at IP1 for a 46.6 GeV electron beam.

angle and energy of the electrons that reach the interaction region. One more feedback loop is thus activated, the E-144 feedback. The energy feedback is done in exactly the same way as described in section 3.2. For the position and angle, both in x and y directions, the BPMs around IP1 are read and compared to some set values, that have been acquired at the end of the steering, when the background tuning is satisfactory. The necessary corrections are done with the help of x and y dither correctors closest to IP1. At the end of the spectrometer section there are two distinct lines emerging. The first one defines the electron path as they are bent down towards the dump by the bend magnets. The second one defines the γ path, for the high energy γ's produced at IP1, which follows a straight line towards the CCD detectors. Tuning the electron beam and setting the E-144 feedback on, does not necessarily guarantee the proper propagation of the produced γ's down the γ line, without causing any undesirable background levels, especially when they encounter the tight apertures located in their
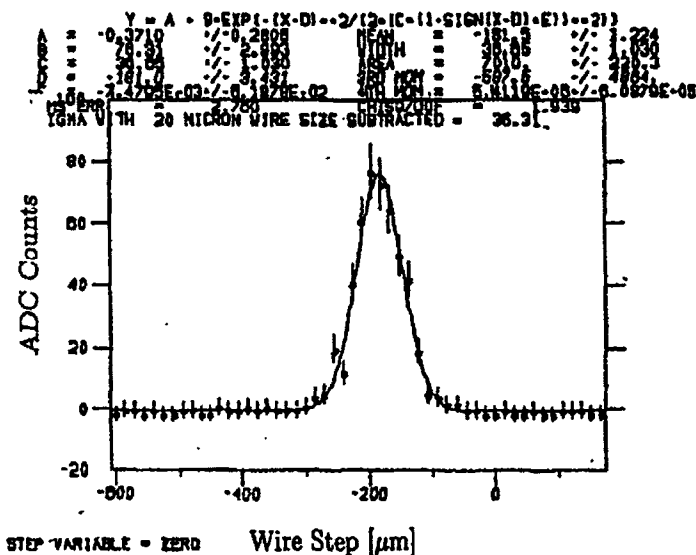
Figure 3.21: Measurement of σ_y of the spot at IP1 for a 46.6 GeV electron beam.

path. The collimators, introduced in the γ line to reduce the synchrotron radiation light on the CCDs, can be aligned prior to the runs by shining a He-Ne laser from the end of the line up to IP1. The steering of the γ's is done by inserting a foil in IP1 and changing the pointing of the electron beam at IP1. The easiest way that this can be achieved, is by changing the set points in the E-144 feedback. A silicon γ detector at the end of the γ line provides us with a diagnostic during this alignment procedure. Some special care is always needed, especially in order to completely eliminate the synchrotron light. The pointing of the electron beam is what matters here and it can be always adjusted with the dither correctors. The E-144 feedback needs to be left undisturbed for some time after every beam tuning change, in order to "catch up". Since most of the collimators in the γ line are not movable, such a correcting procedure to protect the CCDs is always needed.

3.5   49 GeV Beam Set Up
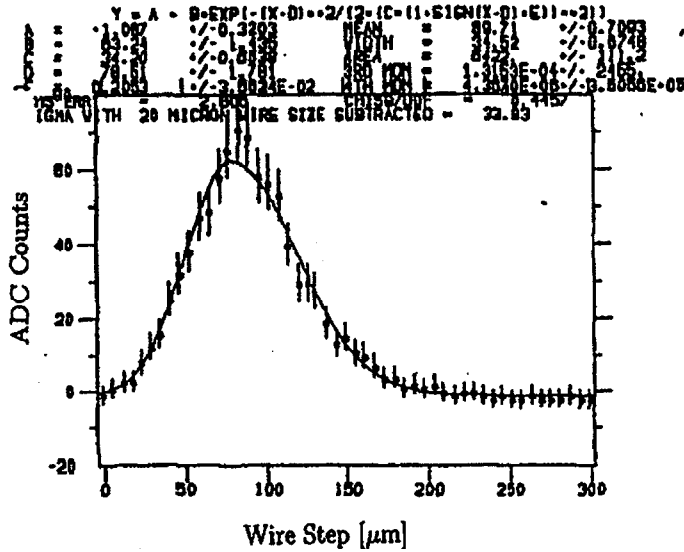
Figure 3.22: Measurement of σ_x of the spot at IP1 for a 49.1 GeV electron beam.

It is interesting to study the nonlinear Compton and positron rates in higher beam energies. The linac itself can deliver beams of up to 55 GeV, but the FFTB design limits the beam energy to about 50 GeV. The FFTB line itself has never been tested for electron energies higher than 46.6 GeV, so it is also interesting to check the experimental limits for FFTB. In principle a successful scaling of the energy of the electron beam that still keeps it on the same path, requires the scaling of all the magnet strengths in the electron line by the same amount. In our case this is not quite straightforward, since several magnets in the FFTB line, especially the ones in the dump line, are already at almost their maximum strength with a 46.6 GeV electron beam. Therefore the FFTB optics need to be rearranged first in such a way so that all the magnet strengths can be scalable to higher values, while the size,

position and pointing of the electron beam at IP1 remains the same. Only then can we try to increase the energy of the electron beam, steer it through the FFTB line and reestablish a small spot size at IP1 suitable for positron data taking.
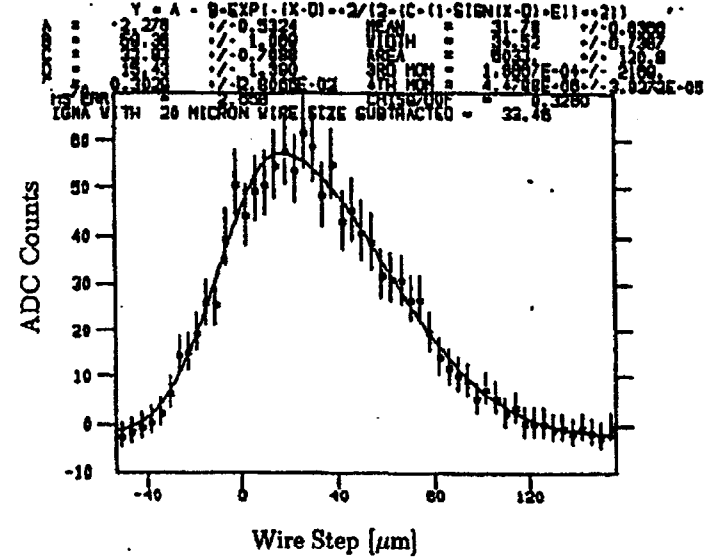
Figure 3.23: Measurement of σ_y of the spot at IP1 for a 49.1 GeV electron beam.

Two magnet configurations, one at 46.6 GeV which is scalable to higher energies, and another at 50 GeV produced by scaling the strengths of all the magnets in the FFTB line by the ratio of $50/46.6 = 1.073$, were prepared by using the online beam simulator DIMAD. These two configurations are used by a knob that will at the same time gradually scale the electron energy in the linac and the magnet strengths in the FFTB line by the same scaling factor, starting from the 46.6 GeV configuration and moving towards the 50 GeV one. After each scaling step the electron beam has to be steered so that it always makes it to the dump. The real restriction to this procedure is the fact that the main dump line bends that guide the electron beam to the dump, are permanent magnets with strengths designed for 46.6 GeV electrons,

and therefore the electron beam needs to be overbend in their entrance and at the same time clear them adequately well so that the radiation levels measured by the loss monitors are much lower than their trip values. There are four soft bend magnets in front of the permanent ones, that can be used for this purpose. The whole scaling process therefore is limited by the maximum field strength that the power supplies for these magnets can deliver. Eventually 49.1 GeV was the highest electron energy achieved, with $\sim 5 \times 10^9$ electrons per bunch. We can then tune again for small IP1 beam sizes as usually. The predicted spot sizes are 30 μm $\times$ 30 μm, and the results of the wire scans at IP1 at the end of the tuning are shown in Fig. 3.22 and Fig. 3.23. The setpoints of the E-144 feedback become an adequate tool for steering the γ line as described in the previous section. On the less bright side of this process, the background levels increased by a factor of 5–10 and repeated steering helped to bring them down to about a factor of 4 higher than the 46.6 GeV case, as described in more detail in chapter 7.

Chapter 4

The Laser System

4.1   Laser System Description

The laser is based on the Chirped Pulse Amplification (CPA) technique [30], [31]. It consists of a mode-locked Nd:YLF oscillator, a Nd:glass regenerative amplifier, a two pass Nd:glass rod amplifier and finally a flashlamp-pumped Nd:glass slab amplifier. A schematic of the laser system is shown in Fig. 4.1.

In order to collide a laser pulse with an electron bunch, the oscillator is locked to the accelerator rf. For this purpose, the 476 MHz drive frequency needs to be transported from the accelerator master clock to the laser room, as is described in section 4.3. After frequency dividing by 8 this signal is used to drive the acoustooptic modelocker of the cw-pumped oscillator at 59.5 MHz, while the phase of the laser pulses with respect to the reference rf is maintained with the help of a phase-locked feedback loop. The low-Q modelocker [32] is driven by the 59.5 MHz rf after it is amplified to 4 W. The Q of the modelocker can be measured by shining a He-Ne laser through its center and using a fast photodiode to measure the light after the 0-th order Bragg reflection. The driving frequency of the modelocker is varied using a synthesizer operating around 59.5 MHz. The photodiode signal is fed to a spectrum analyzer. Fig. 4.2, gives the fractional modulation depth of the He-Ne light. We can

A phase-stabilized, CPA laser system delivers ~10^{18} W/cm^2, 0.5 µm or 1 µm laser pulses at 0.5 Hz with 1.5 ps timing jitter
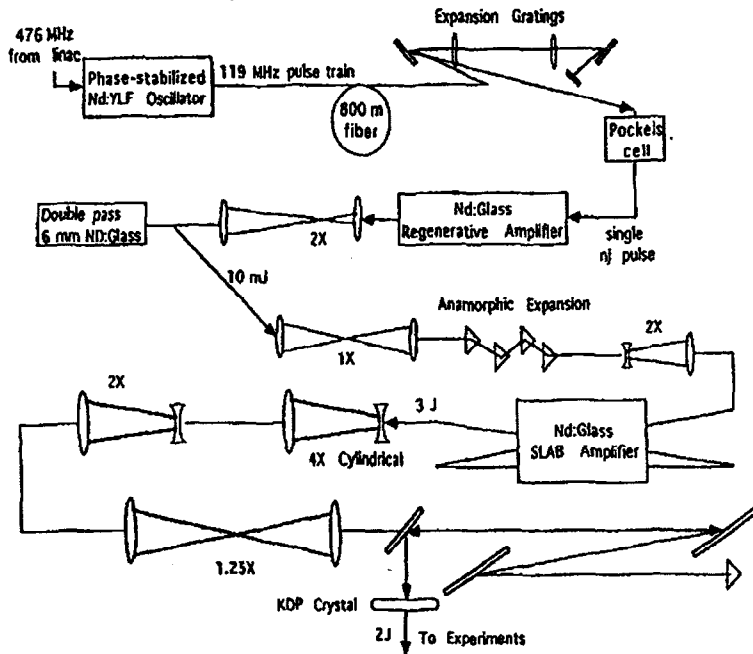
Figure 4.1: Schematic of the laser system.

see that the peak is at $f_0 = 59.47$ MHz, while the FWHM is $\Delta f = 85$ kHz. Then the quality factor can be calculated to be:

$$Q = \frac{2 \times f_0}{\Delta f} = 1400 \qquad (4.1)$$

The modelocker needs to be kept at a constant temperature during operation and for this purpose a cooling system with less than 0.5°C variation has been employed. The Q measurement shown in Fig. 4.3 corresponds to a modelocker temperature of 30.5°C. The optimal temperature that the modelocker needs to be kept, is defined to be the temperature at which the reflected power from the modelocker is minimum.
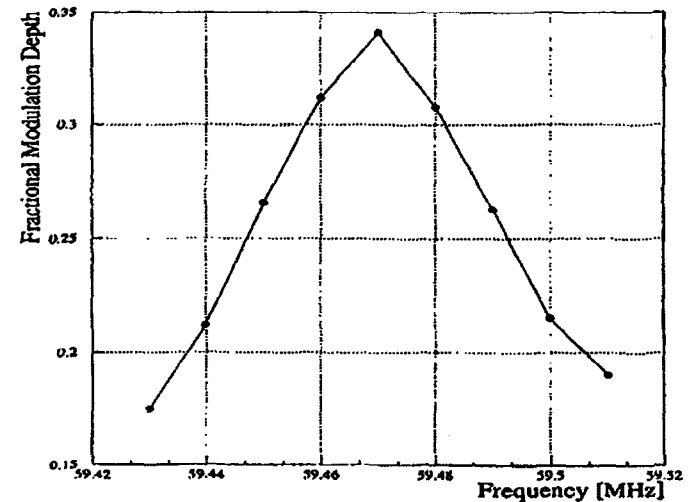
Figure 4.2: Frequency response of the modelocker (ML) crystal. The estimated $Q = 1400$.

Every time that the cooling system is changed the optimal temperature needs to be determined again. This was the case right before the August 1996 data run. Fig. 4.3 shows such a measurement of the optimal modelocker temperature, after the installation of the new cooling system. The modelocker power is kept at 4 W while the cooling temperature is varied and the reflected power from a forward coupler is monitored. Notice that the optimal temperature has changed to about 29.6°C. Then also the optimal frequency that corresponds to maximum modulation depth also changes and it is found to be at 59.5 MHz. The quality factor did not change significantly.

The oscillator produces a 119 MHz pulse train of 50 ps pulses at a wavelength of 1054 nm. The pulse train goes through a Faraday rotator to ensure minimal reflection back to the oscillator cavity, and then through two waveplates, that can be adjusted
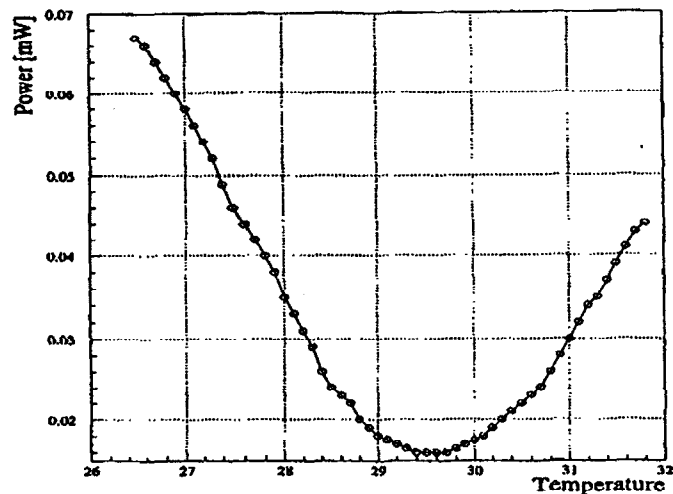
Figure 4.3: Temperature dependence of the reflected power of the modelocker (ML) crystal. The resonance frequency is $f = 59.5$ MHz.

to vary the polarization and power through the optical fiber. The fiber is ~ 1 km long, single mode with a 9 μm core [33]. Inside the fiber the pulses undergo stretching in time and also chirping in frequency due to the effects of Self Phase Modulation (SPM) and Group Velocity Dispersion (GVD) [34]. A spectrometer in the diagnostic line, where part of the laser beam is sent, is used to measure the bandwidth around the 1054 nm wavelength. The spectrometer consists of a narrow vertical slit to allow only a fraction of the laser pulse through, a lens to match the distance to the detector and a grating with 1000 lines/mm with its grooves positioned vertically. The detector is a reticon [35] with only horizontal resolution. It is 14 mm long and it is located 33 cm away from the grating, therefore the maximum angular divergence is 4.24×10^{-2} rad. The grating equation is:

$$\sin\theta_i + \sin\theta_0 = n\frac{\lambda}{D} \qquad (4.2)$$
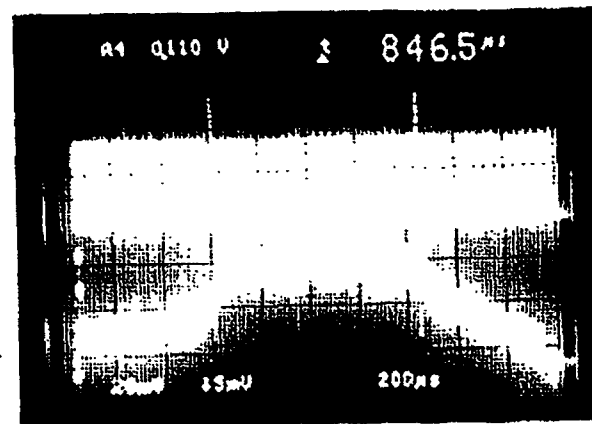
Figure 4.4: A measurement of the oscillator pulse bandwidth after dispersion in the optical fiber. The width at FWHM is shown to be 846 μs and using the calibration factor of 3.8 Å/100 μs we get a bandwidth of 32 Å around the 1054 nm wavelength.
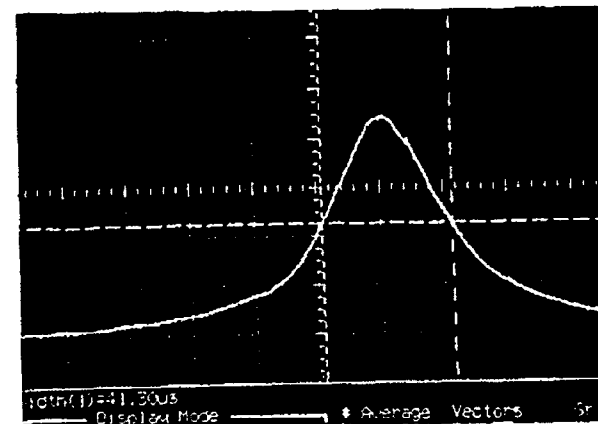
Figure 4.5: A measurement of the oscillator pulse width using a cw autocorrelator. The pulse is compressed with a grating pair. Taking into account the autocorrelator calibration this measurement corresponds to 1.1 ps FWHM pulse width.

where $\theta_i = 23°$ and $\theta_0 = 80°$ are the input and output angles of the laser on the grating measured with respect to the perpendicular to the grating surface, n=1 is the

order of dispersion, λ the wavelength at 1054 nm and D the groove spacing on the grating. After differentiation of Eq. 4.2 and substitution we find:

$$d\lambda = d\theta_0 \cos\theta_0 D = 70 \text{ Å} \qquad (4.3)$$

On the other hand the total length of the reticon corresponds to 1.85 ms on the scope. Therefore we have a calibration of 3.8 Å/100 μs for the spectrometer measurement, as it is displayed on a scope. Fig. 4.4 shows such a bandwidth measurement. Using the calibration factor of 3.8 Å/100 μs, we get a bandwidth estimate of 32 Å around the 1054 nm wavelength. In the same diagnostic line with the grating spectrometer, there also exists a cw autocorrelator that measures the oscillator pulse width, after it has been recompressed with a pair of gratings. The compression is done in order to ensure compressibility of these pulses before they are transmitted through the rest of the laser chain. Fig. 4.5 shows the measurement of a 1.1 ps pulse after taking into account the calibration of the autocorrelator. As mentioned earlier, only part of the laser beam is going through the diagnostic line, while the rest of it is sent directly through the main optics chain. There the laser pulses undergo a further expansion by a pair of expansion gratings. Their pulse width can be measured with a streak camera and their pulse width is found to be approximately 700 ps. Expansion of the laser pulses in the frequency domain is important, because it allows compression in the time domain, as $\Delta\omega\Delta t = 1$ suggests.

At this point the energy of the laser pulse is only about a nanojoule and it is ready to be injected into the regenerative amplifier. Every 2 seconds one pulse out of the 119 MHz pulse train is selected by a Pockels cell and then is seeded into a Q-switched, regenerative amplifier. The amplifier medium is a 6 mm, 160 mm long Nd:glass rod. The pulse train out of the regen is shown in Fig. 4.6. One more Pockels cell is used to select one of these pulses every 2 seconds and it therefore sets the repetition rate of the laser. The selected laser pulse has $\sim$ 1 mJ of energy, 700 ps pulse width and repetition rate of 0.5 Hz. This repetition rate is limited by the cooling requirements of the later amplification stages. Thermal effects on the amplifier material can induce
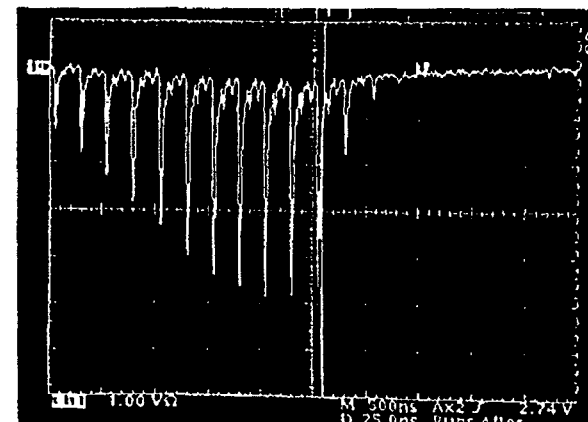
Figure 4.6: Regenerative amplifier pulse train. The missing pulse has been selected by a Pockels cell and it continues through the rest of the laser system.

a preferred axis for the laser polarization. If the polarization of the incoming beam does not coincide with this preferred axis, depolarization effects occur that lead to distortion of the laser pulse wavefront. Therefore sufficient time needs to be allowed for cooling. An important effect to consider is the gain narrowing that occurs during the amplification [36]. At the end of the regen amplification the bandwidth has been reduced to about 12 Å, which can result in a shortest pulse width of $\sim$ 1.3 ps after compression. An air spatial filter up-collimates the laser beam before the double-pass Nd:glass amplifier. Due to depolarization effects when the amplifier operates at high voltages, the maximum energy is kept at 10 mJ. A 1 m long vacuum spatial filter with equal focal length lenses, is used to clean the laser pulse from any intensity variations due to scattering from optics imperfections or air particles, after the second amplification. At the focus of the first lens a 400 μm pinhole is placed that cleans most of such noise, while still 99% of the initial intensity remains [60]. The pressure inside this filter is kept to the level of 10^{-6} Torr, in order to avoid ionization of air molecules at the focus of the laser pulse.
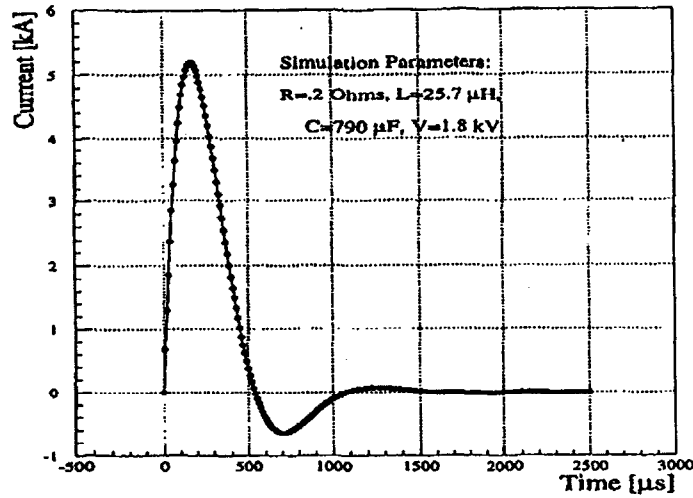
Figure 4.7: Simulation of the current through one of the four flashlamps used to "pump" the slab active medium.

The last amplification stage consists of an Nd:glass slab amplifier. A characteristic of the slab geometry is the Brewster angle input and output faces. In order to extract as much energy as possible from the slab we need to expand the beam anamorphically with an aspect ratio of 4:1. This is done by using prisms, that take advantage of the Brewster law to give a magnification factor equal to the refractive index of each prism [60]. There are 4 prisms made of fused silica which has a refraction index of 1.41. Therefore the magnification achieved is $(1.41)^4 \simeq 4$. A Galilean telescope further expands the beam by a factor of 2. The slab geometry [37], [38] has the advantage of excellent phase front transmission, while retaining high gain and repetition rate in a compact unit. This is due to more efficient cooling compared to a rod of a big diameter. Depolarization effects are eliminated if the electric field is perpendicular to the large surface of the slab. In our case the aperture cross section is 1.1 cm

× 6.5 cm, so that large beams can be used, reducing the peak intensity and related nonlinear effects. The laser beam passes three times through the amplifier in a bow-tie configuration, while the Brewster angle input window, internally reflects the beam in each pass 12 times, increasing the optical path in the active medium.Nd:glass is more preferable in our case, due to its availability in high optical quality and large sizes, and also to its ability of storing high energies before reaching its saturation fluency. The
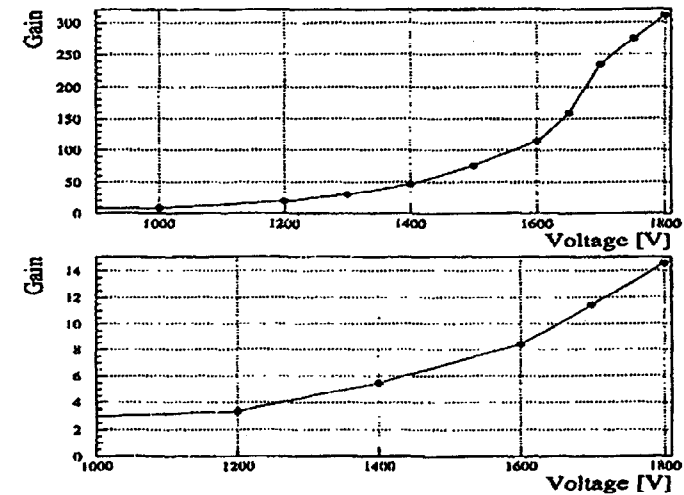
Figure 4.8: Slab (top plot) and 2-pass (bottom plot) gains, as a function of flashlamp voltage settings.

slab active medium is "pumped" by four flashlamps, that discharge a high voltage with peak energy of 1.6 kJ per lamp. The discharge lasts for approximately 200 μs and is regulated by each lamp's current pulse forming network (PFN). The current running through each of the four flashlamps can be approximated by the expression:

$$I = \frac{V_0}{\sqrt{\omega^2 - \alpha^2}\, L}\, e^{-\alpha t}\, \sin\left(\sqrt{\omega^2 - \alpha^2}\, t\right) \tag{4.4}$$

where $\alpha = R/2L$ and $\omega = (\sqrt{LC})^{-1}$. Fig. 4.7 shows a simulation of the lamp current for the indicated parameters. An actual measurement of the current agrees well with the above approximation [60]. For the case of 6 kJ of flashlamp energy, the small signal gain is measured to be as high as 300. Under normal operating conditions a 10–15 mJ input laser pulse at 1054 nm can be amplified to over 2 J of energy. Fig. 4.8, shows the slab gain (top plot) and also the 2-pass gain (bottom plot) as a function of the flashlamp voltage settings.

After the slab the laser beam needs to be recircularized. A pair of cylindrical lenses is used for that purpose. Their alignment is critical to the wavefront quality of the beam further downstream, and especially to the astigmatism introduced to the beam. Both the cylindrical lenses and also a Galilean expansion telescope that follows, increase the size of the beam at the end to about 4.5 cm. A waveplate positioned in between rotates the polarization from vertical, required for the operation of the slab, to horizontal as required by the compression gratings later. A 2.7 m long vacuum spatial filter cleans the pulse once more and it further expands its size to $\sim$ 7.5 cm. The filter again is maintained to a pressure of 10^{-6} Torr. The laser pulse is then directed through the compression stage, which consists of two 1760 lines/mm, gold coated 160 mm × 220 mm holographic gratins [49], used in the near Littrow, double pass configuration with a separation distance of 164 cm. They compress the laser pulse to 1.5 ps. After the compression the laser pulse is frequency doubled using a 4 mm or 8 mm thick Type II KDP crystal. Although the theoretically expected efficiency is 50 %, during the August 1996 run an efficiency of $\sim$ 40% was achieved.

After the laser pulse is transported down to the interaction point (IP), it returns back to the laser room for further diagnostics. The laser energy is measured at the end of the transport line, with an energy monitor appropriately calibrated in order to take into account, the energy losses through the transport line, so that the energy of the input pulse can be deduced. Fig. 4.9, shows the laser energy fluctuations during the whole data taking period. Laser pulses with energies as high as 750 mJ have
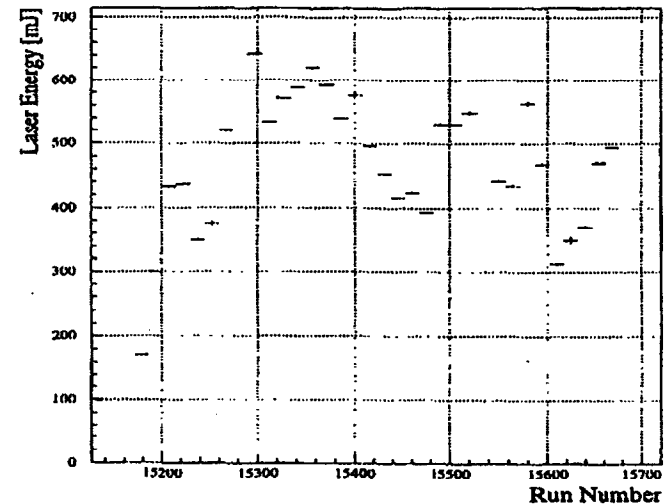
Figure 4.9: Laser energy at the interaction point, as a function of run number. Each point in the plot represents energies averaged over a large number of laser pulses. On a pulse-to-pulse basis, events with energy as high as 750 mJ in the green (527 nm) have been observed.

been observed. The laser pulse width was measured with a single shot autocorrelator but not on a shot-by-shot basis. Such a measurement is shown in Fig. 4.10 and corresponds to 1.5 ps pulse width.

The focal spot size at the interaction point is measured indirectly using the Equivalent Target Plain (ETP) method. The returning laser beam is focused with a 4 m lens and attenuated by reflection off the surface of glass flats, by a factor of 10^6. Further attenuation is provided by neutral density filters. The focus is imaged with a 10 × microscope objective into a CCD camera that has 753 × 244 pixels with dimensions 11.5 μm × 27 μm. The signal in each pixel is proportional to the light intensity on it. The width of the laser pulse in both the x and y directions is deduced in two ways. The first is the so called geometric method. During this method the
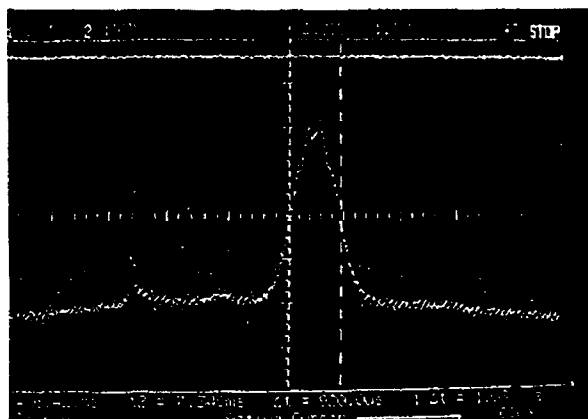
Figure 4.10: A measurement of the green pulse width (FWHM) after it has returned to the laser room from the IP, using a green single-shot autocorrelator. After taking into account the autocorrelator's calibration, the measurement shown gives a FWHM of ~ 1.5 ps.

background is estimated by measuring the signal levels in a 3 pixel wide area around the edges of a square 150 × 150 pixels wide that surrounds the peak of the signal. Clipped pulses that hit the CCD camera on the edge, are thrown away when the ratio of the bottom of the clipped edge to the peak is ≤ 0.67, i.e. when most of the clipped side is lost. The peak of the laser pulse is determined as the average of the four pixels around the one with the highest intensity. The difference between the background and the peak defines the pulse height. The width in each direction is then found by counting the number of pixels in which the signal is higher than $(\sqrt{e})^{-1}$ of the peak signal. The area is determined by multiplying the two widths by 2π. The second method defines the width in each direction by assuming a Gaussian distribution and fitting accordingly. Events with really bad χ^2 are not considered. Again the area is determined by multiplying the two widths by 2π. Fig. 4.11, shows the spot areas predicted by the two methods. The geometric method gives on average a larger spot size by 23 %. In any case the laser area remains fairly constant over the whole run
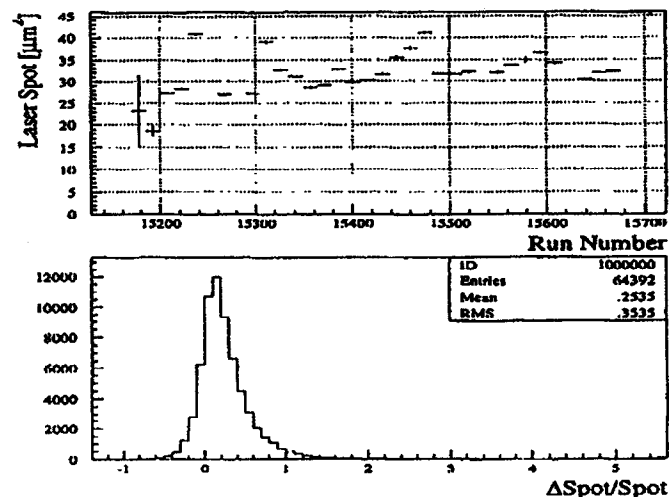
Figure 4.11: The laser spot size at the interaction point as measured using the ETP method. Two different procedures, the geometric that simply counts pixels above a certain background threshold, and a method that assumes Gaussian distributions of the beam intensity on both the x and y directions and fits accordingly, can be used to extract the laser spot size. The top plot shows the areas derived using this last method, as a function of the data runs (run time). The second plot shows the difference in the predictions of the two methods. It is clear that the geometric method can give spot sizes bigger by 23 % of those found by the fit method.

period and between 30–40 μm^2 for most of the time. The ETP method is very sensitive to outside conditions like air currents. Furthermore the quality of the beam wavefront deteriorates sharply with the number of reflections off the mirror surfaces and by going through filters. Therefore the errors assigned to it are really big. If we define the focusing optics by their f number ($f_\#$), which is the ratio of the focal length of the focusing lenses over the limiting aperture of a parallel Gaussian beam that corresponds to the $1/e^2$ of the beam intensity, we find that in our case $f_\# = 6$. The wavelength for a green laser pulse is $\lambda = 0.527$ μm. Therefore we can define the

diffraction limited spot area for a green laser to be:

$$A = \frac{2}{\pi}(f_\# \lambda)^2 = 6.4\,\mu m^2 \qquad (4.5)$$

From the above we can conclude that the measured spot sizes are ~ 4.7 times the diffraction limited ones. Astigmatism is the most obvious reason for this difference, along with misalignments in the optics in the transport line and inside the IP box, as it is discussed later.

4.2 The Laser Transport System and Interaction Point

From the laser room the laser beam needs to be transported 12 m further into the FFTB tunnel and to the interaction point. The laser beam is raised to a height of 2.5 m using a periscope inside the laser room and then it passes through a glass window coated for antireflection in green, before it enters a 10 m long pipe that transports it into the FFTB tunnel, that is under high vacuum, the same maintained in the electron beam pipe (10^{-8} Torr). There the beam is reflected downwards by a 45° mirror, which is placed on stepper motors that can be remotely controlled from inside the laser room. The mirror is located in the upper deflection box (UD), which also contains the return mirror, which is also placed on remotely controlled motors. After been deflected by 45° the laser beam travels downwards until it enters the interaction region. There it is deflected horizontally by another 45° mirror and focused by an Off Axis Paraboloid (OAP) mirror with 30 cm focal length onto the incoming electron beam. The laser beam is then re-collimated using another OAP and deflected upwards with a 45° mirror. All the optics inside the IP are mounted on an invar plate in order to reduce the effects of temperature variations on the laser path length. The laser beam crosses the electron beam at a 17° angle. A schematic of the IP optics is shown in Fig. 4.12. The IP box is placed on magnet movers that
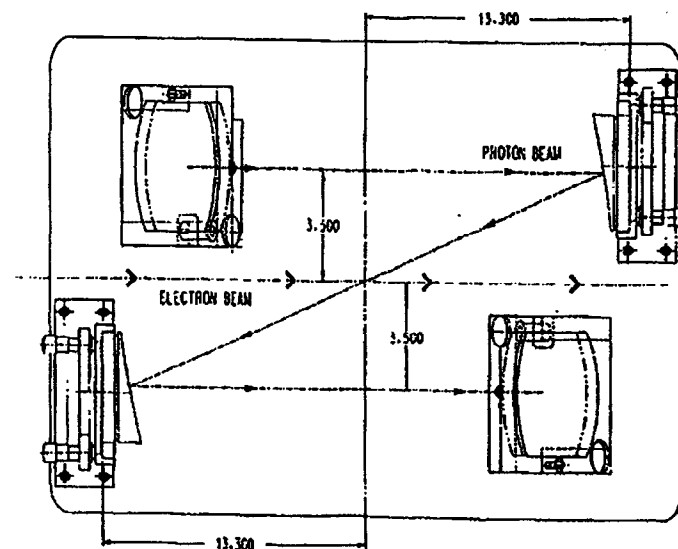
Figure 4.12: Drawing of the optics inside the interaction point box; dimensions are in inches. The focusing of the laser pulse is done in such a way so that it crosses the electron beam in a 17° angle.

can move it in the x (horizontally transverse with respect to the electron beam) and in the y direction (perpendicular to the electron beam) and also rotate it in the xy plane. The three motors are interfaced to the SLAC Control Program (SCP) and are used to scan the laser focus with respect to the electron beam, since the laser path is fixed with respect to the IP box. Some stability issues are of concern, especially since the IP box is on top of a column that sits on the concrete floor of the FFTB tunnel. Long term drifts of the order of μm have been measured and they in fact became evident during the last run. They are due to diurnal thermal expansion of the tunnel. Frequent y-scans of the IP box position had to be performed in order to establish optimal vertical overlap between the two beams.

Good wavefront quality of the beam returning into the laser room from the in-

teraction point, indicates that the alignment of the OAPs is correct and that the pointing of the beam incident on the first OAP coincides with the OAP axis. To maintain the alignment a frequency stabilized cw He-Ne laser is used in a Mach-Zehnder interferometer configuration. A beam splitter sends part of the He-Ne beam down to the transport line and after its return back to the laser room, it interferes with the other part that went through the beam splitter. The absence of any fringes or the presence of at most one indicates a very good alignment of the transport line. The OAP alignment can be done independently in the lab prior to their installation into the IP box by using the same method. There are 5 degrees of freedom over which the OAPs must be aligned to each other: 3 displacements so that their focal points will coincide and 2 rotations to set the optical axis parallel to the OAP axis. After the OAP installation inside the IP box, the rest of the transport line can be aligned using the Mach-Zehnder interferometer described above. The input and return mirror in the Upper Deflection box (UD) can be used for final adjustments. A set of quadrant diodes behind the two 45° deflecting mirrors inside the IP box can be used in order to set the laser beam on a perfectly horizontal line as it propagates through the transport line on both directions and also on a normal direction of incidence on the first OAP.

4.3 Laser-Electron Timing

One of the most important technical challenges for the experiment is the synchronization of the laser pulse with the electron beam, in order to achieve collisions at the interaction point [39]. Since the laser pulse has a pulse-width (FWHM) of ~ 1.5 ps and the electron beam a bunch length of ~ 7 ps, we need to control their relative timing at the 1 ps level. The strategy used is shown in Fig. 4.13. A sub-multiple of the master accelerator frequency drives the mode-locker (ML) of the laser oscillator that sets the timing of the laser pulse launching. An electronic feedback locks the
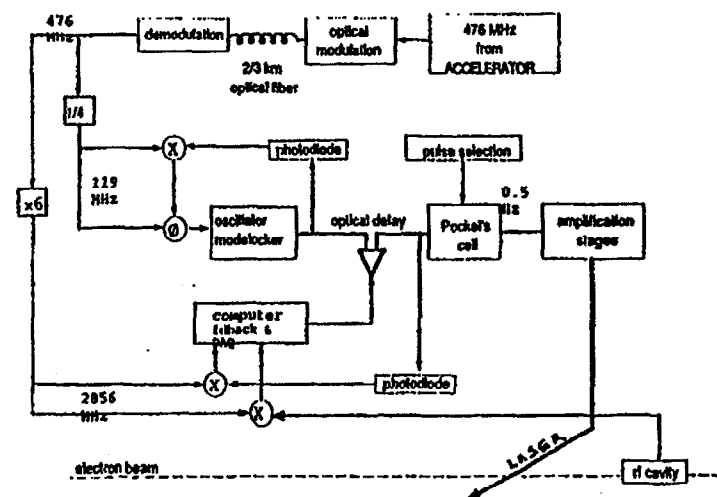
Figure 4.13: Overview of the timing system for the synchronization of the laser pulses with the electron beam (from [60]).

phase of the oscillator to the accelerator rf, by adjusting the phase of the rf driving signal of the ML. The electron-laser fine timing is found by scanning with an optical delay line, while at the same time the products of the laser-electron interaction are monitored, i.e. the linear Compton scatrered electrons into the linear monitor, or the even more sensitive signal of the nonlinear scattered electrons into the nonlinear counters or the electron calorimeter (ECAL). The best timing overlap is at the peak of the interaction yield when it is plotted as a function of the timing delay.

4.3.1 Experimental Setup for Laser-Electron Timing

The accelerator master oscillator located in the injector area, 3 km from the laser room, provides 20 Watts of rf power at 476 MHz. A 360 Hz fiducial is superimposed

on this signal, which provides the firing trigger for the linac klystrons. This signal is transmitted via the Main Drive Line (MDL) [40], a rigid coax cable that runs the whole length of the accelerator's klystron gallery, and is the source of both the rf drive and of all the reference signals for the klystrons and rf devices in the linac. The 476
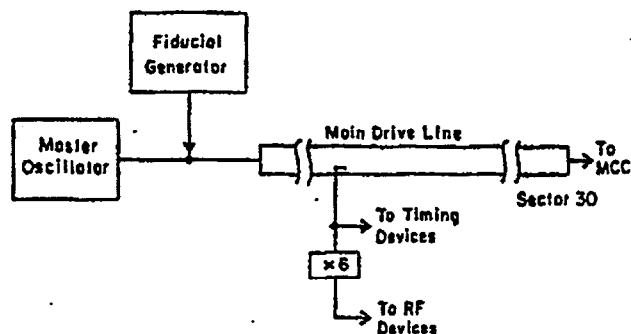
Figure 4.14: Schematic of the SLAC main drive line (from [60]).

MHz internal frequency is multiplied by 6 in each sub-booster in order to produce the rf necessary for S-Band systems, as it is shown in Fig. 4.14. The performance of the accelerator is sensitive to any drifts in the phase of the rf provided by the MDL, so a feedback loop is employed to compensate for any changes in the electrical length of the MDL. This loop is controlled by the software tools that support all slow feedback loops in the SLAC Control Program (SCP), and is a feed-forward loop, i.e. the environmental effects that are responsible for any phase instabilities of the MDL are not controllable and can only be compensated for. The measurement of the phase length of the MDL is done with a single interferometer by introducing a modulated reflection of the rf at the end of the linac (sector 30), allowing instrumentation in the front end (sector 0) to compare the phase of the reflected rf with that of the source. Thus, the accelerator rf signal which is used to synchronize the laser with the electrons, contains, in addition to the main 476 MHz signal, a sideband at 750

Hz (originating from the interferometer) , and sidebands at the harmonics of 360 Hz (originating from the fiducial).

The 476 MHz signal is amplified by a low noise rf amplifier and is then fed into a Fiber-Optic Transmitter (F/T) [41]. The rf modulates the current into a distributed feedback diode (DFB), which in turn produces an intensity modulated optical signal at 1300 nm wavelength that is coupled into a temperature stabilized optical fiber [42], and transported 600 m to the laser room. The fiber solution is more preferable than an rf cable due to lower losses, lower dispersion, and smaller length variations resulting from ambient temperature fluctuations. In the laser room the optical signal is detected by a Fiber-Optic Receiver which utilizes a fast photodiode to convert it to the 476 MHz reference signal. The transmitter/receiver setup is interfaced and monitored by SCP. The 476 MHz signal from the F/O Receiver is amplified and used to drive the Fiducial Output module (FIDO), which contains electronics that extract the fiducial pulse (T-zero) from the reference signal and others that produce the 4th sub-harmonic at 119 MHz. The output of the FIDO consists normally of a 119 MHz sine wave with a missing half cycle to indicate the T-zero. An externally supplied circuit inhibits the fiducial, so that a cleaner 119 MHz pulse is produced. Fig. 4.15, shows the spectrum of the 119 MHz pulse. The 360 Hz and 750 Hz sidebands can also be seen clearly.

The 119 MHz rf is then sent into the timing stabilizer (TS) module [43]. A simplified block diagram of the timing stabilizer is shown in Fig. 4.16. The output of this module is a 59.5 MHz signal in phase with the reference 119 MHz, which after amplification to 4 W drives the oscillator's modelocker. The oscillator produces a 119 MHz pulse train, which is collected by a 2 GHz bandwidth photodiode, after it has undergone chirping and expansion through the fiber and again compression through the diagnostic line compression gratings. The photodiode signal is phase compared in the TS to the reference 119 MHz signal. The output signal of the phase comparator controls the phase of the rf sent to the modelocker. The positioning of the diode
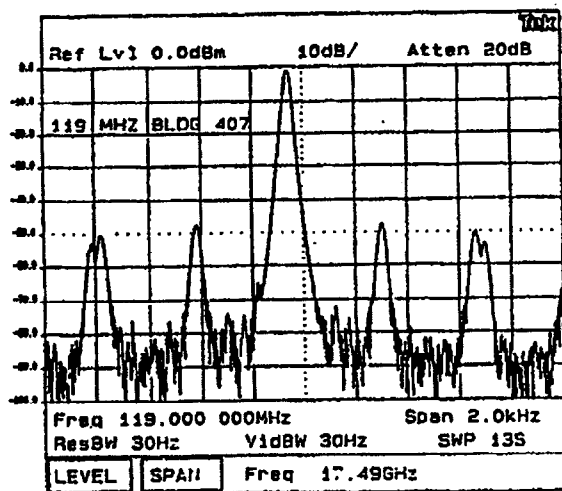
Figure 4.15: Power spectrum of the laser reference rf at 119MHz.

is critical, since both signals that are phase compared must be close to their zero crossing in the time domain. The diode collects the light after the 1 km fiber used for chirping, so that are compensated for any changes in the optical path length due to temperature variations. The diode is placed after the compression gratings where the FWHM of the pulse is ~ 2 ps and therefore the timing information of the rising edge of the pulse is more accurate. With this setup the oscillator pulse train is locked to the master accelerator clock. Every 2 seconds one of the pulses in this train is picked for further amplification and eventually is sent down to the interaction region to collide with one of the electron bunches.

Fig. 4.17 shows the arrangement necessary to set the relative delay. The relative timing of the laser pulse with respect to the electron beam is set by the last Pockels cell in the laser path, which defines the switch-out time for the regenerative amplifier pulse train. The timing of the other two Pockels cells earlier in the line, is then adjusted relative to the switch-out Pockels cell, so that good amplification and good
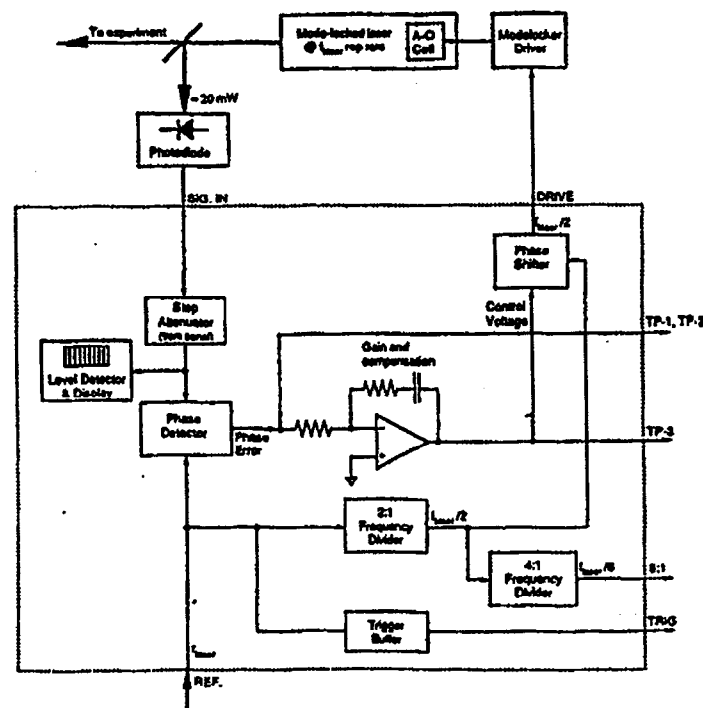
Figure 4.16: Timing stabilizer block diagram (from [43]).

single pulse contrast is achieved. The Pockels cell triggers are based on the software defined SLC triggers, which are also synchronized to the master accelerator clock. These triggers can be adjusted as to repetition rate and delay, from a starting point T_0 which coincides with the injection of the electron beam. The laser trigger starts as a 10 Hz trigger and its delay can be adjusted with a Pulse Delay Unit (PDU) interfaced with SCP. The finest time step of the PDU is 8 ns. The PDU signal is frequency divided to 0.5 Hz and is then fed into two commercial delay units [44] that can be timed in picosecond steps. The first of these units is used for the triggering
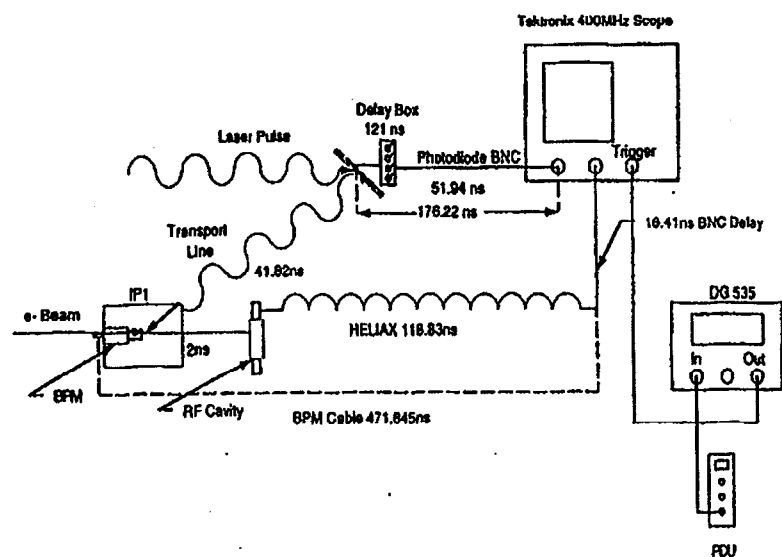
E144 Timing Diagram

Figure 4.17: Experimental setup of the timing system. Different ways of synchronizing the electron and the laser beam and the corresponding cable delays are shown.

of the regenerative amplifier's flash lamps and is irrelevant for timing purposes, since the lamp flash lasts for approximately 200 μs. The second unit is used to trigger the three Pockels cells in the laser path.

After the switch-out time the laser pulse travels through the rest of the laser system and eventually enters the input periscope of the optical transport line, to be delivered to the interaction region (IP). The light leakage from the first mirror in the input periscope, is collected by a photodiode permanently positioned behind it and is used as the timing reference laser pulse (TRLP). Assuming that no path length changes take place in the optical transport, is compared to an electron beam based signal. The electron beam based signal is provided by a ringing cavity installed in the
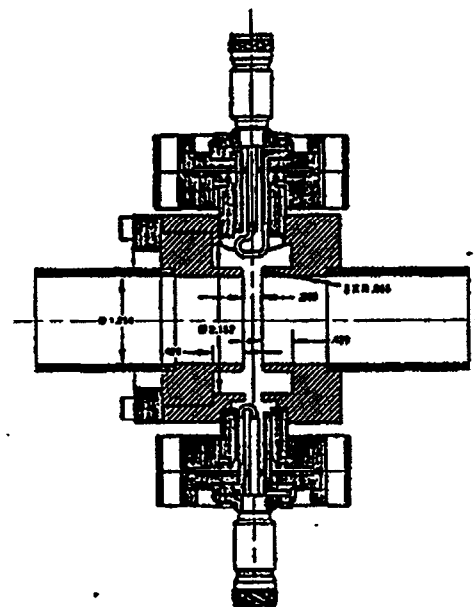
Figure 4.18: Schematic of the ringing cavity (from [60]).

electron beam line 2 feet downstream of the IP. A schematic of this cavity is shown in Fig. 4.18. It has a resonant mode at 2856 MHz (characteristic of S-band systems), and a quality factor $Q = 1300$. It is made of copper and it normally operates at a temperature of 116° Fahrenheit. The length of the cables from the ringing cavity to the laser room as well as of those from the diode, are measured using Time Delay Reflectometry (TDR). The optical transport length is measured by sending the laser pulse through the transport line and using two photodiodes to measure the relative delay between the input and output signals. The TRLP signal is time compared to the one from the ringing cavity using a 400 MHz oscilloscope and a coarse timing of the laser and beam is set by using the PDU. By this method the synchronization can be set to ± 0.5 ns. Table 4.1 and Fig. 4.17 shows the cable and path lengths in units

of ns for all the relevant timing elements, as they were measured prior to the August 1996 data run.   Fine tuning of the relative laser-electron pulse timing is achieved

Timing Element	Ringing Cavity Method
Opt. Trans.	41.82
Cavity Cable	136.44
Path Length	2.00
Diode Cable	176.22
BPM Cable	–

Table 4.1: List of the cable and path lengths for the timing method used for the laser-electron pulse synchronization. The units are in ns. Proper subtraction of the cable lengths results to a relative time difference of 4.04 ns.

by using the variable optical delay line. This line consists of a prism positioned on a stage that can be moved with μm precision either manually or through an GPIB interface of the stage driver, with a PC. Since the stage is 25 cm long it can cover the range of $\pm$ 0.5 ns. The whole setup is integrated with the rest of the data acquisition system, and therefore the correlation between the laser optical delay and the yield of the products of the laser-electron interactions can be monitored. Fig. 4.19 shows such a timing scan. It is clear that optimal timing overlap corresponds to a time delay of $\sim$ 8 ps.

4.3.2   Timing Jitter and Long Term Drift

In the spectrum of the reference 476 MHz rf frequency, any sidebands can translate into phase noise. An estimate of the phase noise, or equivalently of the time jitter, can be obtained from an analysis of the power spectrum [45] of the examined rf. The spectrum of a narrow pulse of frequency ω_0 contains all higher harmonics of ω_0 at frequencies $n\omega_0$ plus a series of amplitude noise sidebands $S_N(\omega - n\omega_0)$ and phase noise
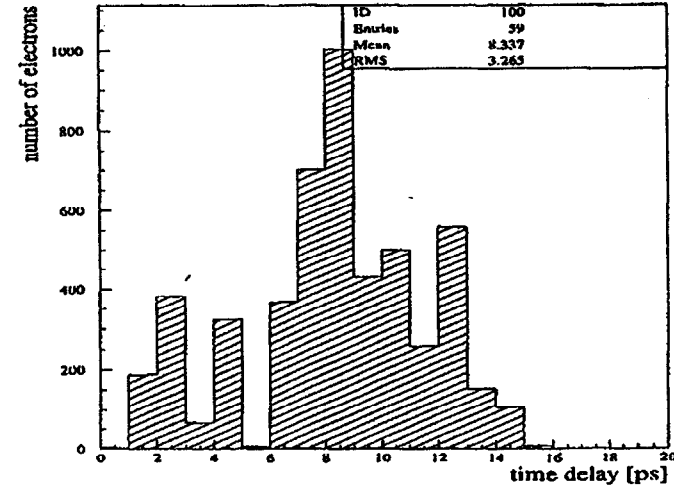
Figure 4.19: A typical timing scan curve. The vertical axis shows the number of electrons detected in the top row of the electron calorimeter (ECAL) as a function of the time delay introduced by the variable optical delay line.

sidebands $n^2\omega^2 S_N(\omega - n\omega_0)$. At harmonics of sufficiently low order the amplitude noise sidebands dominate, while the phase noise sidebands, which are proportional to n^2, become important at the higher order harmonics. The relative power of the sidebands of a high n-th harmonic over the power of the n-th harmonic itself, determines the spectral density $S_J(\omega)$ of the timing jitter of the signal. Then the RMS timing jitter is given by

$$\sigma_J^2 = \frac{1}{\pi} \int_{\omega'_{low}}^{\omega'_{high}} S_J(\omega') d\omega' \qquad (4.6)$$

where we have set $\omega' = (\omega - n\omega_0)$. The lower limit must be chosen so that $\omega'_{low} \Delta T \sim 1$, where ΔT is the duration of the experiment, but often it is imposed by the resolution of the spectrum analyzer and can vary from 50–200 Hz. The upper limit is taken as 25 kHz, although frequencies above 2 kHz contribute little to the timing jitter integral. It
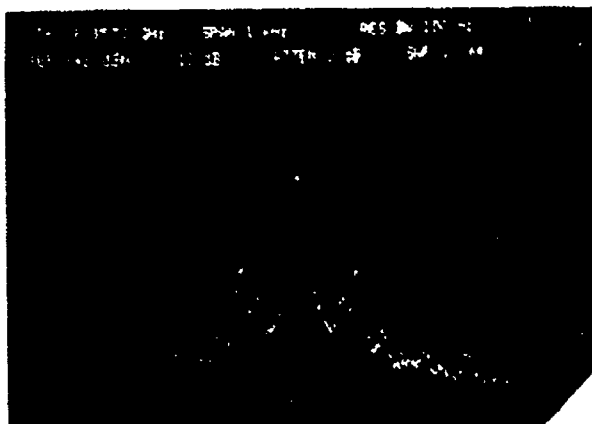
Figure 4.20: Power spectrum of the laser oscillator pulse train.

is obvious that it will be more appropriate to measure the time jitter of the 119 MHz signal at one of its higher harmonics. Since, as we have mentioned in section 4.3.1, the ringing cavity has a resonance at 2856 MHz, we can use the 24-th harmonic to calculate the timing jitter. The power spectrum of the 24-th harmonic of the laser pulse train is shown in Fig. 4.20 and it can be used for such a measurement. An actual measurement performed in some earlier stages of the E-144 experiment, gave an RMS estimate of $\sim$ 2 ps [60]. A theoretical treatment of the phase stability of microwave oscillators is given in [46]. Time jitter measurements can also be performed in the time domain, by displaying the fast photodiode signal of the laser pulse train on a sampling scope [47]. A 7 GHz bandwidth photodiode is used for that purpose. The scope is triggered with the 119 MHz reference rf. The diode is positioned after the compression grating in the laser pulse diagnostic line. In order to reduce the effects of amplitude fluctuations, the lower part of the rising edge of the laser pulse has to be studied. Fig. 4.21, shows such a jitter measurement with a result of $\sigma_{rms}^{total} = 7.3$ ps. However, the trigger jitter needs also to be taken into account. This is done by generating both the trigger and the signal from the 119 MHz reference rf, using a

Figure 4.21: Measurement of the timing jitter in the time domain.

power splitter. This measurement gives a trigger jitter of $\sigma_{rms}^{trigger} = 6.8$ ps. After quadratic subtraction, we find that the real jitter of the laser pulse is $\sigma_{rms}^{laser} = 2.8$ ps. Such a method is characterized by a big error usually of the order of $\sim$ 1 ps.

Another diagnostic of the timing stability of the system is a direct phase comparison of the laser pulse train and the drive rf. This is done at the linac frequency of the 2856 MHz. The 476 MHz output of the optical fiber is multiplied by 6 and fed to one arm of a Double Balanced Mixer (DBM). The other arm has as an input the 24-th harmonic of the 119 MHz laser pulse train. This is selected by using a 2856 MHz Bessel filter. The signal is amplified by 60 db, before it is input to the mixer. When two signals of the same frequency but different phases, are applied to the two inputs of a balanced mixer, the output is a DC voltage whose amplitude is proportional to the phase difference of the two input signals [48]. The mixer output is filtered for DC using a low-pass 50 MHz filter, in order to avoid any leakage of both the main 119 MHz drive rf and its sub-harmonic of 59.5 MHz. The output can be fed either directly into a sampling scope, or through a CAMAC to the SLC Control
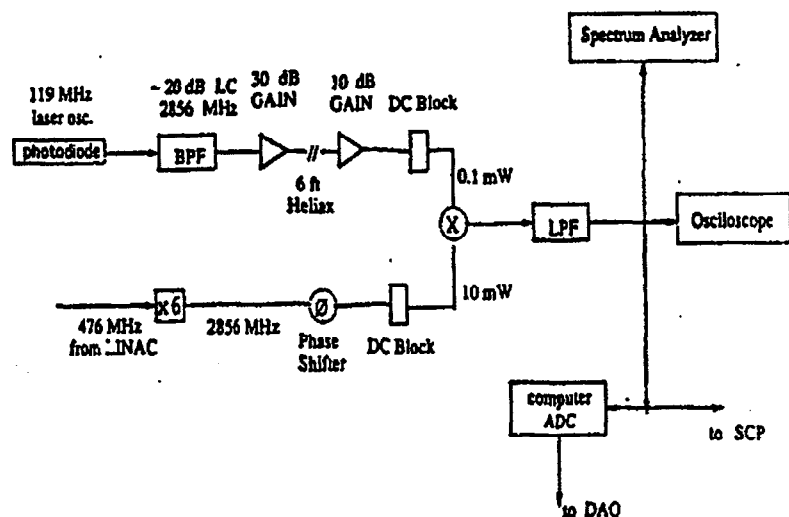
Figure 4.22: Block diagram of the laser pulse phase noise measurement setup (from [60]).

Program (SCP). The whole setup is shown in Fig. 4.22. The calibration of the mixer is done by shifting the phase of the input laser frequency by a known amount using a phase shifter, and reading the mixer output through a scope or through SCP. Such a calibration curve is shown in Fig. 4.23 and results to a conversion factor of 0.79 ps/mV. The voltage output of the mixer as a function of time with an RMS fit, is shown in Fig. 4.24. The RMS is shown to be 1.426 mV. Using the above calibration it translates into a timing jitter of $\sigma^{rms} = 1.13$ ps. The mixer's internal phase noise turns out to be small enough and needs not to be taken into consideration. This last measurement was performed right before the beginning of the August 1996 data run. The phase comparison technique described here, can also provide us with a tool to perform a measurement of the long term drift. Fig. 4.25, shows the results of such a measurement over a time period of 17 minutes. The time step size is 2 seconds. The
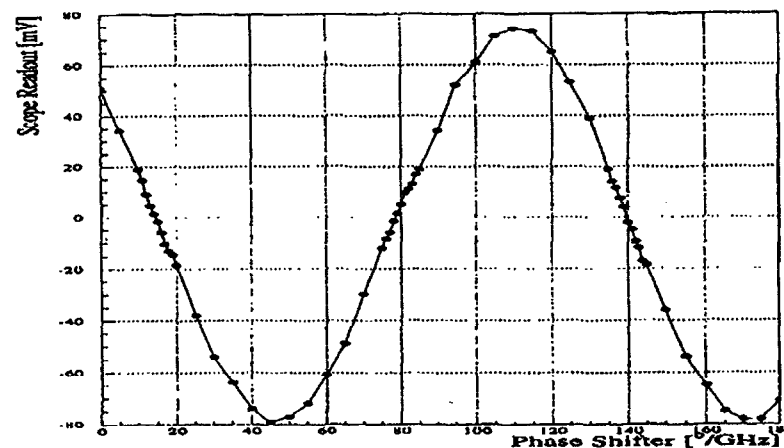
Figure 4.23: Calibration of the phase noise measurement setup taken by shifting one of the arms of the mixer with respect to the other.

slope of the straight line shown, gives us the drift in units of mV per 2 seconds. Using the conversion factor of 0.79 ps/mV we find that the long term drift is 6 ps per hour. This is a considerable drift and can cause the complete loss of the laser-electron pulse synchronization, and therefore frequent scans of the laser's optical delay are needed to reestablish optimal timing overlap. When the timing stabilizer loop is deactivated, drifts of over 100 ps in a time scale of minutes are evident, as Fig. 4.26 shows. The stability of the electron beam with respect to the reference rf can also be checked [60]. Very briefly the results of the measurements indicate that variations over a time scale of 30 minutes are less than 2 ps, while diurnal effects that change the length of the linac do change the electron timing on a timescale of hours.

Several sources can be identified as contributing to the timing jitter measured previously. One is the fiducial sidebands in the power spectrum of the 476 MHz reference rf at 360 and 750 Hz and their harmonics. Its effect on the oscillator pulse train is immediately noticed on the photodiode that monitors the leakage from the

AVERAGE = 0.3038   STD DEV =   1.428
RMS FIT ERROR = 1.428

A =   4.2817E-03   STD DEV =   4.8132E-04
B =   15.65   STD DEV =   0.1425
                                      Y = AX + B
                   RMS FIT ERROR   = 1.807
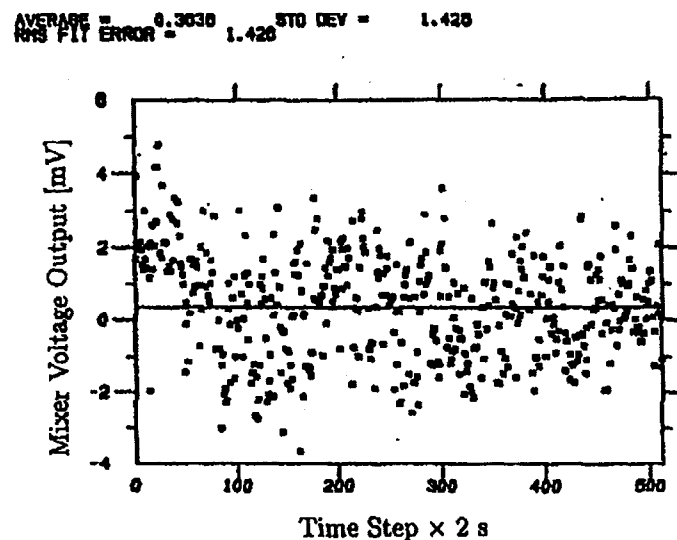
Figure 4.24: Phase noise measurement of the laser oscillator pulses with respect to the reference RF. The vertical scale is the voltage output of the mixer in mV. The horizontal axis is time in seconds. The RMS fit error can be translated to a time jitter using the calibration results of Fig. 4.23.

curved oscillator cavity mirror, as it is shown in Fig. 4.27. The 360 Hz fiducial signal detunes the modelocker causing the appearance of the spikes shown. The solution to this problem is to inhibit the fiducial generating circuit inside the FIDO module, as it has already been mentioned earlier. Unfortunately the 750 Hz sideband can only be inhibited with expensive Phased Locked Loops (PLL) and it is not corrected for in this experiment. An important contribution to the timing jitter, when the stabilizer loop is deactivated, arises from fluctuations in the modelocker temperature. The thermal stability of the modelocker is critical to its performance and subsequently to the timing jitter of the oscillator pulses, as shown in Fig. 4.28 . The top plot shows the mixer output in mV as a function of time. In the same time period, the modelocker temperature in °C is also recorded in the bottom plot. Both quantities
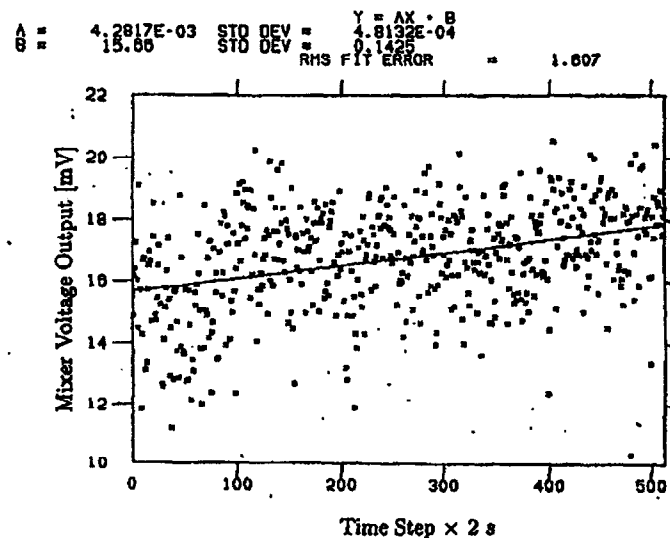
Figure 4.25: Measurement of the long term drift of the laser pulses with the accelerator reference RF. The axes are the same as in Fig. 4.24.

show the same periodicity of $\sim$ 17 minutes. Thermal effects on the oscillator cavity length itself are less important, since the cavity is established on an invar plate. On the other hand, mechanical vibrations of the invar plate, can introduce noise in the frequency spectrum of the oscillator pulse train. This source of jitter, along with amplitude fluctuations in the applied high voltage to the flashlamps are examined in more detail in [60]. The main source for long term instability in the laser-electron timing, is the IP box motion due to ambient temperature variations, which translates into timing drift between the two beams.
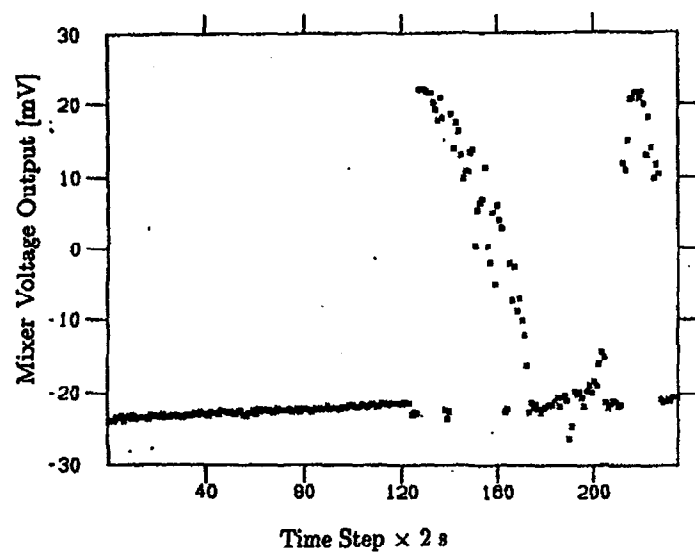
Figure 4.26: Effect of the timing stabilizing feedback on the phase drift measurements. Initially the feedback was turned on and then during the course of the measurement was turned off.
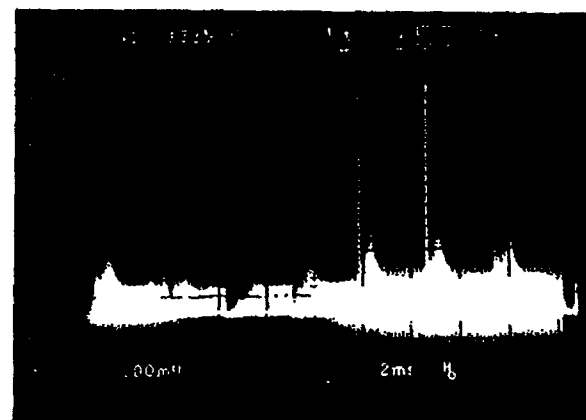
Figure 4.27: Signal from the fast photodiode that monitors the leakage from the curved oscillator cavity mirror The 360 Hz fiducial signal detunes the modelocker causing the appearance of the spikes shown.
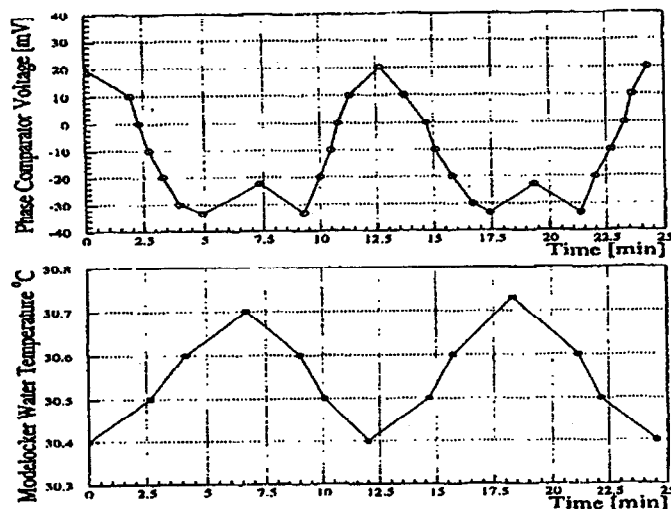
Figure 4.28: Variation of the phase of the laser oscillator pulses with respect to the accelerator reference RF when the timing stabilizer feedback is deactivated. There is a periodicity in this variation which is directly correlated to the temperature fluctuations of the water used for cooling the modelocker, as it is shown in the bottom diagram.

4.4 Laser-Electron Spatial and Temporal Overlap

In the previous section we discussed extensively the timing of the electron and the laser beam at the picosecond level. Although the synchronization of the two beams is the most challenging condition that we need to satisfy in order to have collisions, we also need to accurately place the laser focus at the path of the electron beam.
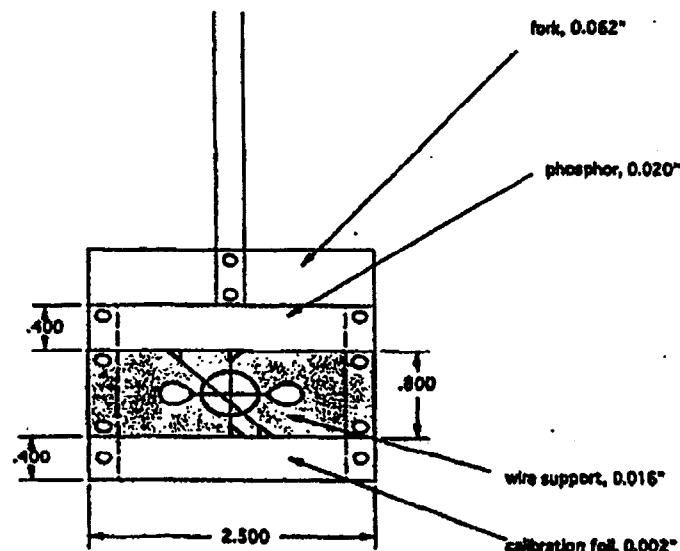
Figure 4.29: A schematic of the IP flag. The top part is the fluorescent screen used to view the electron beam. In the middle three Al wires are mounted used for electron beam measurements and also for aligning the flag at the location of the laser focus. The bottom part contains a Al foil used during the detector calibration.

This task is made easier due to the fact that the electron beam dimensions are much bigger than those of the laser at the focus, by at least a factor of 7. A coarse spatial overlap can be established visually, by using the structure shown in Fig. 4.29 and which is conventionally referred to as the IP flag. The flag can be remotely controlled with a 3-axis stepper motor, mounted on the top of the IP box. As mentioned earlier

in section 4.2, a He-Ne laser is co-injected along with the main laser pulse. The IP flag can be scanned along the z-axis (the axis along the electron beam path), and positioned at the He-Ne focus (which coincides in position with the main laser pulse focus). To find the exact location we make use of the wires mounted on the flag, and take advantage of the fact that the 20 μm thick wires are much bigger than the laser focus, which is only a few microns wide in both the x and y directions. That means that when we are exactly at the laser focus, the wire will completely block any He-Ne light to come back into the laser room, and the Mach-Zehnder interferometer image, described in section 4.2, will be black. Once we have longitudinally positioned the flag at the laser focus, we can use the fluorescent screen on top of the wires, to view the electron beam, with the help of a CCD camera. The He-Ne beam is also visible with this camera. When the fluorescent screen intercepts the electron beam, the repetition rate of the electron bunches has to be dropped temporarily down to 1 Hz, from the normal value of 10 Hz during the data collection period to avoid high radiation levels. Since we can now view both the electron and the He-Ne beams, we can steer the electron beam, using upstream dither correctors, so that it overlaps with the He-Ne. The IP box movers can be used for finer adjustments. The final positioning of the electron beam at the laser focus is done by scanning the wire cross-hair across the electron beam. When the cross-hair intercept the electron beam, bremsstrahlung γ's are produced and can be detected by the gamma monitors downstream. The peak of their signals indicates the best spatial overlap conditions. It is obvious that this procedure needs to be repeated whenever the electron beam steering is modified. We can now remove the flag from the path of the electron beam and let the main laser beam down at the interaction point. Due to thermal effects, long term drifts of the IP box position, can lead to loss of optimal spatial overlap. As long as steering of the electron beam is not involved, the situation is remedied by scanning the IP box in the x and y directions and looking for peaks at the signals of the detectors and especially of those of the nonlinear monitors. Moving the IP box in the x and y directions,

is equivalent to moving the laser focus in the same directions, since the laser path in the interaction region, is fixed with respect to the position of the IP box. Once the laser and electron beams begin to spatially overlap, and assuming that they are not off in time, Compton scattering will occur. Since the nonlinear Compton signal, which is very sensitive to the laser intensity, will occur only when the laser focus is centered on top of the electron beam, it is clear that we need to look at the signals of the nonlinear monitors. Optimal spatial overlap corresponds to the peaks of their signals. This is the main principle underlying the so called X- and Y-Scans and is very similar to the timing scan procedure described in section 4.3.
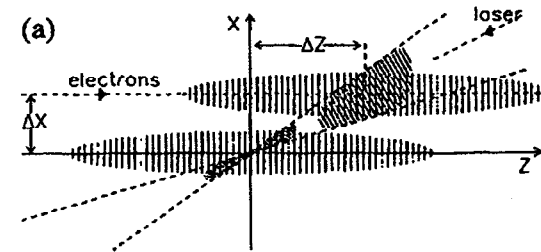
Figure 4.30: Geometry of an XT-scan.Two electron beam bunches offset with respect to the laser pulse either in x or in z(time) or in both, will go through different parts of the laser pulse. The bottom one which is 'right-on' will see the laser pulse when it is at its focus. The top bunch will miss the focus resulting in much lower rates, especially for the higher order processes.

While the y-overlap is unambiguous, the x-overlap depends on the relative timing of the two beams, as it is indicated in Fig. 4.30. Thus it is necessary to carry out 2-dimensional scans in both the IP box x-position, and the relative time delay of the electron and laser pulses. This is called an XT-Scan. Fig. 4.31, shows such a scan, from the perspective of both a linear and a nonlinear monitor Compton signal. The left plot is the linear Compton rate plotted as a function of Δx and Δt. The
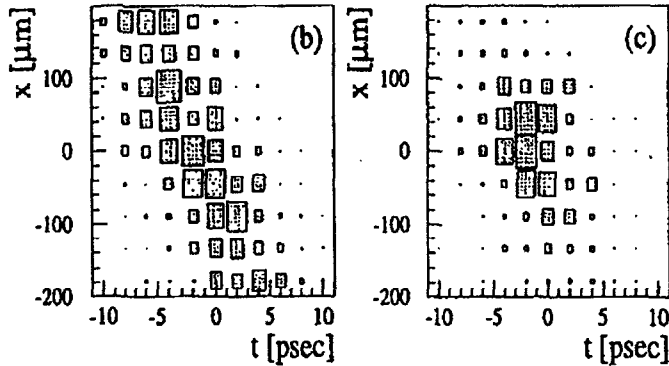
Figure 4.31: Comparison of the linear to the nonlinear ($n = 2$) Compton scattered signal as detected by the linear gamma monitor CCM1 and the top row of ECAL, during an older data run.

correlation between the two offsets,

$$\Delta x \left(\frac{1}{\sin \alpha} + \frac{1}{\tan \alpha} \right) = c \, \Delta t \tag{4.7}$$

is evident. The right plot shows the $n = 2$ Compton rate, as it is detected by the N2 monitor. Here a large signal is obtained only when the electrons cross through the laser beam at the focus. Therefore by performing such a scan we can determine the location in space and time, where the laser intensity is at its highest. XT-Scans are also useful to separate the unwanted linear Compton scattering backgrounds from the desired higher order ones, as it is discussed in more detail in chapter 5. XT-Scans are preceded by a Y-Scan in order to establish optimal vertical relative positioning of the electron and the laser beams, and are followed by a timing scan, to verify collision stability.

A serious drawback of the XT-Scan is that they are time consuming. This can be alleviated in part by introducing a one-dimensional scan across the diagonal on the XT-plane. That means that every time we change the IP box x position by some

specific amount we also automatically change the timing offset by:

$$\Delta t = -3.345 \, \Delta x \tag{4.8}$$

Such a scan is shown in Fig. 4.32. The top two plots show the event rates detected
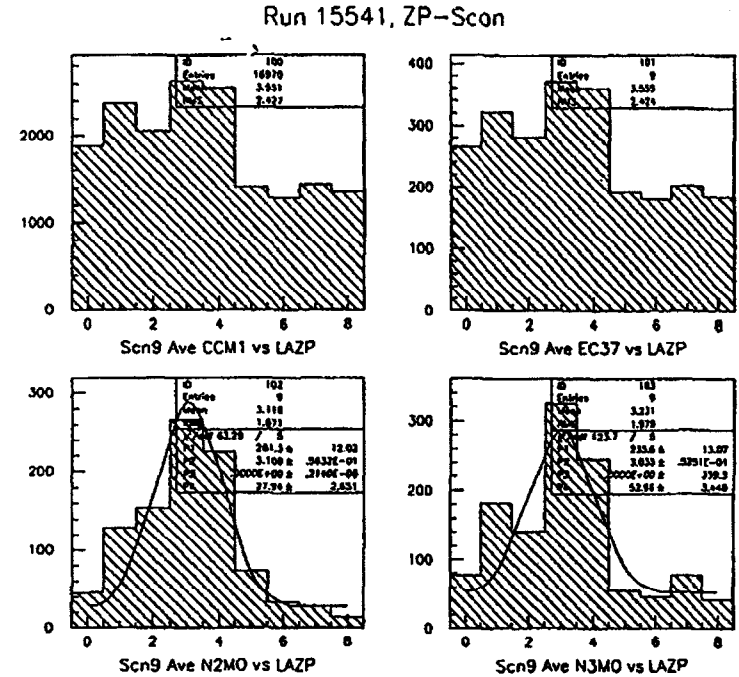
Figure 4.32: An alternative to the XT-scan is a 1-dimensional scan that follows the slope of the signal shown in Fig. 4.31. The two top plots show the signals of two linear monitors, while the two bottom ones the corresponding signals from two nonlinear monitors that look at different order electrons. Notice how much clearer the peaks are in the two last plots.

by the gamma and the electron linear monitors respectively, while the two bottom plots, the rates observed by the two nonlinear monitors N2 and N3. The optimal position in the XT-plane corresponds to the peak of the two bottom plots. This

type of scan is called the z-prime scan (ZP-Scan). It is important that a timing scan is performed before the ZP-Scan in order to find the peak in the linear Compton scattering rates. At the end of either an XT-Scan or a ZP-Scan the IP box x position and the relative time delay between the electron and laser beams, are set to the values of peak interaction rate.

Chapter 5

Detectors

In the previous two chapters we discussed about the electron and the laser beams that are brought into collision at the interaction point (IP). A set of detectors needs to be utilized in order to measure the results of such interactions, like Compton scattering of various orders, or the positron production during light-by-light scattering. Calorimeters positioned at the end, or close to the end of a spectrometer (see Fig. 1.2), so that enough separation of the electrons and positrons produced at the IP can be achieved, can be used to measure the energy of such particles. Compton γ's are also of interest and can be detected by using for example a pair spectrometer based on a bend magnet right after a γ ray converter. Of equal importance is the existence of counters that can be used to monitor the effectiveness and stability of the laser-electron beam collisions. In this chapter we discuss all the different types of detectors and counters used during the data collection and relevant for the later steps of the data analysis. This includes the electron and positron calorimeters and the various linear and nonlinear monitors, their design, calibration and signal reconstruction. CCD pair spectrometers, used as γ detectors, are not discussed in this chapter, mainly due to the fact that are not relevant to the positron production analysis that is the main concern of this thesis. A brief discussion of them is provided in chapter 1.

type of scan is called the z-prime scan (ZP-Scan). It is important that a timing scan is performed before the ZP-Scan in order to find the peak in the linear Compton scattering rates. At the end of either an XT-Scan or a ZP-Scan the IP box x position and the relative time delay between the electron and laser beams, are set to the values of peak interaction rate.

Chapter 5

Detectors

In the previous two chapters we discussed about the electron and the laser beams that are brought into collision at the interaction point (IP). A set of detectors needs to be utilized in order to measure the results of such interactions, like Compton scattering of various orders, or the positron production during light-by-light scattering. Calorimeters positioned at the end, or close to the end of a spectrometer (see Fig. 1.2), so that enough separation of the electrons and positrons produced at the IP can be achieved, can be used to measure the energy of such particles. Compton γ's are also of interest and can be detected by using for example a pair spectrometer based on a bend magnet right after a γ ray converter. Of equal importance is the existence of counters that can be used to monitor the effectiveness and stability of the laser-electron beam collisions. In this chapter we discuss all the different types of detectors and counters used during the data collection and relevant for the later steps of the data analysis. This includes the electron and positron calorimeters and the various linear and nonlinear monitors, their design, calibration and signal reconstruction. CCD pair spectrometers, used as γ detectors, are not discussed in this chapter, mainly due to the fact that are not relevant to the positron production analysis that is the main concern of this thesis. A brief discussion of them is provided in chapter 1.

5.1 Calorimeters

5.1.1 General Description

As it has already been mentioned in chapter 1, there are two calorimeters, one that detects the scattered electrons (ECAL), and the corresponding one that detects positrons (PCAL). Both calorimeters are of similar design. They are made of
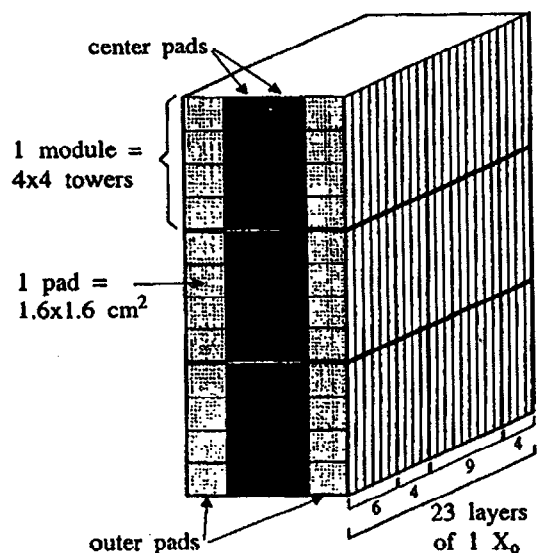
Figure 5.1: Schematic of the electron and positron calorimeters.

alternating layers of silicon and tungsten; each tungsten layer is one radiation length thick and each silicon layer 300 μm thick. Thus the resulting sampling fraction is 1.1%. Each calorimeter layer is divided into 12 rows and 4 columns with 1.6×1.6 cm^2 active area pads. Every 4 rows are separated by a gap made of 1.5 mm of inactive silicon. A schematic of the calorimeters is shown in Fig. 5.1. The longitudinal layers of each tower— groups of 4 pads in the same column— are arranged in 4 segments.

While all 12 ECAL rows are read out, only the bottom 8 rows of PCAL are read out. The calorimeters are read out by using the Redundant Analog Bus Based Information Transfer (RABBIT) system which reads the charge collected by the silicon pads and amplifies it using LACAMP modules. The gain in ECAL is set so that a single 10 GeV electron would be detected, while at a total incident energy of 10 TeV in a single tower, the readout is saturated. The gain in PCAL is 30 times higher than that in ECAL since only individual positrons are detected by it. Electrons and positrons produced at the IP, can normally hit only the two center columns in either PCAL or ECAL, so that we can use the outer pads for background subtraction. The calibration is done by sending a test beam through the FFTB line, characterized by a low electron flux and variable, but controllable, particle momenta. Using the calibration data the resolution of the calorimeters can be deduced and it is found to be [50],

$$\sigma_{\mathcal{E}}^2 = (0.19)^2 \mathcal{E} + (0.4)^2 + (0.05)^2 \mathcal{E}^2 \qquad (5.1)$$

where $\mathcal{E}$ is the electron energy in GeV.

5.1.2 Momentum Map and Acceptances

It is of paramount importance for the whole data analysis to be able to determine the momentum acceptances of both ECAL and PCAL. This relies on the correct tracing of the trajectories of the electrons and positrons of different momenta produced at the interaction point, as they traverse through the bending magnets of the experiment's spectrometer. As already mentioned, the spectrometer resides at the so called dump line of the FFTB and starts at about 4.5 m downstream of the electron-laser interaction region (IP). It consists of six permanent magnets with a mean field of 4.48 kGauss across a 2 inch by 336 inch poleface, providing a transverse kick of 816 MeV/c in the vertical plane on a 46.6 GeV electron. Air core "soft bends" of 0.5 and 0.05 milliradians (at 46.6 GeV) are positioned on each side of the IP in order to reduce synchrotron radiation in the direction of the forward γ's. Fig. 1.2 in chapter 1, shows

the FFTB line around the interaction point, using the PCS coordinate system. A computer program that simulates the paths followed by positive or negative charged

Magnet Name	y_{SCS} [m]	z_{SCS} [m]	ϕ_{SCS} [mrad]	D_z [m]
B04A	76.10636	322.92850	-5.06796	1.0
B05A	76.10062	324.03250	-5.35763	1.0
B05B	76.08794	326.40897	-5.42234	1.0
B04B	76.08190	327.51294	-5.66927	1.0
B06A	76.06986	329.50711	-7.24453	0.944
B06B	76.06094	330.55106	-9.96544	0.944
B06C	76.04917	331.59500	-12.68632	0.944
B06D	76.03457	332.63889	-15.40721	0.944
B06E	76.01711	333.68274	-18.12810	0.944
B06F	75.99683	334.72656	-20.84899	0.944

Table 5.1: Positions and dimensions of the ten spectrometer magnets in the SLAC Coordinate System.

particles that go through the spectrometer magnets, has been developed [51]. The main inputs to this tracking program are the magnet positions, their field map and the positions of the two calorimeters. The coordinate system used for the FFTB line, is a cartesian coordinate system, called the SLAC Coordinate System (SCS), and has its origin at station 100 located at more than 300 m upstream of the FFTB's Final Focus (FF). In this coordinate system the FF is at $y_{SCS} = 76.15526$ m and $z_{SCS} = 312.6726$ m. The electron beam propagates in the $x_{SCS} = 0$ plane and at the FF points downwards at an angle of -0.2755 degrees with respect to $\hat{z}_{SCS}$. For convenience the actual tracking of the charged particles is done by utilizing a cartesian system, called the Private Coordinate System (PCS), that places its origin at the FF and has its $\hat{z}_{PCS}$ axis parallel to the beam trajectory at that point. The coordinate

transformation from SCS to PCS is given by the following expressions:

$$x_{PCS} = x_{SCS} \tag{5.2}$$

$$y_{PCS} = (y_{SCS} - \Delta y_{SCS}^{PCS})\cos(\theta_{SCS}^{PCS}) - (z_{SCS} - \Delta z_{SCS}^{PCS})\sin(\theta_{SCS}^{PCS}) \tag{5.3}$$

$$z_{PCS} = (y_{SCS} - \Delta y_{SCS}^{PCS})\sin(\theta_{SCS}^{PCS}) + (z_{SCS} - \Delta z_{SCS}^{PCS})\cos(\theta_{SCS}^{PCS}) \tag{5.4}$$

Here $\Delta y_{SCS}^{PCS} = 76.15526$ m, $\Delta z_{SCS}^{PCS} = 312.6726$ m and $\theta_{SCS}^{PCS} = -0.2755$ degrees. Table 5.1, shows the position and orientation of the spectrometer magnets in the SCS coordinate system, along with their respective lengths.

For the permanent dipole magnets (the last 6 magnets in table 5.1), the $\hat{x}$-component of the B-field has been measured in the symmetry plane at $x = 0$. A seventh permanent magnet was also measured, but it was never installed due to some damage on its right hand side (looking downstream) pole. The quoted precision is $\sim 0.5\%$. The range and step size of these measurements are shown in table 5.2. The

Magnet Number	Measured Range		Step Size		Installation Order
	y [cm]	z [cm]	y [cm]	z [cm]	(looking downstream
FFTB_1	-25 to -10	-85 to +85	2.5	1.0	
	-10 to +10	-85 to +85	1.0	1.0	not installed
	+10 to +25	-85 to +85	2.5	1.0	
FFTB_2	-11 to +11	-50 to +49	1.0	1.0	5 (B06E)
FFTB_3	-10 to +12	-50 to +49	1.0	1.0	3 (B06C)
FFTB_4	-11 to +11	-50 to +49	1.0	1.0	2 (B06B)
FFTB_5	-11 to +11	-50 to +49	1.0	1.0	6 (B06F)
FFTB_6	-11 to +11	-50 to +49	1.0	1.0	1 (B06A)
FFTB_7	-11 to +11	-50 to +49	1.0	1.0	4 (B06D)

Table 5.2: Range and step size of field measurements for the 7 permanent magnets in the spectrometer, as well as their order of installation in the FFTB dump line.

results of these measurements are presented in Fig. 5.2 and 5.3. From those it is

B$_x$(y,z) of FFTB 1 (reduced range)

B$_x$(y,z) of FFTB 2

B$_x$(y,z) of FFTB 3
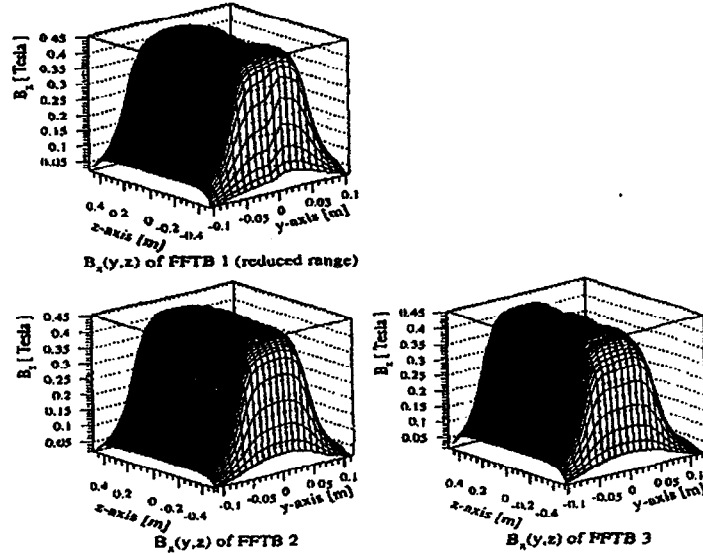
Figure 5.2: Magnetic fields of the 2 first permanent magnets of the FFTB dump line (plots 2 and 3), and of one more permanent magnet (plot 1) that was never installed, due to damages on one of its poles. These results are based on the calibration of the magnets before having them installed in the FFTB tunnel. Note the FFTB_1 has been mapped in a more extensive area than the one shown here.

very clear that the measured area for the magnets installed in the FFTB line is not sufficient for accurate determination of the off energy charged particle trajectories. The field strength along the boundary is still ~ 10% of the peak value. This can be remedied by using the field map of the first magnet, for which the field strength at the boundary drops to less than 1% of its value at the peak. This is valid since all the permanent magnets examined here are designed and constructed in exactly the same way. Unfortunately the first magnet shown in Fig. 5.2, is the one with the damaged pole mentioned earlier, and this can be seen in the plot as an edge in the surface lines drawn there. But due to the symmetry of the dipole field around zero, i.e.

$$B_x(y,z) = B_x(-y,z) \quad \text{for } z < -0.35 \text{ m and } y \leq 0.01 \text{ m, and} \quad (5.5)$$

B$_x$(y,z) of FFTB 4

B$_x$(y,z) of FFTB 5

B$_x$(y,z) of FFTB 6

B$_x$(y,z) of FFTB 7
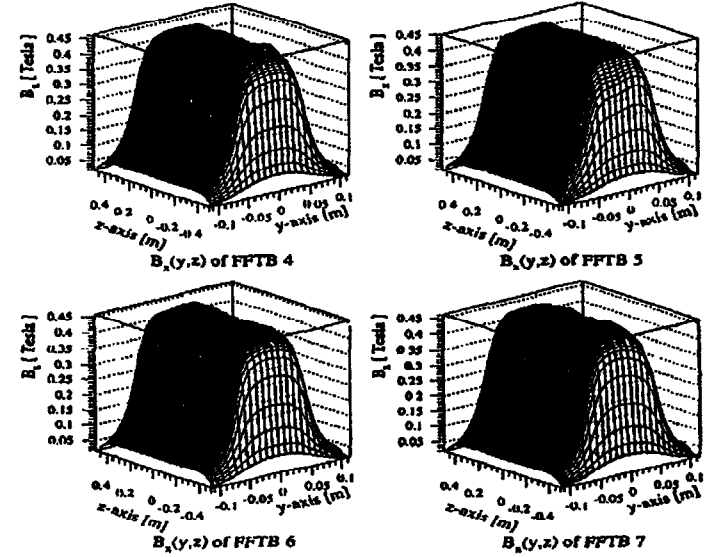
Figure 5.3: Magnetic fields of the 4 last permanent magnets of the FFTB dump line. These results are based on the calibration of the magnets before installation in the FFTB tunnel.

$$B_x(0,z) = B_x(0.01,z) \quad \text{for } z < -0.35 \text{ m} \quad (5.6)$$

we can still use the measurements on the other pole and therefore the field maps of the installed dipoles can be extended to a range of ±25 cm in the $\hat{y}$ and ±85 cm in the $\hat{z}$ axis, resulting to a more accurate tracking of the charged particles. For the soft bend magnets the current is increased when running at 49.1 GeV. In this higher electron beam energy, the strength of these magnets needs to be increased in order to bend the higher energy charged particles by the same amount that they do in the 46.6 GeV case. Table 5.3 shows the field strengths of the first 4 dipoles for the two different energy electron beams used.

Once the field strengths and exact positions of the dipole magnets are specified, we can track the charged particles through the spectrometer and define their vertical

Magnet Name	B_0 (46.6 GeV) [kG]	B_0 (49.1 GeV) [kG]
B04A	0.800	0.8435
B05A	0.100	0.1054
B05B	0.100	0.1054
B04B	0.667	1.4500

Table 5.3: Field strengths for the so called soft bend dipoles located around the laser-electron interaction point, for the two different electron beam energies during the data run, in units of kGauss.

location at the two calorimeters ECAL and PCAL. ECAL can be moved vertically so the momentum range that it sees varies with its vertical distance from the beam pipe. Considering the top row of ECAL, and taking into account the fact that ECAL moves between positions located at -76 mm and -164 mm below the beam pipe, we can specify an ECAL momentum acceptance between 6 GeV and 11 GeV for a 46.6 GeV electron beam. This acceptance shifts slightly towards higher momentum values for the 49.1 GeV case. Such momentum acceptance allows electrons from third or fourth order Compton scattering to reach the top row of ECAL. For PCAL the situation is much simpler, since its position is fixed at 55.3 mm above the beam pipe. As already mentioned, only the bottom 8 rows of PCAL are read out. Because of the positioning of PCAL in the FFTB line, its bottom row (row 8) is completely shielded from any positron signal due to the presence of the vacuum chamber. Therefore only 7 rows contribute to the signal reported and the momentum acceptance of PCAL, for those 7 rows only, is between 6.8 GeV and 21.5 GeV for a 46.6 GeV electron beam. In the case of the 49.1 GeV electron beam it changes slightly to values between 7.4 GeV and 23.6 GeV.

5.1.3   Signal Corrections

The signal measured by one row in ECAL differs from the real energy of the particles incident on that row. The following factors contribute to such an effect:

1. Leakage from adjacent rows into the row under consideration, increases the row signal.

2. Leakage from the row under consideration to adjacent rows, reduces the row signal.

3. Backgrounds due to scattered electrons result to an increased row signal.

The signal leakages between adjacent rows in ECAL are related to electromagnetic shower spreading in the calorimeter. Using the calibration data, the energy response of a specific ECAL row as a function of the electron position with respect to the center of the row, can be plotted. This energy response is fairly independent of the incident electron energy. If we denote the response function as $S_i(y)$, where y is the vertical position at which the electron enters ECAL, we can write it in terms of a kernel function $K(y, y')$ as follows:

$$S_i(y) = \int_{y_i}^{y_i+1} K(y, y')dy' \qquad (5.7)$$

The kernel function is the energy fraction deposited by an electron entering ECAL at position y, in a vertical slice dy' located at a height y' in ECAL. Using a Monte Carlo simulation the kernel function can be parametrized so that it fits reasonably well the data, and such a parametrization for the central ECAL rows has the form:

$$K(y, y') = \frac{w_1}{2b_1} e^{(-\frac{|y-y'|}{2b_1})} + \frac{(1-w_1)}{2b_2} e^{(-\frac{|y-y'|}{2b_2})}, \qquad \int_{-\infty}^{\infty} K(y, y')dy' = 1 \qquad (5.8)$$

The values of the three constants b_1, b_2, w_1 for the three first longitudinal segments used in the analysis grouped together, are 1.94, 9.6 and 0.703 respectively. In the case of the outer rows, the kernel function parametrization becomes:

$$L(y, y') = C\frac{1}{2b_2} e^{(-\frac{|y-y'|}{2b_2})} \qquad (5.9)$$

Here the normalization factor C is 0.0713 and corresponds to the total leakage of the shower to the outer columns of the calorimeter. In the center rows the normalization factor is set to 1. The constant b_2 now becomes 16.9.

We still need to correct the signal for backgrounds. There are three sources of backgrounds on ECAL:

1. The iron window of the vacuum chamber. The $n = 1$ Compton electrons that go through it are scattered and the ones emerging in angles smaller than 30° can reach ECAL. This background is the dominant factor in the first longitudinal segment of ECAL.

2. The beam pipe above ECAL. $n = 1$ electrons hit the walls of the pipe at a small angle of 1°. The produced scattered electrons can hit the top of ECAL at angles $\sim 90°$. This is a serious background source in the top row of ECAL.

3. $n = 1$ electrons exit the beam pipe and hit other materials behind ECAL. Back-splash of such electrons reaches ECAL mainly in the last longitudinal segment.

Changes in the beam pipe and the vacuum chamber window, lead to a reduction of the background from the first two sources in the above list to a level of less than an order of magnitude of the real signal. Pb-bricks stocked behind ECAL reduce the background from back-splash electrons. In addition the last longitudinal segment is not used during the data analysis. The background due to back-splash is fairly uniform and can be subtracted easily. The way the ECAL is positioned, the real signal can appear only in the center columns, while the outer columns report mainly background with an additional signal due to the shower leakage from the center rows. Therefore subtracting the signal of the outer rows from the center rows, eliminates effectively that background source. Backgrounds due to electron scattering on the beam pipe walls or the vacuum chamber window, are less uniform and special care needs to be taken for their subtraction. The background in ECAL has two important characteristics. First it decreases exponentially with the distance of ECAL from the

beam pipe. Second the background levels are higher in the center columns than in the outer columns. The ratio of background in center/outer columns tends to 1 as one examines lower rows in ECAL.

Two correction procedures of the background in the ECAL signal have been developed [52], [53]. They give results compatible with each other. They are both based on the fact that the nonlinear Compton scattering produces an energy spectrum $f(y)$ of scattered electrons hitting the ECAL at height y. Because of fluctuations in the electron-laser overlap, this spectrum varies from pulse to pulse. The general strategy is to reconstruct the spectrum f for each pulse. Of course a continuous spectrum such as f cannot be reconstructed from data in a detector with a finite number of rows. What can be reconstructed is the integral F_i of the spectrum over the row i:

$$F_i = \int_{y_i}^{y_{i+1}} f(y')dy' \tag{5.10}$$

The energy D_i observed in row i is related to the Compton spectrum f by

$$D_i = \int dy f(y) \int_{y_i}^{y_{i+1}} K_i(y,y')dy' = \int dy f(y)S_i(y) \tag{5.11}$$

recalling Eq. 5.7. The index i runs from 1 to 4, corresponding to the top four rows of ECAL. Then the observed energy D_i is related to the desired spectrum F_i by

$$D_i = \sum_j M_{ij}F_j \tag{5.12}$$

and by inverting the last one we get:

$$F_i = \sum_j R_{ij}D_j \quad \text{where } R_{ij} = M_{ij}^{-1} \tag{5.13}$$

The matrix R_{ij} is the solution to the problem. The two reconstruction methods move in different ways to achieve this goal. We follow [54] in order to give a brief description of their basic characteristics.

In the first method Eq. 5.13 is combined with Eq. 5.11 to write

$$F_i = \sum_j R_{ij}D_j = \int dy f(y)\sum_j R_{ij}S_j(y) = \int dy f(y)g_i(y) \tag{5.14}$$

where

$$g_i(y) = \sum_j R_{ij} S_j(y) \tag{5.15}$$

Comparing Eq. 5.15 to Eq. 5.10, we see that the g_i (called "aperture functions") should obey:

$$g_i(y) = \begin{cases} 1, & y_i < y < y_{i+1} \\ 0, & \text{otherwise} \end{cases} \tag{5.16}$$

The matrix R_{ij}, for a given configuration of ECAL, is calculated by a χ^2-minimization process

$$\chi^2 = \sum_{i,k} \frac{(\sum_j R_{ij} S_j(y_k) - g_i(y_k))^2}{\sigma_{ik}^2} \tag{5.17}$$

where the deviates are evaluated at y_k spaced 1 mm apart. Some care in choosing the errors is required. The background energy in row i is written as B_i and it is determined by using the XT-Scans. The reconstruction matrix R_{ij} should produce no signal when applied to the background vector:

$$\sum_j R_{ij} B_j = 0 \tag{5.18}$$

This condition is enforced by adding one more term to the χ^2 in Eq. 5.17 which now becomes:

$$\chi^2 = \sum_{i,k} \frac{(\sum_j R_{ij} S_j(y_k) \ g_i(y_k))^2}{\sigma_{ik}^2} + \frac{(\sum_j R_{ij} B_j)^2}{\sigma'^2} \tag{5.19}$$

Again the tolerances σ' must be carefully chosen.

The second method starts directly from Eq. 5.12. Let's for convenience designate the energy deposited by electrons in front of ECAL (signal electrons) with S and that deposited by the background electrons (predominantly backsplash electrons mentioned earlier) with B. Then the observed energy D_I in the center rows can be written as a vector with the row index i suppressed:

$$D_I = D_{I,S} + D_{I,B} \tag{5.20}$$

Similarly the deposited energy in the outer rows is a combination of backsplash energy and energy leakage from the center rows. If we denote it as D_O we can write:

$$D_O = D_{O,S} + D_{O,B} \tag{5.21}$$

Just as the Compton signal $D_{I,S}$, in the center rows can be related to the Compton spectrum vector F by Eq. 5.12 rewritten in matrix form as

$$D_{I,S} = MF \tag{5.22}$$

in terms of matrix M, there exists a matrix N such that the Compton leakage signal $D_{O,S}$ in the outer rows can be written as

$$D_{O,S} = NF \tag{5.23}$$

The two reconstruction matrices M and N can be found directly by an iterative process in which the integrals in Eq. 5.11 are performed analytically for a "polyline" approximation to spectrum f derived from the F_i of the previous step. The initial hypothesis is that $F_i = D_i$ for both the center and outer rows separately. The key assumption in order to perform the background subtraction, is that the background energy in the center and outer rows are related according to:

$$D_{I,B} = LD_{O,B} \tag{5.24}$$

The matrix L is diagonal and its diagonal elements are determined by XT-Scans when the time offset is such that the $n \geq 2$ signal has vanished, but the $n = 1$ signal, which is less sensitive in such an offset, still remains. ECAL needs to be positioned so that it detects nonlinear Compton scattering of $n \geq 2$. Once the matrices L, M, and N are known, the reconstruction is almost completed. The observed energies in the center rows can now be written:

$$D_I = D_{I,S} + D_{I,B} = MF + LD_{O,B} \tag{5.25}$$

Similarly for the outer rows we can write:

$$D_O = D_{O,S} + D_{O,B} = NF + D_{O,B} \qquad (5.26)$$

On subtracting L times Eq. 5.26 from Eq. 5.25 and noting Eq. 5.24 we have

$$D_I - LD_O = [M - LN]F \qquad (5.27)$$

and hence

$$F = [M - LN]^{-1}(D_I - LD_O) \qquad (5.28)$$

Although the two methods have certain differences, especially in the way that perform the background subtraction by calculating the matrix R, certain relations between their corresponding results exist as it is noted in [54].

In the case of PCAL, we do not have to worry about the background levels that we have encountered in ECAL. This is due to the fact that the positron signal is minimal. We do have in PCAL positrons that are not produced by the electron-laser interactions, but the cleaning up of the PCAL signal from that type of background is more of a data analysis subject and it will be discussed in the following chapter. There is nevertheless an important thing that needs to be done with the PCAL signal and this is the coherent noise subtraction. With coherent noise we mean essentially the electronic noise that is added to the normal data signal. As we have already mentioned in section 5.1.1, the levels of the expected positron signal are normally very low and for that reason the gain of PCAL's readout electronics is set very high. This has as a side effect that the electronic noise is of the same order of magnitude as the real signal.

The idea behind the coherent noise subtraction procedure is the following: Electronic noise is a characteristic of every PCAL pad that is read out, and there is no correlation between the coherent noise of two different pads. Due to its random nature, it results to a higher RMS value for the signal distribution of one specific PCAL pad, from which it is not properly subtracted. If we can find one specific PCAL pad,
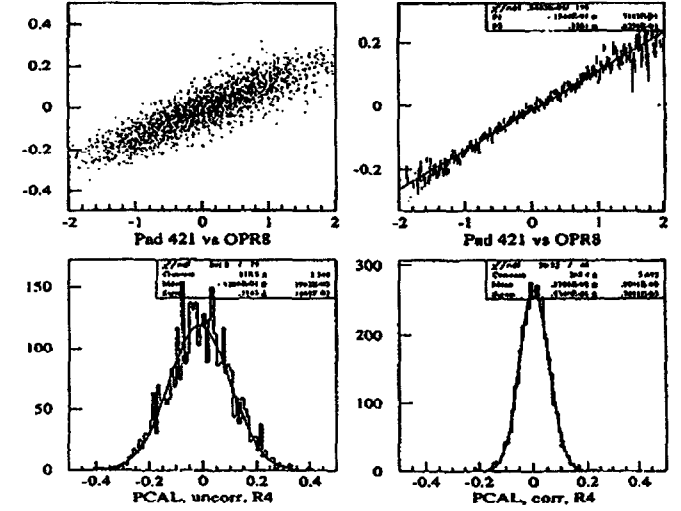
Figure 5.4: Signal correlation of pad (4,2,1) of PCAL, to the total signal in the outer pads of row 8 of PCAL, for run 15323. It is clear that it has a linear form, as it is also demonstrated by the fit performed in the top right plot. The two bottom plots show the difference between the uncorrected and the corrected for coherent noise signal distribution of the same pad respectively. Notice how much narrower the second distribution is.

or a group of pads, for which we are pretty certain that they contain only electronic noise, we can then correlate to it the signals of all the other pads. The type of correlation between the signal of one PCAL pad, to the signal of a PCAL pad with only electronic noise (linear, higher order polynomial, etc.), provides us with the type of correction that needs to be applied. For convenience we denote each PCAL pad with the triplet (i, j, k), where $i = 1\dots8$ is the row number, $j = 1\dots4$ is the column number and $k = 1\dots4$ is the segment number. PCAL is positioned in the FFTB tunnel in such a way that the bottom row (row 8) is completely shielded from any positron signal. Besides, only the center columns are hit by positrons. Therefore the
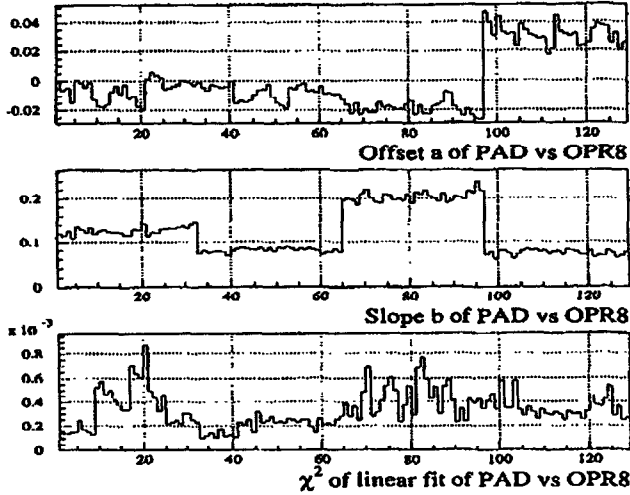
Figure 5.5: Distribution of the two coherent noise subtraction coefficients derived from a linear fit, as described in the text, and of the χ^2 of that fit.

total signal of all the outer pads of row 8 in all the longitudinal segments, *i.e.*

$$opr8 = \sum_{k=1}^{4} pad(8,1,k) + pad(8,4,k) \tag{5.29}$$

is just coherent noise. The correlation of every other $pad(i,j,k)$ signal to this turns out to be of a linear form and by a fitting a line we find the corresponding slope $b(i,j,k)$ and the offset, $a(i,j,k)$. This is shown in the top two plots of Fig. 5.4, where pad (4,2,1) of PCAL is used. We can then subtract from $pad(i,j,k)$ a coherent noise fraction as follows:

$$pad(i,j,k)_{new} = pad(i,j,k)_{old} - a(i,j,k) - b(i,j,k)\, opr8 \tag{5.30}$$

We can then again find the distribution of the new coherent noise corrected pad signal and recalculate the new RMS value. By iterating several times we can find the values of the offset $a(i,j,k)$ and of the slope $b(i,j,k)$ that give us the minimum RMS

value and these are the ones that are used for the final coherent noise subtraction. The difference between the uncorrected and the corrected for coherent noise signal distribution of pad (4,2,1) of PCAL, is shown in the two bottom plots in Fig. 5.4. This procedure needs to be repeated for all the PCAL pads, for every data event and for all the data runs. Fig. 5.5 shows the distribution of the two linear parameters along with the χ^2 of the fit, for all PCAL pads. Only the corrected PCAL data is used for the positron analysis.

5.2 Linear Monitors

5.2.1 General Description

There are two types of linear monitors, which are detectors that measure the rates of the linear Compton scattering. The first type is an air Čerenkov detector that intercepts the forward γ's produced during the linear Compton scattering, and it is generally referred to as CCM1. A schematic of the forward γ monitor is shown in Fig. 5.6. The forward linear γ's are passing through a shower converter made of 0.2 radiation lengths of Al. The e^+, e^- pairs produced in the radiator, emit Čerenkov radiation as they traverse a 25 mm long air tube, located behind the Al converter. A 45° mirror made of polished Al directs the Čerenkov light downwards before been deflected once more by a similar mirror into the photomultiplier tube. The total light path thus, is about 1 m long. The cross section of the initial light channel is 25 mm × 25 mm and it is increased after every deflection in order to retain light rays within a 7° solid angle. This design places the PMT far from the electron beam and allows the placement of lead shielding to reduce backgrounds. The walls during the first few cm of the light pipe are painted flat black. Beyond that they are made highly reflective by applying aluminized Mylar. The photomultiplier has been operated between 1500 and 1800 Volts with a gain of 10^4. A filter, made of Al with a regular pattern of 36 holes, can be inserted into the light path inducing an attenuation of a factor of
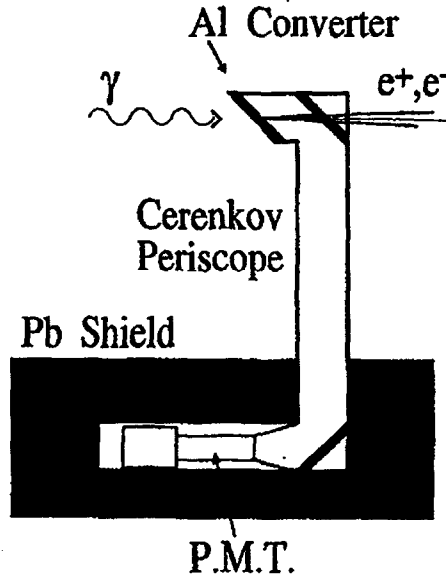
Figure 5.6: Schematic of a Monitor that looks at the γ's from the linear Compton process.

10. This can prevent the monitor from saturation when high γ fluxes are present, especially when the temporal and spatial overlap of the electron and laser beams is optimal. The counter is placed on rails and can be remotely taken out of the path of the γ rays.

The big disadvantage of the CCM1 counter is that when it is inserted into the path of the γ rays, they are prevented from reaching the CCD detectors located further downstream. The CCDs, which are used to detect γ's from higher order Compton scatters, have to be operational during the main data runs. Since the use of the CCM1 monitor is incompatible with CCD running, a second type of linear Compton monitors is used, consisting of two air Čerenkov detectors that can look directly at linear Compton scattered electrons of specific energies. The first of these detectors intercepts 37 GeV electrons and consequently is called the EC37 linear counter, while

the second one intercepts 31 GeV electrons and is called the EC31 counter. These two monitors are the principal linear counters, while CCM1 is still useful for the cross calibration of EC37 and EC31.

5.2.2 Linear Monitor Calibration

We can easily calibrate the forward γ monitor CCM1, by inserting an Al foil into the path of the electron beam and creating bremsstrahlung γ's. The calibration is based on the assumption that the CCM1 acceptance is the same for both the bremsstrahlung and the linear Compton γ's. The Al foil is 50 μm thick and its thickness has been selected so that the flux of the bremsstrahlung γ's is about equal to the flux of the
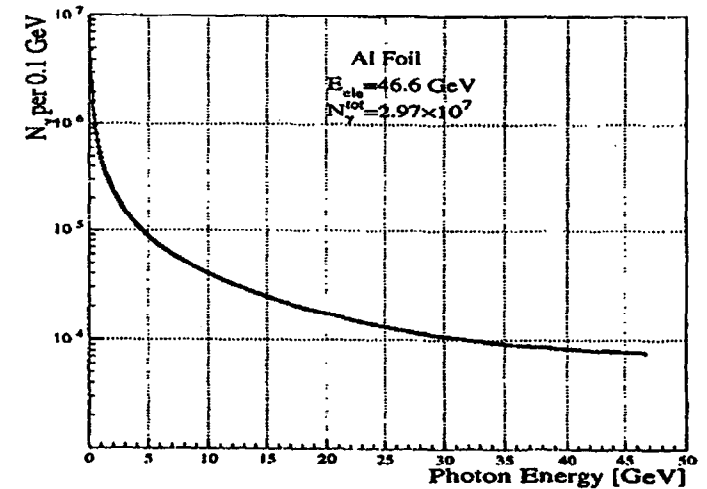
Figure 5.7: The bremsstrahlung spectrum due to 7×10^9 electrons incident on a 50 μm thick Al foil. The differential cross section in Eq. 5.31 has been used. The total number of γ's produced is of the order of 10^7.

linear Compton γ's. The bremsstrahlung differential cross section in the extreme

relativistic regime, when the Coulomb correction is also taken into account is,

$$\frac{d\sigma}{dk} = \frac{4Z^2 r_0^2}{137}\frac{1}{k}[(1 + (\frac{E}{E_0})^2 - \frac{2}{3}\frac{E}{E_0})(\ln(183Z^{-\frac{1}{3}}) - f(Z)) + \frac{1}{9}\frac{E}{E_0}] \quad (5.31)$$

where E_0 and E are the initial and final electron energies in units of the electron rest mass, k is the energy of the emitted photon in the same units, Z is the atomic number of the target material and $r_0 = \frac{e^2}{m_e c^2}$ is the classical electron radius. The function $f(Z)$ depends on the magnitude of Z and is given by,

$$f(Z) = \begin{cases} 1.2021(\frac{Z}{137})^2 & \text{for low } Z \\ 0.925(\frac{Z}{137})^2 & \text{for high } Z \end{cases} \quad (5.32)$$

In Eq. 5.31 we can make the substitution,

$$\frac{E}{E_0} = (1 - \frac{k}{E_0}) \quad (5.33)$$

and by integrating Eq. 5.31 over all the emitted photon energies, we find the total bremsstrahlung cross section σ_{tot} for an Al target ($Z = 13$). Then the total number of bremsstrahlung γ's is

$$N_\gamma = \sigma_{tot}\, \rho_0\, d\, N_e \quad (5.34)$$

where $\rho_0 = 6.03 \times 10^{22}$ cm^{-3} is the density of the Al nuclei, d is the thickness of the foil which was mentioned earlier to be 50 μm, and $N_e = 7 \times 10^9$ is the number of the incident electrons. A bremsstrahlung spectrum, where the parameters given above are used, is shown in Fig. 5.7. During the calibration runs, CCM1 measures the number of forward γ's and returns some number of ADC counts. From the expression in Eq. 5.34 we know how many bremsstrahlung γ's we expect. We can then plot the number of bremsstrahlung γ's as a function of the recorded ADC counts and from their correlation extract the calibration curve. For the case of the 46.6 GeV electron beam the calibration function can be found to have the form:

$$N_{Compton} = 1.83 \times 10^3 \times (CCM1 + 42 + D) \quad \text{where } D = 2 - \frac{480}{CCM1 + 10} \quad (5.35)$$

Here $CCM1$ stands for the number of the ADC counts recorded by the CCM1 counter during each calibration run event. For ADC values greater than 4000, which is the

saturation point of the counter, the attenuated data are used. The only thing that changes is the scaling factor in front of Eq. 5.35, which is now reduced by 5.5% to become 1.73×10^3 [1]. For the 49.1 GeV data sample, the resulting calibration differs from the one derived for the 46.6 GeV data, by less than 1% and therefore is ignored.

Once we have the direct calibration of the CCM1 counter, we can use it to cross calibrate the two electron counters EC31 and EC37. Some important issues need to be taken into consideration. The EC37 signal is split during run 15175. After run 15404 one collimator in the γ line is removed. Finally the EC31 counter becomes active only after run 15188. The results of the cross calibration of the two electron counters are summarized below [55]:

EC37 : Replace $CCM1$ in Eq. 5.35 by :

Before 15175 :	$(EC37 + 2) \times 2.27$
15175 to 15404 :	$(EC37 + 25) \times 4.85$
Until 49.1 GeV :	$(EC37 + 27) \times 5.12$
49.1 GeV :	$(EC37 + 40) \times 7.21$

$$(5.36)$$

EC31 : Replace $CCM1$ in Eq. 5.35 by :

15188 to 15404 :	$(EC31 - 0) \times 1.58$
Until 49.1 GeV :	$(EC31 - 0) \times 1.68$
49.1 GeV :	$(EC31 + 20) \times 1.81$

During the data analysis described in the next chapter, the average of the signals from the two monitors EC31 and EC37, is used as a measure of the linear Compton rates. A rough estimate of their signal error can be made by looking at the fluctuations of the two monitor readouts for the same data event. The difference of the signals of the two monitors is shown in the top left plot in Fig. 5.8 for the case of the 46.6 GeV electron beam. A Gaussian fit returns a $\sigma = 0.19 \times 10^6$. The 49.1 GeV case is basically the same, with the only exception that the Gaussian fit gives $\sigma = 0.21 \times 10^6$. The two electron counters track each other very well, with $< 2\%$ inaccuracy.

---

[1] We have obviously scaled the attenuated data up by a factor of 10 first.
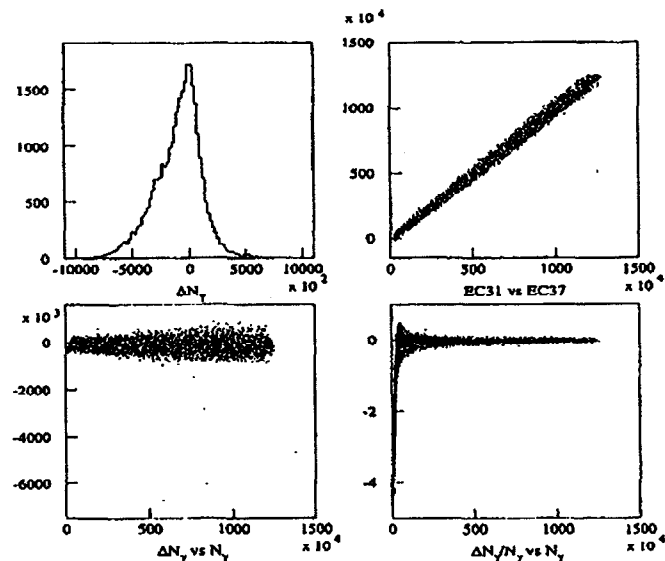
Figure 5.8: Error estimate for the two main linear monitors EC37 and EC31 for a 46.6 GeV electron beam. The top left plot shows the difference of the signals of the two monitors which can be used as an error for their average signal. The top right plot shows the correlation of the two monitors. It is clear that the two linear monitors track each other very well, in fact with a < 2% inaccuracy. The bottom left signal shows the dependence of the difference between the signals of the two linear monitors, on their average signal. As it is expected it broadens as the γ flux increases. Finally the bottom right plot shows the relative error of the linear monitors as a function of their signal. It is fairly stable with the exception of very low values and is in general less than 1%.

5.3   Nonlinear Monitors

5.3.1   Nonlinear Monitor Description

The two nonlinear monitors have a design very similar to the one described for the linear counters. They are gas Čerenkov detectors using ethylene instead of air. The Čerenkov volume cross section at the point where it intercepts the nonlinear Compton

scattered electrons is 19 mm × 19 mm. As the electrons traverse the gas volume they emit Čerenkov light, which in turn is deflected by a 45° mirror made of polished Al towards the photomultiplier tube. Two baffles with progressively increasing cross sections are placed within a distance of 4 in. from each other in order to ensure the collection of light only within a 2° solid angle. Again this results to the PMT being placed at some distance from the electron beam, allowing for some lead shielding to be used in order to reduce the background levels. The high voltages for which the PMT is tested in the lab, are shown in table 5.5 along with their corresponding gains. The first 20 cm of the light pipe is painted flat black, while beyond that the walls are made highly reflective by using aluminized Mylar. A filter of Al with a regular pattern of 64 holes, can be used for a 23% signal attenuation to avoid saturation of the counters. The above design is common for both the N2 and N3 monitors. The two counters are placed in front of the electron calorimeter (ECAL) in order to ensure their accurate calibration.

5.3.2   Monitor Calibration

The two nonlinear monitors are positioned in such a way so that they intercept electrons from second and third order Compton scattering only. The signals from these two detectors are extremely useful in deriving the laser intensity parameter η. Thus the calibration of the two monitors is very important and was done by using a test beam a few days earlier than the actual data run. The test beam contains very few electrons in each bunch (up to 1000) and has low quality emittance and spot size. It is extracted parasitically at the end of the linac from the main electron beam which is used elsewhere. The electron energy can be controlled fairly accurately and the off momentum particles are removed by using the momentum slits at the beginning of the FFTB line. Only electrons within a specific momentum range, which are bent by the dipoles in the E-144 spectrometer, will hit the two counters. Behind them we place the electron calorimeter (ECAL), which has a well known calibration and which can

give us the number of electrons intercepted by the two monitors. Essentially the two counters are cross-calibrated with ECAL. We need two runs to calibrate independently the N2 and N3 monitors and these are the runs 15017 and 15009 respectively. During those two runs the electron beam energy is changed by 0.1 GeV steps every 500 events. Therefore we can estimate the energy of the electrons that hit the two counters from their respective event number as follows:

$$E = \frac{evnr}{500} \times 0.1 + E_{init} \qquad (5.37)$$

The energy units are GeV, $evnr$ is the current event number and E_{init} is the starting electron beam energy. The main characteristics of the two calibration runs are summarized in table 5.4.

Row Number	Run 15009 (N3 Calibration) 7.8–9.8 GeV		Run 15017 (N2 Calibration) 11.5–13.8 GeV	
	Row Center p(GeV)	Row dp (GeV)	Row Center p(GeV)	Row dp (GeV)
1	9.891	1.150	12.425	1.566
2	8.835	0.979	10.965	1.332
3	7.920	0.843	9.754	1.129
4	7.133	0.741	8.717	1.960

Table 5.4: The momenta at the centers of the top four rows of ECAL and the momentum acceptances of the same rows for the two nonlinear monitor calibration runs 15009 and 15017. The energy ranges of the electron beam are shown at the beginning of the table.

Fig. 5.9 and Fig. 5.10 show the results of the calibration runs. The top plots in each of the two figures show the number of ADC counts recorded by each monitor divided by the corresponding number of electrons that hit ECAL. This reduces the effects of the electron beam instabilities, and shows directly the acceptances of the two counters. The triangular shape of the acceptances shown in these two figures
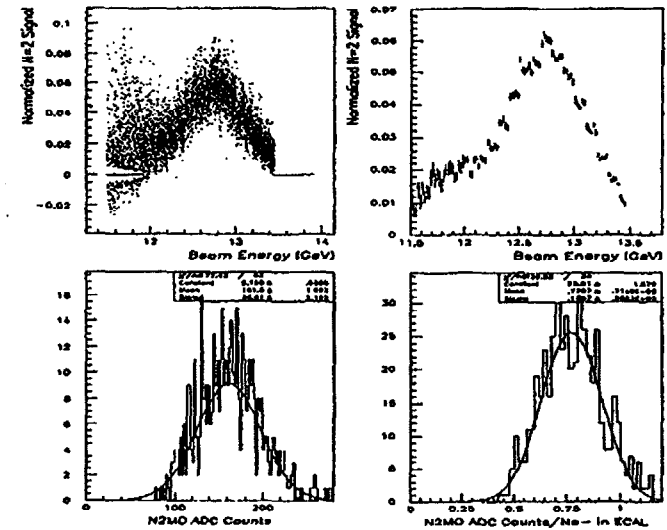
Figure 5.9: Plots from the calibration of the N2 monitor. The top plots show the acceptance of the monitor as a function of different energy electron beams directly hitting the counter. The number of ADC counts recorded by the monitor is normalized to the number of electrons detected by ECAL so that we can reduce the effects of any instabilities of the electron beam. The bottom left plot shows the distribution of the ADC counts for the N2 monitor and the bottom right the distribution of the same ADC counts normalized to the number of electrons recorded by ECAL. Both plots are used for the estimate of the error in the N2 signal as explained in the text.

is consistent with an energy jitter of the electron beam of the order of 200MeV. The whole acceptance analysis described above is valid for the case of a 46.6 GeV electron beam. For 49.1 GeV electron beam we expect these acceptances to change. As mentioned earlier in section 3.5 the strength of the soft bending magnets around the interaction point had to be increased in order to accommodate for the overall increase of the electron beam energy. That means that electrons of the same energy as in the 46.6 GeV case will be bent more and therefore the acceptances of the two
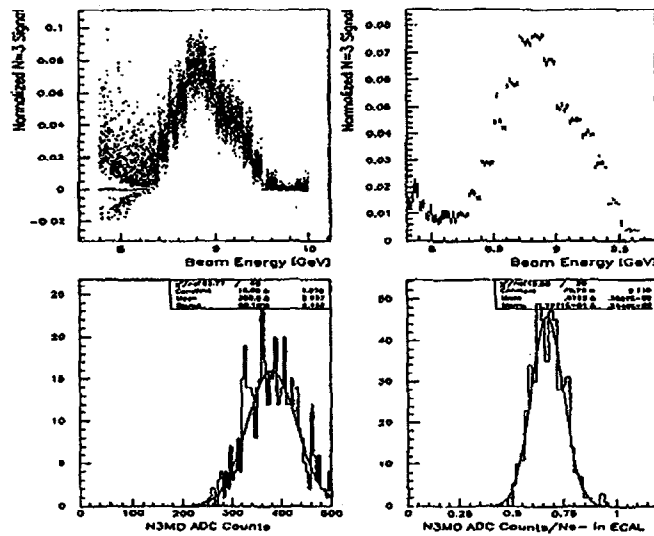
Figure 5.10: Plots from the calibration of the N3 monitor. The top plots show the acceptance of the monitor as a function of different energy electron beams directly hitting the counter. The number of ADC counts recorded by the monitor is normalized to the number of electrons detected by ECAL so that we can reduce the effects of any instabilities of the electron beam. The bottom left plot shows the distribution of the ADC counts for the N3 monitor and the bottom right the distribution of the same ADC counts normalized to the number of electrons recorded by ECAL. Both plots are used for the estimate of the error in the N3 signal as explained in the text.

nonlinear monitors will shift to higher energies. We can find the new acceptances for the 49.1 GeV case once we know the 46.6 GeV acceptances, by using the momentum maps for both energies. Here are the steps that we need to follow:

1. For each energy within the 46.6 GeV acceptance, use the 46.6 GeV momentum map to find the corresponding y-position of the electrons with respect to the path that they would have followed if there were no bending involved at all.

2. For this y-position found in the previous step, use the 49.1 GeV map to find

the corresponding energy and thus construct the new acceptance range.

The above procedure is valid since the two monitors are kept always in the same position. The results for both the 46.6 and the 49.1 GeV electron beam energies are
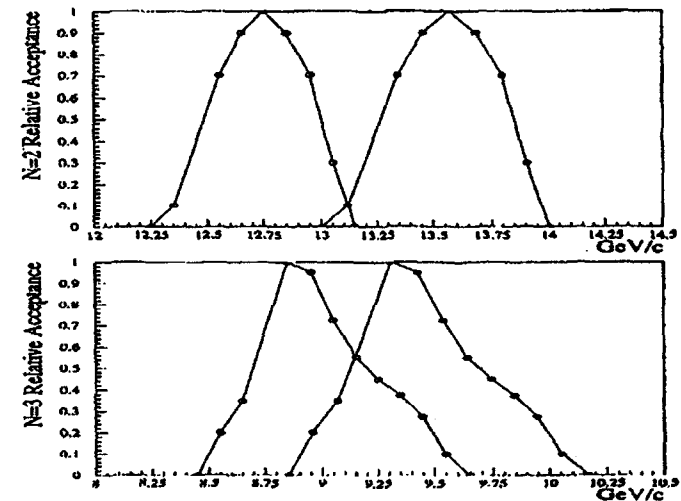
Figure 5.11: Relative acceptances of the N2,N3 monitors based on the plots shown in Fig. 5.9 and 5.10 for the 46.6 GeV cases and on the momentum map for the 49.1 GeV case. The white circles refer to the 46.6 GeV acceptance and the black circles to the 49.1 GeV acceptance. The top plot shows the N2 monitor acceptances and the bottom the N3 monitor acceptances. It is clear that the 49.1 GeV acceptances have shifted to higher energies as expected.

shown in Fig. 5.11. Fig. 5.12, shows the acceptances of the two nonlinear monitors with respect to the Compton scattered electron spectrum for the case of a 46.6 GeV incident electron beam.

Returning to the calibration of the two monitors, there is still some more information that we need to derive. First we need to find the number of electrons that correspond to each ADC count recorded by the two monitors. The bottom left plots
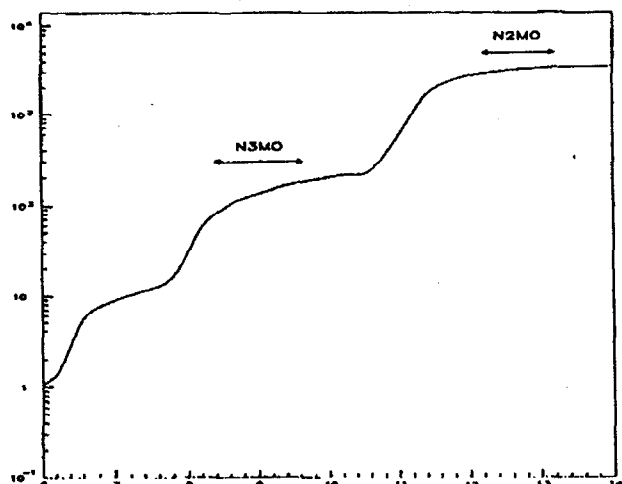
Figure 5.12: The positions of the two nonlinear monitors with respect to the $N2$ and $N3$ electron spectra. The arrows indicate the acceptances of the two monitors. It is clear that the N3 monitor is almost on the edge of the $N3$ electrons plateau.

in Fig. 5.9 and Fig. 5.10 show the distribution of the ADC counts reported by the two counters that correspond to the energy of the peak acceptance. Let's concentrate on the N2 monitor for the moment, since we can follow the same steps in the case of the N3 monitor later. From the bottom left plot in Fig. 5.9, we see that the distribution of the ADC counts follows a Gaussian with a mean of $\sim$ 160 counts. These correspond to 256 e^- detected by ECAL, or to 1.6 e^- per ADC count. The high voltage setting during the calibration is 1.7 kV, while during the actual data runs this changes to 1.4 kV and there is in addition a 23% optical attenuation. Therefore a correction factor of 19.4, as table 5.5 that shows the high voltage settings and the corresponding correction factors implies, needs to be used. This brings the number of e^- per ADC count to $\sim$ 31. If we now fold in the $n=2$ spectrum and the geometrical acceptance of the N2 monitor for this spectrum, this number scales even higher and becomes $\sim$

H.V.	N=2 Monitor		N=3 Monitor	
kV	Correction Factor Attn. IN	Correction Factor Attn. OUT	Correction Factor Attn. IN	Correction Factor Attn. OUT
1.0	303.00	69.70	199.60	45.90
1.1	139.40	32.10	91.50	21.00
1.2	69.70	16.00	44.80	10.30
1.3	36.00	8.29	22.40	5.15
1.4	19.40	4.45	12.50	2.89
1.5	11.30	2.60	7.20	1.66
1.6	6.97	1.60	4.35	1.00
1.7	4.35	1.00	2.68	0.62
1.8	2.94	0.68	1.76	0.40

Table 5.5: High voltage settings with and without attenuation and their corresponding correction factors to be used with the nonlinear monitor calibration.

49 e^- per ADC count. [2] Similarly, in the case of the N3 monitor we have from the ADC counts distribution shown in the bottom left plot in Fig. 5.10 a mean of 380 ADC counts. These again correspond to 570 e^- detected by ECAL. The high voltage setting during the calibration was 1.6 kV, while during the data run was shifted to 1.7 kV. Therefore the correction factor that we need to apply from table 5.5, is 0.616 and this brings the number of e^- per ADC counts down to $\sim$ 0.9. Again folding the $n=3$ spectrum and the geometrical acceptance of the N3 monitor in, we get finally 1.8 e^- per ADC count.

We would also like to estimate the relative errors on the signals of the two monitors. We look again at the bottom plots in Fig. 5.9 and Fig. 5.10, and once more let's

[2]This last step was not done initially with the result that the whole data analysis used the conversion factor of 31 e^- per ADC count. Since the result is a simple change of the scaling factor for the overall $N2$ signal used as an input to the constrained fit algorithm, the analysis was not modified. See also the note in section 6.3.6.

concentrate on the N2 monitor. As mentioned earlier, the distribution of the ADC counts at the energy of the peak acceptance, has a mean of 160 counts. From the bottom right plot in Fig. 5.9, which shows the distribution of the same ADC counts normalized this time to the number of electrons detected by ECAL, we find by fitting a Gaussian, that the relative RMS error is $\sim$ 19%. Recalling that the calibration high voltage setting was 1.7 kV, while during the actual data runs was set at 1.4 kV, we get by looking in table 5.5 a correction factor of 4.45. So therefore we can write:

$$\Delta ADC/ADC = (\frac{160}{4.45 \times ADC})^{1/2} \times 0.19 = 1.13/ADC^{1/2} \qquad (5.38)$$

In the case of the N3 monitor, we look at the two plots in Fig. 5.10 and follow the same steps again. The mean of the ADC counts is $\sim$ 380 and the fluctuations at peak acceptance $\sim$ 11.5%. The calibration of the N3 monitor is done with a high voltage setting of 1.6 kV, while the data runs were at 1.7 kV. The correction factor in this case will be 0.616 and so we can write for the N3 relative signal error:

$$\Delta ADC/ADC = (\frac{380}{0.616 \times ADC})^{1/2} \times 0.115 = 2.86/ADC^{1/2} \qquad (5.39)$$

From design considerations we would expect the ratio of the two constants in the error expressions of the two monitors to be $\sim$ 2.

5.3.3 Dropout Cleanup

If we plot the ADC signal from the two nonlinear monitors vs. the number of γ's produced by linear Compton scattering (as detected by the linear monitor), we see a long line of events for which the two nonlinear monitors do not report any signal although the linear counter does. This is shown in Fig. 5.13. A study of the distribution of the time differences between subsequent laser ON or laser OFF events, shows that this is a trigger misinterpretation problem. Fig. 5.14 shows the distribution of the relative time delays between subsequent events, for both the laser ON and the laser OFF data. The way that the data acquisition system is set up, within the time
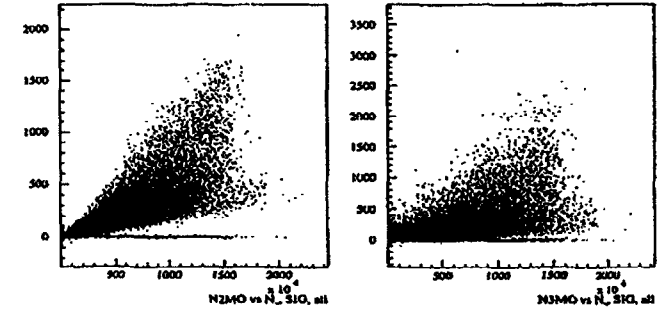
Figure 5.13: Distribution of the event signal for the N2 (left) and the N3 (right) monitors in conjunction to the corresponding linear monitor signal. There is a significant number of events for which the two monitors seem not to return any signal at all.

interval of two laser ON events, which are separated by 2000 ms from each other, two laser OFF (background) events are acquired, separated from each other by a time interval of 1600 ms. As a result laser ON events should be separated by laser OFF events before them by 200 ms. This is not the case for a considerable number of laser ON triggers, as we can see from the bottom plot of Fig. 5.14. The events on the right are clearly laser OFF events that were confused as laser ON. These events are common to the N2 and N3 monitors, since they both have the same readout. We can discard those by selecting the time difference of a laser ON event with respect to the two laser OFF events before and after it, to be somewhere between 150 ms and 250 ms. This immediately fixes the problem as Fig. 5.15 shows. After this selection, which we call the dropout cut, we loose about 5000 laser on events, or $\sim$ 8% of the whole data sample.

One more interesting thing we can see from the middle plot in Fig. 5.14, is that there are laser ON events that are confused as laser OFF events. These are the events at the very far right hand side of the distribution, with relative time delay from the preceding event, greater than 1700 ms. Again in principle the laser OFF events should
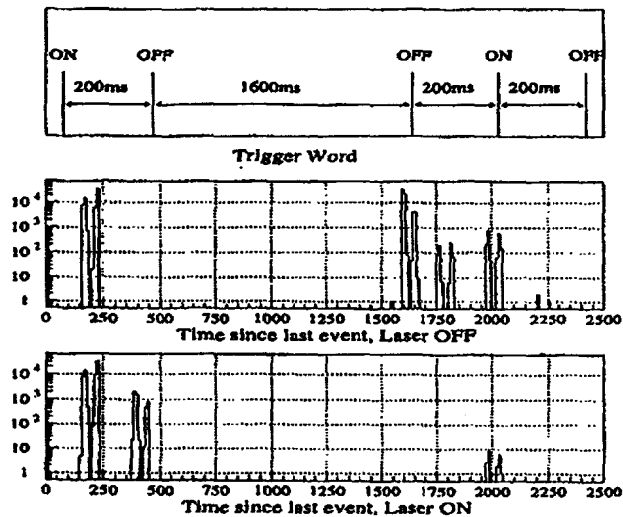
Figure 5.14: Distribution of the relative time delays in ms, between subsequent events for both laser ON (third plot) and laser OFF triggers (second plot). The top plot shows the trigger scheme for the data acquisition. The laser fires every 2 seconds and therefore this is the time difference between two consecutive laser ON events. The data acquisition system though, acquires data three times during this time interval, one laser ON event and two laser OFF (background) events, with the order and time intervals shown here.

be characterized by time differences from the event acquired earlier than them of 200 ms, or at most 1600 ms. We need to discard also these false laser OFF events by keeping only the ones that are below the 1700 ms threshold. In this way we lose 2700 laser OFF events, or $\sim 2\%$ of the whole data sample.
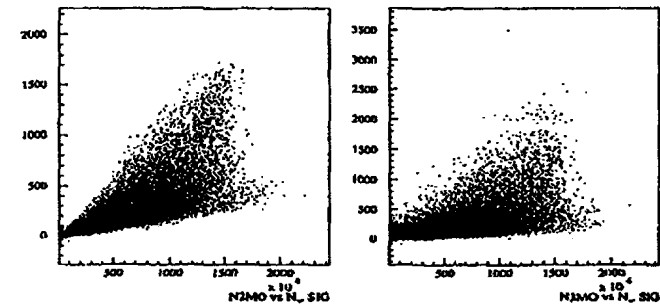
Figure 5.15: Distribution of the event signal for the N2 (left) and the N3 (right) monitors again with respect to the linear monitor signal after cleaning up all the dropout events.

Chapter 6

46.6 GeV Data Analysis

In the previous three chapters a detailed description of the experimental apparatus has been given. In appendix 3 a brief report on the results of the analysis of the nonlinear Compton data, is also given. In this chapter we will concentrate on the analysis of the positron data, which were the main goal of the August 1996 data run. Fig. 6.1, shows the experimental setup. A high energy electron enters a high
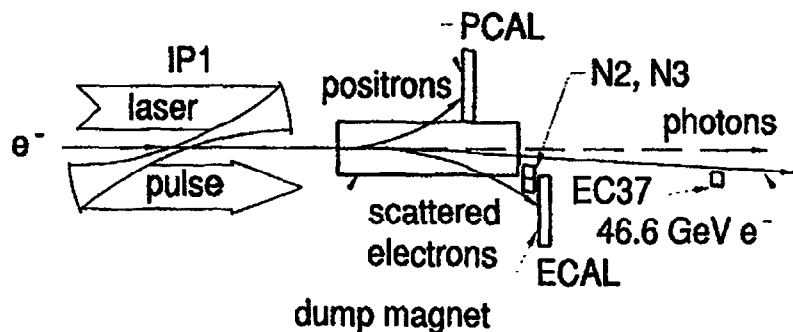
Figure 6.1: Schematic of the experimental setup used for the collection of positron production data.

intensity laser field produced by a tightly focused laser pulse and undergoes a two-step process. During the first step the electron Compton scatters (linearly or nonlinearly)

off the laser photons and gives rise to a high energy gamma. Then during the second step and while the gamma is still inside the intense laser field, the produced gamma absorbs a number of additional laser photons (in most cases four), and produces an e^+e^- pair. The produced positrons are deflected by the bending magnets downstream the laser-electron interaction region (IP), towards the positron calorimeter (PCAL). Due to the rarity of this two-step process (about one positron produced in every 1000 laser pulses), the backgrounds in PCAL need to be kept sufficiently low, so that such a produced positron to be clearly observed. In the same way the electron of the pair will be deflected towards the electron calorimeter (ECAL). But this pair electron will be "lost" in the multitude of nonlinear Compton scattered electrons of various orders, that hit ECAL at the same time. Therefore, PCAL becomes the primary detector for the observation of such a process.

The response of PCAL to a positron signal produced at the IP is studied by inserting a wire into the path of the electron beam at the interaction region, to produced e^+e^- pairs by the Bethe-Heitler conversion of bremsstrahlung photons. This calibration data are used to develop an algorithm that groups PCAL cells where energy is deposited, into clusters associated with a candidate positron event. These clusters are characterized by their positions in the horizontal and vertical direction, and also by the total deposited energy. Using the field maps of the bending magnets around and downstream of the IP, the vertical position can be translated into the momentum of the candidate positron event. Once this cluster search algorithm has been developed, it can be applied to the real positron data. A series of selection criteria need also to be introduced to ensure optimal signal selection (laser induced positrons) and background (non laser induced positrons) rejection. For the selected positron events, their momentum spectrum can then be reconstructed. These steps are the subject of the first two sections of this chapter. It is of paramount importance to correlate the positron yield to the laser intensity, which is represented in a unique way by the parameter η, as defined in chapter 2, not least because it provides us with

a way of directly comparing the data to the theory predictions. The reconstruction of the parameter η, in an unambiguous way using the N1, N2, N3 monitors, is the main subject of the third section in this chapter. Although we will reserve the final comparisons to the theory for chapter 8, some necessary corrections to the simulation predictions (for a description of the simulation itself see Appendix. A), and also a discussion of background levels, is also given in the last section of this chapter. Two positron data samples were taken using electron beams with 46.6 GeV and 49.1 GeV energies. This chapter is dedicated to the 46.6 GeV data sample, while the 49.1 GeV data are presented in the following chapter. The final conclusions are presented in chapter 8.

6.1   Cluster Search Algorithm

The principal positron detector of our experiment is a silicon calorimeter which is called PCAL. It consists of 8 rows, each 16 mm wide, arranged into two 4-row groups separated by a gap of 1.5 mm, and distributed in 4 columns and 4 longitudinal segments 16 mm wide each (Fig. 5.1 shows a picture of PCAL). A set of permanent bending magnets in front of the detector, is used to bend the produced positrons—as well as the background positrons which are mainly due to scrapping of the electron beam on the walls of the accelerator pipe— on to the detector, as described in section 5.1.2 of the previous chapter. The momentum map of PCAL (see section 5.1.2), can be used to directly correlate the impact position on PCAL and the momentum of the incident positron. The positron energy can be measured in principle from the amount of energy deposited on the active silicon of the detector. Due to energy leaks into adjacent rows, the incident positron energy is not deposited entirely on the row of the main impact on PCAL. There is therefore a cluster of rows associated with every detected positron in terms of the measured energy, and this needs to be taken into account in order to correctly reconstruct both the energy and the exact impact

position on PCAL of the incident positron. This is the main aim of the cluster search algorithm described in this section.
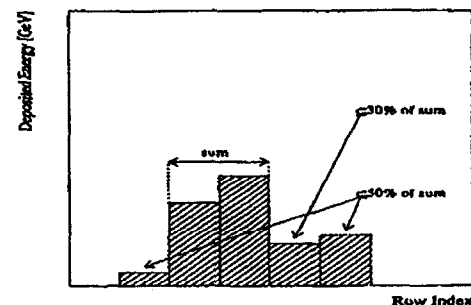
Figure 6.2: Requirements for an examined cluster to be accepted as a real positron hit.

As it is clear from the above, finding the correct cluster of PCAL rows to associate with the detected positron event, is the first and most important step in the algorithm. For each PCAL row a 5-row range is defined consisting of the current row we are looking at and its two closest neighbors on each side. First we need to make sure that the row energy is maximum within the specified range, i.e. that indeed the examined cluster hit the detector somewhere within this row. Once this is verified the row index of the immediately neighboring row with the second highest deposited energy is found and the total energy of those two rows is computed. In order to make sure that we have a well defined cluster in space, we require that the other adjacent row has no more than 30% of the total energy of the two rows mentioned above and that any of the other two further away rows do not contain more than 50% of the total energy, as shown in Fig. 6.2. Then the spatial extend of the examined cluster is redefined using the three center rows out of the initial 5-row selection. Two additional criteria are also checked, mainly that the current cluster does not contain less than 0.4 hits (upper limit of noise fluctuations) and that the specific event does not contain more

than 3 clusters, which in principle should be the case as long as all the previous requirements have been fulfilled (PCAL has only 8 rows and we assign three to every cluster).

Once we have made sure that we have found a real cluster we can go on and reconstruct its energy and vertical position, the latter with respect to the bottom of PCAL. The total energy of the cluster is simply the sum of the energies of the three contributing rows. The situation is a little more complicated for the cluster y position. As we have seen, each cluster consists of three rows and the center row is always the one with the highest deposited energy. There is an exception to this rule, mainly in the case where the peak energy row coincides with the top or bottom row of PCAL, in which case we have only two rows within the cluster. In the case of the 3-row cluster we can always assign as the cluster's y position the middle of the middle row. This is obviously an oversimplified solution which does not take into account the fact that the deposited energy is not necessarily equally distributed within the two neighboring rows, which implies that the incident positron hit closer to the adjacent row with the largest amount of leaked energy. We need therefore to assign a y position to the cluster in such a way that although it remains within the middle row, it is nevertheless closer to the neighbor with the second highest deposited energy. This is achieved by taking the natural logarithm of the ratio of the energy of the second highest row over the energy of the peak row and shift the y position around the middle of the peak row by an amount proportional to that ratio. If this ratio though, is smaller than ~15% *i.e.* the biggest part of the energy is concentrated in the middle row, this method is not so accurate any more. In cases like this the logarithm of the ratio of the energies in the two neighboring rows is used to weigh the cluster position. Only even when this second ratio drops below ~7%, in which case almost the whole cluster energy is within the boundaries of the middle row, the cluster's position is assigned at the middle of the peak row. This is illustrated in Fig. 6.3, where a relation between the natural logarithm of the energy ratios and the
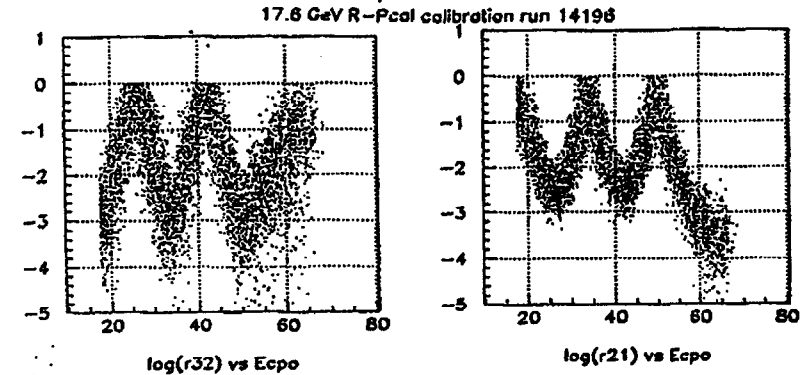
Figure 6.3: Natural logarithms of the ratios of the row with the second highest energy over the peak energy row(r21), and the energy ratios of the two neighboring the peak rows (r32), as a function of PCAL position in mm.

position of PCAL is shown. The inverse slope of the lines shown, is used to adjust the cluster's position closer to the highest energy neighbor. The data were taken using a 17.6 GeV electron beam and moving PCAL vertically. The same procedure is applied for the 2-row clusters with the exception that now the lower limit of the energy ratio can drop down to ~2%. The horizontal position of the cluster with respect to the center of PCAL is also reconstructed using the same method.

A number of other interesting cluster properties are also calculated; namely the fraction of the energy in each longitudinal segment, the total energy in the outer pads, the energy ratio of the left center pad over the sum of both center pads and the width of the cluster in the y and x directions. Special ntuple variables are assigned to each of the calculated above cluster properties to be used in the subsequent data analysis. The cluster search algorithm is completely independent of the energy of the incoming electron beam and therefore can be used simultaneously for both the 46.6 and the 49.1 GeV data samples. The efficiency of the cluster search algorithm will be discussed in a later section.

6.2   46.6 GeV Positron Search

6.2.1   Cluster Selection Cuts

Not all the reconstructed clusters are used in the analysis. Specific selection criteria are applied for the purpose of excluding as many as possible of the background clusters (positrons that hit PCAL but not produced in laser-electron interactions). At first the whole analysis is concentrated on events that contain at most a single hit, or in other words, the ratio of the cluster energy over the nominal momentum (from the momentum map) that corresponds to the vertical position of the cluster on PCAL, should be around 1 ($E_{clu}/p_{clu} = 1$). Due to leakages of the deposited positron energy on PCAL into adjacent rows, but primarily due to resolution limits in the reconstruction of the cluster's vertical position, we expect a Gaussian distribution of the single hit clusters around 1. In order to tune our positron selection criteria for optimal results, we need large enough positron statistics to work with. The data from the
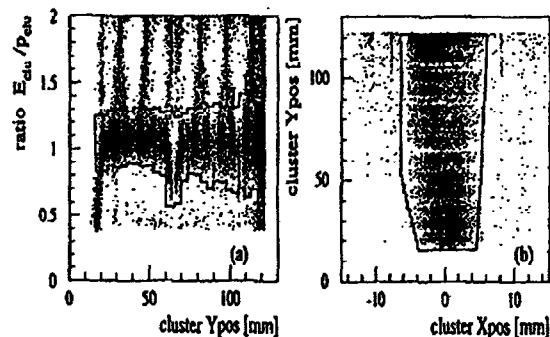
Figure 6.4: Calibration cluster hits and x-position distributions. The lines indicate a $\pm 3\sigma$ and $\pm 1.2\sigma$ selection as discussed in text.

laser-electron interactions do not provide sufficiently large positron rates. During the 46.6 GeV running period, a large sample of calibration data was taken by inserting at the interaction point a thin 20 μm aluminum wire, and thus producing positrons that

hit PCAL through the bremsstrahlung process. The number of positrons produced in this way is fairly big, and these data can be used to check the distribution of the ratio E_{clu}/p_{clu} with the cluster vertical position in PCAL, and also the distribution of the horizontal position of the cluster within PCAL. These two distributions provide the main positron data selection mechanisms, and are shown in Fig 6.4 for the calibration data sample.
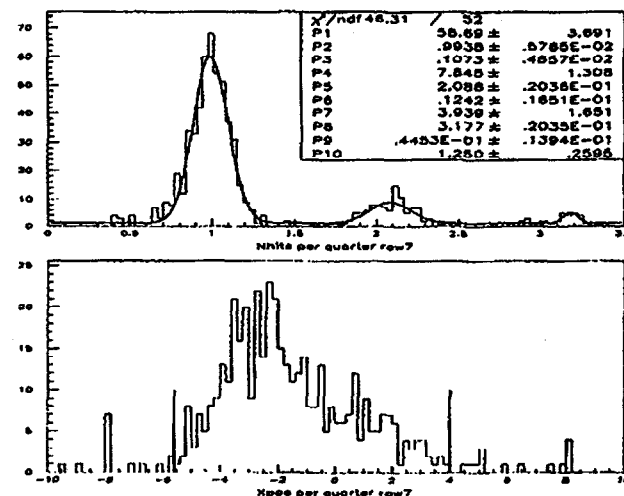
Figure 6.5: Calibration cluster hits and x-position distributions for the seventh quarter row of PCAL starting from the bottom.

It is clear that these distributions depend strongly on the vertical position within PCAL. For example the width of the number of hits distribution around 1, increases as we move higher in PCAL. This is because the higher rows in the detector look at lower energy positrons and the resolution of both the energy and position reconstruction becomes worse. This can also be seen in the horizontal position distribution which becomes narrower for lower PCAL rows. The gap in the middle of both plots

corresponds to the 1.5 mm gap at the end of the fourth row of PCAL. The bands that are discernible especially at the distribution of the number of hits, correspond to the individual PCAL rows. The bottom row does not show any signal because it is completely shielded by the vacuum chamber wall around the beamline. Looking at Fig. 6.4 we reach the conclusion that our selection of a cluster sample for further analysis, based on the single hit requirement and possibly on the horizontal position, must be row dependent. It must also take into account the gap at the end of the fourth row.

By slicing the first plot in Fig. 6.4 into 32 quarter rows along the horizontal axis starting from the left, and projecting them on the vertical axis, we get the distribution of the number of hits for each quarter row. As an example, the distribution of 1, 2, 3 hit clusters in the seventh quarter row, is shown in the left plot of Fig. 6.5. Each is fitted with a Gaussian plus an offset and the σ of the result gives as an estimate of the width of the distribution in that particular quarter. The closed line shown in Fig. 6.4 marks an area $\pm 3\sigma$ wide in the vertical direction around the 1 hit distribution. It can be seen that it becomes wider as we are moving higher in PCAL and that it also follows the gap pretty nicely.

The bottom plot in Fig. 6.5 shows the x-position distribution of the single hit clusters within the range of $\pm 3\sigma$, again for the seventh quarter row. Here we cannot fit a Gaussian any more, but we can still get an upper and lower bound at the points where $\sim 3\%$ of the distribution is excluded. This is what the two vertical lines in the plot show. In this way we can define again a σ as being the half of the total range defined by those two bounds. By repeating this for all the quarter rows, we create a line like the one shown in the second plot of Fig. 6.4. The actual width of that particular line is $\pm 1.2\sigma$ for reasons that will become apparent a little later.

6.2.2   Cluster Selection Cuts Tuning

In the previous section we saw how we can use the calibration data to introduce a positron data selection based on the hit and the x-position distributions, that is row dependent and also takes into account the 1.5 mm gap at the end of the fourth row of PCAL. We are in a position now of applying this selection mechanism to the real positron data produced by laser-electron interactions. It is also interesting to know how our data sample responds to different tuning of the 1 hit cluster and the x-position selection ranges. Three are the quantities of interest here: First, the number of the detected positrons itself. Second, the statistical significance of the positron signal, which is defined as the ratio of the number of positrons found, over their respective error. Third, the signal to noise ratio defined as the ratio of the number of laser ON positrons over the number of laser OFF positrons. As already mentioned in chapter 1, the data acquisition system collects data not only when there is a laser pulse that interacts with the electron beam (laser ON triggers), but also when there is no laser pulse available (laser OFF triggers), in order to measure electron beam induced background levels. In fact twice as many laser OFF than laser ON data are collected this way, and therefore when we calculate the signal to noise ratio, the number of laser OFF positrons has to be scaled down by the ratio of the laser OFF over the laser ON triggers. We will refer to the laser OFF positrons as the background positrons and to the laser ON as the signal positrons, very often in this chapter. Every time that a new positron selection requirement is introduced (first the 1 hit cluster selection range, then the x-position selection range), we expect both the statistical significance and the signal to noise ratio to improve, since more background positrons are discarded (we may loose some signal positrons too, but the background reduction will be more pronounced). Further tuning of each individual selection range itself, will further optimize the signal. In fact, the areas shown in Fig. 6.4 are the results of such a tuning. In the case of the single hit distribution, different ranges in units of the Gaussian σ around the center of the fitted Gaussian in each quarter row and for
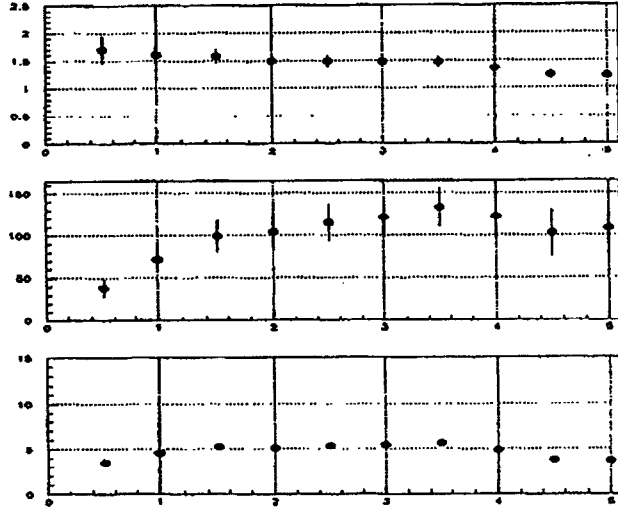
Figure 6.6: Ratio of signal to noise, number of positrons and statistical significance as a function of single hit cluster range in units of σ.

all quarter rows are tried. In the case of the x-position distribution the end points are moved closer or further away from each other in a symmetric way, σ being still defined as half of the resulting range and expressed in units of the original σ that is defined in the last paragraph of section 6.2.1.

The results of such a tuning are shown in Fig. 6.6 for the single hit range, and in Fig. 6.7 for the x-position range. The first plot in both figures shows the ratio of signal positrons over background positrons—the latter being scaled down by the appropriate ratio of the laser ON over the laser OFF triggers which is approximately 2—as a function of the selection range in units of σ, as it is defined in section 6.2.1. The errors on this ratio are estimated using the formula

$$\delta R = \sqrt{\frac{S}{a^2 B^2} \left(1 + \frac{S}{B}\right)} \qquad (6.1)$$
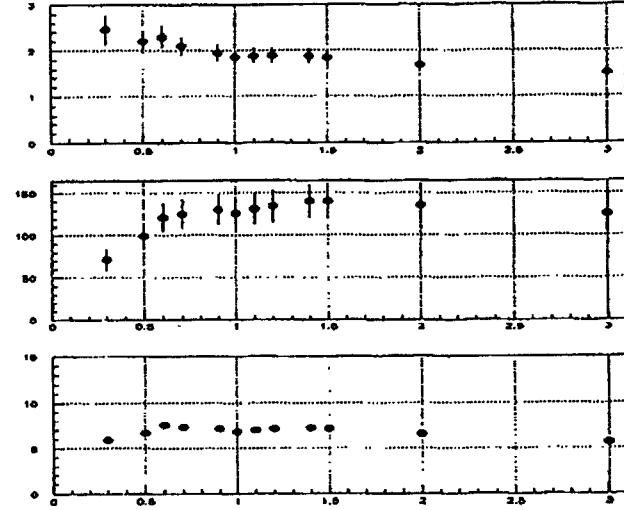
Figure 6.7: Ratio of signal to noise, number of positrons and statistical significance as a function of cluster x-position selection range in units of σ as defined in text.

where S the number of laser ON positrons, B the number of laser OFF positrons and a the scaling factor according to trigger ratio as mentioned earlier. The second plot shows the number of positrons after background subtraction as a function of the selection range. The background is subtracted by using the expression

$$N = S - aB \qquad (6.2)$$

and the error on the number of positrons by

$$\delta N = \sqrt{S + a^2 B} \qquad (6.3)$$

where the symbols are the same as before. Finally the third plot shows the statistical significance i.e. the ratio of the background subtracted positrons over their corresponding error as defined in Eq. 6.2 and 6.3 respectively.
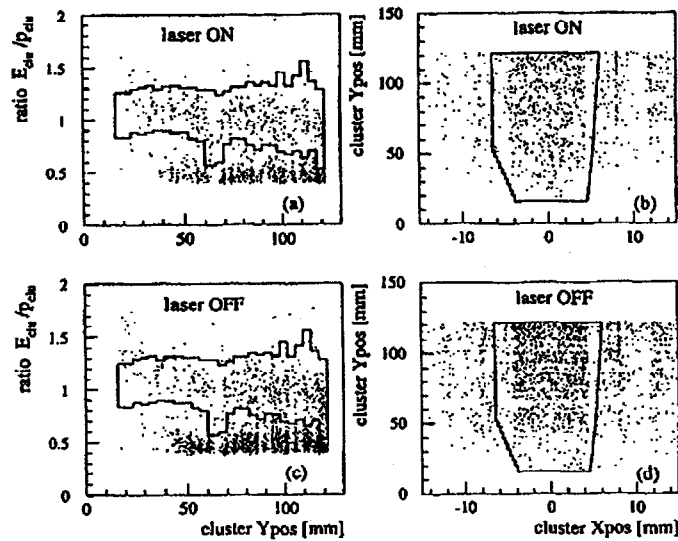
Figure 6.8: Data clusters selection ranges. Laser ON are the events that the laser fired, while laser OFF the events without a laser beam. The plots on the left in both cases show the single hit selection range at $\pm 3\sigma$ and the plots on the right the x-position range at $\pm 1.2\sigma$.

In the case of the single hit selection range the best results are achieved with a range of $\pm 3\sigma$. Although the signal to noise ratio seems to be better for a smaller range, the number of positrons on the other hand is much smaller, which means that besides throwing away the background, we are cutting most of the signal too. For big ranges the signal to noise ratio becomes worse while the number of positrons is stable within error. In this case we have essentially included all the signal and by increasing the range we are just adding more background clusters. The x-position tuning was done by keeping the single hit selection range fixed at $\pm 3\sigma$, the optimum value from the previous step. We expect that as the position range becomes more and more loose the signal to noise ratio and the number of positrons will approach the ones found in the previous step. The main justification of this cut is the significant improvement of

the statistical significance of our signal as compared to without using it. A selection of a $\pm 1.2\sigma$ range gives us the best results. In Fig. 6.8 the selected ranges on the real data are shown for both laser ON and laser OFF clusters.

6.2.3 Overlap Cut Tuning. Results

In this section and in the rest of the analysis, with overlap we mean the N=1 overlap. This is defined as the ratio of the number of the measured γ's in the N=1 monitor (for calibration and description of these monitors see chapter 5) over the expected rate from the theory. In principle for perfect space-time overlap of the electron with the laser beam, we expect this ratio to be at most 1. In our data this ratio exceeds
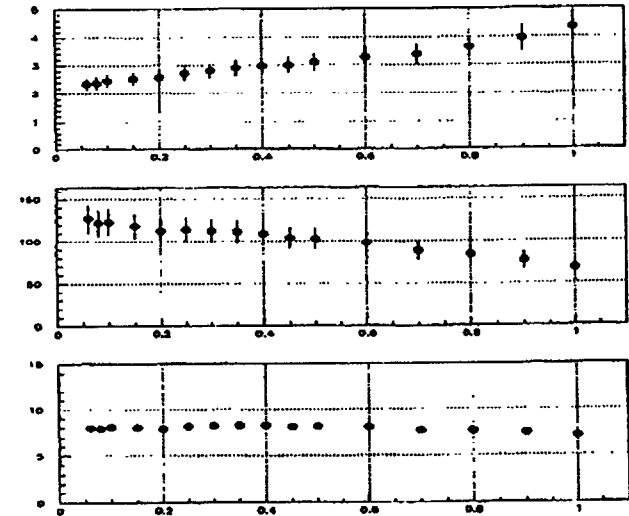
Figure 6.9: Ratio of signal to noise, number of positrons and statistical significance as a function of different N=1 overlap cuts.

1 and reaches values of up to 1.5, which can be explained by a $\sim 10\%$ error in the

calibration constants. High overlap conditions ensure higher probability for positron production at the interaction point and it is natural to introduce a cut of such a form on the laser ON data. Again, this cut was tuned by looking at the familiar by now quantities of the signal to noise ratio, the positron yield and the statistical significance of the signal. These are shown in Fig. 6.9.

As expected, the signal to noise ratio improves every time we implement a higher overlap cut because more and more background positrons are excluded. Of course on the other hand the positron yield reduces simultaneously. More useful in selecting the overlap cut is the statistical significance of the signal. At first we note that there is an overall improvement in this aspect compared to the results that do not include an overlap cut. At the same time we can see that the statistical significance begins to drop at very high overlap cuts. We picked 0.4 as an optimum cut value. The background subtracted positrons and the error bars shown are computed by using Eq. 6.1, 6.2 and 6.3.

46.6 GeV Data Results						
Cut Type	Laser ON	Laser OFF	Trig. Ratio ON/OFF	Sig/Noise	Ne^+	Statistical Significance
Optimal Cuts	21962	121216	0.1812	2.55±0.23	106±14	7.7σ
Loose Cuts	30810	121216	0.2542	2.10±0.17	118±16	7.4σ
Medium Cuts	21962	121216	0.1812	2.73±0.28	93±12	7.4σ
Tight Cuts	17189	121216	0.1418	4.05±0.53	70±10	7.2σ

Table 6.1: Results of the different cut types on the 46.6 GeV data. Although the positron yield is different in each case the statistical significance is the same.

Introducing now the cluster selection criteria, as they were described in section 6.2.2, and also the above overlap cut, we find 106±14 e^+ above background, with a statistical significance of 7.7σ. Three more sets of cuts can also be tried in order to check the signal dependence on the cut selection. These cuts are defined below:

1. "Loose" cuts: Here the single hit range is ±3σ, the x-position range ±1.5σ and the overlap cut set at 0.15.

2. "Medium" cuts: Here the single hit range is ±2σ, the x-position range ±0.9σ and the overlap cut set at 0.4.

3. "Tight" cuts: Here the single hit range is ±1.5σ, the x-position range ±0.6σ and the overlap cut set at 0.6.

The results from the different cut cases are summarized in table 6.1. The fact that independent of the cut selection, the statistical significance stays the same, reassures us that we have a real positron signal.

6.2.4 Positron Momentum Spectra

The momentum spectrum of the produced positrons is shown in Fig. 6.10. In the first plot the momentum spectra of the laser ON and the laser OFF positrons are plotted separately, the laser OFF ones after been scaled down by the ratio of the laser ON over the laser OFF triggers, as it is shown in the first line of table 6.1. The momentum bins have an equal width of 2 GeV/c each. The bottom plot shows dNe^+/dp where dNe^+ is the number of background subtracted positrons per momentum bin and dp the width of the momentum bin, in our case 2 GeV/c. The vertical error bar is calculated using Eq. 6.3 divided by dp. The horizontal error bar corresponds to the momentum bin width. The solid line is the theory prediction. At first glance it seems that the agreement of the data with the theory is not complete. However there is one more requirement that we can introduce in the data selection. We will return back to this in chapter 8.

We can obtain momentum spectra for the positrons selected with different cut sets, as shown in table 6.1. A statistical comparison of these spectra with the one shown in Fig. 6.10 using the chi-square method, can be performed. Here the chi-square per
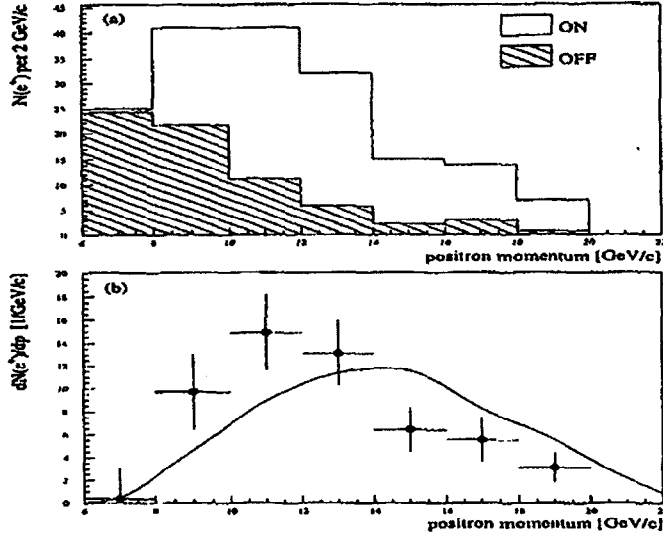
Figure 6.10: Momentum spectrum for the produced 46.6 GeV positrons. The top plot shows the momentum spectra of the laser ON and laser OFF clusters, the latter being scaled down with the appropriate trigger ratio. The second plot shows the momentum spectrum of the background subtracted positrons. The solid line is the theoretical prediction.

degree of freedom χ^2/ν is computed for each spectrum using the formula

$$\chi^2 / \nu = \frac{1}{N} \sum_{n=1}^{N} \frac{(y_{1n} - \alpha\, y_{2n})^2}{\sigma_{1n}^2 + \alpha^2\, \sigma_{2n}^2} \tag{6.4}$$

where

$$N = 8 \quad \text{and} \quad \alpha = \frac{Sum(ID1)}{Sum(ID2)} \tag{6.5}$$

and ID1 the reference spectrum and ID2 the spectrum to be compared with. Table 6.2 contains the results of the χ^2 test along with the Kolmogorov test. Also the positron spectrum for the runs 15273-15323 is also shown for the optimal cut values. These runs are characterized by the highest laser energies achieved during the 46.6 GeV data

ID1	ID2	Kolmogorov Test	χ^2/ν	χ^2-Probability
Optimal Cuts	Loose Cuts	100.00%	0.0494	99.99%
Optimal Cuts	Medium Cuts	100.00%	0.0983	99.93%
Optimal Cuts	Tight Cuts	100.00%	0.0991	99.92%
Optimal Cuts	15273-15323	98.67%	0.4504	89.10%

Table 6.2: Statistical tests of the compatibility of the different positron momentum spectra using both the χ^2 and the Kolmogorov tests.

taking, and as a result they have the highest positron yield. Both tests conclude with at least 90% probability that all the different spectra come from the same mother distribution. From now on and for the rest of the 46.6 GeV data analysis the optimal set of cuts will be used.

6.3 Estimates of the Laser Intensity Parameter η

6.3.1 Initial Considerations

It is very important to correlate the positron yield with the laser intensity, in our case with the parameter η as defined in chapter 2. In a logarithmic scale this curve will be a straight line with a slope indicative of the order of the multiphoton pair process, i.e. to the number of photons absorbed by the energetic γ ray in order to produce the e^+e^- pair. This result can be directly compared to the theoretical prediction and therefore can provide an accurate test of the theory. In principle by knowing the laser pulse's energy and spatial and temporal extend we can uniquely determine the variable η. Although we believe that we know the pulse energy with a less than a 10% error on a pulse-to-pulse basis, we have no measurements of the laser pulse width and the focal spot area estimates are of limited reliability. A way around however can be found, if we make use of $N1,N2$ and $N3$, the number of electrons intercepted by the

gas Čerenkov counters EC37, N2 and N3, of first-, second- and third-order Compton scattering, respectively. Using these counters we can derive η in a self consistent way, by applying the method of Least Squares with constraints. The main idea here is the fact that the parameter η^2 is a linear function of either one of the two monitor signal ratios $N2/N1$ and $N3/N2$, when $\eta^2 \ll 1$. We can write therefore:

$$\eta^2 = k_1 \frac{N2}{N1} \tag{6.6}$$

$$\eta^2 = k_2 \frac{N3}{N2} \tag{6.7}$$

The coefficients k_1 and k_2 depend on the efficiency and the acceptances of the monitors. For larger η^2's the relation may not be linear any more, but it can always be approximated by a polynomial of some higher order. What is important is that η can be deduced from any of the two ratios $N2/N1$ and $N3/N2$, but the predictions of the one ratio has to be compatible to the predictions of the other ratio. This is our main constraint and that is why the method of least squares with constraints needs to be employed. This method not only has several important optimal properties in a statistical sense, but also leads to a simple solution, usually written in terms of matrices and vectors, which can be easily realized on a computer. No special assumption needs to be made about the distribution of measurement errors. In the following sections the mathematical foundations of the least squares method are presented, followed by a detailed description of its application to our specific problem. At the end the final results along with a discussion of the systematic errors and accuracy of the method are shown.

6.3.2 The Least Squares Method [56]

Consider a set of measured random variables, which consists of n values $y_i, i = 1 \ldots n$. They are assumed to be measurements of the true values $\overline{y_i}$ without bias, i.e.

$$E(y_i) = \overline{y_i}. \tag{6.8}$$

There is a covariance matrix $V(y)$ for the above set of measured values. A known functional relationship (model) exists between the true values and which in most cases, but not necessarily in all, depends also on additional variables $a_j, j = 1 \ldots p$, called parameters, for which no direct measurement exists. In general the model can be expressed as a set of m equations of the form

$$f_k(\overline{a}, \overline{y}) = 0, \qquad k = 1 \ldots m, \tag{6.9}$$

called conditions or constraints, and where $\overline{a}$ and $\overline{y}$ are the vectors of the true values of the parameters and of the measured variables respectively. The simplest case is when $p = 0$, i.e. when there are no unmeasured parameters. In this case the measured values y_i will not exactly fulfill the conditions, and corrections Δy_i have to be determined such that $y_i + \Delta y_i$ fulfill the equations. The least squares principle requires the weighted sum of the squares of the corrections

$$S(y) = \Delta y^T W \Delta y, \qquad W = V(y)^{-1} \tag{6.10}$$

to attain a minimum. This last expression reduces to the familiar sum of the squares of the corrections, if the covariance matrix is diagonal (the measured variables are uncorrelated) and the standard deviations are equal. In general the conditions are not linear and therefore the use of the method of the Lagrange multipliers is introduced. In this method m additional parameters λ_k are introduced, one for each constraint. The function to be minimized now changes to

$$L(y) = S(y) + 2 \sum_{k=1}^{m} \lambda_k f_k(a, y) \tag{6.11}$$

The necessary condition for a local extremum of this function with respect to all parameters y, a and λ is then equivalent to the necessary condition for a minimum of $S(y)$ under the conditions of Eq. 6.9.

If the conditions are linear the solution is determined in one step. In the case of nonlinear conditions, the solution is reduced to a sequence of linear problems by linearizing the conditions. This linearization requires some starting values for the

variables involved. For the measured variables these can be the measured values. For the unmeasured parameters they can be determined by methods specific to the problem at hand. The linearization is expressed in each iteration in terms of corrections Δy and Δa to the initial values y and a as follows:

$$f_k(a^*, y^*) + \sum_j \frac{\partial f_k}{\partial a_j}(\Delta a_j - \Delta a_j^*) + \sum_i \frac{\partial f_k}{\partial y_i}(\Delta y_i - \Delta y_i^*) \approx 0 \qquad (6.12)$$

Here Δy^* and Δa^* are the corrections obtained in the previous iteration. The functions and their respective partial derivatives are evaluated at $a^* = a + \Delta a^*$ and $y^* = y + \Delta y^*$ (for the first iteration $\Delta a^* = 0$ and $\Delta y^* = 0$). In vector notation Eq. 6.12 becomes

$$A\,\Delta a + B\,\Delta y = c \quad \text{with} \quad c = A\,\Delta a^* + B\,\Delta y^* - f \qquad (6.13)$$

and

$$A = \begin{pmatrix} \partial f_1/\partial a_1 & \partial f_1/\partial a_2 & \cdots & \partial f_1/\partial a_p \\ \partial f_2/\partial a_1 & \partial f_2/\partial a_2 & \cdots & \partial f_2/\partial a_p \\ \vdots & \vdots & & \vdots \\ \partial f_m/\partial a_1 & \partial f_m/\partial a_2 & \cdots & \partial f_m/\partial a_p \end{pmatrix} \qquad (6.14)$$

$$B = \begin{pmatrix} \partial f_1/\partial y_1 & \partial f_1/\partial y_2 & \cdots & \partial f_1/\partial y_n \\ \partial f_2/\partial y_1 & \partial f_2/\partial y_2 & \cdots & \partial f_2/\partial y_n \\ \vdots & \vdots & & \vdots \\ \partial f_m/\partial y_1 & \partial f_m/\partial y_2 & \cdots & \partial f_m/\partial y_n \end{pmatrix} \qquad (6.15)$$

$$f = \begin{pmatrix} f_1(a^*, y^*) \\ f_2(a^*, y^*) \\ \vdots \\ f_m(a^*, y^*) \end{pmatrix} \qquad (6.16)$$

Eq. 6.11 in matrix form, also becomes:

$$L = \Delta y^T W \Delta y + 2\lambda^T (A\Delta a + B\Delta y - c) \qquad (6.17)$$

Differentiating we obtain the necessary condition for an extremum in matrix form:

$$W\,\Delta y + B^T \lambda = 0 \qquad (6.18)$$

$$A^T \lambda = 0 \qquad (6.19)$$

$$B\,\Delta y + A\Delta a = c \qquad (6.20)$$

This system consists of $n + m + p$ equations with unknowns Δy, Δa and λ. We can rewrite it in the form of one matrix equation as follows:

$$\begin{pmatrix} W & 0 & B^T \\ 0 & 0 & A^T \\ B & A & 0 \end{pmatrix} \begin{pmatrix} \Delta y \\ \Delta a \\ \lambda \end{pmatrix} = \begin{pmatrix} 0 \\ 0 \\ c \end{pmatrix} \qquad (6.21)$$

The system can be solved as usually by calculating the inverse of the matrix on the left hand side of Eq. 6.21. The expressions in the general case can become very complicated.

For simplicity let us consider the case of no unmeasured variables in which Eq. 6.21 is reduced to:

$$\begin{pmatrix} W & B^T \\ B & 0 \end{pmatrix} \begin{pmatrix} \Delta y \\ \lambda \end{pmatrix} = \begin{pmatrix} 0 \\ c \end{pmatrix} \qquad (6.22)$$

We can then write the inverse of the matrix on the left hand side of Eq. 6.22

$$\begin{pmatrix} W & B^T \\ B & 0 \end{pmatrix}^{-1} = \begin{pmatrix} C_{11} & C_{21}^T \\ C_{21} & C_{22} \end{pmatrix} \qquad (6.23)$$

The final solution therefore can be written in the form:

$$\begin{pmatrix} \hat{y} \\ \hat{\lambda} \end{pmatrix} = \begin{pmatrix} y \\ 0 \end{pmatrix} + \begin{pmatrix} C_{11} & C_{21}^T \\ C_{21} & C_{22} \end{pmatrix} \begin{pmatrix} 0 \\ c \end{pmatrix} \qquad (6.24)$$

$$= \begin{pmatrix} y + W^{-1}B^T W_B c \\ -W_B c \end{pmatrix} \qquad (6.25)$$

where

$$W_B = (BW^{-1}B^T)^{-1} \qquad (6.26)$$

By error propagation we can derive the covariance matrix for the combined vector $\hat{y}$ and $\hat{\lambda}$. The result is:

$$V \begin{pmatrix} \hat{y} \\ \hat{\lambda} \end{pmatrix} = \begin{pmatrix} C_{11} & 0 \\ 0 & -C_{22} \end{pmatrix} \qquad (6.27)$$

Thus the covariance matrix of the improved values is the first $n \cdot n$ submatrix C_{11}. For the case of unmeasured parameters, it merely expands to:

$$V \begin{pmatrix} \hat{y} \\ \hat{a} \\ \hat{\lambda} \end{pmatrix} = \begin{pmatrix} C_{11} & C_{21}^T & 0 \\ C_{21} & C_{22} & 0 \\ 0 & 0 & -C_{33} \end{pmatrix} \qquad (6.28)$$

The weighted sum of squares, as defined in Eq. 6.10 can be calculated using the formula

$$\hat{S} = -\lambda^T c \qquad (6.29)$$

A necessary condition for convergence is that the changes ΔS of S become small, e.g. $\Delta S < 10^{-3}$. In addition the constraints need to be fulfilled for the new and improved values $a + \Delta a$ and $y + \Delta y$ with a certain numerical precision, e.g.

$$F = \sum_k |f_k(a + \Delta a, y + \Delta y)| < \varepsilon , \qquad (6.30)$$

where the value of ε depends on the problem—typical values can be as low as 10^{-9}. This criterion requires all conditions to be of the same order of magnitude, which can be achieved by a proper selection of scaling factors. If the value F increases during one of the iterations, one can reduce the correction for that step by some factor until a smaller value F is obtained.

6.3.3   The Constrained Fit

As we mentioned earlier, we cannot use directly the measurements of the laser pulse parameters for an accurate calculation of the field intensity, as it is defined by the parameter η. We can, on the other hand, use the number of electrons $N1$, $N2$,

$N3$ detected by the Čerenkov counters N1,N2,N3 associated with the first-, second- and third-order Compton scattering. Each of these counters can be in principle used independently to extract the laser field intensity. However, due to temporal and spatial overlap instability—jitter—this is not advisable. But if we make the fundamental assumption that the signal of each counter has the same dependence on the overlap fluctuations, we can still use the ratios of the signals of those monitors to extract the parameter η. This can be easily seen in the case of $\eta^2 \ll 1$. Here the signal of each one of the monitors varies to a good approximation as a linear function of η^2 raised to a power equal to the order of the Compton scattered electrons that each counter intercepts, i.e.

$$N1 \sim \eta^2 \tag{6.31}$$

$$N2 \sim (\eta^2)^2 \tag{6.32}$$

$$N3 \sim (\eta^2)^3 \tag{6.33}$$

Any factors in front of η^2 in the above expressions, will depend primarily on overlap but also on the acceptances of the three monitors, as well as the spectrum of the scattered electrons. If we apply now the earlier assumption about the similar overlap dependence of each monitor's signal, the ratios $N2/N1$ and $N3/N2$ will still be fairly linear functions of η^2, but any overlap dependence will be canceled out. In reality η^2 is not necessarily small and therefore the functional dependence of the two ratios on η^2 will be some higher order polynomial. This functional dependence, or equivalently, that of η^2 on each of the two ratios independently, can be derived by a numerical simulation of the different order Compton processes, where the signals of the N1, N2, N3 monitors are calculated once their respective acceptances, for their nominal positions, are folded in. This is shown in Fig. 6.11, for 46.6 GeV simulated data points. Although the fit utilizes second order polynomials, it can be seen that even linear expressions can be sufficiently accurate approximations for most of the η^2 range. If the signals measured by the three monitors are consistent with each other, the η^2's
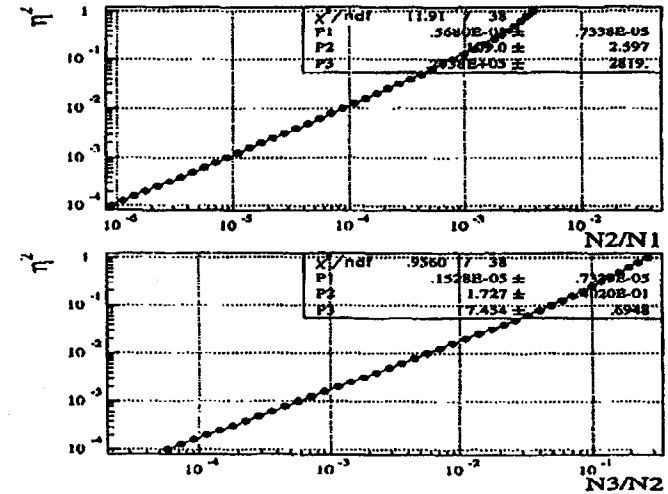
Figure 6.11: Polynomial fits of η^2 as a function of either of the ratios $N2/N1$ and $N3/N2$ using 46.6 GeV simulation data. The η^2's derived by each of the two expressions, have to be the same for a specific event where all the three counters have reported signal.

predicted by the fit expressions in Fig. 6.11 will have to be the same or,

$$\eta^2(N2/N1) = \eta^2(N3/N2) \tag{6.34}$$

We now have all the necessary ingredients in order to set up a least squares fit with constraints and apply that on each data point. For each event we have the measurements of the three monitors $N1$, $N2$, $N3$ along with their corresponding errors, as they are estimated in section 5.3. Assuming that the signals in each of these monitors are independent of each other, we can construct the variance matrix, which will be a diagonal matrix with each of the diagonal elements being the square of the corresponding error. The three monitor signals need to satisfy the condition in Eq. 6.34. So we are in a position of applying the procedure of section 6.3.2. For each

data event the values of the three counter measurements are varied, within their error ranges, so that the condition 6.34 is adequately satisfied. For the new values that the fit comes up with, the expression in Eq. 6.10 is computed, which is a measure of the χ^2 of the fit for this step. Also the function in Eq. 6.30 is calculated. Then for the new signal values the previous step is repeated once more and the difference ΔS of the new χ^2 with respect to the previous one is derived. These iterations continue until the $\Delta S \le 10^{-3}$ and at the same time the functional expression in Eq. 6.30 becomes $\le 10^{-9}$, in which case we consider that the fit has converged. The new signal values for the three counters are output along with the new covariance matrix, from which the errors on these values are calculated. We can now use them, along with any of the two fit expressions shown in Fig. 6.11, to find η. In fact the two values derived from any of the two expressions shown there, are very close to each other, and their average is used as the final answer. The error on η is calculated using the general expression [57]:

$$(\Delta f)^2 = \sum_{m,n} \frac{\partial f}{\partial x_n} \frac{\partial f}{\partial x_m} V_{mn} \qquad (6.35)$$

Here V_{mn} is the variance matrix as it is computed by the constrained fit and the derivatives are taken with respect to the new monitor signals calculated by the fit. We have again two different errors on η depending on which of the expressions in Fig. 6.11 we use to find η. To get the error on the average η we add quadratically the two errors just found. This error on η is purely statistical and it is different from the systematic errors that will be discussed later.

6.3.4   Tests of the Fit Algorithm

For debugging purposes and also in order to test the speed of convergence of the fit algorithm, a Monte Carlo simulation of the three monitor signals can be used. Their values, smeared around their randomly generated true values according to a Gaussian distribution centered at zero and having a $\sigma = 1$, along with their corresponding errors, are the inputs to the least squares fit. As long as the input parameters are

completely independent from each other, the probability distribution of all the events at the end, should be a horizontal line. The probabilities for each event processed by the constraint fit, are derived from the χ^2 of the fit for that specific event, so that the higher the χ^2 the smaller the corresponding probability. A horizontal probability distribution means that the output results remain independent from each other too, i.e. that there is no bias in the fit algorithm. The results of such a test are shown in
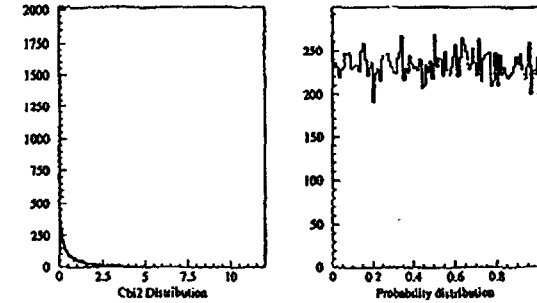
Figure 6.12: The χ^2 (left) and the probability (right) distribution of the constrained fit using 30,000 simulated monitor signals. The probability distribution follows a horizontal line, which is expected when the input parameters to the fit are independent from each other.

Fig. 6.12.

Some useful checks of the constrained fit code can be performed once the results of the fit are available. At first we can construct the following three types of residuals:

$$true - fit \quad , \quad (true - fit)/error \qquad (6.36)$$
$$true - start \quad , \quad (true - start)/error \qquad (6.37)$$
$$fit - start \quad , \quad (fit - start)/error \qquad (6.38)$$

Here true stands for the randomly generated values before any Gaussian smearing is done, start are the initial values used as an input to the fitting routine, and fit are the values that the fit outputs after convergence. The second type of residuals

should always give an RMS of 1 as long as the smearing is done using a Gaussian with $\sigma = 1$. This turns out to be the case. The $(true - fit)/error$ residual shows how much the fit results differ from the randomly generated true value before any kind of smearing. Finally the $(fit - start)^2/error^2$ shows the contribution to the χ^2 of that specific correction. Three different error cases are examined:

1. The errors of the three monitors are the ones estimated in section 5.3.

2. All three monitors have fixed errors such that $\langle e_i/N_i \rangle$ is the same.

3. The three monitors have the same relative error, e.g. 5%.

The results are shown in table 6.3. In the first case we can see that the χ^2 contribution

	Monitor	$\sigma(\frac{N_i^t - N_i^f}{e_i})$	$\langle \frac{(N_i^t - N_i^f)^2}{e_i^2} \rangle$
Case	N1	0.99	0.02
1	N2	0.79	0.32
	N3	0.62	0.57
Case	N1	0.91	0.13
2	N2	0.63	0.56
	N3	0.87	0.22
Case	N1	0.91	0.15
3	N2	0.58	0.60
	N3	0.91	0.17

Table 6.3: Residuals when the three monitor errors are calculated according to section 5.3 (Case 1), when the errors are fixed such that $\langle e_i/N_i \rangle$ $i = 1, 2, 3$ are the same for the three monitors (Case 2), and finally when the same relative error is used (Case 3).

of the N1 monitor is minimal. This is mostly because the relative error for this monitor is much smaller than the relative errors of the other two monitors. In the other two cases where the errors for all the three monitors are roughly the same, the constrained

fit treats them in a comparable way, which means that the χ^2 contributions are at least of the same order. Why not exactly the same as someone might have expected? If we look a little more carefully we can conclude that it is not the χ^2 contribution of each monitor that should be the same, but the χ^2 contribution divided by the change of the expression in Eq. 6.30 for that specific change in the value of one of the three counter signals. This makes some sense, i.e. why should the fit vary the value of a monitor that it weakly depends upon and pay the price in the resulting χ^2? In a more rigorous way this can be shown as follows:

$$\chi^2 = \sum_{i=1}^{3} \frac{(n_i - N_i)^2}{e_i^2} + 2\lambda f(n_i) \implies \quad (6.39)$$

$$\frac{\partial \chi^2}{\partial n_i} = \frac{2(n_i - N_i)}{e_i^2} + 2\lambda \frac{\partial f(n_i)}{\partial n_i} = 0 \quad \text{for minimum } \chi^2 \implies \quad (6.40)$$

$$\lambda = -\frac{\Delta N_i}{e_i^2} \frac{1}{\partial f/\partial n_i} \implies \quad (6.41)$$

$$-1 = \frac{\Delta N_i}{e_i^2} \frac{1}{\lambda} \frac{1}{\partial f/\partial n_i} \quad (6.42)$$

That means that if we plot the last expression above, we should get a distribution
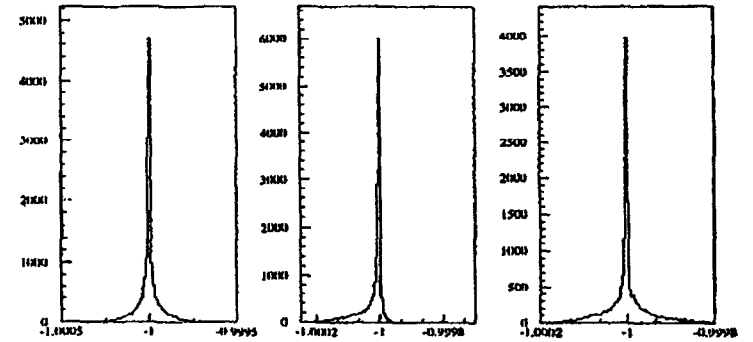
Figure 6.13: Distribution of the expression $\frac{\Delta N_i}{e_i^2} \frac{1}{\lambda} \frac{1}{\partial f/\partial n_i}$ for each of the three monitors. According to our expectations it should have a mean value of -1.

that has a mean value of -1. This is shown in Fig. 6.13.

Going back to Fig. 6.11 we can see that in principle a linear fit is a good approximation for most of the value range of η^2 and certainly for $\eta^2 \ll 1$. If we use this linear approximation, the expression for the function to be minimized becomes very simply [58],

$$\chi^2 = \sum_{i=1} 3 \frac{(n_i - N_i)^2}{e_i^2} + 2\lambda(n_2^2 - kn_1 n_3) \qquad (6.43)$$

The four parameters n_i and λ are adjusted to minimize χ^2. This means that we set the derivatives of χ^2 to 0. The resulting system of four equations can be solved analytically for the four unknown variables. Therefore we can directly compare the solutions n_i for each of the three monitors derived above to the ones that the constrained fit predicts on an event-by-event basis. If the fit algorithm is correct their differences should not be substantial. This is shown in Fig. 6.14 for each of the three monitors
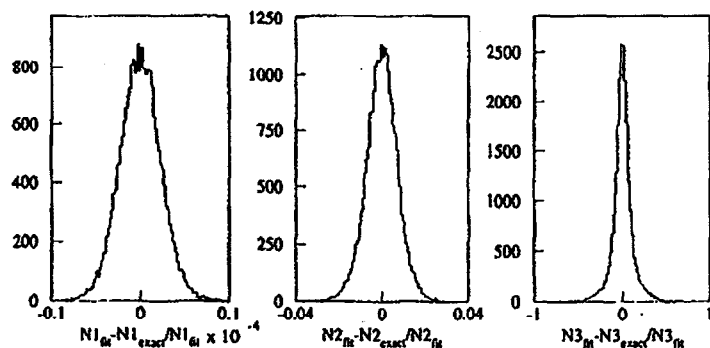
Figure 6.14: Distribution of the relative differences between the constrained fit solutions and the analytical solutions derived under the assumption of a linear constraint, for each of the three counters separately.

separately. As we can see the relative difference increases for monitors that intercept higher order electrons, which is expected since higher order Compton scattering is more sensitive to the value of η. But we should also notice the fact that indeed the relative differences are in all the cases much less than 1%, which reassures us once

more for the correctness of the constrained fit algorithm. Some qualitative insights can be deduced from the analytic approximation. If the Lagrange multiplier is "small", then the analytic solutions for the three monitors can be written as:

$$n_1 \approx N_1 \left(1 + \lambda N_2^2 \frac{\sigma_1^2}{N_1^2}\right) \qquad (6.44)$$

$$n_2 \approx N_2 \left(1 - 2\lambda N_2^2 \frac{\sigma_2^2}{N_2^2}\right) \qquad (6.45)$$

$$n_3 \approx N_3 \left(1 + \lambda N_2^2 \frac{\sigma_3^2}{N_3^2}\right) \qquad (6.46)$$

where N_i $i = 1, 2, 3$ the measured signals of the three monitors and σ_i $i = 1, 2, 3$ the corresponding errors. As we can see from the last expressions above, the monitor with the smallest relative error will change only by very small amounts, and will contribute very little to the χ^2. This is exactly what the fit seems to do as we have noticed earlier.

6.3.5 The Probability Cut

The constrained fit provides us with an excellent tool to overcome one serious problem with the N3 monitor. As we can see at the top plot in Fig. 6.15, the distribution of the N3 monitor ADC counts for the laser OFF events, is not quite Gaussian but has a very long tail towards the higher values, which is expected only when the monitor detects some kind of signal. This behavior is not consistent with any of the signals from the other two counters and it can be attributed to some defect in the monitor's performance. What is really worrisome is that it will offset the signal of the laser ON events also by some unknown amount, thus influencing the quality of the constrained fit convergence. We can try to see whether we can predict the effect of the N3 tails on the constrained fit results. Using the Monte Carlo simulator, 3800 events are created for the N1, N2 and N3 monitors, and the last ones in addition, are smeared according to the distribution shown at the top of Fig. 6.15. These events then are used as an input to the constrained fit and the probability distribution, as it is derived from the
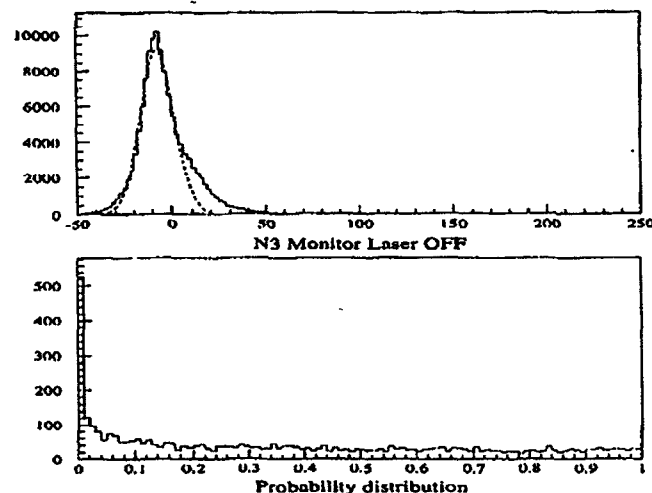
Figure 6.15: The top plot shows the distribution of the N3 monitor ADC counts when the laser is OFF. Notice the long tail that goes up to 250 counts or 450 e^- according to the calibration. This is certainly a defect in the counter's performance. The dashed line shows a Gaussian fit without using the bins in the tail of the distribution. The bottom plot shows the probability distribution, as it is derived from the χ^2 of the fit for each particular event, for 3800 simulated events where the input to the fit N3 signal is smeared using the ADC counts distribution shown in the top plot. Notice the big peak around zero while the rest of the distribution remains flat.

χ^2 of the fit for each input event, is plotted. We would expect, as we mentioned in section 6.3.4, this distribution to be flat. This is not the case as the bottom plot of Fig. 6.15 shows. We can see in this plot that there is a peak around the small probabilities while the rest of the distribution is still flat. Are the events in this peak the ones that happen to fall in the tail of the N3 laser OFF distribution? If we count them we see that there are about 530 events. We can also count the events in the tail of the N3 laser OFF distribution. To do that we fit a Gaussian excluding from the fit all the bins that belong to the tail, since otherwise they will bias the fit. The result

is the dashed curve shown in the top plot of Fig. 6.15. Counting now the events that are beyond the tail of this Gaussian, we find that there are $\sim 19,400$ out of a total of $\sim 124,000$ events. Scaling this last number to the number of events used in the simulation, we find 590 events, very close to the number of points in the peak of the probability distribution. We can claim therefore that the effect of the N3 tails is the peak at the low values of the probability distribution and we should not use them in the constrained fit.

In the case of the data, things are not so simple. We need to arrange the input signals from the three monitors and their respective errors, so that the output probability distribution will look like the one in Fig. 6.15. This can be done in two steps. First we scale the $N1$ signal so that the average χ^2 is minimized and for that specific $N1$ scaling factor we scale the $N2$ error so that the RMS value of the probability distribution is minimized. It turns out that the $N1$ scaling factor equals to 2.25 making $\langle \chi^2 \rangle = 4$ and after that the $N2$ error scaling factor is 3.15 giving a $\langle \chi^2 \rangle = 2.5$. This means that both the input $N1$ signal and the input $N2$ error are systematically scaled for each event by the above factors no matter what their measured values are. The probability distribution for all the 46.6 GeV data points, after introducing the above scaling factors, is shown in Fig. 6.16. It has exactly the form that the distribution from the simulation shown in Fig. 6.15 has. We can always instead of scaling the $N2$ error, scale the $N1$ error and get again a probability distribution like the one in Fig. 6.15. In fact this was done using a smaller data sample and the event and run numbers of the points in the peak of the distribution were compared one by one to the ones where the $N2$ error was scaled instead. Almost 90% of those points were found to be exactly the same confirming once more our suspicion that those are due to the effect of the N3 tails on the constrained fit. So we can safely cut away the events in the peak. This is shown in the right plot in Fig. 6.16. This plot is just the zoom in of the left plot in the same figure and the vertical line shows very clearly the probability cut at 1.6%. About 2,200 (11%) of the events are cut this way. It
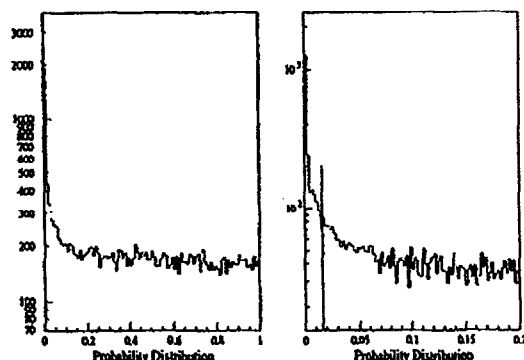
Figure 6.16: Using the constraint fit to introduce a cut on probability. The N3 tails cause the probability distribution to have a peak at the lower probability values. This is exactly how the distribution looks after scaling the $N1$ signal by 2.25 and the $N2$ error by 3.15 and it is shown in the left plot. The right plot is a zoom in of the left plot in order to show more clearly the position of the probability cut, which is the vertical line shown.

is obvious from the above that the probability cut requires that we process the data through the constrained fit once, by scaling the $N1$ signal and the $N2$ error by the scaling factors mentioned above. This rearranges the probability distribution of the data at the end of the constrained fit in such a way so that a probability cut can be safely applied. The data events that survive this cut are then processed once more through the constrained fit, in order to extract the parameter η.

6.3.6   Scaling of the Input Signal

We have already seen in the previous section that some scaling of the input monitor signals and their respective errors, might be necessary. Of course in that case we are trying to create some specific probability distribution which can be used to introduce a probability cut. A lot more serious considerations give rise to a different scaling of the input monitor signals. If we use as the initial input to the constrained fit the
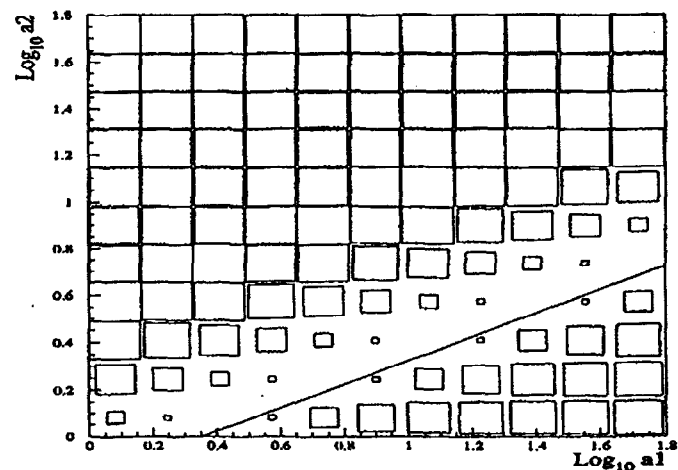
Figure 6.17: A two-dimensional histogram that shows the variation of the $\langle \chi^2 \rangle$ for different combinations of the scaling factors a_1 and a_2 for the $N1$ and $N2$ signals respectively. The logarithms of the two scaling factors are shown in each axis. Notice that there is always a combination of scaling factors that can minimize the $\langle \chi^2 \rangle$ independently of how big the actual scaling is. The solid line along the "valley" shows the functional relation of such a combination of scaling factors. We can write $a_1 = 2.25\, a_2^2$.

measured $N1, N2$ and $N3$ signals along with their respective errors, then the final $\langle \chi^2 \rangle$ is large (of the order of 10 or even more) and the convergence of the fit on an event-by-event basis becomes very problematic. In fact this tells us that the fit itself needs to adjust the signals of the three monitors to a considerable extend in order to achieve convergence. The two nonlinear counters are the ones affected mostly and in fact the fit systematically tends to lower their respective signals. It is possible that one of the counters, or even all of them, report a much higher signal than what they are supposed to. We can test whether the quality of the fit improves when we start to scale down the signals of any of the three monitors or a combination of them. Fig. 6.17 shows such a two-dimensional scan of the scaling factors for the $N1$ and

$N2$ signals. One characteristic of this plot is the long "valley" of small $\langle \chi^2 \rangle$ values for different combinations of the two scaling factors. This plot shows us two things. First, that we can indeed improve the quality of the constrained fit convergence, once some scaling of the input signal is introduced. Second that we do not have a specific scaling scheme that we can use, since different scalings can lead to equally small $\langle \chi^2 \rangle$ values. In fact the solid line in Fig. 6.17 shows a functional relation between the two scaling factors a_1 and a_2 that needs to be satisfied in order to get an equally small $\langle \chi^2 \rangle$. We can write,

$$a_1 = 2.25\, a_2^2 \tag{6.47}$$

Up to this point we have kept the $N3$ signal unscaled. An obvious generalization of Eq. 6.47 will be, when we include a scaling factor for $N3$,

$$a_1\, a_3 = 2.25\, a_2^2 \tag{6.48}$$

The quadratic dependence on the a_2 scaling factor should not surprise us once we recall from section 6.3.3 that $N2$ is used in both signal ratios.

Overlap considerations can give us a tool to select the appropriate signal scaling factors. Let's concentrate on Fig. 6.18 and especially on the last two triplets. They both show the same thing, what we tend to call the overlap distributions for the three counters, one using a linear vertical scale and the other a logarithmic scale. The overlap in all three cases is defined as the ratio of the measured signals by the three monitors over the predicted signals from the simulation. One would expect these ratios to go at most up to 1. This is not the case in any of the three monitors. In fact the overlap ratios tend to go to higher and higher values as we look at counters that intercept electrons from higher orders of Compton scattering. [1]   Apart from

---

[1] It is rather surprising that the two nonlinear counters N2 and N3 have such a difference in their overlap values, since they are using the same readout electronics. In fact it turns out that this is not the case. A more careful calibration of the N2 monitor introduced a different conversion factor between ADC counts and number of electrons detected, and the overlaps for the two monitors became almost the same, along with their scaling factors. Unfortunately this was done after this analysis was finished and since the only effect would have been to introduce a different scaling factor for the $N2$ signal used by the fit without essentially changing the result, the scaling scheme was left the way it was.
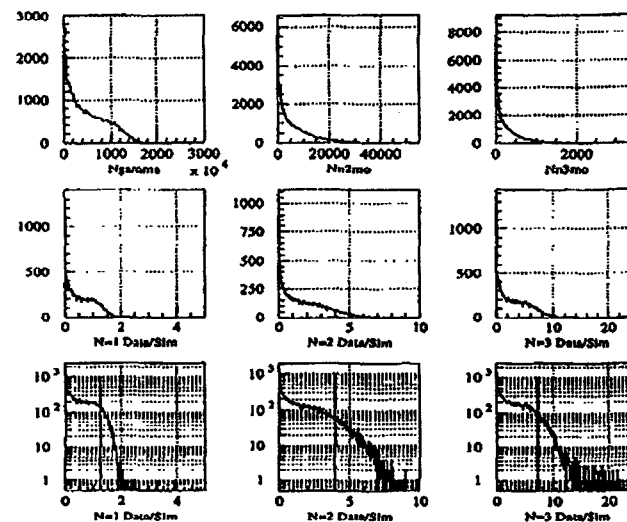
Figure 6.18: Overlap plots for the 46.6 GeV data. The top triplet shows the distributions of the three counter signals. The second and the third triplets show, in linear and logarithmic scales respectively, what we define as the $N1$, $N2$ and $N3$ overlaps. In principle these are defined as the ratios of the measured signals of the three monitors over the predicted signals from the simulation. We would expect these ratios to go up to 1 at most, but as it is clear from all the three plots, they reach much higher values, which are increasing with the order of the nonlinear Compton scattering that each counter detects. This is an indication that the three monitors may overestimate their respective signals.

suspecting the simulation (will come back to this later, but it turns out not to be the case), the only other conclusion we can reach is that the three counters overestimate their respective signals by some factor. We can estimate this factor in the following way. First we need to find the horizontal axis value where 90% of the histogram contents are included. This is what the vertical lines drawn in the plots of the bottom triplet indicate. We can scale then down all the three monitor signals by the three numbers found. But there is one thing that we need to remember. From Eq. 6.48

we have concluded that it needs to be satisfied by any signal scaling factors so that $\langle \chi^2 \rangle$ to be minimum. We need therefore to adjust the scaling factors that we derived by looking at the overlap plots, so that this is true. For $N1$ we find a factor of 1.25 not too far away from 1 and we can therefore leave it as it is. But for the other two monitors we find 4.1 and 7.2 respectively. We need to multiply both by some constant x such that,

$$\frac{1}{1.25} \times \frac{1}{7.2\,x} = 2.25 \times \frac{1}{4.1^2\,x^2} \tag{6.49}$$

or,

$$x = \frac{2.25 \times 1.25 \times 7.2}{4.1^2} \tag{6.50}$$

The last one gives us $x = 1.22$ and so finally the three monitor scaling factors become:

$$a_1 = 1.25 \quad a_2 = 4.97 \quad a_3 = 8.79 \tag{6.51}$$

Even when this scaling of the input monitor signal is done, there is still a fairly high $\langle \chi^2 \rangle$, which we would like to reduce more. This can be achieved by scaling one of the monitor errors. We choose the $N2$ error. We can try different scaling factors for this error and look at their effect on the probability distribution's RMS value. The results of such a scan are shown in Fig. 6.19. The minimum RMS value is achieved for a scaling factor of 3.5. Taking into account the fact that the average $N2$ error, as it was estimated in section 5.3, is about 4%, such a scaling won't increase it to more than 15% and in fact it will bring it much closer to the average $N3$ error estimated in the same section. We can always try to scale the $N1$ error instead by applying the same method and in fact this will be examined as one of the possible sources of our systematic errors. Scaling the $N3$ error is not so appealing, since it will lead to some rather unacceptable high value. Choosing to scale the $N2$ error by a factor of 3.5, brings the $\langle \chi^2 \rangle$ down to 0.91.

One thing that has not been mentioned earlier, is the fact that by choosing different scaling factors for the input signals from the three monitors, the predicted η's and their respective errors from the constrained fit vary significantly. In fact the lower the
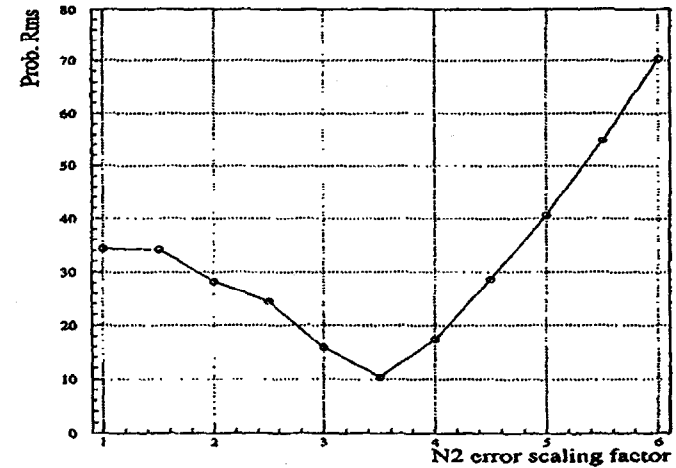
Figure 6.19: A scan of the $N2$ error scaling factor by looking at the RMS of the probability distribution. The minimum is achieved for a scale factor of 3.5.

scaling factor the higher the predicted η's become, and also the errors show the same tendency. This becomes very important when after settling down with a specific set of scaling factors for the three monitor signals, we proceed with the constrained fit, derive η's on an event-by-event basis, and use them as an input to the simulation to predict the corresponding monitor rates. From them we can create new overlap plots, like the ones shown in Fig. 6.18, and as a result derive new scaling factors and after going through the constrained fit once more, eventually get new η's. It turns out that after repeating these steps a few times the $\langle \eta \rangle$ differs from the previous step by at least a few %. Taking into account the fact that even a 10% variation in η can change the simulation predictions by at least half an order of magnitude, we would like to investigate whether all this scaling scheme will ever converge, i.e. whether we reach a point that the relative difference between the $\langle \eta \rangle$'s of two consecutive steps becomes insignificant. The results of such a study are shown in table 6.4. The table shows that

Iteration #	$\Delta\langle\eta\rangle/\langle\eta\rangle$	$N1$ Sc. Factor	$N2$ Sc. Factor	$N3$ Sc. Factor
2	-2.6%	1.24	3.73	4.99
3	-2.2%	1.26	3.95	5.50
4	-1.9%	1.26	4.09	5.91
5	+1.8%	1.24	5.96	12.73
6	-0.14%	1.25	4.97	8.79

Table 6.4: Relative change of the constrained fit $\langle\eta\rangle$ after every iteration of the constrained fit using the results of the previous step. The relative difference becomes smaller and smaller but very slowly as the first three steps show. In iteration 5 the η's of the previous step were scaled by 0.8, before repeating the constrained fit. Apparently we overshot and in iteration 6 we scale them only by 0.9 and the fit converges. The corresponding scaling factors for the three monitor signals are also shown in each iteration.

indeed the relative difference in $\langle\eta\rangle$ becomes smaller and smaller after each iteration, but not fast enough. In iteration 5 the input η's, as they are calculated from iteration 4, are scaled by a factor of 0.8 to speed up the convergence process. Apparently we overshot and therefore in iteration 6 the input η's, again as they are calculated from iteration 4, are scaled by a factor of 0.9. After this last step the relative difference becomes indeed small and the same is true also for the average η error, which has a relative difference of only 0.16% with respect to the previous step. The scaling factors that are shown in Eq. 6.51 are the results of the last iteration in table 6.4. These are the ones that have to be used to compute the final η values for each data event.

6.3.7 η Estimates and Verification

After the final selection of scaling factors for the three monitor signals that are used as an input to the constrained fit, we can run through the data and calculate the η for each event. The distribution of the fit η's is shown in Fig. 6.20, along with the η's as they are estimated using the laser parameters, i.e. the measured laser energy and

Focal η,C-Fit and Laser Parameters

Focal η,C-Fit

Focal η,Laser-Parameters
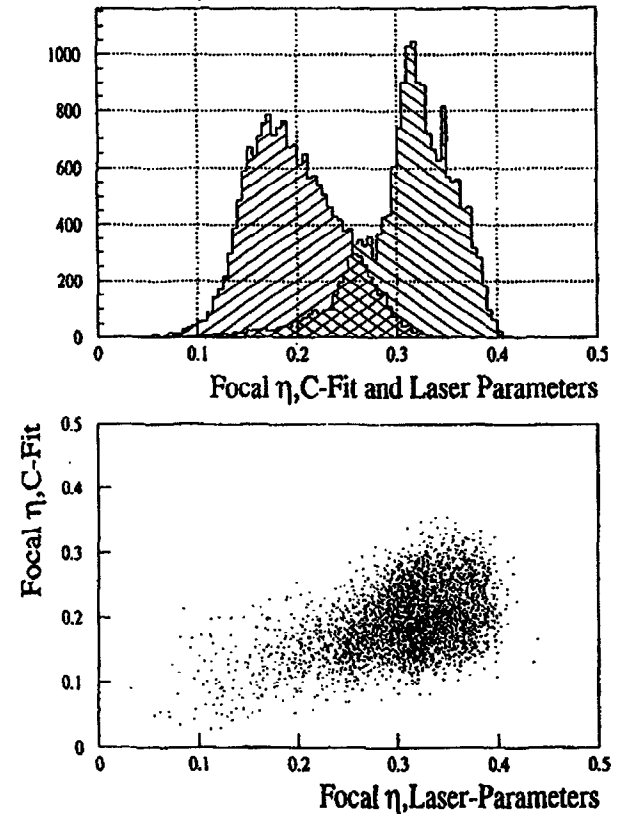
Figure 6.20: Comparison of the η's calculated using the constrained fit with those from the laser parameters. The top plot shows the η distributions according to the two methods, while the bottom is just the scattered plot of the previous one. It is very clear from the two plots that the η estimated from the laser parameters is just an upper limit of the fit η.

keeping the focal area and the pulse width fixed at 30 μm^2 and 1.5 ps respectively.

The constrained fit returns,

$$\langle \eta \rangle = 0.1958 \pm 0.0219 \quad \text{or} \quad \langle \eta \rangle = 0.1958 \pm 11.2\% \text{ statistical error} \quad (6.52)$$

It is quite obvious that the laser parameters overestimate η considerably.

How can we verify that the fit η's are really correct? There is one more detector that can look at the Compton scattered electrons and this is the electron calorimeter (ECAL). For several data runs ECAL was moving vertically, its top row intercepting every time electrons with different momenta ranging from the second up to the fourth order Compton scatterings. We can use the estimated η's from the fit as a final input to the simulation, along with the acceptance of the detector, to predict the expected rates and compare them with the measured rates. If the fit η's are correct both simulation and data should be very close, since we believe that we know how to measure correctly the nonlinear Compton scattering and we have verified the validity of the theoretical prediction in earlier run periods [59], [60]. Three different ECAL

Runs	$\langle E_{laser} \rangle (mJ)$	$\langle \eta \rangle$
15212,15216,15225,15228	440	0.234
15271,15273	540	0.183
15296,15299,15302,15304	650	0.251

Table 6.5: Laser energy and average η for the three run groups used to check the validity of the η's calculated from the constrained fit.

scan groups are examined, each one of them characterized by a specific laser energy and η as it is shown in table 6.5. The first group has the smallest laser energy of all, and therefore someone would expect that it should also have the smallest event rates too. On the other hand, according to the η calculated from the fit, the second group should have the smallest event rates. Looking at Fig. 6.21, 6.22, 6.23, we can clearly see first of all that the second group of runs has the smallest rates, which cannot be explained by using the laser parameters to compute η, i.e. based essentially on the
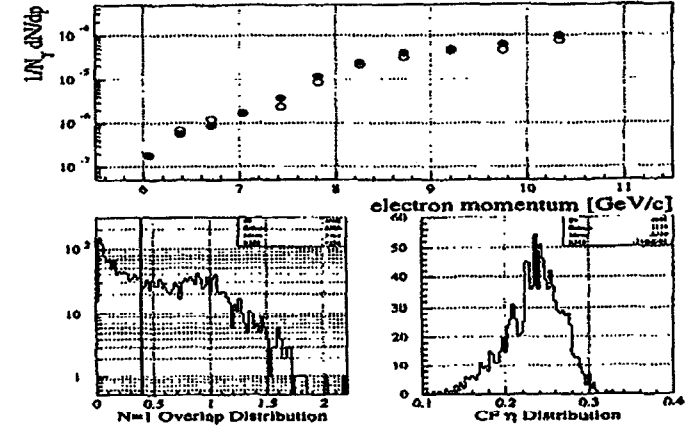
Figure 6.21: Verification plots for runs 15212, 15216, 15225, 15228. The top plot shows the number of electrons per momentum bin normalized to the total number of linear Compton photons, as a function of the momentum of the intercepted electrons. The black dots are the data points and the white the simulation results. The bottom left plot shows the distribution of the $N1$ overlap as it is defined in section 6.3.6. The vertical line is the overlap cut used throughout the whole 46.6 GeV analysis. The bottom right plot shows the distribution of the η's from the constrained fit.

measured laser energy and keeping the laser area and pulse width fixed. Second that there is an excellent agreement between the simulation based on the η's computed by the constrained fit and the data as they are measured by ECAL. From all the above we conclude that the constrained fit gives us a useful tool to express the laser intensity through the variable η.

There is one last thing that we need to verify. During the whole constrained fit process we have tacitly assumed that the nonlinear monitor signals have the same dependence on the spatial and temporal overlap. This essentially means that the two ratios $N2/N1$ and $N3/N2$ are independent of any overlap fluctuations, and so they can indeed give us a valid measure of the parameter η. As we have probably mentioned several times up to now, η is a measure of the laser intensity and therefore
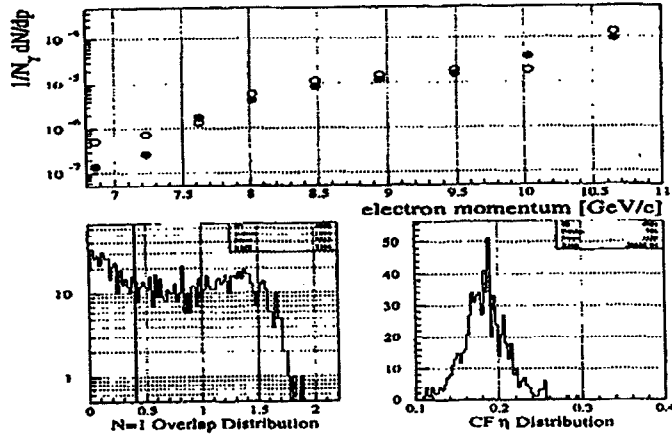
Figure 6.22: Same as in Fig. 6.21 using runs 15271, 15273.
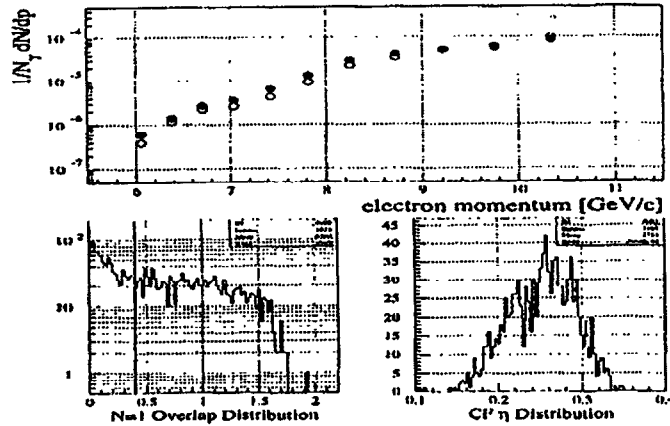
Figure 6.23: Same as in Fig. 6.21 using runs 15296, 15299, 15302, 15304.
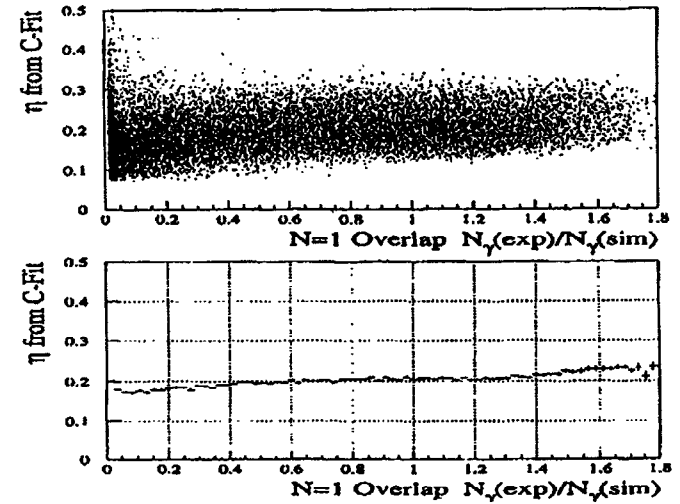
Figure 6.24: Stability of η with the N=1 overlap. Here the overlap is defined in the same way as in section 6.3.6, *i.e.* as the ratio of the measured $N1$ rate over the expected from the simulation. It is clear that for overlap greater than 0.4, which is what we have been using in the whole 46.6 GeV data analysis, η remains pretty much stable.

it has to be completely independent from overlap. Fig. 6.24 shows the dependence of the constrained fit η on the N=1 overlap, as it is defined in section 6.3.6. If we concentrate on the points above 0.4, which is the N=1 overlap cut that we have been using during the whole 46.6 GeV analysis, we can clearly see that η does not fluctuate much and in any case not more than 10%. This is already smaller than the statistical or the systematic errors that we have assigned to η. Fig. 6.25, shows the dependence of the η's calculated by the constrained fit with the number of the measured N=1 γ's. This last number once it is normalized to the laser energy and the electron beam charge (number of electrons per bunch), depends only on the N=1 overlap variations and it can be used as a measure of the N=1 overlap. Again η is stable for most of
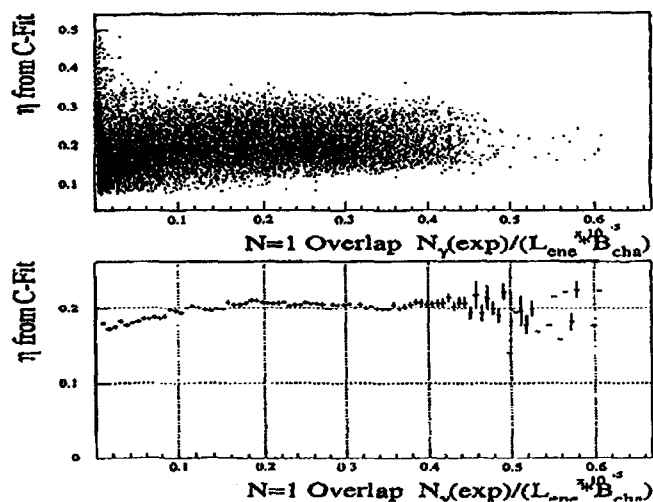
Figure 6.25: Stability of η with the number of γ's measured by the linear Compton monitor. This number once it is normalized over the laser energy and the electron beam charge, it depends only on the overlap fluctuations, and it can therefore provide us with an alternative measurement of N=1 overlap.

the range shown. We can conclude therefore that the constrained fit does offer us a valid estimate of η, independent of any overlap fluctuations as it should be.

6.3.8 Systematics on η

There are several sources of systematic errors in the previous η analysis. Here is a list of the ones that we will examine in some detail:

1. Contamination of the N2 and N3 monitors.

2. Background offsets in the N2 and N3 monitors.

3. Different N1 error scaling factors.

4. Different selection of signal scaling factors from the overlap plots.

The contamination of the two nonlinear monitors can be of three different types. First, part of the N2 signal can be some fraction of the linear signal. Second, part of the N3 signal can be some fraction of the linear signal. Third, part of the N3 signal can be some fraction of the second order Compton scattering signal. In general the result of such a contamination would be that the N2 or N3 readouts are offset by an amount proportional to the overall linear or nonlinear signal that contaminates the two nonlinear monitors. These proportionality factors are the variables in our
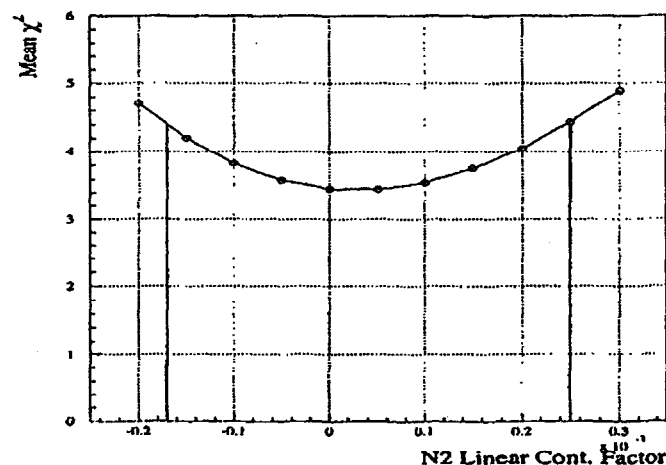
Figure 6.26: A scan of the proportionality factor used for the N2 linear contamination study. The vertical lines show the values of the proportionality factor for which $\langle \chi^2 \rangle$ changes by 1 on both sides of the minimum.

case. The method of study is rather straightforward. We scan through different values of the proportionality factors, which can always be either positive or negative, we multiply the overall linear or nonlinear signal that is the source of the examined contamination, and we add it to the signal that the nonlinear monitors read. We

have then a new $N2$ or $N3$ signal which we can use as an input to the constrained fit. This is repeated for all data points and the $\langle \chi^2 \rangle$ for each different proportionality factor that we try, is calculated. The values that give us a $\langle \chi^2 \rangle$ that differs by +1 on both sides of the minimum—definition of an 1σ error—are used to further calculate the $\langle \eta \rangle$ over the whole data sample and compare it to the default case, which is of course no contamination at all. An example of such a scan over different values of the proportionality factor in the case of linear contamination of the $N2$ signal, is shown in Fig. 6.26. It is quite obvious from this figure that the N2 monitor has no essential levels of linear contamination. It turns out that this is the case for the N3 monitor too. The background offsets in the two nonlinear monitors are quite similar things and are treated in the same way as the contamination systematics, although the source for these errors has nothing to do with different orders of Compton scattering signal. Again the study shows that the two nonlinear counters have no appreciable background offsets in their signals.

Type of error	$\Delta \langle \eta \rangle$
Contamination	+0.0089
	-0.0166
Background Offset	+0.0128
	-0.0177
$N1$ Error Scaling	+0.0006
	-0.0000
Signal Scaling	+0.0009
	-0.0044
Overall	+0.0156
	-0.0247

Table 6.6: List of the systematics due to the four cases described in the text. The numbers are absolute differences with respect to the default $\langle \eta \rangle$ which is 0.1958.

The systematic error due to different scaling of the $N1$ error, is a little different. In principle we do not have any particular reason to scale the $N2$ error instead of the $N1$ error. So we can always try to scale the $N1$ error by a factor of 2 and also by a factor of 4, which is closer to the scale factor for the $N2$ error, repeat the constrained fit again and find the relative difference of the average η with respect to the default case, where only the $N2$ error is scaled. In the same way we can study the systematic error due to different methods for computing the input to the fit signal scaling factors, using the overlap plots. Currently we have been applying the cut off at 90%, but we can also try 80% or 95%, recompute $\langle \eta \rangle$ and compare it to the default case.

The results of the systematic errors studied in the above four cases are summarized in table 6.6. We can therefore write finally:

$$\langle \eta \rangle = 0.1958 \pm 11.2\%(stat.)^{+7.97\%}_{-12.61\%}(syst.) \tag{6.53}$$

6.4 Inefficiency Corrections and Background Levels

In the previous sections we have discussed the extraction of the positron signal from our 46.6 GeV data and also the estimate of the laser intensity parameter η using the linear and nonlinear Compton scattering measurements in the three monitors. Although in principle we are in position to correlate our positron signal to the laser intensity and directly compare it to the theoretical predictions, there are a few things that we need to discuss prior to doing that. First we have to adjust the simulation predictions for the laser-electron overlap and the cluster search algorithm inefficiencies. This is because the model calculation assumes perfect spatial and temporal overlap between the laser and the electron beams and also 100% positron reconstruction efficiency. Second we have to show that the observed signal is indeed incompatible to any residual background levels that we have. These two issues are the main subjects of the discussion in this section.

6.4.1 Overlap Inefficiency Estimates

The calculated rates from the simulation and their correlations to η assume always a perfect spatial and temporal overlap of the electron and laser beams. This of course is not the case with the real data. We have therefore to correct the absolute theoretical event rates for this inefficiency before we try to compare them with the data. As already mentioned in section 4.4, during the data acquisition we periodically perform xt-scans in order to reestablish sufficient overlap conditions between the two interacting beams. We can also move the interaction region in x (X-Scan), or perform a timing scan, independently from each other. All the recorded x-positions of the
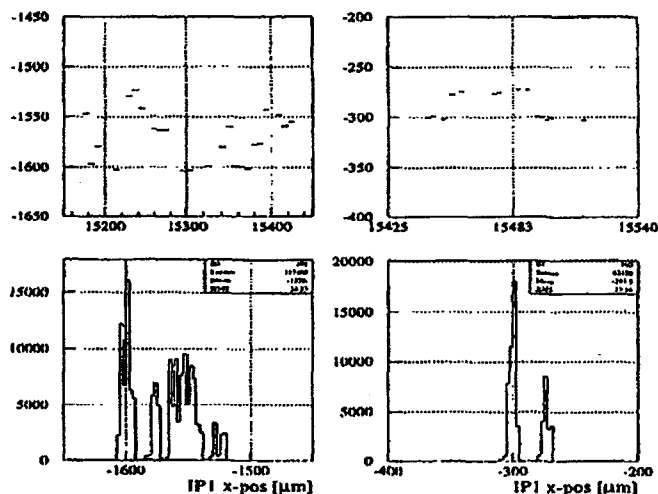
Figure 6.27: IP1 x-positions during the acquisition of the 46.6 GeV data. There are two run periods characterized by distinct x-positions. The pointing of the electron beam may have changed between those two run periods. The top doublet shows the average x-position for each data run, while the bottom triplet shows the distribution of the x-positions for the corresponding run period.

interaction region, at the end of such X-Scans, are shown in Fig. 6.27. There are

two run periods which are characterized by quite different positions and those are shown separately. The highest RMS value that we get is 25 μm. Let's assume that the different measured x offsets by the X-Scans, are nothing else but jitter in the x-position overlap, which follows a Gaussian distribution with a standard deviation of $\sigma = 25$ μm. In Fig 6.18 in the N=1 overlap plot, we can see that the 90% cutoff is at 1.25 and that we have introduced during the data analysis an overlap cut of 0.4. This, in other words, means that from the whole data sample we accept event rates as low as 33% of the expected rate at perfect overlap both in space and time. Using the simulation data, this can be translated into a timing offset. In Fig. 6.28 the
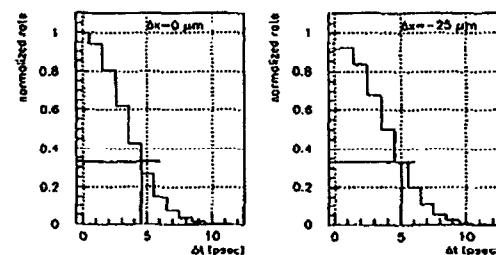
Figure 6.28: Normalized positron rate for different time and x offsets, with respect to the case where $\Delta x = 0$ and $\Delta t = 0$. The left plot has $\Delta x = 0$ μm, while the right one has $\Delta x = 25$ μm. A rate reduction by 33% is equivalent to a time offset of at most 5 ps.

results of such a simulation are shown for different time offsets and for two x-position offsets. The event rate is normalized with respect to the perfect overlap case i.e., $\Delta x = 0$ and $\Delta t = 0$. We can see that a rate reduction of 33% is equivalent to a time offset of 5 ps at most. In principle we tend to plot the positron rate normalized to the number of linear Compton γ's $Ne^+/N1$, as a function of the laser parameter η. We can therefore try different offset cases both in time and space and see by how much the normalized positron yield varies. The results are summarized in table 6.7.

Offset		Weight		Rates
x-range [μm]	t-range [ps]	σ_x [μm]	σ_t [ps]	$\langle Ne^+/N1 \rangle$
±25	0-5	25	5	0.883
±30	0-5	25	5	0.852
±20	0-5	25	5	0.913
±25	0-6	25	5	0.875
±25	0-4	25	5	0.890
±25	0-5	∞	5	0.870
±25	0-5	25	∞	0.880
±25	0-5	∞	∞	0.867
±30	0-6	∞	∞	0.813

Table 6.7: List of corrections that we need to apply to the simulation normalized positron rates due to overlap inefficiency. Different cases of x and time offsets are shown here. A weighing of the positron signal using a 2-D Gaussian with the σ's shown is done.When $\sigma = \infty$ the weighing distribution is flat. The overall scaling factor for the simulation rates is 0.88 ± 0.07.

The simulation rates are weighed by a two-dimensional Gaussian distribution, with the σ's shown in the table, centered around the $\Delta x = 0$ and $\Delta t = 0$ case, assuming that the off peak signal distribution follows a Gaussian curve both in space and time. The case where $\sigma = \infty$ makes the rather unrealistic assumption of a flat distribution. In all the above, only the x-axis offset is studied. We can always have an offset in the y-axis too. Similar studies for such a case show that the normalized to the peak signal positron yield does not change significantly for any reasonable y offset. We can therefore conclude that the correction factor that we need to apply to the simulation results due to spatial and temporal overlap inefficiencies, is 0.88 ± 0.07.

6.4.2 Cluster Search Algorithm Efficiency

There is one more correction that we need to apply to the simulation data and this has to do with the inefficiency of the cluster search algorithm described in section 6.1. Although in principle this algorithm should have 100% efficiency in detecting positron clusters in the data sample, this nevertheless is not necessarily the case, especially when the positron signal is buried under high levels of background. Fortunately the background levels during the data runs were adequately low and therefore we expect sufficiently high efficiency of the cluster search algorithm. To study this, 5000 simulated positron events are created using a Monte Carlo method that takes into account the whole geometry of the accelerator's area between the electron-laser interaction point and the positron detector (PCAL), including the settings of the bending magnets in the spectrometer and the thickness of the pipe walls and the surrounding vacuum chamber enclosures. These simulated positron events hit PCAL at specific positions according to the momentum map described in section 5.1 and therefore their momentum and also their position and their incident angle on PCAL are well known. To these "real" events we add background using events from runs arranged in five groups that span the whole duration of the 46.6 GeV data taking period. The five groups are:

1. GROUP 1: Runs 15188, 15195. Early runs, small laser energy.

2. GROUP 2: Runs 15296, 15299, 15304, 15323. Good runs, high laser energy.

3. GROUP 3: Runs 15422, 15424. Runs with small signal and bad overlap conditions.

4. GROUP 4: Runs 15371, 15381, 15385, 15389. Runs with intermediate laser energies.

5. GROUP 5: Runs 15494, 14495, 15497, 15509. Last 46.6 GeV runs.

Laser OFF Background		laser ON background	
Group Number	Inefficiency (%)	Group Number	Inefficiency(%)
1	6.5	1	7.2
2	5.7	2	7.1
3	5.9	3	6.9 ·
4	5.9	4	6.7
5	5.7	5	5.9
Average	5.9	Average	6.8

Table 6.8: Inefficiency of the cluster search algorithm when different background cases are used. It is obvious that laser ON based background leads to a slightly higher inefficiency of the cluster search code.

Then we apply the cluster search algorithm to find the simulated positron clusters, along with their positions on PCAL and their corresponding momenta, and we compare their values to the ones that we already know for the simulated positron events. If they match we know that we have retrieved a "real" positron. The portion of the input simulation positrons that we are able to retrieve in this way gives us a measure of the efficiency of the cluster search algorithm. We can add two types of background from the runs listed above, either using laser OFF events, or laser ON events. Both cases are examined and the results are shown in table 6.8. It is clear from the table that the efficiency of the cluster algorithm is very high, although there is a slight difference between the efficiencies when the added background is based on laser ON or laser OFF data. The worst case gives us a correction factor of 0.93 to use with the simulation event rates.

6.4.3   Backgrounds

We can always try to plot the number of positrons found per laser shot as a function of the laser intensity parameter η. Such a plot is shown in Fig. 6.29. The solid line
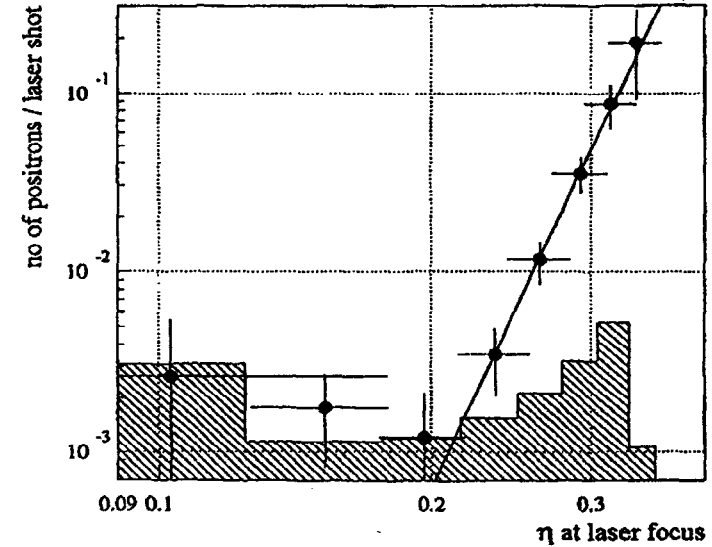
Figure 6.29: Dependence of the positron rate per laser shot on the laser intensity parameter η. The solid line shows a power law fit to the data. The shaded distribution is the 95% confidence limit on the residual background from showers of lost beam particles after subtracting the laser off positron rate.

is a power law fit to the data and it will be discussed in more detail in chapter 8. Of bigger importance to our present discussion, is the shaded region shown in that plot. It shows the 95% confidence limit on the residual background, which can be attributed to showers of lost beam particles, after subtracting the laser OFF rates. This 95% confidence limit is calculated, assuming a Poisson distribution of the background signal, as follows: During the 46.6 GeV data analysis, we have found 379 background positron clusters in 121216 laser OFF triggers. This gives us $\sim 3 \times 10^{-3}$ background positrons per laser OFF trigger over the whole 46.6 GeV data sample. Now in order to plot the number of signal positrons per laser shot as a function of η, we have binned them in 8 bins, each one of them containing some specific number of laser ON triggers adding up to 17328, the total number of laser ON triggers examined. Since we know

the average number of background positrons per laser OFF trigger, we can multiply it with the number of laser ON triggers in each of the 8 bins in Fig. 6.29, and find the average number of background positrons in each bin. Let's call this number a. We can then find the Poisson distribution that corresponds to this average number of background positrons in the examined bin. The 95% confidence limit is nothing else but the number of background positrons, call it n, for which with 95% probability, the number of background positrons is n or less. The difference n-a divided by the number of laser ON shots in each bin, is the 95% confidence limit shown in Fig. 6.29. It is clear that the data points at the lower η values, although statistically consistent with the multiphoton pair production process, do indeed indicate the presence of such residual background of 2×10^{-3} positrons per laser shot.

Chapter 7

49.1 GeV Data Analysis

In this chapter we present the analysis procedure followed for the 49.1 GeV data sample. It follows the same steps as the 46.6 GeV data analysis where the more cumbersome details can be found. There are nevertheless a few differences. The first, related to the higher background levels, results in a different way of selecting the initial data sample that will be analyzed. This is the main subject of section 7.1. The second is statistics. The reconstruction of the laser intensity parameter η using the constrained fit method, requires a certain quality of monitor signal, otherwise either it will fail, or it won't be applicable any more. As mentioned in chapter 5, many N2, N3 events are lost with the dropout cuts which are not related to monitor malfunctioning, but rather to trigger misinterpretation. Real positron events for which the triggering of the N2 and N3 readouts was confused, will be lost. In the 46.6 GeV data sample, this did not cause any serious problems, because the signal positrons were fairly numerous and in any case they were not reduced substantially. This is not the case any more for the 49.1 GeV data, for which the signal positron sample is very limited due to the existing background levels and to the smaller efficiency of the laser-electron interactions. We need therefore to recover all the "lost" positron events for which the constrained fit was unable to reconstruct an η from the monitor signal, by finding an alternative method for computing η. As it will be shown in section 7.3.3, ECAL can

be used to this end. Besides those two main differences in the analysis of the 49.1 GeV data sample, this chapter otherwise resembles much the previous chapter, and it therefore assumes a certain familiarity with most of the issues discussed there. As in the 46.6 GeV data analysis chapter, the final results, along with a comparison to the 46.6 GeV results, is reserved for the next chapter.

7.1   Selection of the Data Sample

One major difficulty that the 49.1 GeV data analysis has to face, is the existence of higher background levels. As mentioned in the electron beam chapter, raising the energy of the electron beam is an operation for which some aspects of the FFTB line are not well suited, and more important, an operation for which not much previous experience existed. For example, the field of the permanent bending magnets at the dump line, was fixed at a value appropriate only for a 46.6 GeV beam. As described in section 3.5, the magnetic field of the soft bends around the interaction region (IP), had to be raised to their maximum values, resulting in a less stable configuration. The FFTB dump line is in general an area of tight apertures and scrapping of the electron beam here, is the major cause for higher background levels. This is more likely to happen with higher electron beam energies. Beam tuning in the way that it was described in chapter 3, can improve the situation.

The effect of beam tuning on the observed background levels, during the 49.1 GeV data taking, is shown in Fig. 7.1. The figure shows the number of laser OFF clusters found in PCAL per laser OFF trigger, for each individual data run. It is clear that during the first half of runs, the background levels are getting worse as we are moving on in time, and become really high after run 15600. After run 15620, a considerable steering of the electron beam took place, especially by adjusting the position of the quads in the Beta Match region of the FFTB line. The vertical line in the plot indicates the end of the beam steering effort. It is obvious that the backgrounds
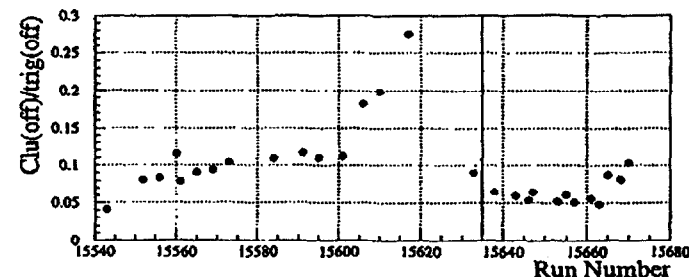
Figure 7.1: Number of background positron clusters per laser OFF trigger for each of the 49.1 GeV data runs. Notice that the background reaches very high levels, especially after run 15600. At the end of run 15617 a considerable beam steering takes place in order to lower the background levels. The vertical line shows the end of such steering and the start of normal data taking again. Only the runs after this line, for which the background levels are on average considerably lower, have been used for the 49.1 GeV data analysis.

have dropped considerably, on average by about a factor of 2 with respect to the runs before. One more important change took place during the same period. The compressor voltage was set to 42 MV, increasing the bunch length from 4.7 ps FWHM during the earlier 49.1 GeV runs, to 8.6 ps for the rest of the 49.1 GeV data taking period, as the table 3.1 in chapter 3 shows. This led to an improvement in the laser-electron time overlap.

Taking into account these two last modifications, the 49.1 GeV data sample judged suitable for further analysis, is restricted to runs 15637 and higher. These include the last 12 out of a total of 28 49.1 GeV data runs and contain about 32,000 laser ON and laser OFF triggers. For the earlier runs the high background levels make it impossible to retrieve any meaningful positron signal out of the data.

7.2   49.1 GeV Positron Search

7.2.1   Cluster Selection Cuts Tuning

The cluster selection algorithm described in section 6.1 of the previous chapter, is applied to this data sample. It is very important during this step to use the correct momentum map, when we translate the vertical position of an incident positron in PCAL into a momentum value. This affects the efficiency of the cluster search al-
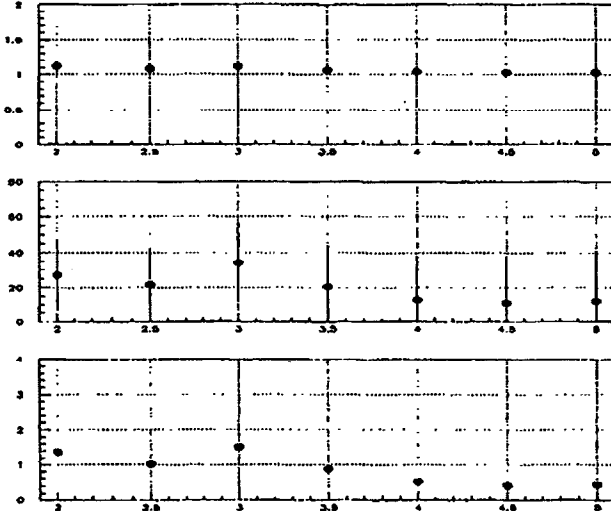
Figure 7.2: Ratio of signal to noise, number of positrons and statistical significance as a function of single hit cluster range in units of σ.

gorithm itself, and even more so the validity of E_{clu}/p_{clu} (what we call number of positron hits N_{hit}), as a function of the vertical position in PCAL plot. The selection of the single positron hits is the first important selection criterion that we apply to our data sample and the correctness of the E_{clu}/p_{clu} map is essential. Fig. 7.2 shows

the tuning of the E_{clu}/p_{clu} range. The units are again in Gaussian σ's, as defined in section 6.2.2. We show the signal to noise ratio, the number of positrons found and the statistical significance. The vertical error bars for the first two quantities are
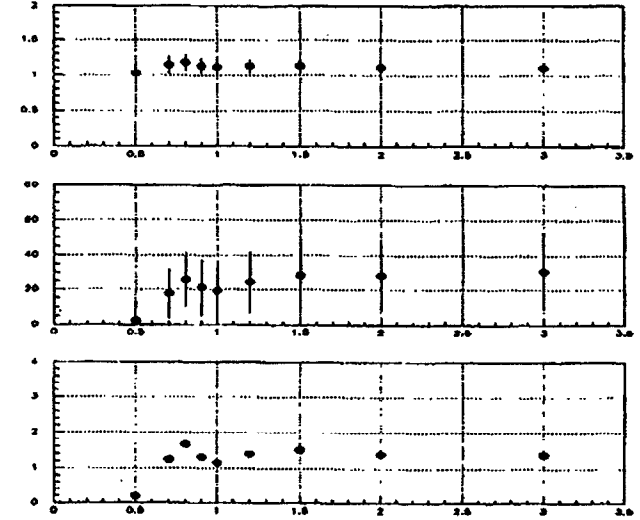
Figure 7.3: Ratio of signal to noise, number of positrons and statistical significance as a function of cluster x-position selection range in units of σ as defined in text.

and the statistical significance. The vertical error bars for the first two quantities are calculated by the expressions

$$\delta R = \sqrt{\frac{S}{a^2 B^2}\left(1 + \frac{S}{B}\right)} \qquad (7.1)$$

$$\delta N = \sqrt{S + a^2 B} \qquad (7.2)$$

where R the signal to noise ratio, B the number of background positron clusters, S the number of signal positron clusters and a the ratio of the laser ON over the laser OFF triggers. Looking at Fig. 7.2, the best results correspond to a selection range of $\pm 3\sigma$.

For this single hit selection range, we can go ahead and tune the horizontal PCAL position selection range as in section 6.2.2. Fig. 7.3 shows the results of such tuning with the same quantities as in Fig. 7.2 plotted. The horizontal axis is in units of σ where 1σ is defined as half the range that excludes the lower and upper 3% of the horizontal incident positron position, as described in section 6.1 of the previous chapter. The optimal x-position selection range is $\pm 0.8\sigma$.

7.2.2   Overlap Cut Tuning. Results

Comparing Fig. 7.3 to Fig. 6.7 of chapter 6, we see very clearly that the positron signal in the 49.1 GeV data sample is much lower than the one from the 46.6 GeV data. We still need to apply the overlap cut, defined as the ratio of the measured $n = 1$ gammas, over the number expected from the simulation $N_\gamma^{data}/N_\gamma^{sim}$. The introduction and the tuning of this final cut is shown in Fig. 7.4. It is interesting to note first that the statistical significance of the signal improves considerably, and second that the number of positrons does not seem to be affected much, unless we require very high overlap values, in which case most of the signal normally will be cut away. The reason behind this is not difficult to explain. As already mentioned in section 7.1, the current 49.1 GeV data sample consists of only those data taken after the bunch length of the electron beam has been increased considerably. This results in improved overlap conditions, since a longer electron beam bunch has a higher probability to collide with a laser pulse. Essentially the selection of the 49.1 GeV data sample, already resembles some kind of an overlap cut. Looking at Fig. 7.4, the best overlap cut is that for which $N_\gamma^{data}/N_\gamma^{sim} \geq 0.6$. Table 7.1 summarizes the results of the positron search analysis. Notice that the signal to noise ratio is half that from the 46.6 GeV case, reflecting the higher background levels. Also the statistical significance is only 2.2σ, as compared to more than 7σ for the 46.6 GeV data.

Fig. 7.5 shows the 49.1 GeV positron spectrum. The top plot shows the momentum spectra for the laser ON and the laser OFF positrons separately, the latter after being
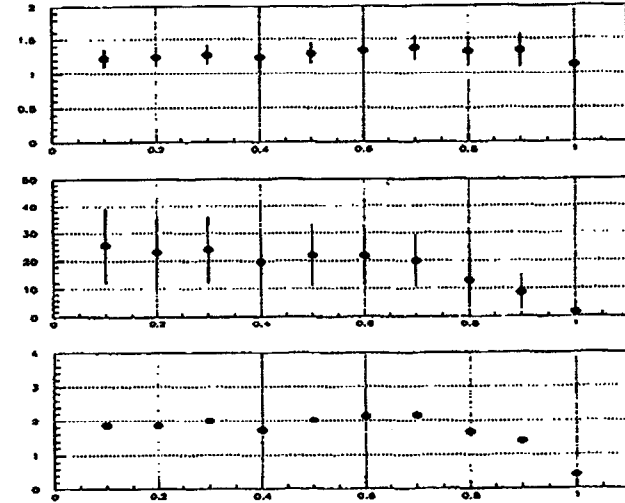
Figure 7.4: Ratio of signal to noise, number of positrons and statistical significance as a function of different N=1 overlap cuts.

49.1 GeV Data Results						
Cut Type	Laser ON	Laser OFF	Trig. Ratio ON/OFF	Sig/Noise	Ne^+	Statistical Significance
Optimal Cuts	5159	21034	0.2453	1.33±0.16	22±10	2.2σ

Table 7.1: Results from the 49.1 GeV data after introducing all the cluster selection criteria and the overlap cut, as mentioned in the text.

scaled down according to the ratio of the laser OFF over the laser ON triggers shown in table 7.1. There are 9 momentum bins, each 2 GeV/c wide. The bottom plot shows the momentum spectrum of the background subtracted positron signal per GeV/c. The vertical error bars have been calculated by using Eq. 7.2, while the
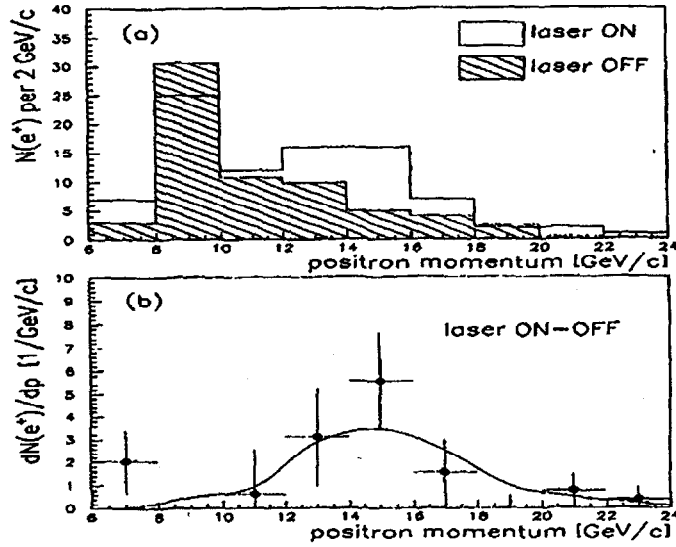
Figure 7.5: Momentum spectrum for the produced 49.1 GeV positrons. The top plot shows the momentum spectra of the laser ON and laser OFF clusters, the latter being scaled by the appropriate trigger ratio. The second plot shows the momentum spectrum of the background subtracted positrons. The solid line is the theoretical prediction.

horizontal error bars reflect the 2 GeV/c momentum bin width. The solid line shows the expected theoretical spectrum which agrees with the data within the large errors.

7.3 Estimates of the Laser Intensity Parameter η

7.3.1 Constrained Fit Setup

As for the 46.6 GeV data sample, the constrained fit method is used for the 49.1 GeV data in order to reconstruct the laser intensity parameter η from the signal rates reported by the three monitors N1, N2, N3. Either of the two signal ratios N2/N1

or N3/N2 can be used to give us η, and the η estimates of the two ratios have to be the same, resulting in the constraint expression,

$$\eta^2(N2/N1) = \eta^2(N3/N2) \tag{7.3}$$

For $\eta^2 \ll 1$, the functional dependence of η^2 on either of the two ratios N2/N1 or
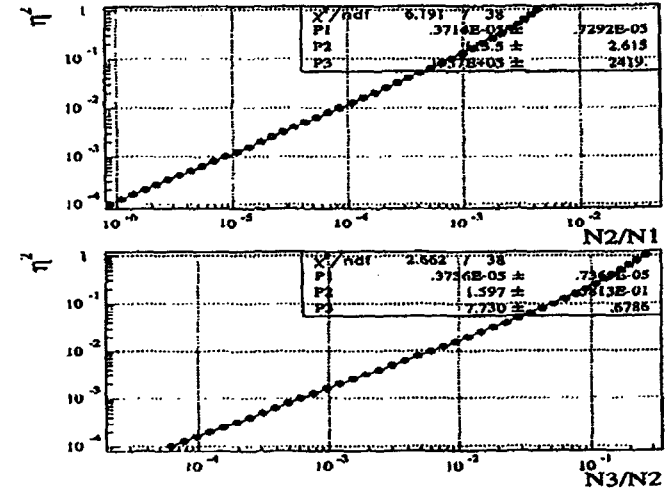
Figure 7.6: Polynomial fits of η^2 as a function of either of the ratios N2/N1 and N3/N2 using 49.1 GeV simulation data. The η^2's derived by each of the two expressions, have to be the same for a specific event where all the three counters have reported signal.

N3/N2, is rather linear. For larger η^2 values though, this is not quite the case, and a more accurate relation can be obtained by using the predictions of the simulation for the signals of the three monitors N1, N2, N3, once their acceptances are folded in. For the 49.1 GeV data sample, this is shown in Fig. 7.6. The functional expressions shown in that plot are the ones that need to be used in the constraint of Eq. 7.3. The steps followed by the constrained fit algorithm are identical to the ones described in

the 46.6 GeV data analysis. The error on the final estimates of η is also computed in the same way,

$$(\Delta f)^2 = \sum_{m,n} \frac{\partial f}{\partial x_n} \frac{\partial f}{\partial x_m} V_{mn} \tag{7.4}$$

where V_{mn} is the variance matrix as is computed by the constrained fit and the derivatives are taken with respect to the new monitor signals calculated by the fit. In the above equation f denotes some general functional expression, and in our case we need to use the ones from Fig. 7.6.

We can also use the constrained fit to introduce a probability cut on the 49.1 GeV data. As already mentioned in the previous chapter, we need to find scaling factors for the N1 monitor signal and the N2 monitor error, so that the probability distribution of the data at the end of the constrained fit, is fairly flat for most of the range and has a peak at the very low probabilities, as shown in Fig. 6.15 in the previous chapter. This is because we have shown that if the N3 monitor signal were not characterized by the long tails towards the higher values apparent in the laser OFF events, the probability distribution would be flat. The effect of the N3 monitor signal tails is the peak at the lower probabilities. By cutting the events at the peak, we are cutting the events for which this effect is more pronounced. For the 49.1 GeV data examined here, the N1 monitor signal needs to be scaled by a factor of 2, and the N2 monitor signal error by a factor of 2.25. The resulting probability cut is set at 1.6%, the same way that Fig. 6.16 in chapter 6 shows. After applying this cut we lose about 270 laser ON events. As in the 46.6 GeV case, the probability cut requires to perform the constrained fit once for the data, with the signal and error scaling mentioned earlier, apply the cut on the resulting probability distribution and then repeat the fit on the remaining data events once more, in order to reconstruct η.

7.3.2 Scaling of the Input Signal

In the 46.6 GeV data analysis, we have decided that constrained fit convergence issues force us to scale the input signals from the three monitors N1, N2, N3. It turns out
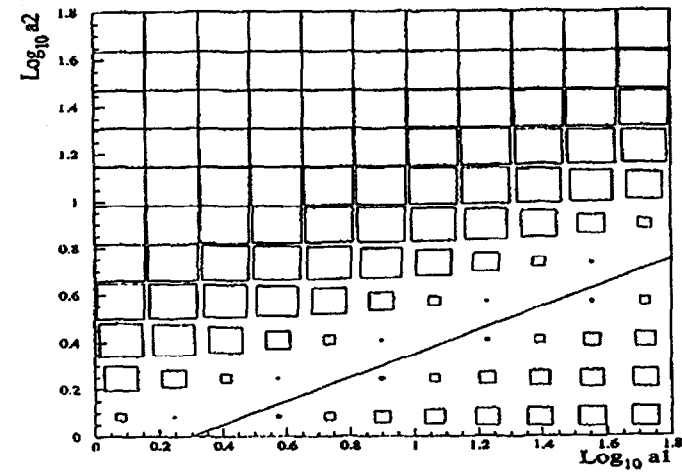
Figure 7.7: A two-dimensional histogram that shows the variation of the $\langle \chi^2 \rangle$ for different combinations of the scaling factors a_1 and a_2 for the N1 and N2 signals respectively. The logarithms of the two scaling factors are shown in each axis. Notice that there is always a combination of scaling factors that can minimize the $\langle \chi^2 \rangle$ independently of how big the actual scaling is. The solid line along the "valley" shows the functional relation of such a combination of scaling factors. We can write $a_1 = 2.0\, a_2^2$.

that this is the case for the 49.1 GeV data sample too. It is not clear at first glance how we should scale the signals of those monitors. Fig. 7.7 demonstrates this ambiguity in choices. Here different scaling factors a_1 and a_2 for the input signals from the N1 and N2 monitors respectively are tried simultaneously, and the $\langle \chi^2 \rangle$ of the whole data sample at the end of the constrained fit is calculated. It is clear again by looking at the plot, that there is a wide range of different a_1 and a_2 scaling factor combinations, that give an equally small $\langle \chi^2 \rangle$. The "valley" shown there, which corresponds to the minimum $\langle \chi^2 \rangle$ values, is described by the relation between the scaling factors examined,

$$a_1 = 2.0\, a_2^2 \tag{7.5}$$

and generalizing in order to include an N3 signal scaling factor a_3,

$$a_1 a_3 = 2.0 a_2^2 \qquad (7.6)$$

As argued in chapter 6, the quadratic dependence on the $N2$ scaling factor is expected.

The N=1, N=2, N=3 overlap distributions, as defined in section 6.3.6, give us the tool to select the appropriate scaling factors. At first we need to find the cutoff values that contain 90% of each of the overlap distribution contents. These numbers need to be adjusted so that they satisfy Eq. 7.6. The final scaling factors obtained for the three monitor signals are: [1]

$$a_1 = 1.01 \quad a_2 = 3.79 \quad a_3 \simeq 7.11 \qquad (7.7)$$

To normalize the $\langle \chi^2 \rangle$ to ~ 1 we can also scale the $N2$ error by a factor of 2.25. The choice between scaling the $N2$ or the $N1$ error is one of the sources of our systematic errors. The study of whether this scaling factor procedure does converge to a specific set of η values, after a number of iterations where the results of the previous iteration are used as inputs to the next, needs to be repeated for the 49.1 GeV data. Table 7.2 shows the results of this study. As in the 46.6 GeV data analysis, some scaling of the η's of the previous step before we used them as an input to the next step, is done to speed up the convergence process. In step 3 the scaling factor of 0.8 is too low and in steps 4 and 5 it is increased to 0.85 and 0.86 respectively for better results. Step 6 does not involve any scaling of the output η's from step 5. After the last iteration the relative change of the error on η $\langle \Delta \delta \eta / \delta \eta \rangle$, becomes also small and about 0.08%. So also for the 49.1 GeV data the monitor signal scaling method converges.

7.3.3   Recovery of Lost Data Points with ECAL

At the end of the constrained fit, we find that the number of laser ON triggers for which η is reconstructed is 4254. Therefore we lost from the initial input number of

[1]The 49.1 GeV analysis was carried out before the error in the N2 monitor calibration was fixed, as in the 46.6 GeV case. When the N2 calibration is properly corrected, the $N2$ and $N3$ scaling factors become almost identical.

Iteration #	$\Delta\langle\eta\rangle/\langle\eta\rangle$	$N1$ Sc. Factor	$N2$ Sc. Factor	$N3$ Sc. Factor
2	-3.7%	1.01	2.86	4.04
3	+1.5%	1.01	4.23	8.86
4	+0.4%	1.01	3.85	7.35
5	+0.14%	1.01	3.79	7.09
6	-0.07%	1.01	3.79	7.11

Table 7.2: Relative change of the constrained fit $\langle\eta\rangle$ after every iteration of the constrained fit using the results of the previous step. In order to speed up the convergence process the η's from step 2 are scaled by a factor of 0.8 before they are used as an input for step 3. Apparently we overshot and in step 4 the η's from step 2 are scaled by a factor of 0.85. In order to improve the relative change of $\langle\eta\rangle$, the η's from step 2 are scaled once more by a factor of 0.86 before being used as an input in step 5. For step 6 the output η's from step 5 are used directly as an input without any scaling. The corresponding scaling factors for the three monitor signals are also shown in each iteration.

5159 Laser ON triggers 905 events. What is really bad is that out of the 22 signal positrons that we were able to find after applying the positron selection criteria and the overlap cut, we are left with only 14 for which an η estimate exists. There are several reasons that explain the loss of those 905 laser ON events. The first and most important is the dropout cuts applied on the N2 and N3 monitor signals, as described in section 5.3.3. Due to this cut we lose ~ 600 events. The second reason is the probability cut, which costs us 270 laser ON events. The remaining few events are due to fit convergence failures. Careful inspection shows that all the 8 positrons come from events that are thrown away by the dropout cut. In principle these positron data are perfectly valid, since the dropout cuts are introduced to resolve a trigger misinterpretation problem, and are not related to monitor malfunctioning. We are faced with a severe problem of low statistics, which we can partially alleviate if we can find a way to estimate the η of those events for which the constrained fit cannot.

The electron calorimeter (ECAL) can provide us with such an alternative. ECAL
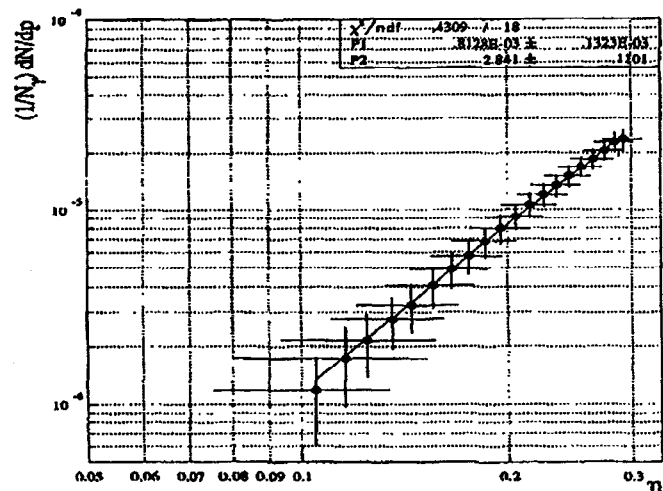
Figure 7.8: Functional dependence of the simulated ECAL rate $\frac{1}{N_\gamma}\frac{dN}{dp}$, with dN the number of electrons within the momentum bin dp, and η the laser intensity parameter calculated by the constrained fit. They follow each other pretty well in a power law expression, as the fit shows.

is a movable detector that can be moved vertically probing different orders of nonlinear Compton scattered electrons. This results in a variable momentum acceptance for each one of its rows, according to its vertical position. For the 49.1 GeV data used in the positron analysis, ECAL is kept fixed in one position, for which its top row looks at $n = 3$ Compton scattered electrons. That means that we can compute the momentum acceptance of that row using the momentum map and this acceptance remains fixed for all the 49.1 GeV data analysed. For events for which η is reconstructed from the constrained fit, we can use the simulation prediction—η is the main input to the simulation— to compute the expected normalized ECAL rate defined as

$$\dot{R} = \frac{1}{N_\gamma}\frac{dN}{dp} \tag{7.8}$$

where N_γ, the linear monitor signal, dN the number of electrons that the top row of ECAL detects and dp the momentum acceptance of that row from the momentum
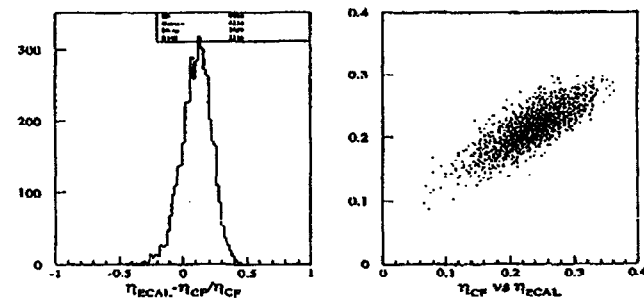
Figure 7.9: Comparison of the η's calculated by both the ECAL method, described in the text, and the constrained fit method, for all the events that the results from both methods are available. The ECAL reconstructed η is bigger than the constrained fit η, by about 10%.

map. As we will see in Appendix 3, the simulated ECAL rate R, as defined in Eq. 7.8, agrees with the corresponding measured ECAL data rate R to within less than a factor of 2, which is compatible to an error of the η estimate from the constrained fit of $\sim 10\%$. Since we have the constrained fit η estimates and the simulation predictions for the ECAL rate in the form of Eq. 7.8, we can plot them in a logarithmic plot and extract a law that translates ECAL rates to η value predictions. This law can then be used with the measured ECAL rates, again brought in the form of Eq. 7.8, to give us an η value for those data events for which the constrained fit failed to do so. Such a plot of the ECAL rate as a function of η in a logarithmic scale is shown in Fig. 7.8. Since ECAL was kept fixed in a position where the top row intercepts $n = 3$ Compton scattered electrons, we expect a straight line with a slope that indicates the order of the nonlinear Compton scattering process, as it is clear in Fig. 7.8. In this plot we have used 20 equally wide bins in η. The vertical and horizontal error bars correspond to the RMS values of the ECAL rate R and η distributions in each bin

divided by the corresponding number of points, added in quadrature to the average statistical errors of R calculated as,

$$\delta R = \sqrt{(\frac{1}{N_\gamma^2}\frac{dN}{dp}\delta N_\gamma)^2 + (\frac{1}{N_\gamma dp}\delta dN)^2} \qquad (7.9)$$

and of η as given by the output of the constrained fit. The slope of the straight line fit is ~ 3 (for an explanation why it is 3 and not 4 as expected from $2(n-1)$ with $n = 3$, see [50] and also Appendix 3). We have now a simple expression that provides us with the means to translate measured ECAL rates in the form of Eq. 7.8, to η estimates for data events that the constrained fit cannot provide us with an η value. The error on η calculated in this way will be,

$$\delta\eta = \frac{\eta}{R\,b}\,\delta R \qquad (7.10)$$

where δR is the error on the ECAL rate from Eq. 7.9, and b is the slope of the straight line shown in Fig. 7.8. Fig. 7.9, shows a comparison between the η's returned by the constrained fit and the η's computed from ECAL as described above. The ECAL η's are on average higher than the fit η's by $\sim 10\%$. This turns out to be compatible with the average error on η from the constrained fit. The 10% difference between the two estimates shouldn't surprise us, since the employment of the simulation predictions to extract a law that translates measured ECAL rates to η estimates, introduces an intrinsic error on η of that order.

7.3.4 η Estimates and Verification

Once we have estimated the η's on an event-by-event basis, it is interesting to compare them with the η estimates from the laser parameters, *i.e.* the measured laser energy and the fixed laser area and pulse width at 30 μm^2 and 1.5 ps respectively. Fig. 7.10, shows the results of such a comparison. The η values from the fit, contain reconstructed η's from both the constrained fit and ECAL. It is clear that the laser parameters systematically overestimate η by more than 30%. The average value and
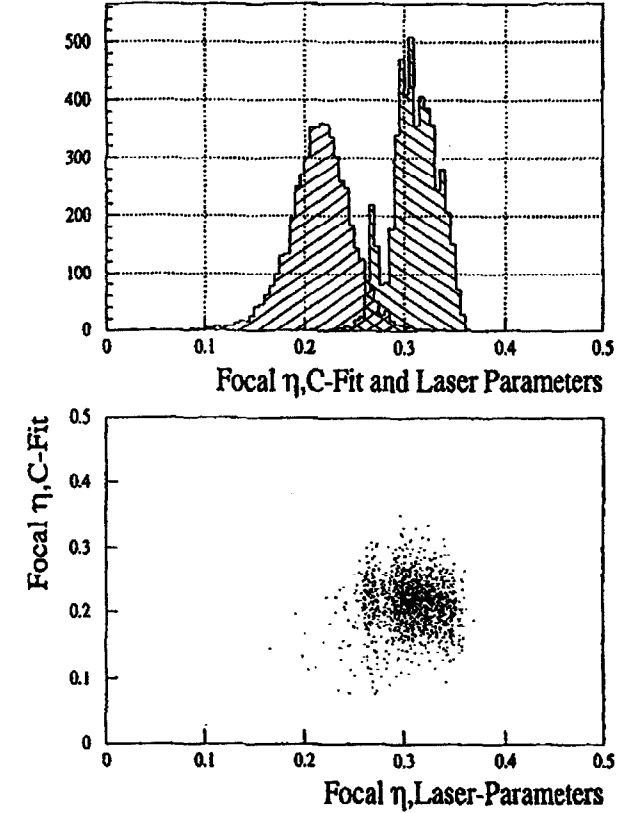
Figure 7.10: Comparison of the values of η calculated using the constrained fit or ECAL, with those from the laser parameters. The top plot shows the η distributions according to the two methods, while the bottom is a scatter plot of the two η values. The η estimated from the laser parameters is larger than the reconstructed η.

error of the reconstructed η is:

$$\langle\eta\rangle = 0.218 \pm 0.02 \quad \text{or} \quad \langle\eta\rangle = 0.218 \pm 9.2\% \text{ statistical error} \qquad (7.11)$$

In the case of the η values reconstructed by the constrained fit we can still try to check their validity by using ECAL data. As for the 46.6 GeV data, 49.1 GeV ECAL scans are used for this purpose. We look at the normalized electron rate of the top row of ECAL, as defined by Eq. 7.8, and compare the measured rate with the one predicted by the simulation, when the η's reconstructed by the constrained fit are used as an input. Fig. 7.11 shows such a comparison. There are only four data runs
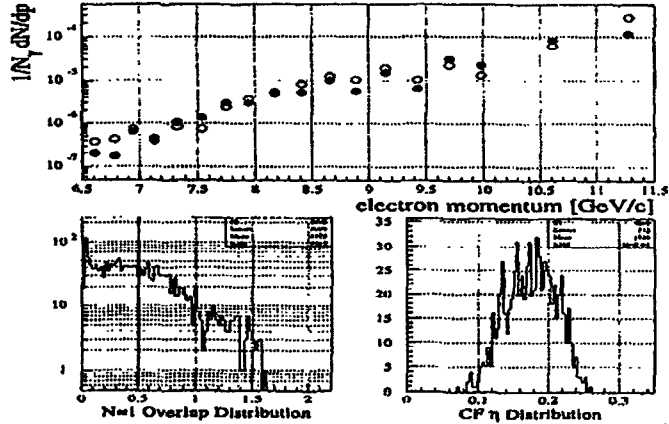
Figure 7.11: Verification plots for the 49.1 GeV runs. The top plot shows the number of electrons per momentum bin normalized to the total number of linear Compton photons, as a function of the momentum of the intercepted electrons. The black dots are the data points and the white the simulation results. The bottom left plot shows the distribution of the $N1$ overlap as it is defined in section 7.3.2. The vertical line is the overlap cut used. The bottom right plot shows the distribution of the η's from the constrained fit. For all the plots the 49.1 GeV ECAL scans 15565, 15606, 15610 and 15617 are used.

during which ECAL was scanned, runs 15565, 15606, 15610 and 15617. The data from all these ECAL scans are used. Although all four ECAL scans used here are not included in the 49.1 GeV data sample used to search for positrons, we can still reconstruct the η values for their laser ON events, using the constrained fit. Fig. 7.11,

is the only plot in this chapter that contains data outside the 49.1 GeV data sample, as selected in section 7.1. Everywhere else in this chapter we refer only to that data sample.
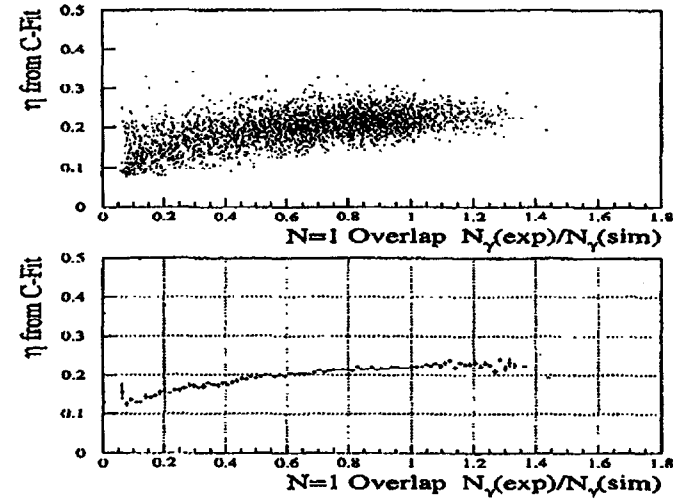
Figure 7.12: Stability of η with the N=1 overlap. Here the overlap is defined in the same way as in section 7.3.2, i.e. as the ratio of the measured $N1$ rate over that expected from the simulation. It is clear that for overlap greater than 0.6, which is what we have been using in the whole 49.1 GeV data analysis, η remains pretty much stable.

There is one more thing that we need to verify, and this is how independent the reconstructed by the constrained fit η is from the N=1 overlap efficiency. Since η is a measure of the laser intensity, it has to be independent of any overlap fluctuations. Fig. 7.12 shows the dependence of η on the N=1 overlap, as defined in section 7.2.2. We can see that the reconstructed η's for data points with overlap greater than 0.6, which is the overlap cut used in the analysis, are fairly stable. Another way of defining the N=1 overlap, is by looking at the number of the measured forward γ's. In order
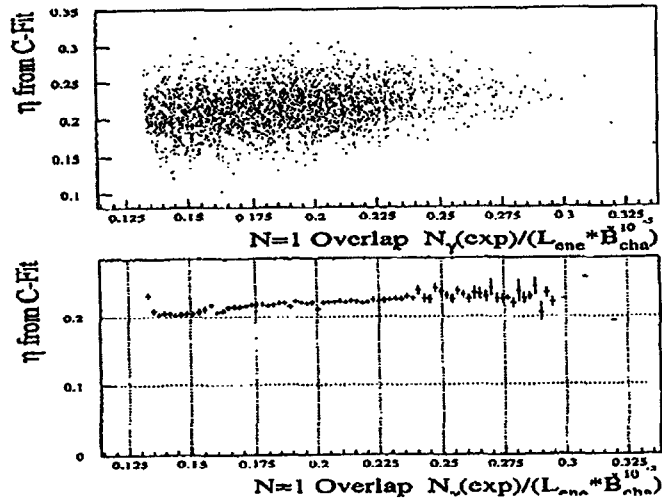
Figure 7.13: Stability of η with the number of γ's measured by the linear Compton monitor. This number once it is normalized over the laser energy and the electron beam charge, it depends only on the overlap fluctuations, and it can therefore provide us with an alternative measurement of N=1 overlap. Only events with N=1 overlap greater than 0.6 are used.

to avoid the effects of the fluctuations of the laser energy and the beam charge, they have to be normalized to those two quantities. Fig. 7.13, shows the reconstructed η dependence on the N=1 overlap defined in this way. Only events with overlap greater than 0.6, are used. Again the stability of the reconstructed η is very good.

7.3.5   Study of Systematics

The study of the systematics on η for the 49.1 GeV data is done in the same way as the similar study on the 46.6 GeV data. The sources for the systematics examined are:

1. N2 and N3 monitor contamination.

2. Background offsets in the N2 and N3 monitors.

3. $N1$ error scaling instead of the $N2$ error.

4. Different signal scaling factors, using the overlap plots.

The contamination of the N2 monitor signal, has again its source in the linear Compton scattered electron signal. The N3 monitor signal can contain both linear and second order contamination. For the study of the contamination systematics, the concept of scaling factors that define the portion of the total linear or second-order Compton scattered signal that contaminates the two monitors, is introduced in the same way that this is done in section 6.3.8 of the previous chapter. Different values of these scaling factors are applied, both positive and negative, and the resulting fraction of the linear or second-order Compton signal is added to the monitor readout signals. These new resulting monitor signals are processed through the constrained fit code, and the average $\langle \chi^2 \rangle$ is estimated, for all processed events. This method gives us a way of deciding whether the two monitors are indeed affected by any severe contamination levels. As in the 46.6 GeV case, it turns out that this is not the case, since the minimum $\langle \chi^2 \rangle$ occurs when no contamination or insignificant contamination is introduced. In addition, we can deduce the ranges for which the $\langle \chi^2 \rangle$ changes by $\pm 1\sigma$, and that forms a quantitative measure of the systematic error. The background offsets are also studied in a similar way, as explained in section 6.3.8.

The systematic error due to the scaling of the $N1$ error instead of the $N2$ error is treated in a different way from the previous cases. The $N1$ error is scaled by a factor of 4, which is close to the factor that the $N2$ error has been scaled by, and the effect on the resulting η values from the constrained fit is evaluated. Their value difference from the $N2$ error scaling, gives the systematic error due to the different monitor error scaling. As in the 46.6 GeV case, this source of systematic errors, is the least significant. The different monitor signal scaling factors deduced from the overlap

plots, are also a source of systematic errors on η that can be studied in the same way. As mentioned in section 7.3.2, the 90% cutoff in the overlap plots is used. Two other different cutoff values at 95% and 80% can also be used to derive new scaling factors for the monitor signals, and compute the η values from the constrained fit. The differences of these new η's from the 90% case, give the systematic error estimate due to different scaling factors.

Table 7.3 summarizes the results of the above studies on the systematic errors on the η values. To these systematic error estimates the +10% discrepancy between the η

Type of error	$\Delta\langle\eta\rangle$
Contamination	+0.0083
	-0.0134
Background Offset	+0.0082
	-0.0151
$N1$ Error Scaling	+0.0004
	-0.0000
Signal Scaling	+0.0000
	-0.0025
Overall	+0.0117
	-0.0204

Table 7.3: List of the systematic errors due to the four cases described in the text. The numbers are absolute differences with respect to the default $\langle\eta\rangle$ which is 0.2183.

values calculated by the constrained fit and the measured ECAL rates, as discussed in section 7.3.3, needs to be added. Then the overall systematic error becomes $\langle\eta\rangle^{+0.0117}_{-0.0306}$. Thus the average value of η for this data sample is:

$$\langle\eta\rangle = 0.2183 \pm 9.2\%(stat.)^{+5.35\%}_{-14.02\%}(syst.) \tag{7.12}$$

7.3.6 Efficiency Estimates

As for the 46.6 GeV data sample, a study of the overlap and the cluster search algorithm efficiencies, is also needed for the 49.1 GeV data, so that the simulation prediction, which does not account for them, is properly corrected. We start again with the overlap. Fig. 7.14, shows the measured x-positions of the IP box, during the
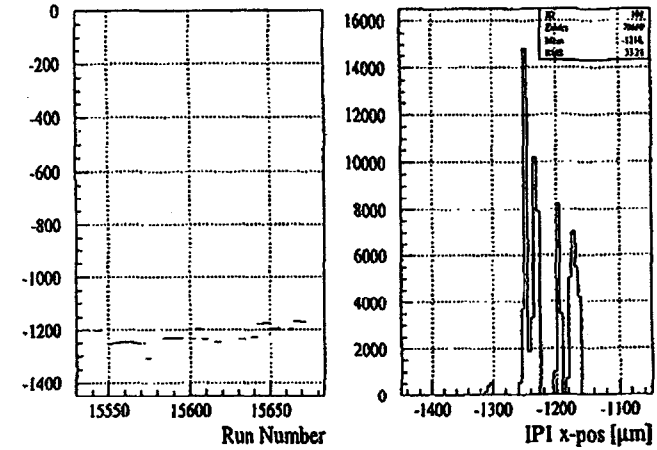
Figure 7.14: IP1 x-positions during the acquisition of the 49.1 GeV data. The left plot shows the variation of the x-position that the IP box was set at the end of an X-Scan, as a function of the run number. The right plot shows the distribution of the x-position for the whole 49.1 GeV data taking.

49.1 GeV run period. The RMS value of the distribution of the different x-positions is 33 μm, which we suppose represents a jitter in the x-position measurement that follows a Gaussian distribution. In section 7.2.2, we saw that an overlap cut of 0.6 has been introduced. Taking into account, from section 7.3.2, that the $n = 1$ overlap cutoff is at ~ 1, it means that we accept events with $n = 1$ rate as low as 60% of the expected rate at perfect overlap. This can be translated into a timing offset by using
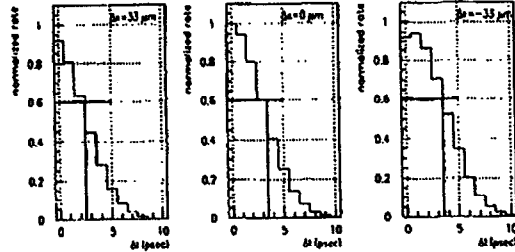
Figure 7.15: Normalized positron rate for different time and x offsets, with respect to the case where $\Delta x = 0$ and $\Delta t = 0$. The left plot has $\Delta x = 33$ μm, while the right one has $\Delta x = -33$ μm. A rate reduction by 60% is equivalent to a time offset of at most $4 ps$.

the simulation data. Fig. 7.15, shows the positron rates normalized to the perfect overlap ($\Delta x = 0$ and $\Delta t = 0$) rate, for different timing offsets and for 3 different x-position offsets $\Delta x = 33$ μm, $\Delta x = 0$ μm and $\Delta x = -33$ μm, starting from the left. As we can see from the three plots shown, a 60% positron yield with respect to perfect overlap conditions, corresponds to about 4 ps in timing offset.

We are primarily interested in the effect that these offsets in the x-position and in time have on the average positron yield normalized to the number of the $n = 1$ γ's, or symbolically $\langle Ne^+/N1 \rangle$. We assume that the normalized positron yield follows a Gaussian distribution around the perfect overlap case, and therefore it needs to be weighed by a two-dimensional Gaussian distribution centered around $\Delta x = 0$ μm and $\Delta t = 0$ ps. The default case is taken to be a Gaussian with $\sigma_x = 33$ μm and $\sigma_t = 4$ ps. The results of the default case along with some other cases studied, are shown in table 7.4. The cases where $\sigma_x = \infty$ or $\sigma_t = \infty$, assume a flat distribution of the signal in the horizontal direction or in time respectively and they are obviously extreme cases. Similar studies can be made in the case of y-position offsets. As in the 46.6 GeV case, no significant effect on the positron yield is observed. From table 7.4, we

Offset		Weight		Rates
x-range [μm]	t-range [ps]	σ_x [μm]	σ_t [ps]	$\langle Ne^+/N1 \rangle$
± 33	0–4	33	4	0.881
± 44	0–4	33	4	0.825
± 22	0–4	33	4	0.916
± 33	0–5	33	4	0.859
± 33	0–3	33	4	0.882
± 33	0–4	∞	4	0.860
± 33	0–4	33	∞	0.867
± 33	0–4	∞	∞	0.857
± 44	0–5	∞	∞	0.777

Table 7.4: List of corrections that we need to apply to the simulation normalized positron rates due to overlap inefficiency. Different cases of x and time offsets are shown here. A weighing of the positron signal using a 2-D Gaussian with the σ's shown is done. When $\sigma = \infty$ the weighing distribution is flat. The overall scaling factor for the simulation rates is 0.87 $\pm$ 0.09.

can conclude that the overall correction to the simulation normalized positron yields that needs to be applied in order to account for overlap inefficiencies, is 0.87 $\pm$ 0.09.

For the study of the cluster search algorithm, the same method, as described in section 6.4.2 of the previous chapter, is applied. Data runs at the beginning, the middle and the end of the 49.1 GeV data run period examined, are used. Again 5000 simulated positron events on PCAL, with known incident positions and energies, are used, and to these events background from laser ON or laser OFF events from the data runs selected, is added on an one-to-one basis. The results are shown in table 7.5, for the two cases of laser ON or laser OFF added background. From the table we

Laser OFF Background		laser ON background	
Run Number	Inefficiency (%)	Group Number	Inefficiency(%)
15638	6.4	15638	8.1
15647	5.5	15647	6.9
15653	5.7	15653	9.5.
15661	5.9	15661	6.9
15670	9.5	15670	9.3
Average	6.8	Average	8.1

Table 7.5: Inefficiency of the cluster search algorithm when different background cases are used. It is obvious that laser ON based background leads to a slightly higher inefficiency of the cluster search code.

can see that when laser ON background is used along with the simulated positron events, the inefficiency is a little higher on average. We can introduce a correction factor for the simulation predicted positron yields that accounts for the cluster search algorithm inefficiencies, of 0.92. This correction factor is slightly smaller than the one in the 46.6 GeV data sample, and is justified by the higher background levels prevailed during the 49.1 GeV data runs.

Fig. 7.16 shows the 95% confidence limit of the residual background, for the 49.1 GeV data sample (the solid line shown in the plot represents a power law fit and it will be discussed in the next chapter). This background can be attributed to lost beam particles scraping on the accelerator pipe walls. The 95% confidence limit is defined in the same way as was done for the 46.6 GeV data sample. It is clear that the data at the lowest η value, although consistent with the multiphoton pair production process, indicate the presence of such a residual background of the order of 6×10^{-3} positrons per shot.
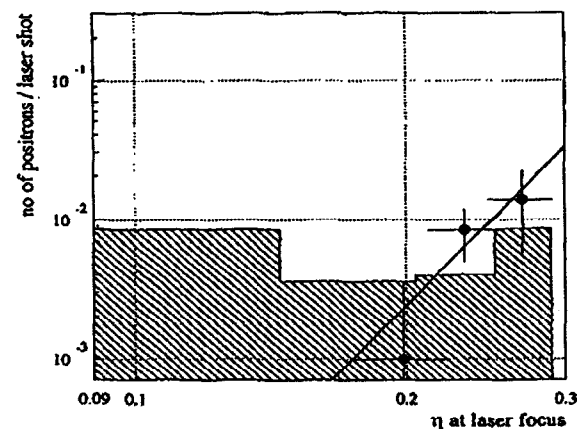
Figure 7.16: Dependence of the positron rate per laser shot on the laser intensity parameter η. The solid line shows a power law fit to the data. The shaded distribution is the 95% confidence limit on the residual background from showers of lost beam particles after subtracting the laser off positron rate.

Chapter 8

Conclusions

In this chapter the final results from both the 46.6 GeV and the 49.1 GeV data samples are presented and a comparison with the theoretical prediction is made. To achieve this, the positron yield is plotted as a function of the laser intensity parameter η. Final estimates of statistical and systematic errors are also given for all cases. In the last section of this chapter we discuss the interpretation of the positron data as a manifestation of spontaneous vacuum breakdown.

8.1 Multiphoton Breit-Wheeler Pair Production Results

Some of the results discussed in this section regarding the multiphoton Breit-Wheeler pair production, have already been presented in the previous two chapters. As mentioned in chapter 6, for the case of the 46.6 GeV data sample, a total of 106 ± 14 background subtracted positrons were found and the momentum spectrum is shown in Fig. 6.10 of that chapter. Of more importance is the dependence of the positron yield per laser shot on the laser intensity parameter η. This is shown in Fig. 8.1 in a log-log plot. In section 6.4.3 of chapter 6, we commented about the residual background levels from beam showering, the 95% confidence level of which is represented

Figure 8.1: Dependence of the positron rate per laser shot on the laser intensity parameter η. The solid line shows a power law fit to the data. This plot is useful for determining the order of the multiphoton Breit-Wheeler pair production process.

by the shaded area in that plot. The solid line is a power law fit to the data and gives $R_{e^+} \propto \eta^{2n}$ with $n = 5.1 \pm 0.2$ (stat.), where the statistical error is from the fit. To this statistical error a systematic error that reflects the effects discussed in more detail in section 6.3.8, as well as the choice of the bin size in η, needs to be included. The effects of these sources of systematic errors are listed in table 8.1. The errors shown in that table are absolute differences of the fitted slope with respect to the default value of $n = 5.1$. Including the overall systematic error in the slope estimate from the power law fit, gives for n:

$$n = 5.1 \pm 0.2 \text{ (stat.) } {}^{+0.5}_{-0.8} \text{ (syst.)} \tag{8.1}$$

We conclude that the positron production rate is a highly nonlinear process varying as the 5th power of the laser intensity. This is in good agreement with the fact that

Type of error	Slope Error
Contamination	+0.3467
	-0.3344
Background Offset	+0.2297
	-0.2293
$N1$ Error Scaling	+0.0309
	-0.4057
Signal Scaling	+0.0000
	-0.5146
Binning	+0.3333
	-0.1884
Overall	+0.5339
	-0.7933

Table 8.1: List of the systematics on the slope of the power law fit. The numbers are absolute differences with respect to the default case of $n = 5.1$.

the rate for multiphoton processes involving n laser photons are (refer to chapter 2) proportional to η^{2n} when $\eta^2 \ll 1$, and with the kinematic requirement that 5.3 photons (including the backscattered high energy gamma) are needed on average to produce a pair near threshold.

In section 6.2.4 of chapter 6, the momentum spectrum of 106 positrons (after background subtraction) was presented (reproduced here in Fig. 8.2(b)). The data points that correspond to low values of η, are more likely to be due to background, as can be seen in Fig. 8.1. If then we restrict our data to events with $\eta > 0.216$ (excluding the data points in the first three bins of Fig. 8.1), we find that from the initial sample of 106 positrons, 69 ± 9 positrons satisfy $\eta > 0.216$. For these positrons the agreement of their observed momentum spectrum to the theoretical prediction, is significantly improved as shown in Fig. 8.2(d).
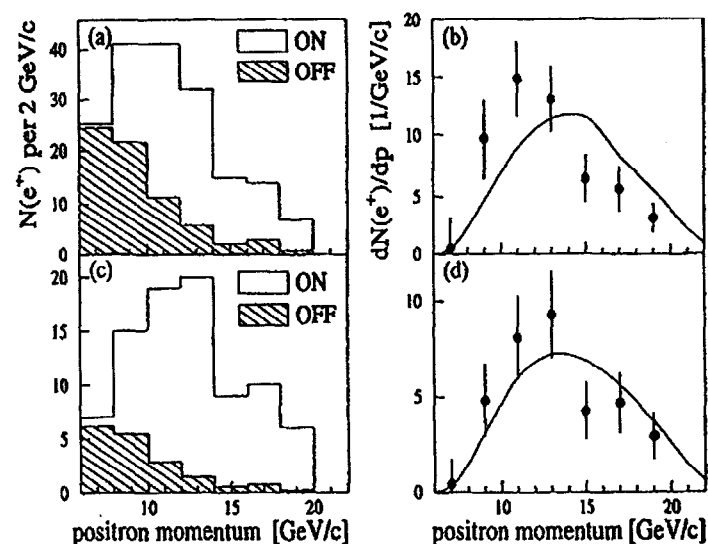
Figure 8.2: Positron energy spectra from the 46.6 GeV data sample. Plot (a) shows the number of positron canditates vs. momentum for laser ON pulses and for laser OFF pulses scaled according to the ratio of the laser OFF over the laser ON triggers. Plot (b) shows the spectrum of signal positrons obtained after subtracting the laser OFF from the laser ON distribution. The curve shows the expected spectrum from the model calculation. Both top plots are reproduced from Fig. 6.10 in chapter 6. Plots (c) and (d) are the same as (a) and (b), but with the additional requirement that $\eta > 0.216$.

In Fig. 8.3 the observed positron rate is given, after being normalized to the number of linear Compton scatters, the latter deduced from the average of the measured rates by the two linear monitors EC31 and EC37. This procedure minimizes the effect of the uncertainty in the laser focal volume and in the effective overlap of the electron-laser beams. The solid line represents the results from the model calculation. The model prediction has already been corrected by a factor of 0.82, resulting from the product of the two correction factors due to the laser-electron beam spatial and temporal overlap inefficiency (0.88) and to the cluster search algorithm inefficiency
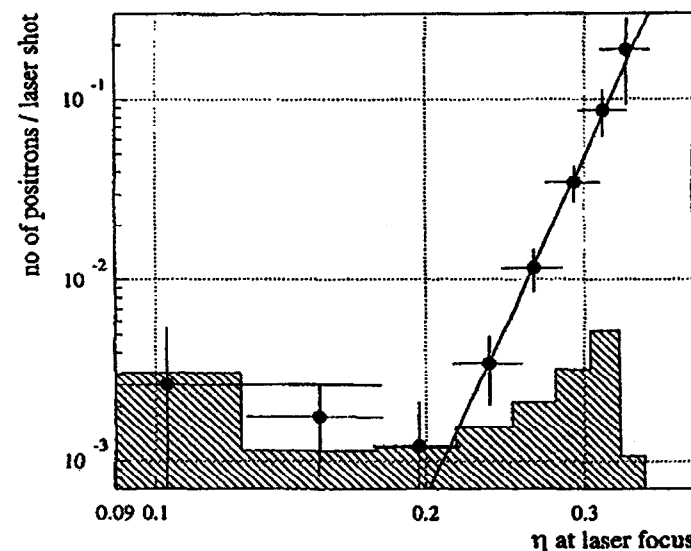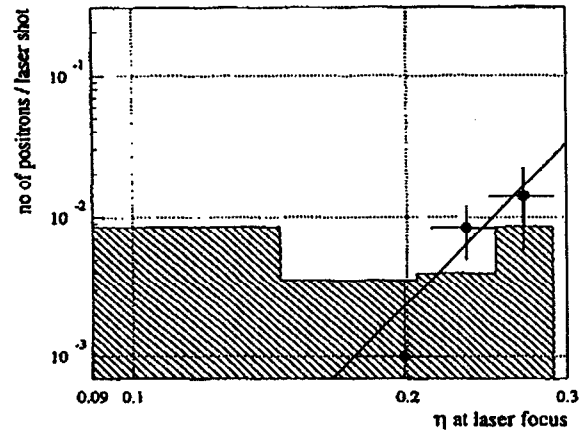
Figure 8.4: Dependence of the positron rate per laser shot on the laser field intensity parameter η. The solid line represents the result of a power law fit to the data. The slope of this fit in a logarithmic scale, gives us an estimate of the order of the multiphoton Breit-Wheeler pair production process.

ing to the multiphoton Breit-Wheeler process 1.5. Some aspects of this calculation are presented in section A.2.4 in appendix A, while more details are included in [61]. The results of this simulation indicate that in the present experimental setup the contribution of the trident process is negligible, as shown in Fig. 8.3 by the dashed line.

Let us now switch our attention to the 49.1 GeV data sample. As already mentioned in chapter 7 we found 22 ± 10 positrons and their corresponding momentum spectrum was shown in Fig. 7.5. We concluded there that the model calculation for the momentum spectrum agreed with the data, within the large error bars. In general the 49.1 GeV analysis is characterized by small statistics and as a result by large error bars. This is more clear in Fig. 7.16 of chapter 7, reproduced here as Fig. 8.4. As in
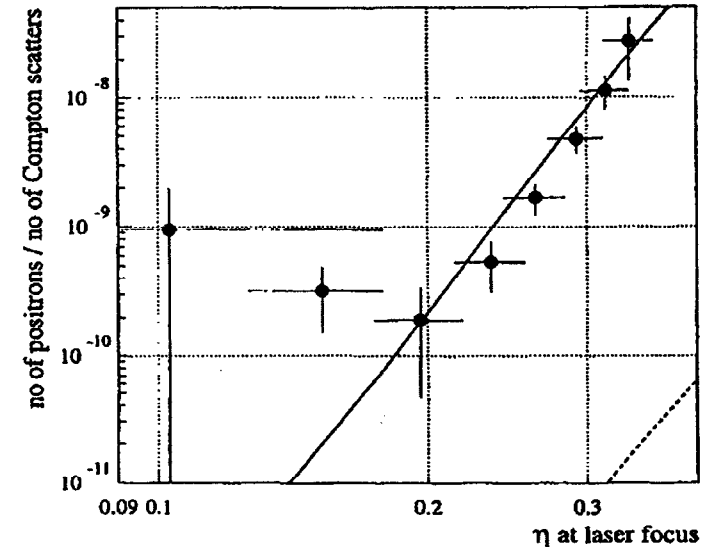
Figure 8.3: Dependence of the positron rate normalized to the number of the measured linear Compton scatters on the laser field intensity parameter η. The solid line is the model calculation of the two-step multiphoton Breit-Wheeler process, as described in text. The dashed curve represents the simulation results of the trident process.

(0.93), as derived in section 6.4 of chapter 6. The data are in good agreement with the theoretical prediction both in magnitude of the observed rate and in their dependence on η. As already mentioned in the first chapter, the pair production is viewed as a two-step process, interaction 1.4 that results to the creation of the backscattered high energy gamma and interaction 1.5 of the gamma with n laser photons to produce the pair, with both processes taking place within the same laser focus. Thus in principle we cannot distinguish the two-step process from the trident process 1.6. A complete theory of multiphoton trident production does not exist. For the needs of this experiment the trident reaction was treated as a two-step process in which the beam electron emits a virtual photon according to the Weizsäcker-Williams approximation and then the virtual photon combines with n laser photons to yield e^+e^- pairs accord-

the 46.6 GeV case, the plot shows the number of measured positrons per laser shot as a function of the laser intensity parameter η, in a log-log plot. The line is a power law fit to the data, and its slope indicates the number of laser photons that participated during the multiphoton Breit-Wheeler pair production. For the 49.1 GeV data we find $n = 3.2 \pm 0.9$, where the error is the statistical error from the fit. To this error we need to add a systematic error due to the same effects already described for the 46.6 GeV data. Table 8.2 lists their contributions to the overall systematic error. We

Type of error	Slope Error
Contamination	+0.4981
	-1.3142
Background Offset	+0.4285
	-1.3304
$N1$ Error Scaling	+0.0000
	-0.4253
Signal Scaling	+0.0000
	-0.3978
Binning	+0.0000
	-2.5208
Overall	+0.6570
	-3.1123

Table 8.2: List of the systematics on the slope of the power law fit. The numbers are absolute differences with respect to the default case of $n = 3.2$.

can therefore write for the 49.1 GeV data:

$$n = 3.2 \pm 0.9 \text{ (stat.) } {}^{+0.7}_{-3.1} \text{ (syst.)} \tag{8.2}$$

Although the data are by no means conclusive, we mention that the simulation predicts an average of 4.7 photons. It is clear that both the statistical and the systematic

errors are large and that they are due to the low statistics of the data sample analyzed. This is caused by the increase of the background levels by roughly a factor of 2 with respect to the 46.6 GeV data sample, as well as by the lower laser intensity achieved on average during the 49.1 GeV data runs. This can be seen if we compare the two plots in Fig. 8.1 and Fig. 8.4 for the 46.6 and the 49.1 GeV data samples, where we can see that the η range is restricted to much smaller values. Nevertheless we can try to directly compare the pair yield to the theoretical prediction, as shown in Fig. 8.5, where the number of positrons is normalized to the number of measured linear Compton scatters. The solid line is the model calculation for the multiphoton Breit-Wheeler process, corrected by a factor of 0.8 resulting from the product of the two correction factors due to overlap (0.87) and cluster reconstruction (0.92) inefficiencies. The dashed line respresents the trident simulation. Again no firm con-
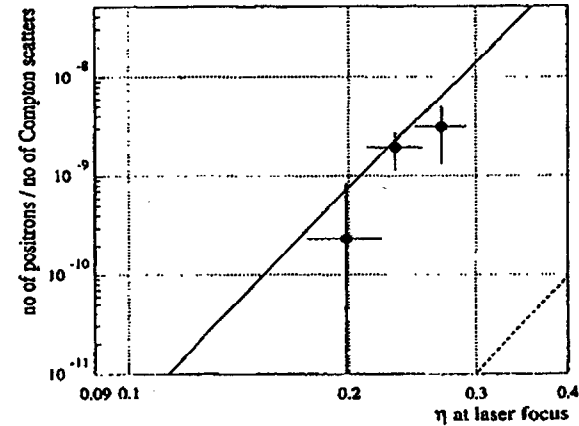
Figure 8.5: Comparison of the measured positron rate normalized to the number of the linear Compton scatters, to the theoretical prediction represented by the solid line. The dashed line indicates the results of the trident process simulation.
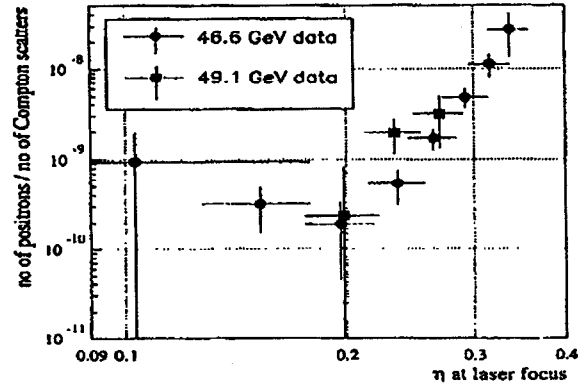
Figure 8.6: Comparison of the measured positron rate normalized to the number of the linear Compton scatters, for the two different electron beam energies. Neglecting the low η points, we can see that the measured 49.1 GeV rate is about 2.5 times higher than the 46.6 GeV case.

clusions can be drawn, but the data seem to follow the η dependence predicted by the theory.

The original motivation for acquiring the 49.1 GeV data, was to examine how the positron production rate increases with the electron beam energy. According to the simulation, the positron rate normalized to the number of the linear Compton scatters, should increase by about a factor of 3, when the electron beam energy is raised from 46.6 GeV to 49.1 GeV. This is shown in Fig. 8.6. Excluding the data at the lower η values, we can see that indeed the 49.1 GeV rate is about 2.5 times higher on average than the 46.6 GeV rate, close to our expectation. In conclusion we believe, that despite the large systematic errors, the 49.1 GeV data seem to agree with the theoretical predictions. An increase of the data sample, would have resulted

to a reduction of the systematic errors, but not to a significant change in the form of the momentum spectra or of the dependence of the positron yield on the laser intensity parameter η.

8.2 Spontaneous Vacuum Breakdown Results

In section 2.5 of chapter 2, we have argued that a possible interpretation of the positron data, as a manifestation of the spontaneous vacuum breakdown, would indicate that the positron yield per laser shot, should vary as $\sim \exp\left(-\pi g(1/\eta)/\Upsilon\right)$.
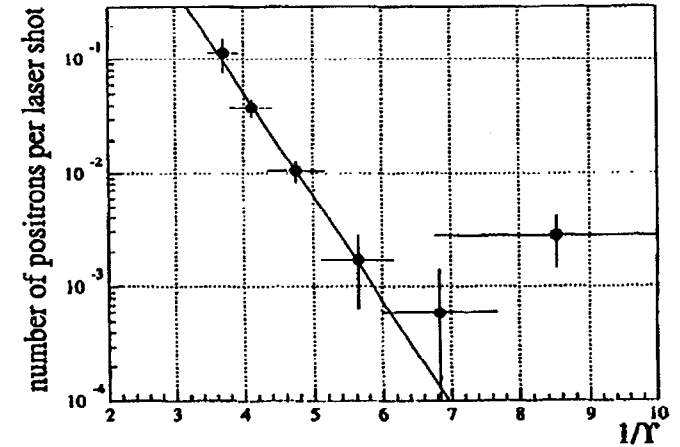
Figure 8.7: Dependence of the positron yield per laser shot on $1/\Upsilon$, the latter as defined in section 2.5, for the 46.6 GeV data sample.

This means that in a semi-logarithmic plot, where the positron yield per laser shot is plotted as a function of $1/\Upsilon$, the slope should be $-\pi g(1/\eta)$; the function $g(1/\eta)$ is a smooth and monotonically increasing function of η and takes into account the

Type of error	Slope Error
Contamination	+0.0000
	-0.4335
Background Offset	+0.0000
	-0.3325
$N1$ Error Scaling	+0.0185
	-0.1818
Signal Scaling	+0.0000
	-0.0731
Binning	+0.1811
	-0.2731
Overall	+0.1821
	-0.6414

Table 8.3: List of the systematics on the slope of the exponential fit shown in Fig. 8.7. The values are absolute differences with respect to the default case of 2.4.

fact that the laser field intensity is such that we are between the perturbative and non-perturbative regimes. Fig. 8.7, shows this plot for the 46.6 Gev data sample. The solid line represents an exponential fit, which results to a slope of $\pi g(1/\eta) = 2.4 \pm 0.1$, where the error is only the statistical error from the fit. An additional systematic error needs to be added, that takes into account the effects discussed in chapter 6, and also the possible choice of different bining in $1/\Upsilon$. Table 8.3, lists these errors, along with their overall contribution. Including the systematic error, we find:

$$\pi g(1/\eta) = 2.4 \pm 0.1 \text{ (stat.) } {}^{+0.2}_{-0.6} \text{ (syst.)} \qquad (8.3)$$

In all the above Υ is defined according to Eq. 2.153, i.e. on the incident beam electron's rest frame, and the RMS value of the laser induced electric field is used. The prediction of Eq. 2.157 for $\langle\eta\rangle = 0.2$, which is the average value of η for the 46.6

GeV data sample, is $\pi g(1/\eta) = 1.62$. The result from the exponential fit needs to be corrected for two factors. First, in Eq. 2.157 the peak value of the electric field is used to define both Υ and η, while in Fig. 8.7 the RMS value is used instead. Second, Υ in Eq. 2.157 is defined in the rest frame of the produced pair and not of the incident beam electron. Assuming that the majority of the pairs were produced by a 29.2 GeV backscattered gamma, the result in the expression 8.3, needs to be reduced by a factor of $46.6/29.2 = 1.6$ and increased by a factor of $\sqrt{2}$. In addition the theoretical prediction needs to be adjusted for an $\langle\eta\rangle$ scaled by a factor of $\sqrt{2}$. This leads to the final results

$$\pi g(1/\eta) = 2.12 \pm 0.09 \text{ (stat.) } {}^{+0.18}_{-0.53} \text{ (syst.)} \qquad \text{observed}$$

$$\pi g(1/\eta) = 1.93 \qquad\qquad\qquad\qquad \text{predicted}$$

which compare pretty well in spite of the large systematic error.
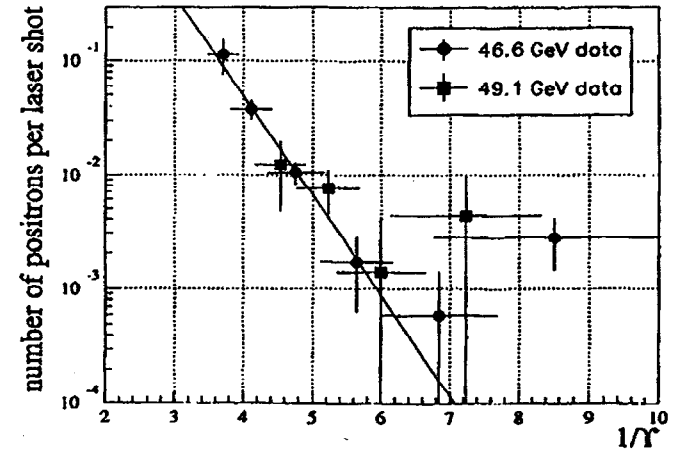
Figure 8.8: Dependence of the positron yield per laser shot on $1/\Upsilon$, the latter as defined in section 2.5, for both the 46.6 GeV and 49.1 GeV data samples.

It is clear from the above, that the positron yields per laser shot for different electron beam energies, can be combined in the same plot as a function of $1/\Upsilon$. This is shown in Fig. 8.8, where both the 46.6 GeV and the 49.1 GeV data points follow the same line, with the exception of points that correspond to low Υ, which are much more subject to residual backgrounds. The solid line in the plot represents an exponential fit with a slope,

$$\pi g(1/\eta) = 2.01 \pm 0.12 \text{ (stat.)} \tag{8.4}$$

while the systematics are the same as for the 46.6 GeV data. Applying to this result the corrections listed previously, the observed slope is:

$$\pi g(1/\eta) = 1.78 \pm 0.11 \text{ (stat.)} \tag{8.5}$$

Comparing to the theoretical prediction for $\langle \eta \rangle = 0.2 \times \sqrt{2}$, for which $\pi g(1/\eta) = 1.93$, we see that the agreement is still good. We conclude that the positron data presented here can be interpreted either in terms of the multiphoton Breit-Wheeler process, or as resulting from the spontaneous breakdown of the vacuum as seen in the rest frame of a fast moving electron.

Bibliography

[1] G. Breit and W. Wheeler, 'Collision of Two Light Quanta', Phys. Rev. **46**, 1087 (1934).

[2] H. A. Bethe and W. Heitler, Proc. Roy. Soc. **A146**, 83 (1934).

[3] O. C. De Jager *et al.*, 'Estimate of the Intergalactic Infrared Radiation Field from γ-Ray Observations of the Galaxy Mrk421', Nature **369**, 294 (1994).

[4] H. R. Reiss, 'Absorption of Light by Light', J. Math. Phys. **3**, 59 (1962). Also 'Production of Electron Pairs from a Zero-Mass State', Phys. Rev. Lett. **26**, 1072-1075 (1971).

[5] A. I. Nikishov and V. I. Ritus, 'Quantum Processes in the Field of a Plane Electromagnetic Wave and in a Constant Field', Soviet Physics JETP **19**, 529 (1964).

[6] N. B. Narozhnyi, A. I. Nikishov and V. I. Ritus, 'Quantum Processes in the Field of a Circularly Polarized Electromagnetc Wave', Soviet Physics JETP **20**, 622 (1965).

[7] V. Balakin *et al.*, 'Focusing of Submicron Beams for TeV-Scale e^+e^- Linear Colliders', Phys. Rev. Lett. **74**, 2479 (1995).

[8] C. Bamber *et al.*, '0.5 Hz, Phase-Stabilized Terawatt Laser System with a Nd:Glass Slab Amplifier for Nonlinear QED Experiments', Laser Physics **7**, 135 (1997).

[9] S. C. Berridge *et al.*, 'Beam Test of the SLD Silicon-Tungsten Luminosity Monitor', IEEE Trans. Nuc. Sci. **37** (1990) 1191.

[10] C. Field, Nucl. Instrum. Methods A **360**, 467 (1995).

[11] K. T. McDonald, 'Proposal for Experimental Studies of Nonlinear Quantum Electrodynamics', Princeton U. Report DOE/ER/3072-38, September 1986.

[12] L. D. Landau and E. M. Lifshitz, 'The Classical Theory of Fields', 4th ed. Pergamon Press, 1975.

[13] T. W. B. Kibble, 'Refraction of Electron Beams by Intense Electromagnetic Waves', Phys. Rev. Lett. **16**, 1054 (1966).

[14] D. M. Volkov, 'Über eine Klasse von Lösungen der Diracschen Gleichung' Z. f. Phys. **94**, 250 (1935).

[15] V. B. Berestetskii *et al.*, 'Quantum Electrodynamics', Pergamon Press, 1982.

[16] D. D. Meyerhofer, 'Summary of Gaussian Focusing', E-144 internal note, June 1994.

[17] U. Fano, J. Opt. Soc. **39**, 859 (1949).

[18] K. Shmakov, 'Polarization Effects in Positron Production and Multiphoton Compton Scattering in Interaction of Intense Laser with Relativistic Electrons (46.6 GeV, 250 GeV)', E-144 internal note, March 1997.

[19] J. Schwinger, 'On gauge Invariance and Vacuum Polarization', Phys. Rev. **82**, 664 (1951).

[20] W. Heisenberg and H. Euler, Zeits. f. Phys. **98**, 718 (1936); see also F. Sauter, Zeits. f. Phys. **69**, 742 (1931).

[21] W. Greiner and J. Reinhardt, 'Quantum Electrodynamics', Springer, Berlin, 1994.

[22] E. Brezin and C. Itzykson, 'Pair Production in Vacuum by an Alternating Field', Phys. Rev. D **2**, 1191 (1970).

[23] R. L. Holtzapple, 'Measurements of Longitudinal Phase Space in the SLC Linac', SLAC-PUB-95-6841 (1995).

[24] E. D. Courant and H. S. Snyder, Ann. of Phys. **3**, 1 (1958).

[25] Helmut Wiedemann, 'Particle Accelerator Physics', Springer-Verlag, 1993.

[26] K. D. Jacobs *et al.*, in *Proceedings of the 1989 Particle Acceleration Conference*, edited by F. Bennett and J. Kopta (IEEE, Piscataway, 1989) p.1526.

[27] P. Tenenbaum, 'FFTB Beam to Dump Procedure', FFTB/E-144 internal note, November 1995.

[28] P. Tenenbaum, 'Expanded Studies of Linear Collider Final Focus Systems at the Final Focus Test beam', Ph.D. Thesis, SLAC-Report-95-475, December 1995.

[29] S. Hartman, P. Tenenbaum, 'FFTB β-Match Procedure', FFTB/E-144 internal note, March 1995.

[30] D. Strickland and G. Mourou, 'Compression of Amplified-Chirped Optical Pulses', Opt. Comm. **55**, 447 (1985).

[31] M. Pessot, P. Maine and G. Mourou, '1000 Times Expansion/Compression of Optical Pulses for Chirped Pulse Amplification', Opt. Comm. **62**, 419 (1987).

[32] Model ML-59.503B1 Acousto-optic Modelocker, IntraAction Corp., Bellwood, IL.

[33] Flexcore Single Mode Waveguide, Corning Co., Corning, NY.

[34] O. Svelto, 'Principles of Lasers', Plenum Press, 1989.

[35] Model RC0100 reticon, EG&G, Sunnyvale, CA.

[36] W. Koechner, 'Solid State Laser Engineering', Springer-Verlag, 1992.

[37] M. J. Shoup III and J. H. Kelly, 'A High-Energy, Short-Pulse, Multiwavelength, Slab-Geometry Nd:Phosphate Glass Laser Source', presented at CLEO '89, Baltimore, MD, (April 1989).

[38] Steven John Boege, 'Evidence of Light-by-Light Scattering with Real Photons', Ph.D. Thesis, University of Rochester UR-1458 (1996).

[39] T. Kotseroglou et al., 'Picosecond Timing of Terawatt Laser Pulses with the SLAC 46 GeV Electron Beam', Nuclear Instruments & Methods in Physics Research A 383 (1996) 309-317.

[40] K. Jobe, 'MDL Length Studies', SLAC Memo, August 1988.

[41] RF/Microwave fiber-optic transmitter, Model 3540A and receiver, Model 4510A, Ortel Co.

[42] Low Thermal Coefficient of Delay Time Optical Fiber Cable, 6HJ-9336A, Sumimoto Electric Industries Ltd., Yokohama Japan.

[43] Model 1000 Timing Stabilizer, Lightwave Electronics Co., Mountain View, CA, USA.

[44] Model DG535, Digital Delay/Pulse Generator, Stanford Research Systems, Sunnyvale, CA, USA.

[45] M. J. W. Rodwell, D. M. Bloom and K. J. Weingarten, IEEE J. Quantum Electronics 25 (1989) 817.

[46] R. B. Blackman and J. W. Tukey, 'The Measurement of Power Spectra', Dover, 1959.

[47] Model CSA-803 Communications Signal Analyzer with an SD-24 TDR Sampling Head, Tektronix, Beaverton, OR, USA.

[48] RF/IF Designer's Handbook, Mini-Circuits Co. Brooklyn, NY., USA.

[49] J-Y Optical Systems, Edison, NJ., USA.

[50] Konstantin Dmitrievich Shmakov, 'Study of Nonlinear QED Effects in Interactions of Terawatt Laser with High Energy Electron Beam', Ph.D. Thesis, University of Tennessee, Knoxville (1997).

[51] C. Bula, 'Tracking of Electrons and Positrons Through the IP1 Spectrometer', E-144 internal note, May 1996.

[52] G. Horton-Smith, 'E144 ECAL Best Aperture Reconstruction', E-144 internal note, September 1995.

[53] K. Shmakov, 'E144 ECAL Reconstruction', E-144 internal report, September 1995.

[54] K. T. McDonald, 'E-144: Comparison of Methods of Reconstruction of Nonlinear Compton Scattering via ECAL Data', E-144 internal report, December 1996.

[55] R. C. Field, 'CCM1 Calibration Constants for August 1996', E-144 internal report, October 1996.

[56] S. Brandt, 'Statistical and Computational Methods in Data Analysis', 2nd ed. North-Holland,Amsterdam 1983.

[57] Particle Data Group, 'Particle Physics Booklet', 205 (1996).

[58] K. T. McDonald, 'Analytic Approximation to the Constrained Solution for η^2 as a Function of Monitors $N1$, $N2$ and $N3$', E-144 internal note, February 1997.

[59] C. Bula *et al.*, 'Observation of Nonlinear Effects in Compton Scattering', Phys. Rev. Lett. **76**, 3116 (1996).

[60] Theofilos Kotseroglou, 'Observation of Nonlinear Compton Scattering', Ph.D. Thesis, University of Rochester UR-1459 (1996).

[61] C. Bula and K. T. McDonald, 'E-144: The Weizsäcker-Williams Approximation to Trident Production in Electron-Photon Collisions', E-144 internal report, February 1997.

[62] Christian Bula, 'A Numeric Integration Program to Simulate Nonlinear QED Processes in Electron-Laser or Photon-Laser Collisions', E-144 internal report, June 1997.

[63] Christian Bula, 'LOOKUP: An interface Program to the Lookup Tables for Compton Scattering', E-144 internal report, October 1995.

[64] G. Horton-Smith, internal communication.

Appendix A

Simulation Code Description

A.1 Introduction

In the following sections we present a brief description of the simulation code that was developed in order to predict nonlinear QED processes in interactions of high-energy electron or photon beams with intense laser pulses. The description is based on the more extensive documentation provided by the author of the code [62]. The method used in this simulation is a numeric integration of differential reaction rates over both space and time in the beam-laser interaction region. Although a Monte-Carlo based simulation also exists, only the results from the numeric integration approach were used to compare the experimental data with the theoretical predictions, as they are presented in the chapters of this thesis. In a numeric integration simulation, unlike the Monte-Carlo approach where a single particle is stepped through the interaction region and in each step a decision is made regarding which one of a number of possible processes will take place based on a pseudo-random number generator, whole particle densities are used and all the possible cases are accounted for simultaneously by multiplying them with interaction probabilities and combining the final results at the end of the simulation. Space and time are divided in small elements and interaction yields are computed for each one of them.

The main advantage of a numeric integration based simulation is speed of execution. It is important to note here that the whole data acquisition and data analysis of the E-144 experiment was based on 486 and Pentium PC's and as a result the memory and speed limitations of the DOS environment had to be faced. In order to ensure fast program execution, a number of speed optimizations were implemented in terms of selectable program options. As a result a price in accuracy of the simulation results was paid. Later the whole code, which is written in C, was successfully transferred to the LINUX and AIX operating systems with the GNU C-compiler, increasing speed and flexibility. In fact the simulation results presented in this thesis, were obtained by running the numeric integration code (NI) under these better conditions with program options that improved significantly the accuracy of the results.

Several processes were simulated with the numeric integration code. The primary process is the n-th order $n = 1, 2, \ldots$ Compton scattering of monoenergetic beam electrons with laser photons. A number of secondary processes involving the scattered electrons and high energy gammas resulted from the Compton scattering while they are all still inside the laser focal area, are considered. These secondary processes include further n-th order Compton scatterings off laser photons, as well as pair production by the absorption by the high energy gammas, of several laser photons (multiphoton Breit-Wheeler process). In all the above cases the geometry of the interaction region is taken into account, along with the inevitable attenuation of the initial electron beam as it traverses the laser focus due to the Compton scattering. All the above processes will be examined in some detail, since their results are important for comparison to the analyzed data. In addition to these processes, which are collectively called the IP1 processes, some additional processes—unfortunately never realized by the E-144 experiment—, can also be studied by the numeric integration code. These processes, called the IP2 processes, include a direct high energy gamma-laser photon interaction and as secondary cases, further Compton scattering and pair production by the resulting particles. The initial gamma beam can have either a

bremsstrahlung or a nonlinear Compton scattering spectrum, although no correlation between the spatial position within the pulse and the corresponding energy is taken into account. Such processes will not be discussed here, since they were not useful in the data analysis. The interested reader can refer to the detailed documentation of the code mentioned earlier.

The following list defines most of the standard symbols used throughout the remaining sections:

e, m	electron charge and mass
c	speed of light
p_μ, p'_μ	4-momentum of electron or positron, initial or final state
E_-, E_+	electron, positron energy
γ_-, γ_+	electron, positron Lorentz factor
β_-, β_+	electron, positron velocity, i.e. $\beta_\pm = \sqrt{1 - 1/\gamma_\pm^2}$
ρ_-, ρ_+	electron, positron density
$\omega_\mu, \omega, \rho_\omega$	4-momentum, frequency and density of laser photons
$\omega'_\mu, \omega', \rho_{\omega'}$	4-momentum, frequency and density of high energy gammas
δ	crossing angle between laser pulse and electron or photon beam, e.g. $\delta = 0$ for head-on collision
α	$\alpha = \pi + \delta$
θ, ϕ	polar and azimuthal angle of the final state particle, i.e. gamma for Compton scattering, positron for pair production
n	number of participating laser photons (order of multiphoton process)
η	field strength intensity
$\bar{m}$	effective mass of electron

The natural system of units is used, where $\hbar = c = 1$. The differential rates per unit volume and unit time are presented, e.g. $dW_n(\omega')/d\omega'$ is the differential probability

per unit volume and time that an electron interacts with n laser photons and emits a single photon with frequency ω'. Then the number of interactions within a given volume element dV, time interval dt and energy bin $d\omega'$ will be

$$N(dV, dt, d\omega') = \frac{dW_n}{d\omega'} \cdot dV \cdot c \, dt \cdot d\omega' \cdot \frac{1}{\hbar c} \qquad (A.1)$$

where the last factor is required to make the expression dimensionless.

A.2 Basic Formulas

A.2.1 General Relations

The dimensionless and invariant parameter η is defined as

$$\eta = \frac{e\mathcal{E}_{rms}}{m\omega} = \frac{e}{m}\sqrt{\frac{\rho_\omega}{\omega}} \qquad (A.2)$$

where $\mathcal{E}_{rms}$ is the root-mean-square electric field of the laser. Notice that η needs to be multiplied by $\sqrt{2}$ in order to coincide with the definition given in chapter 2. The 4-momentum of a charged particle inside a strong electric field is altered due to continuous absorption and emission of photons. For a charged particle with 4-momentum p_μ outside the field, the effective 4-momentum q_μ is

$$q_\mu = p_\mu + \frac{\eta^2 m^2}{2p_\mu \omega^\mu}\omega_\mu \qquad (A.3)$$

with ω_μ the laser photon 4-momentum. The effective mass of the charged particle inside the field $\bar{m}$ is then defined as:

$$\bar{m}^2 = q_\mu q^\mu = m^2(1 + \eta^2) \qquad (A.4)$$

Under the experimental conditions for E-144, we can see that $E_{beam}/m \sim 10^5$, or in other words the beam energy is much larger than the electron rest mass. This allows us to introduce two basic approximations, *i.e.*

$$\theta \sim 1/\gamma \ll 1 \quad \text{and}$$

$$\eta \ll \gamma \qquad (A.5)$$

Both approximations are used to derive the formulas implemented in the numeric integration code.

A.2.2 Nonlinear Compton Scattering

The differential reaction rate for a circularly polarized laser beam is given by:

$$\frac{dW_n(\omega')}{d\omega'} = \frac{e^2 m^2 \rho_\pm}{16\pi E_\pm^2} \left\{ -4J_n^2(z) + \eta^2 \left(2 + \frac{u^2}{1+u}\right)(J_{n-1}^2(z) + J_{n+1}^2(z) - 2J_n^2(z)) \right\} \qquad (A.6)$$

where

$$z = \frac{2\eta}{u_1}\sqrt{\frac{u(u_n - u)}{1 + \eta^2}} \qquad (A.7)$$

$$u_1 = \frac{2\omega_\mu q^\mu}{m^2(1+\eta^2)} \simeq \frac{2E_\pm \omega(1 - \cos\alpha)}{m^2(1+\eta^2)} \qquad (A.8)$$

$$u = \frac{\omega_\mu \omega'^\mu}{\omega_\mu q'^\mu} \simeq \frac{\omega'}{E_\pm - \omega'} \qquad (A.9)$$

$$u_n = n u_1 \qquad (A.10)$$

Similarly the differential interaction rate for linear polarization is:

$$\frac{dW_n(\omega')}{d\omega'} = \frac{e^2 m^2 \rho_\pm}{2\pi^2 E_\pm^2} \int_0^{\pi/2} d\phi \left\{ -A_0^2 + \eta^2 \left(2 + \frac{u^2}{1+u}\right)(A_1^2 - A_0 A_2) \right\} \qquad (A.11)$$

where $A_i \equiv A_i(n, a, b), i = 0, 1, 2$ and they are defined as in chpater 2, while the parameters a and b are given by

$$a \equiv \sqrt{2}m\eta \left(\frac{\varepsilon_\mu p^\mu}{\omega_\mu p^\mu} - \frac{\varepsilon_\mu p'^\mu}{\omega_\mu p'^\mu}\right) \qquad (A.12)$$

$$b \equiv 4m^2\eta^2 \left(\frac{1}{\omega_\mu p^\mu} - \frac{1}{\omega_\mu p'^\mu}\right) \qquad (A.13)$$

with $\varepsilon_\mu = (\varepsilon_0, \vec{\varepsilon})$ the polarization 4-vector of the laser photons. Notice that a is the equivalent of α as defined in chapter 2, but b is defined with opposite sign compared to β in the same chapter. The polarization of the emitted photon becomes important for the subsequent steps of pair production. Since this last process was studied only

for linearly polarized laser photons, only for this case the differential interaction rates are modified accordingly and they become

$$\frac{dW_n^{\|}(\omega')}{d\omega'} = \frac{e^2 m^2 \rho_\pm}{2\pi^2 E_\pm^2} \int_0^{\pi/2} d\phi \left\{ -2\eta^2 \sigma' A_0^2 + \eta^2 \left(2 + \frac{u^2}{2(1+u)}\right)(A_1^2 - A_0 A_2)\right\} \quad (A.14)$$

$$\frac{dW_n^{\perp}(\omega')}{d\omega'} = \frac{e^2 m^2 \rho_\pm}{2\pi^2 E_\pm^2} \int_0^{\pi/2} d\phi \left\{ -(1 - 2\eta^2 \sigma') A_0^2 + \eta^2 \frac{u^2}{2(1+u)}(A_1^2 - A_0 A_2)\right\} \quad (A.15)$$

where

$$\sigma' = -\left[\frac{1}{2} + \frac{n}{4b} + \left(\frac{a}{8b}\right)^2\right] \quad (A.16)$$

and $\|$, $\perp$ indicate high energy gammas produced with polarizations parallel or perpendicular to that of the interacting laser photons respectively.

A.2.3 Multiphoton Pair Production

The differential interaction rate for a circularly polarized laser beam and unpolarized high energy gammas is

$$\frac{dW_n(E_\pm)}{dE_\pm} = \frac{e^2 m^2 \rho_\omega}{8\pi \omega'^2} \left\{ 2J_n^2(z) + \eta^2(2u-1)\left(J_{n-1}^2(z) + J_{n+1}^2(z) - 2J_n^2(z)\right)\right\} \quad (A.17)$$

with

$$z = \frac{2\eta}{u_1}\sqrt{\frac{u(u_n - u)}{1 + \eta^2}} \quad (A.18)$$

$$u_1 = \frac{\omega_\mu \omega'^\mu}{2m^2(1+\eta^2)} \simeq \frac{\omega\omega'(1 - \cos\alpha)}{2m^2(1+\eta^2)} \quad (A.19)$$

$$u = \frac{(\omega_\mu \omega'^\mu)^2}{4(\omega_\mu q^\mu)(\omega_\mu q'^\mu)} \simeq \frac{\omega'}{4E_\pm(\omega' - E_\pm)} \quad (A.20)$$

$$u_n = nu_1 \quad (A.21)$$

Due to energy conservation $n \geq n_0$ the minimum number of photons needed to produce one pair defined us:

$$n_0 = \frac{2m^2(1+\eta^2)}{\omega\omega'(1 - \cos\alpha)} \quad (A.22)$$

In the case of linearly polarized laser beam the corresponding differential rate is

$$\frac{dW_n(E_\pm)}{dE_\pm} = \frac{e^2 m^2 \rho_\omega}{2\pi^2 \omega'^2} \int_0^{\pi/2} d\phi \left\{ A_0^2 + 2\eta^2(2u-1)(A_1^2 - A_0 A_2)\right\} \quad (A.23)$$

where again $n \geq n_0$ and also $A_i \equiv A_i(n, a, b), i = 0, 1, 2$ with a and b defined as in the nonlinear Compton case. As with the nonlinear Compton scattering, the linear polarization case is more accurately treated by introducing the polarization of the initial high energy gamma. Then the differential rate is modified to take into account the different polarization states and becomes

$$\frac{dW_n^{\|}(E_\pm)}{dE_\pm} = \frac{e^2 m^2 \rho_\omega}{2\pi^2 \omega'^2} \cdot 2 \cdot \int_0^{\pi/2} d\phi \left\{ 2\eta^2 \sigma' A_0^2 + 2\eta^2(u-1)(A_1^2 - A_0 A_2)\right\} \quad (A.24)$$

$$\frac{dW_n^{\perp}(E_\pm)}{dE_\pm} = \frac{e^2 m^2 \rho_\omega}{2\pi^2 \omega'^2} \cdot 2 \cdot \int_0^{\pi/2} d\phi \left\{ (1 - 2\eta^2 \sigma') A_0^2 + 2\eta^2 u(A_1^2 - A_0 A_2)\right\} \quad (A.25)$$

with σ' as defined in Eq. A.16 and $\|$ and $\perp$ indicating the same polarization states as in the nonlinear Compton scattering case.

A.2.4 Multiphoton Trident Pair Production

With the term of multiphoton trident pair production we mean the process

$$e + n\omega \longrightarrow e'c^+e^- \quad (A.26)$$

A complete theory of such a process does not exist. In the numeric integration code, the differential rate of such an interaction is estimated by assuming a two-step process during which the beam electron emits a virtual photon according to the Weizsäcker-Williams approximation and then the virtual photon combines with n laser photons to form a pair according to the multiphoton Breit-Wheeler pair production process. Therefore we can rewrite reaction A.26 as:

$$e \longrightarrow e' + \omega' \quad (A.27)$$

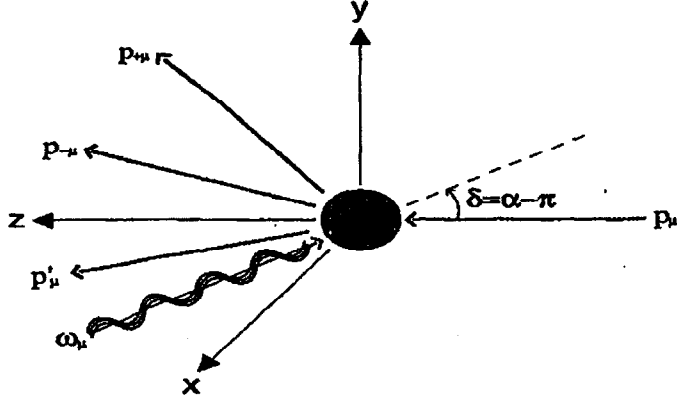$$\omega' + n\omega \longrightarrow e^+e^- \quad (A.28)$$

Figure A.1: Schematic of the multiphoton trident pair production. The kinematic variables shown are defined in the laboratory frame (from [62]).

The relative 4-vectors are listed bellow:

$$\omega_\mu = (\omega, \vec{k}) \qquad \text{laser photon 4-vector}$$

$$p_\mu = (E, \vec{p}) \qquad \text{initial 4-momentum of charged particle}$$

$$p'_\mu = (E', \vec{p}') \qquad \text{final 4-momentum of charged particle}$$

$$p_{\pm_\mu} = (E_\pm, \vec{p}_\pm) \qquad e^+ \text{ and } e^- \text{ from pair production}$$

$$\omega'_\mu = (\omega', \vec{k}') \qquad \text{intermediate virtual photon 4-momentum}$$

The kinematic variables for the trident process are shown in Fig. A.1. The minimum number of laser photons required to produce a pair is:

$$n_0 = \frac{4m^2(1+\eta^2)}{E\omega(1-\cos\alpha)} \tag{A.29}$$

The differential reaction rate for the trident process, assuming the two-step model shown earlier, is

$$\frac{dW^{(WWBW)}(E_\pm)}{dE_\pm} = \frac{2\alpha}{\pi} \sum_{n \geq n_0} \int_{s'_{min}}^{s'_{max}} \frac{ds'}{s'} \ln\left(\frac{s'_{max}}{s'}\right) \frac{dW_n^{(MPBW)}(E_\pm)}{dE_\pm} \tag{A.30}$$

where WWBW is used here as a short term for the multiphoton trident process, MPBW denotes the multiphoton Breit-Wheeler pair production process, α is the fine structure constant and s is the square of the center-of-mass energy. In the last expression above the integration limits are defined as:

$$s'_{min} = 4m^2(1+\eta^2) \tag{A.31}$$

$$s'_{max} = \left(\sqrt{s} - m\sqrt{1+\eta^2}\right)^2 \tag{A.32}$$

In Eq. A.30 it is more physically transparent to replace the integration over s' with one over ω'. Then the following substitutions need to be made:

$$ds'/s' = d\omega'/\omega'$$

$$s'_{max}/s' = \omega'_{max}/\omega'$$

$$\omega'_{max} = \frac{s'_{max}}{2n\omega(1-\cos\alpha)} = \frac{\left(\sqrt{m^2(1+\eta^2) + 2En\omega(1-\cos\alpha)} - m\sqrt{1+\eta^2}\right)^2}{2n\omega(1-\cos\alpha)}$$

$$\omega'_{min} = \frac{s'_{min}}{2n\omega(1-\cos\alpha)} = \frac{2m^2(1+\eta^2)}{n\omega(1-\cos\alpha)}$$

Using these last expressions, Eq. A.30 becomes:

$$\frac{dW^{(WWBW)}(E_\pm)}{dE_\pm} = \frac{2\alpha}{\pi} \sum_{n \geq n_0} \int_{\omega'_{min}}^{\omega'_{max}} \frac{d\omega'}{\omega'} \ln\left(\frac{\omega'_{max}}{\omega'}\right) \frac{dW_n^{(MPBW)}(E_\pm)}{dE_\pm} \tag{A.33}$$

A.3 Space-Time Integration

In order to find the total interaction rates for the various processes discussed in the previous section, we need to integrate them over space and time. For this purpose both space and time are divided into small space-time elements (STE), and for each of them the yields of the beam-laser interactions are calculated. At the end of the integration the different space-time element results are combined to give the total interaction rate. In such an approach it is assumed that the electron and laser photon densities —which are defined in the same way as in section 2.3.2 of chapter 2— remain constant within each STE and therefore the integration grid needs to be defined in
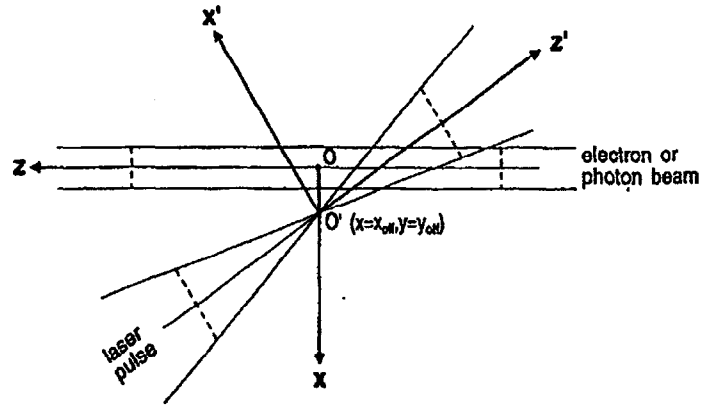
Figure A.2: Schematic of the two coordinate systems employed by the numeric integration code as described in text (from [62]).

such a way so that this is accurately true. In addition the definition of the integration grid needs to take into account the fact that the laser beam is focused and therefore the step sizes should become smaller as we approach closer to the laser focus.

For calculation simplification, two coordinate systems (CS) are defined. The first one, called the laser CS (x', y', z'), has its z'-axis parallel to the direction of the laser propagation. The second coordinate system, called the electron CS (x, y, z), has its z-axis parallel to the direction of the electron beam propagation. The origin O' of the (x', y', z') system is at the laser focus, while the origin O of the (x, y, z) system is chosen so that the density of the beam electrons is symmetric around it and so that O' is at $z = 0$. The two coordinate systems are shown in Fig. A.2. An offset in the two CS origins in x and y has also been accounted for. The transformation between the two coordinate systems is:

$$x' = -z \sin \alpha + (x - x_{off}) \cos \alpha \qquad (A.34)$$

$$y' = y - y_{off} \qquad (A.35)$$

$$z' = z \cos \alpha + (x - x_{off}) \sin \alpha \qquad (A.36)$$
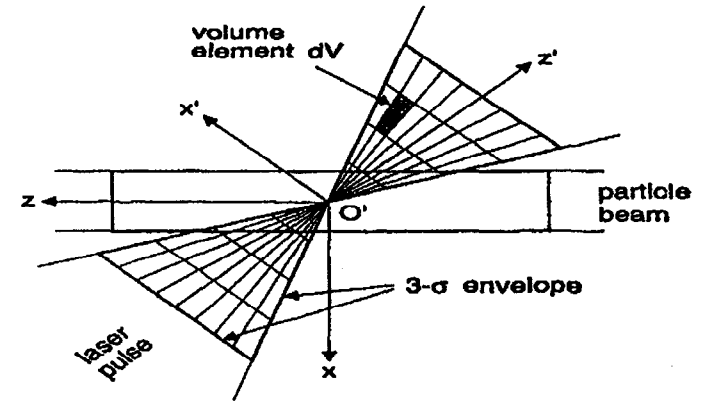
Figure A.3: Schematic of the integration grid along the x'-axis and the z'-axis. The variable size of the volume element dV as a function of z' is evident. For this example $n_{x'}^\sigma = n_{y'}^\sigma = 3$ and $n_{x'}^\Delta = n_{y'}^\Delta = 8$ (from [62]).

The above equations can be viewed as a generalization of the ones shown in section 2.3.2 of chapter 2, when also an offset between the two interacting beams is present.

The integration grid in space is defined in the laser CS and in units of $\sigma_{x'}(z')$, $\sigma_{y'}(z')$ and $\sigma_{x'}$, where the latter are defined in Eq. 2.117 and Eq. 2.118 of chapter 2. In this case a single STE has a spatial volume

$$dV(z') = dx'(z') \cdot dy'(z') \cdot dz' = \frac{2n_{x'}^\sigma \sigma_{x'}(z')}{n_{x'}^\Delta} \cdot \frac{2n_{y'}^\sigma \sigma_{y'}(z')}{n_{y'}^\Delta} \cdot \frac{2n_{x'}^\sigma \sigma_{x'}}{n_{x'}^\Delta} \qquad (A.37)$$

where

$n_{x'}^\sigma, n_{y'}^\sigma, n_{x'}^\sigma$: size of the integration volume in x', y', z' in units of $\sigma_{x'}(z'), \sigma_{y'}(z'), \sigma_{x'}$

$n_{x'}^\Delta, n_{y'}^\Delta, n_{x'}^\Delta$: number of elements in the integration volume along x', y', z'

It is clear from the above expressions that the STE dimensions along the x'-axis and the y'-axis depend on z'. An example of the integration grid in the $x' - z'$ plane is shown in Fig. A.3, in which $n_{x'}^\sigma = n_{y'}^\sigma = 3$ and $n_{x'}^\Delta = n_{y'}^\Delta = 8$. The step size in time

Figure A.4: Procedure to find the initial and final times for the numerical integration (from [62]).

and far end, which means that the $\sigma_{x'}$ is calculated at the laser focus. Initially the two ellipses are positioned at time $t = 0$ taking into account any offset in x or t. Then they are moved along z and z' both in negative and positive directions, until they share no more common area. The dist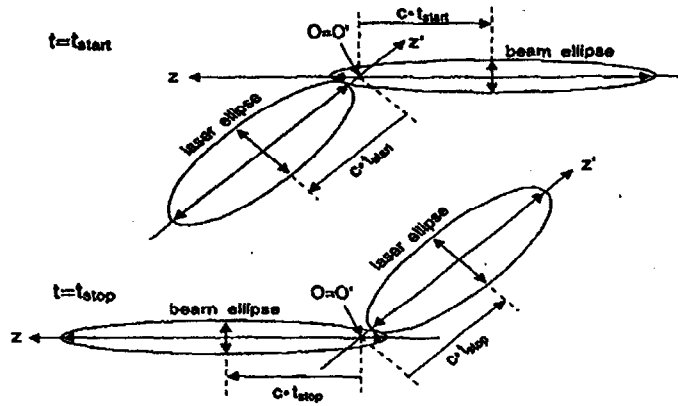ance from these two points to the original position defines t_{start} and t_{stop} respectively. This procedure tends to overestimate the time integration range especially when a y offset is present too. In practice though, this has only a minor effect on the CPU time.

A.4 Secondary Processes

The above space-time integration essentially refers only to the interaction of the initial electron beam with the laser photons, i.e. the n-th order Compton scattering. We will refer to this process as the primary process. The products of such an interaction quite often are still inside the laser field and therefore can undergo further interactions with the laser photons. These are the so called secondary processes. In particular the scattered electrons can undergo further Compton scatterings, while the produced

should be comparable to the step size along the z'-axis, and can be specified by the ratio

$$R^{dt}_{dz'} = \frac{c\,dt}{dz'} \tag{A.38}$$

The integration over space and time for a specific process X [1] proceeds as follows:

1. For a given time t, loop over all the volume elements dV in the integration grid.

2. Use the expressions in section A.2 to find the interaction rate W_X (this involves integration over the energy, with a specified step size) and thus the interaction yield from:

$$N^{STE}_X = W_X \cdot dV \cdot dt \tag{A.39}$$

3. Add the yield found to the total up to this point yield for process X, i.e.:

$$N^{total}_X = N^{total}_{X_0} + N^{STE}_X \tag{A.40}$$

4. Advance in time by a step size of $c \cdot dt$ and start over at 1.

Fig. A.4 shows the procedure to find the initial t_{start} and the final t_{stop} times for the integration over time, which are essentially the times that the two beams (treated as ellipses) start and stop to overlap with each other. The ellipse axes for the two beams are defined as:

$$a_{laser} = n^\sigma_{x'} \cdot \sigma_{x'} \tag{A.41}$$

$$b_{laser} = n^\sigma_x \cdot \sigma_{x'}(z'_{max}) \tag{A.42}$$

$$a_{beam} = n^\sigma_{x'} \cdot \sigma_x \tag{A.43}$$

$$b_{beam} = n^\sigma_{x'} \cdot \sigma_x \tag{A.44}$$

where a and b are the ellipse axes parallel and perpendicular to each beam's direction of propagation and z'_{max} is defined as the distance between the laser ellipse center

---

[1] In the case of the IP1 processes which are examined here, process X means the nonlinear Compton scattering.
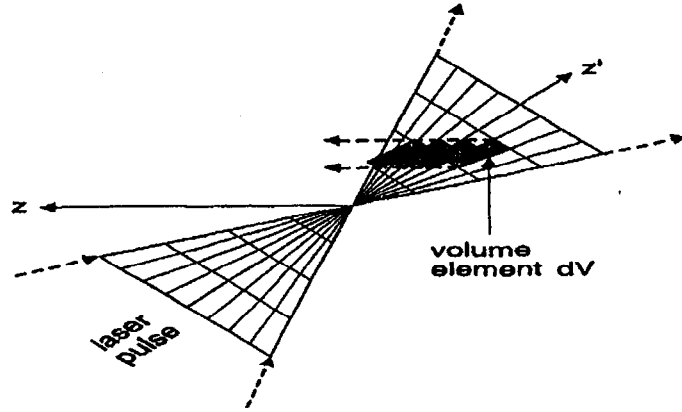
Figure A.5: Integration grid for secondary processes, as defined in text (from [62]).

high energy gammas can absorb several laser photons and result to pair production according to the multiphoton Breit-Wheeler process. This last secondary process is of extreme importance for the E-144 experimental setup, since it represents the only way to pair creation. It is therefore imperative to account for such secondary processes in the numeric integration code.

In numeric integration terms this leads to one more integration over time t' for each volume element dV. The volume element dV is kept constant in size and it moves along the z-axis of the electron beam, while at the same time the laser pulse continues to propagate along the z'-axis. This is shown schematically in Fig. A.5. Here the basic assumption that all the produced particles are moving along the z-axis is made. This is fairly accurate since the angular divergence of the products of the Compton scattering are of the order of $\sim 1/\gamma$ or of about 10 μrads. The step size $c \cdot dt'$ should be comparable to the linear dimensions of the volume element dV at the current location (x'_s, y'_s, z'_s). This is achieved by choosing a step size according to the formula

$$c \cdot dt'(x'_s, y'_s, z'_s) = \min \left[c \cdot dt'_1(x'_s, y'_s, z'_s), c \cdot dt'_2(x'_s, y'_s, z'_s) \right] \qquad (A.45)$$
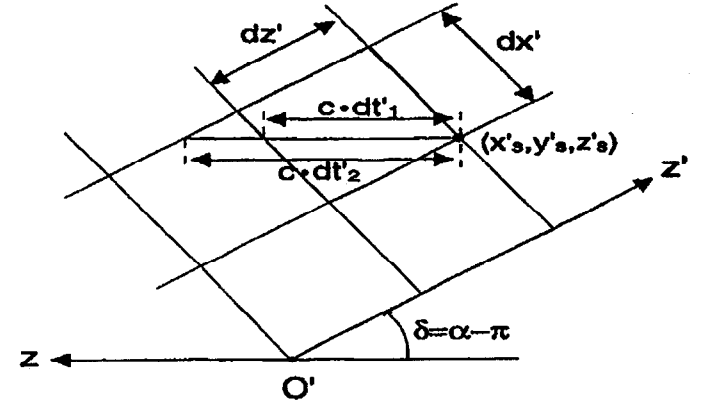
Figure A.6: Procedure to calculate the time step size $c \cdot dt'$ for the secondary processes (from [62]).

where

$$c \cdot dt'_1(x'_s, y'_s, z'_s) = \frac{dz'(x'_s, y'_s, z'_s)}{|\cos \alpha|} \qquad (A.46)$$

$$c \cdot dt'_2(x'_s, y'_s, z'_s) = \frac{dx'(x'_s, y'_s, z'_s)}{|\sin \alpha|} \qquad (A.47)$$

and $dx'(x'_s, y'_s, z'_s)$, $dz'(x'_s, y'_s, z'_s)$ are defined in Eq. A.37. This procedure is outlined in Fig. A.6.

The starting point for the time integration is of course the location in time of the primary STE. The first step size in the time integration is only half of the one indicated by Eq. A.45, because we assume that the first half of that time is spent for the production of the secondary particles from the primary interaction. The end point is taken to be the time at which the secondary particle is outside the laser field. The criterion employed by the numeric integration to that end, requires that the product $P_{\eta 2dV} \equiv \eta^2 \cdot dV$ to be below a certain threshold, i.e.

$$P_{\eta 2dV} < F_{\eta 2dV} \cdot P_{\eta 2dV}^{max} \qquad (A.48)$$

where $P_{\eta 2dV}^{max}$ is the maximum of $P_{\eta 2dV}$ for all primary STE's and $F_{\eta 2dV}$ is a user

input parameter to the numeric integration. During the computation of the secondary processes, *the interactions of the produced particles with the electron beam is ignored.*

A.5 Program Flow

The program consists of three main parts. The first part is the initialization section. Here unknown parameters (like η and Υ) are calculated from input parameters or read from external files, memory is allocated, counters are initialized and all the input parameters are written in the "log-file". The second part is the actual integration part where the loop over all the STE's is performed. For each primary process specified by the user (P1_X) the yields are calculated and the energy spectra, along with the corresponding counters are updated at the end of each STE. Then the secondary processes (P2_X) are calculated and the corresponding counters and energy spectra are also updated. At the end of the calculation for each separate STE, the results of the secondary process calculations and those of the primary process are added to the total energy spectra. The calculation of either a primary or a secondary process in each STE contains three additional loops. The first is over the input energies (for primary processes the initial beams are monoenergetic so there is really *no loop* here), the second over the different numbers of laser photons participating in each multiphoton process and the last over the final energies. The third part writes the results in the "log-file" and also frees the allocated memory. The program flow is summarized in Fig. A.7. A large number of user selectable histograms are booked in the analysis initialization routine. For primary processes these histograms (which can be process specific) are filled at the end of each primary STE. This is also done at the end of each secondary process STE. The analysis routines are fully dedicated to this task. The most detailed information can be provided by histograms filled during the so-called "innerst loop analysis" where results are stored in histograms after each step in the input energy and participating photon number n loops. In the final
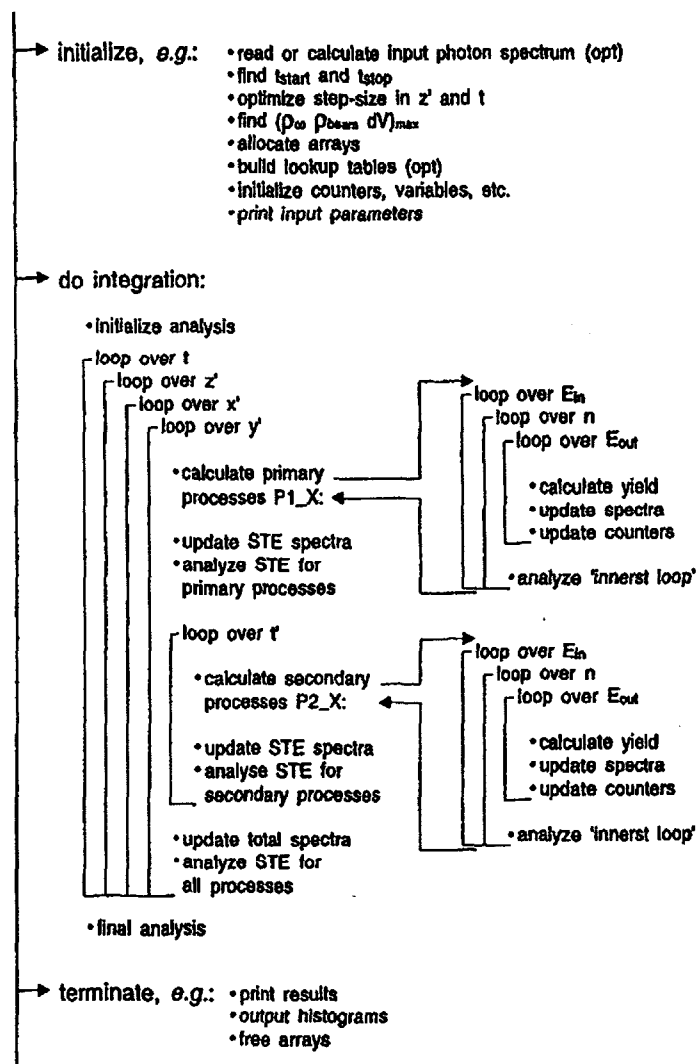
Figure A.7: Numeric integration program flow summary (from [62]).

analysis call, the results of both primary and secondary processes are combined in histograms where the total yields are displayed. It is clear that the analysis routines can considerably slow down the program execution.

A.6 Second Order Corrections

A.6.1 Effective Crossing Angle

Although in a macroscopic level the crossing angle between the electron and the laser beam is $\delta = 17°$, in a microscopic level the actual crossing angle between the electrons and the laser photons (which we will call the effective crossing angle) depends on the position of the crossing point with respect to the laser focus. This is because the laser beam is focused and the focusing angle can be defined as

$$\tan \xi \equiv \lim_{z' \to \infty} \frac{r(z')}{z'} \approx \frac{r_0}{z_R} = \frac{1}{2\sqrt{2}f_\#} \tag{A.49}$$

where $r(z')$ the $1/e$ radius of the laser field intensity as defined in Eq. 2.115 of chapter 2, z_R, r_0 the Rayleigh range as given by Eq. 2.113 and the $1/e$ radius of the field intensity at the laser focus as given by Eq. 2.112 respectively, again in chapter 2 and finally $f_\#$ the f-number of the focusing optics introduced in section 2.3.2 of chapter 2. The effective crossing angle needs to be calculated for each STE for both primary and secondary processes and the angle α in all the expressions presented in section A.2 needs to be replaced by $\alpha_{eff} = \pi + \delta_{eff}$.

The average direction of propagation of the laser photons at the point (x_0', y_0', z_0') is taken to be along the direction of the tangent $\vec{R}$ to the "$1/r$ envelope" of the laser field intensity at this point in the plane P, defined by (x_0', y_0', z_0') and the laser axis as shown in Fig. A.8. The $1/r$ envelope is defined by the points (x', y', z') with

$$\rho_\omega(x', y', z') = \frac{1}{r} \cdot \rho_\omega(0, 0, z') \tag{A.50}$$

and r given by

$$r = \frac{\rho_\omega(x_0', y_0', z_0')}{\rho_\omega(0, 0, z_0')} \tag{A.51}$$
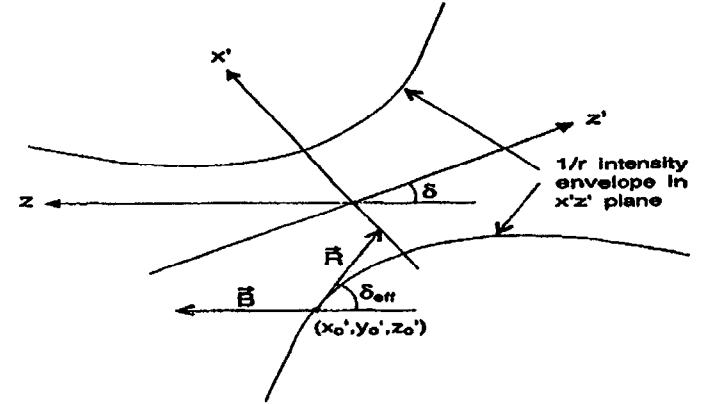
Figure A.8: Effective crossing angle between the laser photons propagating along $\vec{R}$ and the electron beam moving along $\vec{B}$ at the interaction point (x_0', y_0', z_0') (from [62]).

In the plane P the envelope is described by the line

$$e(z') = \frac{\sqrt{x_0'^2 + y_0'^2}}{r(z_0')} \cdot r(z') \tag{A.52}$$

where $r(z')$ is the same as in Eq. A.49.

If $\vec{B}$ is a unit vector pointing along the beam, the effective crossing angle is given by

$$\tan \delta_{eff} = -\frac{|\vec{B} \times \vec{R}|}{\vec{B} \cdot \vec{R}} \tag{A.53}$$

with

$$|\vec{B} \times \vec{R}| = \sqrt{k^2 y_0'^2 + k^2 x_0'^2 \cos^2 \delta + z_0'^2 \sin^2 \delta + 2k x_0' z_0' \cos \delta \sin \delta}$$

$$\vec{B} \cdot \vec{R} = +k x_0' \sin \delta - z_0' \cos \delta \quad \text{for } z_0' > 0$$

$$= -k x_0' \sin \delta + z_0' \cos \delta \quad \text{for } z_0' \leq 0$$

$$k = \frac{z_0'^2}{a z_R^2 + z_0'^2}$$

and a the ratio between the effective and the diffraction limited focal spot area as defined in section 2.3.2 of chapter 2.

A.6.2   Effective Beam Density

In the calculations of the interaction yields during the numeric integration, the density of the beam particles is needed. In general the density of the beam particles is calculated from the expression shown in Eq. 2.119 of chapter 2. Nevertheless for STE's which are already some distance inside the laser focus, part of the beam particles will be lost due to previous interactions with the laser focus. The beam density needs to be corrected for these losses, which increase with the distance covered inside the laser focus and with the field strength.

Figure A.9: Procedure for calculating the effective density of beam particles. The currently examined STE is moved backwa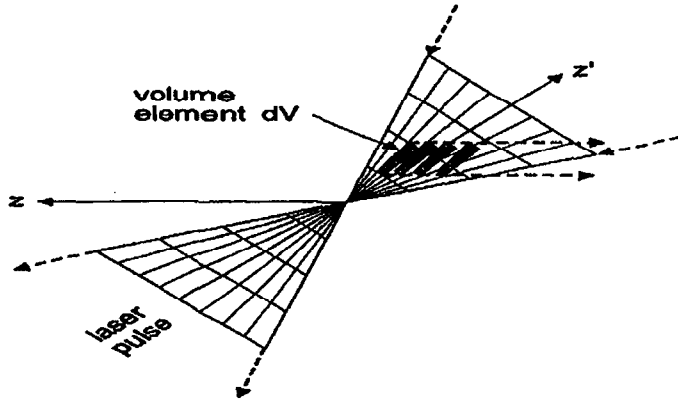rds in time and the total interaction yield of beam particles using the Klein-Nishina approximation is computed (from [62]).

In the numerical integration code this correction to the beam density is introduced only for the electron beam particles. This is because of the following reasons:

1. The probability of electrons to Compton scatter, is orders of magnitude larger than for high energy gammas to convert into e^+e^- pairs through the Breit-Wheeler or the trident process.

2. The total probability for any order n of Compton scattering can be fairly ac-

curately approximated by the Klein-Nishina probability describing the linear Compton scattering.

3. Finally all the E-144 measurements are done using an initial electron beam.

The Klein-Nishina formula describing the total interaction rate for the linear Compton scattering has the form:

$$W = \frac{e^2 m^2 \rho_{\pm}}{16\pi E_{\pm}} \eta^2 \left[\left(1 - \frac{4}{u_1} - \frac{8}{u_1^2}\right) \ln(1 + u_1) + \frac{1}{2} + \frac{8}{u_1} - \frac{1}{2(1 + u_1)^2} \right] \quad (A.54)$$

where

$$u_1 = \frac{2\omega_\mu p^\mu}{m^2} \simeq \frac{2E_{\pm}\omega(1 - \cos\alpha)}{m^2} \quad (A.55)$$

Fig. A.9 shows the method for calculating the new beam density. The current STE is propagated backwards in time through the laser field in steps defined by Eq. A.45, and the total interaction yield using the expression in Eq. A.54 is computed. The new "effective" beam density is then derived by subtracting this yield from the initial beam density.

A.7   Speed Optimizations

As already mentioned several times, speed of execution was one of the main driving goals during the creation of the numeric integration code. An extensive array of speed optimizations has been implemented to that end, after the following requirements and observations:

1. The photon, electron and positron spectra produced by the simulation and compared to the experimentally observed ones, should be affected as little as possible.

2. Due particularly to the overestimated range of the time integration, many STE's are characterized by low particle densities and contribute only slightly to the total interaction yields.

3. Higher order processes, which involve a larger number of simultaneously interacting laser photons, vary nonlinearly with η^2 and their yields are dominated by few STE's characterized by high laser intensity.

4. Most of the CPU time is spent during the calculations of the secondary processes.

All the speed optimization options are either in the form of program options or of input parameters, so that the user can have the maximum possible control over them. This is highly desirable, since their effect on both the CPU time and on the simulated spectra can be substantial.

A.7.1   Variable Step Size in z' and t

In section A.3, we discussed the ways of defining the range of the integration grid and the step sizes in each axis x', y' and z' and also in time. From the discussion there it is clear that although the step sizes in the x' and y' axes depend on the location on the z' axis, the step sizes along the z'-axis and consequently in time are constant. Therefore choosing a big step size dz' along the z'-axis, will result to possibly serious inaccuracies in the simulation around the laser focus area, where the photon density is at its maximum and in general varies quickly with z'. On the other hand a small step size that will allow for more accurate simulation results, will increase the CPU time by a large amount. The solution to such a situation is to introduce a variable step size along z' and t, that becomes smaller as we approach closer to the laser focal point.

Ignoring the Gaussian profile of the laser beam along the z'-axis, the variation of the photon density due to focusing is given by

$$\rho(z') = \rho_0 \cdot \frac{a \cdot A_0}{A(z')} = \rho_0 \cdot \frac{a}{a + (z'/z_R)^2} \tag{A.56}$$

where ρ_0 is the normalized photon density at the laser focus, a is the ratio of the effective A_{eff} and the diffraction limited A_0 focal-spot sizes and $A(z')$ is the laser
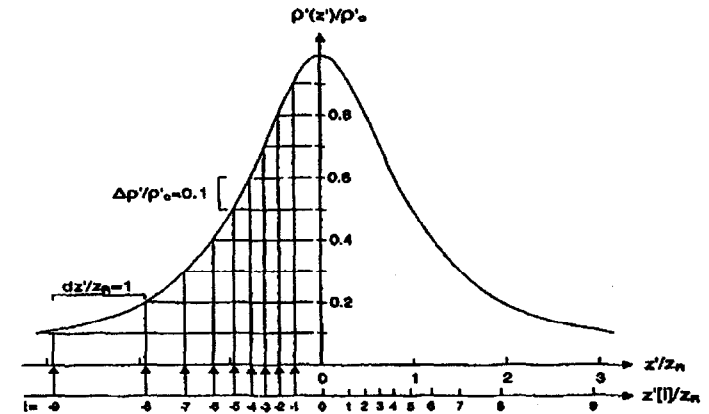
Figure A.10: Example for the creation of the variable step grid along the z'-axis. Here $\Delta k = 0.1$ and the default step size is $dz' = z_R$ (from [62]).

area defined as:

$$A(z') \equiv \pi r(z')^2 = A_0 \left[a + (z'/z_r)^2 \right] \tag{A.57}$$

The distance $z'(k)$ for which the photon density has dropped by a factor of $(1 - k)$ with respect to the one at the focal point, i.e.

$$\rho(z'(k)) = (1 - k) \cdot \rho_0 \tag{A.58}$$

is found to be using Eq. A.57:

$$z'(k) = \pm z_R \cdot \sqrt{\frac{ak}{1 - k}} \tag{A.59}$$

Therefore a grid of points with central values $z'[\pm i]$ along the z'-axis and also along time, centered around point $z'[0] = 0$, the focal point, can be determined following the expression

$$z'[\pm i] = z'(i \cdot \Delta k) \tag{A.60}$$

with Δk the maximum allowable change in the photon density between the two steps. Once the distance between the centers of two consecutive points in the grid $\Delta z' =$

$z'[i+1]-z'[i]$ is equal or greater to the default step size dz', as shown in Eq. A.37, then the variation of the step size stops and the rest of the steps are kept fixed and equal to dz'. The steps along time dt are then adjusted accordingly following Eq. A.38. The whole process is illustrated in Fig. A.10.

A.7.2 Low Interaction Yields

A considerable number of STE's are characterized by low photon and beam densities and as a result contribute very little to the total interaction yields of the various processes examined by the simulation. It is useful to determine these STE's and exclude them from the numeric integration loops. This can be done by testing the quantity $P_{\rho \rho dV} = \rho_\omega \cdot \rho_{beam} \cdot dV$, the product of the photon and beam densities with the volume element. The interaction yield of the linear Compton scattering, which is characterized by the highest interaction probability of any of the processes considered in the numeric integration, is proportional to $P_{\rho \rho dV}$. If this quantity is small therefore, then the corresponding STE can be safely omitted from any further calculations. In order to test $P_{\rho \rho dV}$, we need first to find the maximum value $P_{\rho \rho dV}^{max}$ that this quantity can attain throughout the whole integration grid. This does not necessarily happen at the laser focus, since in general the two interacting beams can be characterized by certain offsets in space (x_{off}, y_{off}) and in time t_{off}, and so a loop over all STE's is needed to determine $P_{\rho \rho dV}^{max}$. Then, during the integration, only the STE's with

$$P_{\rho \rho dV} > R_{\rho \rho dV} \cdot P_{\rho \rho dV}^{max} \tag{A.61}$$

are considered, with $R_{\rho \rho dV}$ is an input parameter to the code and represents the minimum ratio between $P_{\rho \rho dV}$ and $P_{\rho \rho dV}^{max}$.

A.7.3 CPU Intensive Processes

All the processes for which more than one laser photon is involved are nonlinearly dependent on the laser intensity parameter η (in reality on η^2). This means that a

significant contribution to them arises only from STE's characterized by very high field intensities. Again a selection of only those STE's that result to substantial contributions to the total interaction yield can be made, by looking at the quantity $P_{\eta 2ndV} = \eta^{2n} \cdot dV$. As in the previous section, the yields of the nth order Compton scatterings are proportional to this quantity. In order to use it we need to determine the maximum value $P_{\eta 2ndV}^{max}$ can attain in the whole integration grid. Then once more only the STE's with

$$P_{\eta 2ndV} > R_{\eta 2ndV} \cdot P_{\eta 2ndV}^{max} \tag{A.62}$$

are considered, where $R_{\eta 2ndV}$ is the minimum ratio between $P_{\eta 2ndV}$ and $P_{\eta 2ndV}^{max}$.

Nevertheless applying this procedure to very high order processes, may result in discarding all the STE's with the exception of the one that corresponds to $P_{\eta 2ndV}^{max}$, even if the minimum ratio $R_{\eta 2ndV}$ is small, as it is normally the case (a typical value can be as low as 10^{-3}). This is true even for very small variations in the value of η. For example in a process of order $n = 100$ and with η being still 90% of its maximum value, the ratio $P_{\eta 2ndV}/P_{\eta 2ndV}^{max}$ is as low as 7×10^{-7}. Keeping only one STE may be too drastic of an optimization. In order that extreme cases like this to be avoided, a second quantity $P_{\eta 2dV} = \eta^2 \cdot dV$ is also calculated and compared to a maximum value determined by the integration grid as usually:

$$P_{\eta 2dV} = R_{\eta 2dV} \cdot P_{\eta 2dV}^{max} \tag{A.63}$$

Here $R_{\eta 2dV}$ is the minimum ratio between $P_{\eta 2dV}$ and $P_{\eta 2dV}^{max}$ selected by the user. It is usually set to a value around 0.5. Only STE's for which at least one of the above two criteria is satisfied are included in the integration. It is clear that for low orders $R_{\eta 2ndV}$ is the main selection factor, while for higher orders $R_{\eta 2dV}$ dominates.

A.7.4 Optimization of Secondary Compton Scattering

The optimizations discussed in this section concern only the calculation of the secondary processes and do not affect at all any of the primary processes. The first
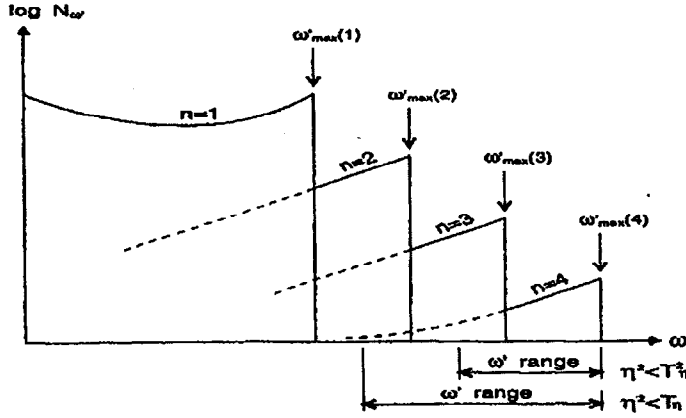
Figure A.11: Gamma spectra produced during the first 4 orders of Compton scattering. At the bottom of the plot the ω'_{min} value for the integration over the gamma energies during the numeric integration is shown for $n = 4$ and for both selection criteria based on the field strength, as discussed in the text (from [62]).

optimization is based on the fact that secondary processes are important only when their total yields are comparable to those of a higher order primary process, e.g. a double linear Compton scattering (a linear primary Compton scattering followed by a secondary linear Compton scattering), is comparable to the second-order primary Compton scattering for scattered electron energies below the $n = 1$ edge. Above the electron energy $n = 1$ edge, the spectrum is completely dominated by the primary linear Compton scattering since no secondary processes of lower order exist. We can therefore safely ignore the secondary Compton scatterings for the cases when the scattered electron energy is above a cutoff E_{max} without any essential effect on the derived electron or photon spectra.

Fig. A.11 shows the energy spectrum of the high energy gammas for the first 4 orders of Compton scattering. Several characteristics are evident:

1. The energy spectrum of a gamma produced in an nth order Compton scattering, extends to higher energies than the spectra of the gammas produced during

lower order Compton scatterings.

2. The interaction yields differ between two consecutive order Compton scatterings by a factor of $\sim 1/\eta^2$, especially when $\eta \ll 1$.

3. The spectrum peaks close to the endpoint $\omega'_{max}(n)$.

The above observations suggest that the secondary processes of order n involving the high energy gammas, can be limited to those gamma energies ω' for which their contribution is dominant and in particular to the ones which are higher than the maximum gamma energy of the previous order. The algorithm employed by the numeric integration code to decide the initial gamma energy ω'_{min} from which the integration over the gamma energies is started, takes into account the laser field intensity parameter η and is described by the following two equations:

$$\eta^2 \leq T_{\eta 2}^2 : \quad \omega'_{min} = \frac{\omega'_{max}(n-2) + \omega'_{max}(n-1)}{2} \quad \text{for } n > 2 \quad (A.64)$$

$$= 0.95 \cdot \omega'_{max}(1) \quad \text{for } n = 2 \quad (A.65)$$

$$= 0 \quad \text{for } n = 1 \quad (A.66)$$

$$\eta^2 \leq T_{\eta 2} : \quad \omega'_{min} = \frac{\omega'_{max}(n-3) + \omega'_{max}(n-2)}{2} \quad \text{for } n > 3 \quad (A.67)$$

$$= 0.95 \cdot \omega'_{max}(1) \quad \text{for } n = 3 \quad (A.68)$$

$$= 0 \quad \text{for } n \leq 2 \quad (A.69)$$

The parameter $T_{\eta 2}$ is an input parameter defined by the user.

A.7.5   Optimizing the Breit-Wheeler Pair Production

A basic characteristic of the multiphoton Compton scattering, is that the resulting energy spectra of the scattered electrons, or the produced high energy gammas, have a shape and an energy range that strongly depends on the order n of the Compton scattering. In contrast, the energy spectra of the electrons or positrons of the pairs produced during the multiphoton Breit-Wheeler process, and as a result also the

trident energy spectra the way treated in the numeric integration code, do not have such a dependence on the order n. These spectra are fairly symmetrical around the half energy of the initial high energy gamma used for the pair production. This means that different orders of multiphoton pair production contribute only to the total electron and positron yield without affecting essentially the form of their energy spectrum.

As already discussed in section A.5, for both primary and secondary processes a loop over the number n of interacting photons (different orders of multiphoton processes) is made. Evidently it is advantageous in terms of required CPU time, to stop this loop over n at a point where the contribution to the total yield of the primary or secondary multiphoton Breit-Wheeler or trident pair production becomes negligible. The numeric integration keeps track of the total probability $W_{e^+e^-}(n)$ of the specific order n and terminates the loop as soon as

$$W_{e^+e^-}(n) < W_{e^+e^-}^{max} \cdot R_{BW} \qquad \text{(A.70)}$$

i.e. the contribution $W_{e^+e^-}(n)$ of the last calculated order has dropped below the fraction R_{BW} of the maximum contribution $W_{e^+e^-}^{max}$ of all orders calculated so far. The ratio R_{BW} is a user input.

A.7.6 Effect of Optimizations

It is important to estimate the effect of all the previously described speed optimizations. As an example, the case of an electron beam colliding with a circularly polarized green laser is taken. The processes considered are the primary multiphoton Compton scattering (P1_NLCS), the primary trident multiphoton pair production (P1_WWBW), the secondary multiphoton Compton scattering (P2_NLCS) and the secondary multiphoton Breit-Wheeler pair production (P2_MPBW), all up to the order of $n = 20$ and with typical input parameters for the laser pulse, electron beam and space-time grid. Only the optimization discussed in section A.7.1 is not studied

separately, as it is by default included in the calculation procedure and is essential for better result accuracy.

The numeric integration results monitored during these estimates are the following:

- N_{ph}, all: the total number of photons produced.
- $N_{e^+e^-}$, all: the total number of pairs produced.
- $N_{e^+e^-}$, trident the total number of trident pairs produced.
- N_{e^-}, $n = 1$, 19-20 GeV: the number of scattered electrons with energies between 19 and 20 GeV produced primarily by $n = 1$ Compton scattering.
- N_{e^-}, $n = 2$, 14-15 GeV: the number of scattered electrons with energies between 14 and 15 GeV produced primarily by $n = 2$ Compton scattering.
- N_{e^-}, $n = 3$, 9-10 GeV: the number of scattered electrons with energies between 9 and 10 GeV produced primarily by $n = 3$ Compton scattering.
- N_{e^-}, $n = 4$, 6-7 GeV: the number of scattered electrons with energies between 6 and 7 GeV produced primarily by $n = 4$ Compton scattering.

The number of calls to the integration routines for each process examined and the total CPU time is used to measure the effect on the speed:

- calls to NLCS: the number of calls to the multiphoton Compton scattering routine.
- calls to MPBW: the number of calls to the multiphoton Breit-Wheeler pair production routine.
- calls to WWBW: the number of calls to the multiphoton trident pair production routine.
- total calls: the total number of calls to all the multiphoton processes routines.
- total CPU: total CPU time measured in SLAC CPU seconds.

	Speed Optimizations						
	none	R_{ppdy} =10^{-2}	⊕ $R_{\eta 2ndy}$ =10^{-3}	$R_{\eta 2dy}$ =0.6	⊕ E'_{max} =20	⊕ $T_{\eta 2}$ =0.1	⊕ R_{BW} =10^{-3}
N_{ph}, all	2.25x10^7	95.6 %	95.6 %		94.7 %	94.7 %	94.7 %
N_{e+e-}, all	4.66x10^{-2}	99.8 %	98.6 %		98.6 %	98.6 %	98.6 %
N_{e+e-}, trid	2.47x10^{-5}	100 %	96.9 %		96.9 %	96.9 %	96.9 %
N_{e-}, n=1 (19-20 GeV)	1.09x10^8	95.7 %	95.7 %		95.7 %	95.7 %	95.7 %
N_{e-}, n=2 (14-15 GeV)	3.59x10^4	99.4 %	99.3 %		99.0 %	99.0 %	99.0 %
N_{e-}, n=3 (9-10 GeV)	1.41x10^3	99.7 %	99.6 %		99.5 %	99.4 %	99.4 %
N_{e-}, n=4 (6-7 GeV)	1.22x10^1	99.8 %	99.6 %		99.5 %	99.2 %	99.2 %
calls to NLCS	2162x10^6	29.1 %	3.81 %		2.14 %	1.23 %	1.23 %
calls to MPBW	483x10^6	53.7 %	4.05 %		4.05 %	4.05 %	2.25 %
calls to WWBW	131x10^6	23.6 %	0.63 %		0.63 %	0.63 %	0.63 %
total calls	2775x10^6	33.1 %	3.70 %		2.40 %	1.69 %	1.38 %
total CPU (SLAC sec)	25742	30.7 %	3.77 %		2.49 %	1.80 %	1.56 %

Figure A.12: Effect of the various speed optimizations on the precision and execution speed of the simulation (from [62]).

The table in Fig. A.12 shows the results of such a study. Each column represents a different optimization element introduced in the simulation, in addition to any ones already introduced earlier (this is what the symbol ⊕ indicates) and it shows the fraction of the monitored values with respect to their initial values when no speed optimizations are included. The optimization in the second column, rejects all

STE's characterized by a low reaction yield, as discussed in section A.7.2. The third column shows the additional effect of the optimization of the CPU intensive processes P1_WWBW, P2_NLCS and P2_MPBW, as discussed in section A.7.3. The fourth and fifth columns show the individual effect of the two speed optimizations introduced for the P2_NLCS process, as discussed in section A.7.4. Finally the last column shows the effect of the multiphoton Breit-Wheeler secondary process optimization, as discussed in section A.7.5. In brief the table shows that the introduction of the speed optimizations does not affect any of the monitored values by more than 5% in the worst case, while on the other hand it improves the CPU time by a factor of $\sim$ 65. Clearly the numbers presented in Fig. A.12 depend on the type of the simulation and the input parameters used.

A.8 Saving Results

The principle simulation outputs are particle spectra for a variety of different processes. Each spectrum is stored in the form of an array sp[..] with dimension m and an array index i within the range $[0, m - 1]$. Each array element represents an energy bin of width $\Delta E = E_{max}/m$ with E_{max} the upper limit of the energy spectrum specified as an input parameter by the user. The most important of them, in terms of the type of data taken and analyzed by the E-144 experiment are:

P1_NLCS : primary nonlinear Compton scattering,

P1_WWBW : primary multiphoton trident pair production,

P2_NLCS : secondary nonlinear Compton scattering,

P2_MPBW : secondary multiphoton Breit-Wheeler pair production.

The number of processes to be simulated is selected by the user and their final results are summarized in the form of energy spectra for all the photons, electrons and positrons produced in the collision. Since a lot of the processes listed above are interdependent, the final particle spectra contain the contributions from all the selected

processes. For example, the Compton backscattered gammas from the P1_NLCS process, can be used to produce e^+e^- pairs under the secondary multiphoton Breit-Wheeler process P2_MPBW and thus affect not only the positron but also the electron spectrum.Similarly the resulting electrons and positrons can in their turn undergo further nonlinear Compton scattering producing more backscattered photons, thus affecting the photon spectrum *etc.*.

In addition to the photon, electron and positron spectra, the combined spectra of the produced pairs and the polarization of the backscattered photon beam as a function of photon energy, are also stored in the form of arrays. Therefore the total number of spectra calculated by the numeric integration for nonlinear QED (NLQED) processes is:

> phsp_nl[..]   : total photon energy spectrum (NLQED),
>
> elsp_nl[..]   : total electron energy spectrum (NLQED),
>
> posp_nl[..]   : total positron energy spectrum (NLQED),
>
> pasp_nl[..]   : total e^+e^- pair energy spectrum (NLQED),
>
> phpo_nl[..]   : total photon polarization spectrum (NLQED).

Each STE is calculated independently of all the other STE's for every primary process, and therefore the total particle spectra are the sum of the spectra of each individual STE

$$xxsp\_nl[..] = \sum_{STE_s} stp\_xxsp\_nl[..] , \qquad (A.71)$$

where stp_xxsp_nl[..] stands for one of the following STE specific spectra for NLQED processes:

> stp_phsp_nl[..]   : photon energy spectrum for STE (NLQED),
>
> stp_elsp_nl[..]   : electron energy spectrum for STE (NLQED),
>
> stp_posp_nl[..]   : positron energy spectrum for STE (NLQED),
>
> stp_pasp_nl[..]   : e^+e^- pair energy spectrum for STE (NLQED),
>
> stp_phpo_nl[..]   : photon polarization spectrum for STE (NLQED).

Fig. A.13, shows the method for updating the various energy spectra in a simulation that includes the NLQED processes P1_NLCS, P1_WWBW, P2_NLCS and P2_MPBW, defined earlier.

The most effective way of storing and retrieving simulation data, over a wide range of input parameters, is by creating lookup tables. This method takes full advantage of the numeric integration's flexibility in handling different inputs and its speed of execution. The lookup tables are output data files in ASCII or binary form, that contain energy spectra, like the ones described earlier, produced for a wide range of the following seven input parameters:

1. leta: the laser field intensity parameter η, varying between 0.01–1.00 in 41 equal logarithmic steps.

2. lare: the laser area in units of μm^2, varying between 10–50 μm^2 in 21 steps of 2 μm^2 each.

3. lwid: the laser pulse FWHM in units of ps, varying between 1–3 ps in 21 steps of 0.1 ps each.

4. bsix: the electron beam σ_x in units of μm, varying between 10–60 μm in 21 steps of 2.5 μm each.

5. bsiy: the electron beam σ_y in units of μm, varying between 10–60 μm in 21 steps of 2.5 μm each.

6. bwid: the electron beam bunch FWHM in units of ps, varying between 2–12 ps in 21 steps of 0.5 ps each.

7. toff: the electron-laser beam timing offset in units of ps, varying between 0–10 ps in 21 steps of 0.5 ps each.

The output data files can be merged in one master lookup table file, which can be used either directly via an interface program that reads and prints the simulation predictions for a specific value of the above input parameters [63], or more conveniently translated into the form of ntuples and used by the analysis codes directly for
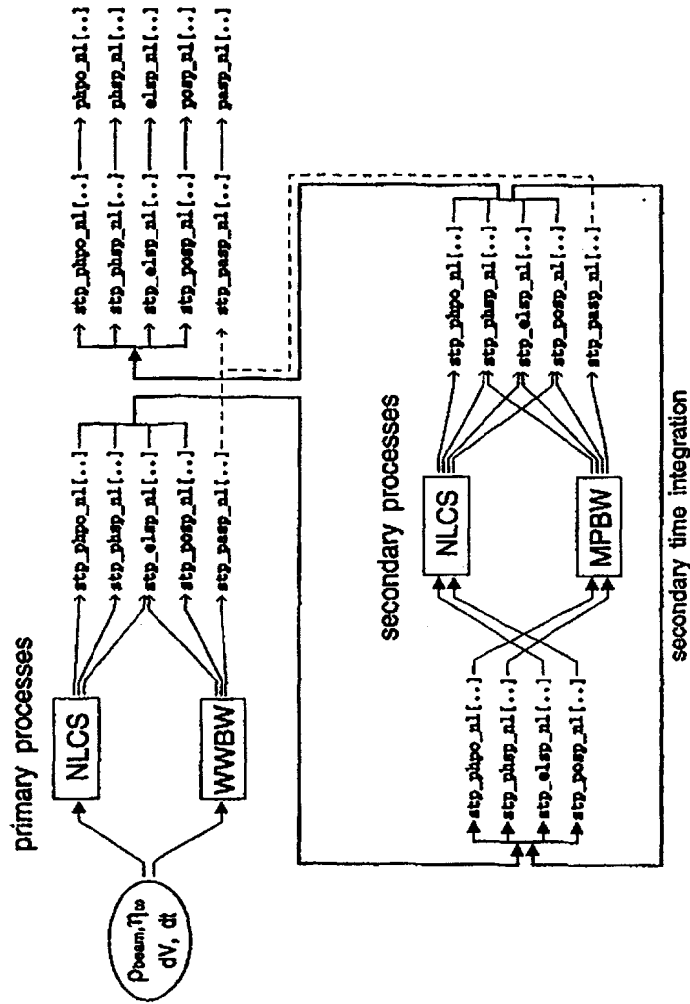
Figure A.13: Schematic that shows the procedure for updating the various energy spectra for a nonlinear QED simulation that includes the processes P1_NLCS, P1_WWBW, P2_NLCS and P2_MPBW (from [62]).

comparisons with the measured data. Since the plotting of the measured data rates is done versus η, its range was extended so that it covered three orders of magnitude and consequently became the most important input for the creation of the lookup tables.

Appendix B

Event Selection

During the main chapters of the thesis and especially during the 46.6 GeV data analysis, we discussed several cuts introduced to the data sample, aiming mainly at improving the quality of the selected data. For this reason all those cuts were applied exclusively on the laser ON events. The number of events lost after the application of those cuts was also discussed there. What was not mentioned in those sections, is that the data sample on which all the data analysis cuts were applied, was selected by an even larger data sample including both laser ON and laser OFF (the latter give an estimate of the background levels) events, after introducing specific requirements for the electron beam. This in fact was the first step for selecting the events that were further analyzed. In this appendix a description of the event selection based on the electron beam requirements is given. In the following sections we tend to call these requirements the beam related cuts, or more simply the beam cuts. One more sophisticated beam related cut, the so called "shazam" cut is examined separately at the end.

B.1   Beam Related Cuts

The E-144 data acquisition system, in addition to a large array of other useful quantities, also monitors a number of electron beam related quantities. These quantities are called the electron beam parameters. Below follows a list of the electron beam parameters, where each one is defined by the same symbol used also in the data acquisition code:

- BCHA: the electron beam charge (e^-/bunch).
- BENE: the electron beam energy offset with respect to the 46.6 GeV, or the 49.1 GeV when the beam energy was subsequently raised, nominal energy in units of GeV.
- BXPO: the electron beam x-position at the interaction point (IP) in units of μm.
- BYPO: the electron beam y-position at the IP in units of μm.
- BXAN: the electron beam pointing angle in the x direction in units of μrads.
- BYAN: the electron beam pointing angle in the y direction in units of μrads.
- BPHA: the klystron 91 rf phase.
- BLOS: the difference of the beam charge between two toroids, located close to the entrance and close to the dump of the FFTB line.

All the above beam parameters, with the exception of the beam charge related ones, are reported by the accelerator feedback loops active during the data collection time and their values are present on an event-by-event basis.

The selection of the data sample for both the laser ON and the laser OFF events, by looking at the beam parameters, is based on the fact that events with large fluctuations in any of the beam parameters listed above, should be discarded. Large fluctuations in the beam charge for example, mean that there is significant beam scrapping on the accelerator pipe walls creating enormous background levels. Large
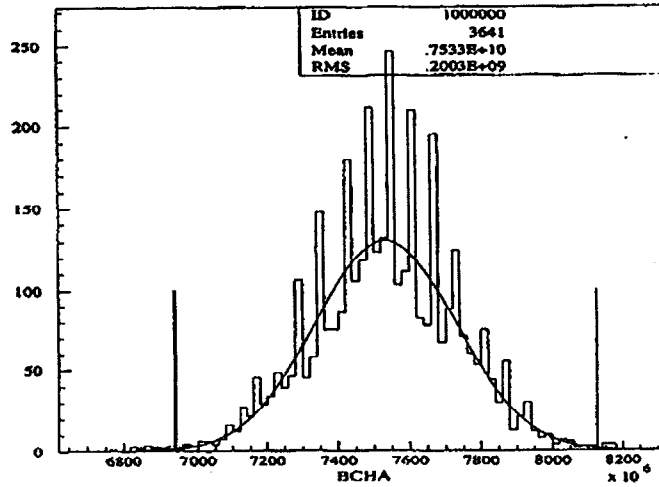
Figure B.1: An example of the derivation of the beam cut value for the case of the electron beam charge and for run 15323.The vertical lines show the limits of the $\pm 3\sigma$ range, based on the Gaussian fit σ.

offsets in the position or the pointing angle of the electron beam at the IP can affect seriously the spatial and temporal overlap conditions between the laser and the electron beams. Finally energy offsets, besides of introducing beam steering problems, it can also seriously affect the event production rates. To avoid therefore large beam parameter fluctuations, the $\pm 3\sigma$ rule is introduced. For each run all the above listed eight beam parameters are plotted separately and the statistical rms distribution is extracted. The plots then are redrawn within the $\pm 3\sigma_{rms}$ limits around the mean value and a Gaussian is fitted. The σ of this last Gaussian fit defines the final $\pm 3\sigma$ range within which the data events are kept. Fig B.1 shows such a plot for the case of the electron beam charge and for run 15323. An indicator, called the BFLA, is assigned then to each data point. Events for which BFLA=0, are characterized by all their beam parameters being within the $\pm 3\sigma$ range, while events with BFLA>0, have
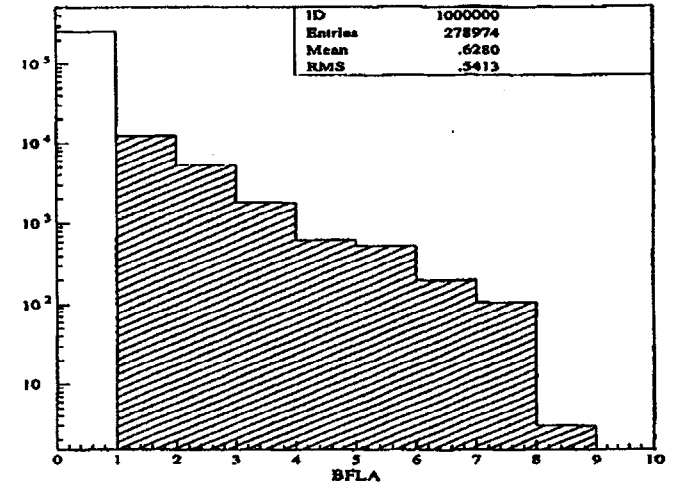
Figure B.2: Distribution of the beam cut parameter BFLA for the total 46.6 and 49.1 GeV data sample. The shaded area corresponds to events for which at least one of the beam parameters was not within the $\pm 3\sigma$ range, as defined in the text.

at least one beam parameter that lies outside the $\pm 3\sigma$ range. The value of BFLA in this case is indicative of the number of beam parameters for that specific event, that were found outside the $\pm 3\sigma$ range and can vary between 1 (one parameter only is outside) up to 8 (all parameters are outside). Only data events for which BFLA=0 are kept and subsequently analyzed. Fig. B.2, shows the BFLA distribution for all the laser ON and laser OFF events used in the 46.6 GeV and 49.1 GeV data analysis described in the main part of the thesis. About 21,000 events are found to have BFLA>0, which correspond to $\sim 7.5\%$ of the initial data sample.

B.2   The Shazam Cut

There are data events that are characterized by high background levels, which can be seen, for example, in all ECAL rows, even the ones far away from the beam pipe, like rows 5, 6, 7, 8, which in principle are not supposed to see any signal at all. These background events have no laser origin, but are characteristic of poor electron beam conditions; for example events where the linac energy feedbacks do not perform well. From the accelerator operator's point of view, they look like big electron flashes hitting all over the accelerator pipe walls and producing background electrons or positrons of various energies. We call these events the "shazam" events. Fig. B.3 shows the shazam events for the case of the 49.1 GeV data. The top three plots show the signal of the center pads of row 5 of ECAL versus that of row 1, both for the laser ON (left) and the laser OFF (center) events. It is clear from the laser OFF plot that we have at least three events that are characterized by high energy backgrounds. These are seen much better when the distribution of the signal from row 5 of ECAL is shown independently (right plot). The second plot triplet shows exactly the same correlations, but now the signal from the outer pads of row 5 of ECAL is used.

Although the shazam events do not seem to be too many—they are usually encountered more often during the initial time of linac operation—we would like to cut them away. The best way of doing that is by subtracting from the signal of the center pads of row 5 of ECAL, the signal from the corresponding outer pads of the same ECAL row, the latter being scaled by some factor, i.e.

$$ECR(5) - a\,EOR(5) \tag{B.1}$$

The scaling factor needs to be chosen in such a way so that the shazam events will still be visible for the laser OFF events, but not for the laser ON events, when we will try to correlate this subtracted row 5 signal to the signal from the center pads of row 1 of ECAL. If this is achieved, then we can introduce a shazam cut without hurting any of the laser ON data. The best way of choosing the scaling factor is to find the
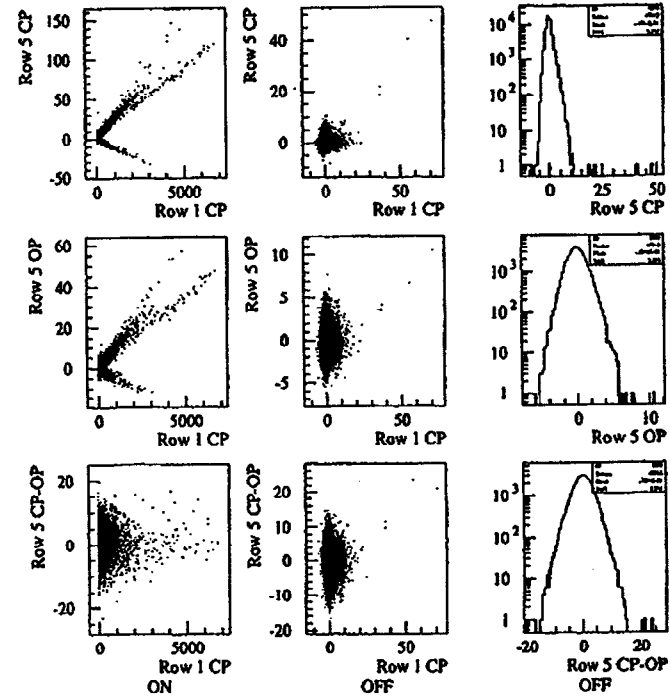
Figure B.3: Demonstration of the shazam cut effect. This is a cut applied in order to clean up events where the electron beam scrapes the accelerator pipe and produces abnormal background levels.

slopes of the correlation plots shown on the left sides of the top and center triplets in Fig. B.3, and determine their ratio. The resulting scaling factor found in this way is $a = 2.5$. The bottom triplet in Fig. B.3 shows the correlation of the signal resulting from Eq. B.1 with $a = 2.5$, with the signal from the center pads of row 1 of ECAL for both the laser ON (left plot) and laser OFF (center plot) events, along with its energy distribution (right plot). From this last plot we can introduce a shazam cut

at ±20 GeV without loosing any of the laser ON events. The total number of shazam events encountered in the whole data sample is ~ 10 and almost all of them belong to the 49.1 GeV data sample.

Appendix C

Nonlinear Compton Scattering Results

In this appendix we briefly discuss the results from the nonlinear Compton scattering data, taken during the August 1996 run. Although the main goal of that run was the observation of positron events from multiphoton Breit-Wheeler pair production, the experimental arrangement provided us also with the opportunity of simultaneously collecting data useful for studying the higher order Compton scattering processes [50]. The main reason for presenting the measured nonlinear Compton scattering data here, is that their comparison with the simulation data, which are based on the input η values, can check the validity of these values calculated from the linear and nonlinear monitor signals, as described in chapter 6. Although in that chapter we had a quick glance at the ECAL data, only the analysis of the complete ECAL data sample can provide us with the means of fully checking the reconstructed η values, since the ECAL data probe higher orders of nonlinear Compton scattering than the nonlinear monitors do.

C.1 Experimental Setup

For the nonlinear Compton scattering process, the electron calorimeter (ECAL) becomes the primary detector. Fig. C.1 shows the experimental setup for nonlinear Compton data collection. Briefly, high energy electrons interact with the tightly
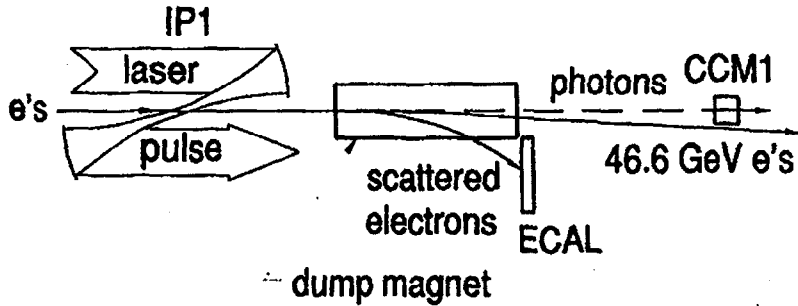

Figure C.1: Setup for the study of the nonlinear Compton scattering.

focused laser beam, according to the reaction

$$e + n\omega_0 \longrightarrow e' + \omega_\gamma \qquad (C.1)$$

as already described in the main part of the thesis (see for example chapter 1). The laser is linearly polarized with a wavelength of 527 nm (green) and a pulse FWHM of the order of 1.5 ps. The laser energies vary between 250 mJ and 750 mJ. The produced high energy gammas, move forward and they can be detected by the forward gamma Čerenkov detector, called CCM1. The scattered electrons are bent by the permanent bending magnets, located after the interaction region (IP), towards ECAL. ECAL itself is moving vertically during the runs, so that more than one orders of multiphoton Compton scattering are measured. To avoid saturation of the detector, the upper limit of its vertical motion is placed well below the kinematic edge of the $n = 1$ scattered electrons. For these runs, only the signal from the top row of ECAL has been analyzed,

since this row shows the smallest signal reconstruction errors (for details about the ECAL reconstruction method, see section 5.1.3). Consequently, only $n = 3$ and $n = 4$ Compton electrons have been analyzed. In order to accurately compare the data with the theory, the simulation needs a value for the laser intensity parameter η as an input (see appendix A for a description of the simulation code). As already described in chapter 6, the η values are reconstructed by the measured signals from the N1, N2 and N3 monitors which intercept first-, second- and third-order Compton scattered electrons. If the η reconstruction on an event-by-event basis is done correctly, the simulated data should be in good agreement with the data measured by ECAL, since the last essentially also looks at Compton scattered electrons, albeit higher order ones. It is important to stress here that agreement between the simulation and the measurement does not necessarily indicate agreement with the theory describing the physical processes, but merely the validity of the η reconstruction method. Older data samples, for which η was independently reconstructed by the measured laser parameters, have already confirmed the validity of the theoretical description (see for example [60], [50], [59]). For normalization to the $n = 1$ Compton signal, the reported signal of the two Čerenkov counters that look at linearly scattered Compton electrons, described in section 5.2, is used, instead of the gamma monitor CCM1 signal, which for the reasons stated in that section, was used only during calibration measurements.

C.2 Data Analysis and Results

Two main data samples were taken, the first one using an electron beam of 46.6 GeV, and the second one an electron beam of 49.1 GeV. We will discuss results from both data samples. For a detailed description of the data analysis of the nonlinear Compton scattering data shown here, see [50]. The event selection criteria were the same for both data samples analyzed, so we will present them together here. Five types of selection cuts have been used:

1. Electron beam cuts. Electron beam parameters are required to be within $\pm 3\sigma$ of their normal values (see Appendix B for a discussion of the beam parameter cuts).

2. Overlap cut. The ratio of the measured γ flux over the simulated one without jitter, *i.e.* N_{data}/N_{sim}, needs to be more than 0.7.

3. DAQ cut. A cut on the DAQ trigger time difference, for both laser ON and laser OFF events is introduced. This is to ensure that events that were wrongly confused as laser ON or laser OFF events, will not be considered in the data analysis (see a discussion of such a type of cut in section 5.3.3).

4. Laser cut. Only events for which the laser intensity parameter η is available, and for which therefore a simulation prediction exists, are considered.

5. ECAL cut. Events for which ECAL is saturated are discarded.

More than 5000 events are lect after applying the above cuts from the 46.6 GeV data sample, and about 1000 events from the 49.1 GeV data sample. For both data samples the ECAL rate is normalized to the measured $n = 1$ rate according to the formula

$$\text{ECAL rate} = \frac{1}{N_\gamma} \frac{dN_e}{dp} \qquad (C.2)$$

where dN_e the number of electrons detected within the momentum acceptance dp.

In the case of the 46.6 GeV data sample, the data were grouped in 9 η bins with $\Delta\eta$ of 0.02 within the range of $0.14 \le \eta \le 0.32$. The data within each of the 9 η bins, were further grouped according to their momentum, into momentum bins with Δp of 0.4 GeV, in the momentum range of $p_{e^-} = 6\text{-}11$ GeV. We have therefore a total of ~ 110 bins. Within each one of those 110 bins, the average signal $\langle S \rangle$ value is found using the formula

$$\langle S \rangle = \sum_{i=1}^{N} \frac{w_i s_i}{w_i} \qquad (C.3)$$

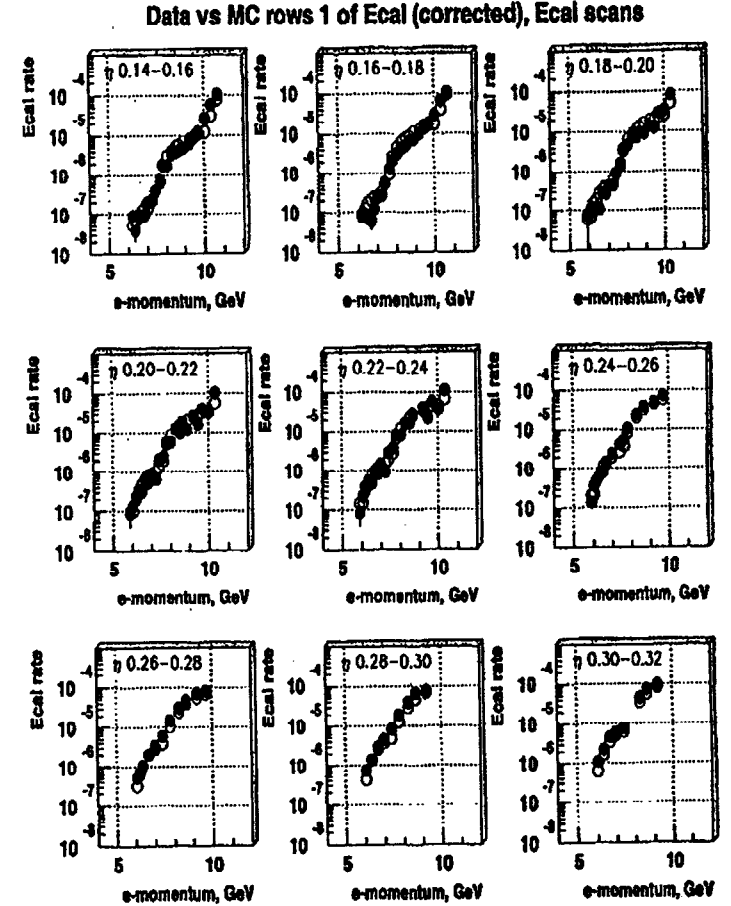**Data vs MC rows 1 of Ecal (corrected), Ecal scans**

Figure C.2: Results on the nonlinear Compton scattering showing the scattered electron momentum spectra, using a linearly polarized green laser beam and a 46.6 GeV electron beam. Solid circles show the measured rates, while open circles the simulated rates.

where $w_i = 1$ and N is the number of events in the bin, along with the RMS value of the signal distribution. Errors then are calculated as $\frac{RMS}{N}$ for each bin. Fig. C.2, shows the comparison of the measured nonlinear Compton rates in each of the 9 η

bins as function of the electron momentum, to the simulation data. The average error from the η reconstruction is $\langle \frac{\delta\eta}{\eta} \rangle \approx 11\%$ and therefore the expected uncertainty on the simulation data is of the order of 2. The measured data agree with the simulation within this error, verifying the validity of the η reconstruction. The $n = 3$ plateau is clearly visible, while due to energy smearing the $n = 4$ is not. Fig. C.3 shows the variation of the nonlinear Compton rates as a function of the laser intensity parameter η, for 9 different electron momenta. Again both the measured and the simulated data are shown. In the $n = 3$ region the data follow an η^3 power law. This is not exactly the expected $\eta^{2(n-1)} = \eta^4$ power law ($\eta^{2n} = \eta^6$ for $n = 3$ processes, "minus" η^2 for normalizing with respect to the $n = 1$ signal), because the electron spectrum for a fixed momentum range of ECAL changes with the field intensity η, resulting to the ECAL measuring different parts of the $n = 3$ energy spectrum for different field intensities. For the same reasons, the $n = 4$ region follows a power law of η^5 and not of η^6, as expected from the theory.

In the 49.1 GeV data sample the same procedure is applied. Again the data are grouped in 9 η bins with η values in the range of 0.12–0.24 and with $\Delta\eta = 0.02$. Within each η bin the data are arranged in momentum bins 0.4 GeV wide, according to their electron momentum p_{e-}, in the range of 6–11 GeV. This arrangement results again to a total of ~ 110 bins. The signal average values and the errors are calculated in the same way as in the 46.6 GeV data sample. Fig. C.4 shows the measured and the simulated data in each of the 9 η bins as a function of the electron momentum p_{e-}. There is again good agreement within the simulation uncertainty of a factor of 2 that corresponds to an average error in the η reconstruction of $\langle \frac{\delta\eta}{\eta} \rangle \approx 10\%$. Similarly Fig. C.5 shows the variation of the simulated and the measured nonlinear Compton rates with the laser intensity parameter η, for 7 different electron momenta. Although the agreement is not bad, it is worse than in the 46.6 GeV data sample, mainly due to the lower statistics. The same power law behaviors, as the ones for the 46.6 GeV data sample are observed here too.
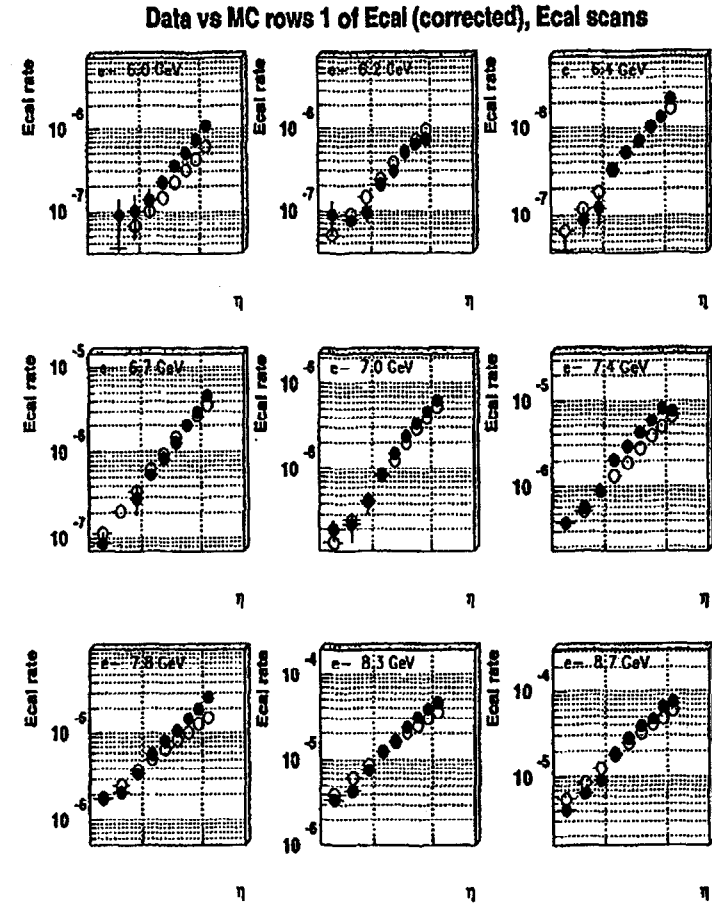
Figure C.3: Results on the nonlinear Compton scattering showing the signal dependence on the laser intensity, using a linearly polarized green laser beam and a 46.6 GeV electron beam. Solid circles show the measured rates, while the open circles the simulated rates.

Independently of the previous discussion of the comparison of the measured ECAL data with the simulation, looking at the electron spectra, does not provide us with a clear cut between the nonlinear Compton scattering and the multiple Compton scat-

Data vs MC rows 1 of Ecal (corrected), Ecal scans 49 GeV
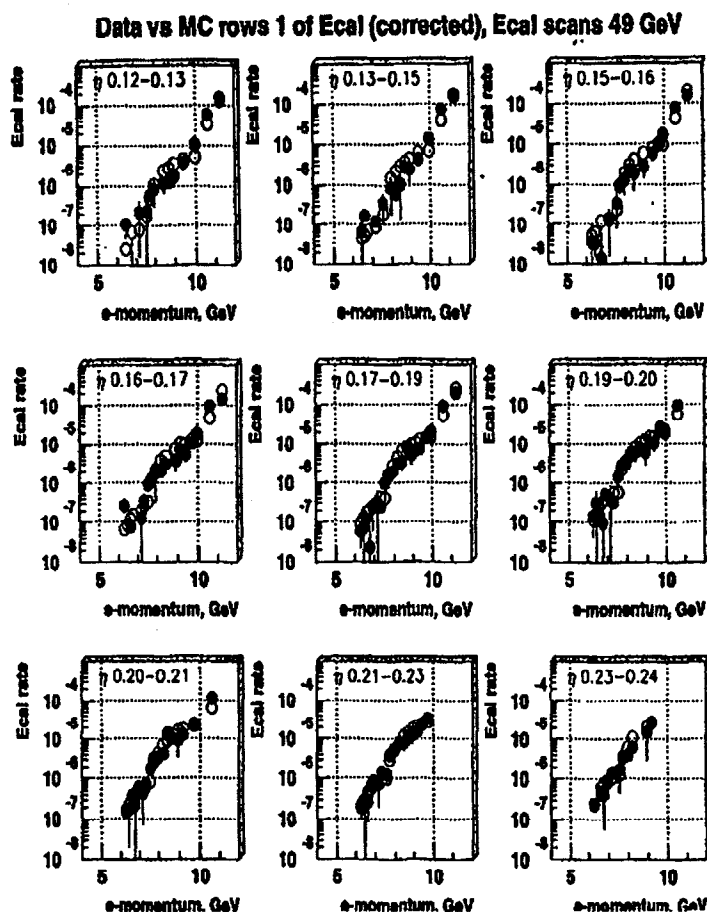

Figure C.4: Results on the nonlinear Compton scattering showing the scattered electron momentum spectra, using a linearly polarized green laser beam and a 49.1 GeV electron beam.

tering. The first process involves the scattering of a high energy electron entering the intense laser field by more than one laser photons at the same space-time point and the production of a high energy gamma, while the scattered electron as a result becomes

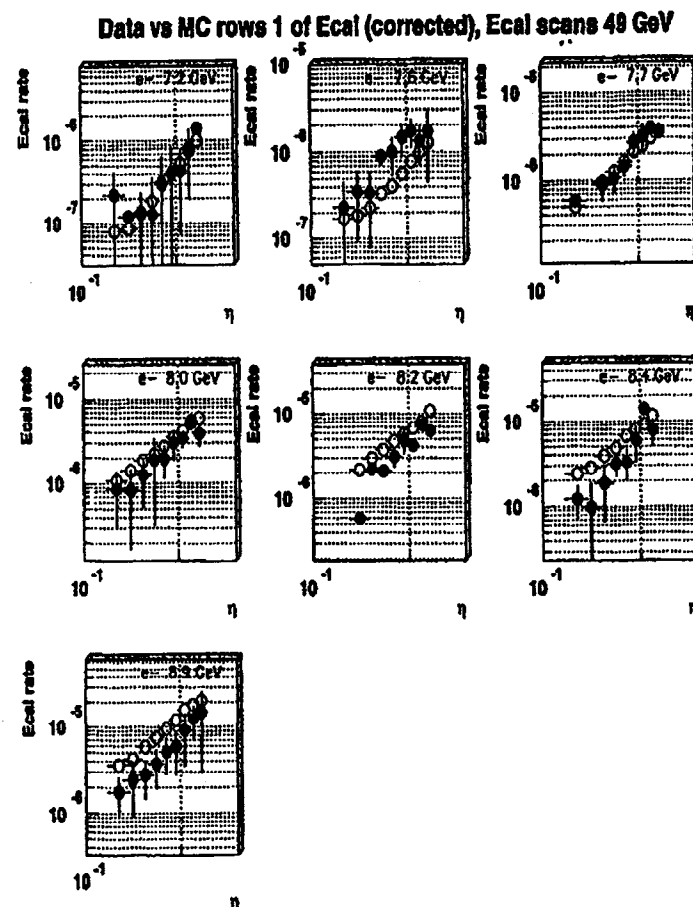**Data vs MC rows 1 of Ecal (corrected), Ecal scans 49 GeV**

Figure C.5: Results on the nonlinear Compton scattering showing the signal laser intensity dependence, using a linearly polarized green laser beam and a 49.1 GeV electron beam.

much less energetic. It is therefore a coherent process, since more than one laser photons participate simultaneously. The second process on the other hand, involves the Compton scattering of the high energy electron off single laser photons, several times
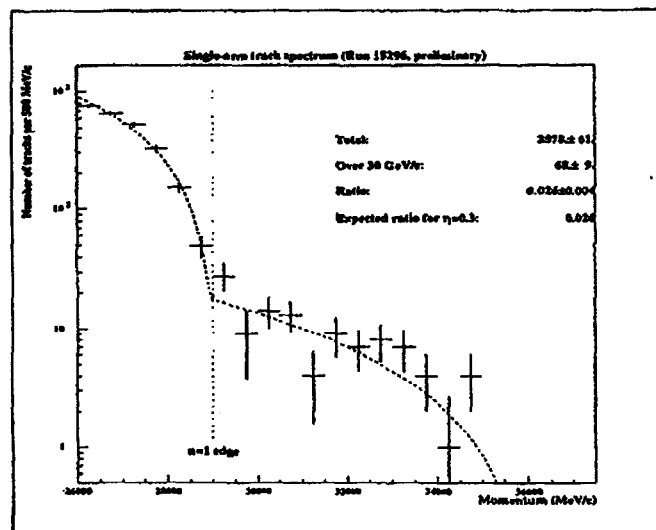
Figure C.6: Preliminary results that show the second order Compton γ energy spectrum.

during its traversal of the laser focus. It is therefore an incoherent process, since only one laser photon participates every time. It turns out that the kinematics for these two processes are exactly the same, resulting in the same kinematic edges observed in the scattered electron spectrum. Although, as it has been shown elsewhere [60], their expected rate is fully incompatible with the observed scattered electron rate in ECAL, only a look at the emitted gammas can provide us with an unambiguous way of separating the "coherent" from the "incoherent" Compton scattering. The gammas produced by multiple linear Compton scatterings, are less energetic than the gammas produced in a single nonlinear Compton scattering. The CCD detectors described in the previous section provide us with the means of measuring the energy spectra of those γ's.

As mentioned in section 1.2, in order to measure the spectrum of the forward γ's, a thin converter (foil or wire) was placed in the 0° line, and the produced electrons and positrons were diverted horizontally by a bending magnet onto the four CCD pairs, positioned on either side of the line. In view of the high event rate no attempt was made to reconstruct the γ's, but the positron or electron spectrum reflects the spectrum of the parent gamma. Such a spectrum is shown in Fig. C.6 [64]. It is based on the events of a single data run (run 15296), where a total of 2578 events after the selection cuts are used. Out of this number of events, 68 are found to be above the 30 GeV/c line, which characterizes the $n = 1$ edge in the case of a laser intensity parameter $\eta = 0.3$ and they can therefore be interpreted as γ's produced by a second-order Compton scattering. The dashed line shown in the same plot, represents the expected theoretical spectrum, which as it can be seen, agrees well with the measured data. We can conclude therefore that we have definitely observed nonlinear Compton scattering, and this is verified in an unambiguous way by the measured γ spectrum.